

UC San Diego

UC San Diego Electronic Theses and Dissertations

Title

Microstructure Investigation of Non-equiatomic FeNiCoAl-Based High Entropy Alloys

Permalink

<https://escholarship.org/uc/item/4t7805gg>

Author

Zhang, Cheng

Publication Date

2018

Peer reviewed|Thesis/dissertation

UNIVERSITY OF CALIFORNIA SAN DIEGO

Microstructure Investigation of Non-equiatomic FeNiCoAl-Based
High Entropy Alloys

A dissertation submitted in partial satisfaction of the
Requirements for the degree Doctor of Philosophy

in

Materials Science and Engineering

by

Cheng Zhang

Committee in charge:

Professor Kenneth Vecchio, Chair
Professor Renkun Chen
Professor Jian Luo
Professor Marc Meyers
Professor Kesong Yang

2018

The Dissertation of Cheng Zhang is approved, and it is acceptable in quality and form for publication and electronically:

Chair

University of California San Diego

2018

DEDICATION

In recognition of the guidance and patience he has provided over the past five years, this dissertation is dedicated to my advisor, Dr. Kenneth Vecchio.

Additionally, in recognition of all the support they have given me in getting to graduation, this dissertation is dedicated to my parents, Yixin Zhang and Qiling Chen.

TABLE OF CONTENTS

Signature Page.....	iii
Dedication.....	iv
Table of Contents	v
List of Abbreviations	viii
List of Figures	ix
List of Tables	xvii
Acknowledgements.....	xviii
Vita.....	xxi
Abstract of the Dissertation	xxiii
Chapter 1 Introduction	1
1.1 High Entropy Alloys and Non-equiatomic High Entropy Alloys	1
1.2 Microstructure and Related Property	6
1.2.1 Heterogeneous lamella structure and related properties.....	15
1.3 Martensite and Shape Memory Alloys	21
1.3.1 Introduction to martensite and martensitic transformation.....	21
1.3.2 Shape memory alloys and superelastic alloys.....	23
1.4 Research objectives and outline of dissertation.....	28
References	31
Chapter 2 Enhancement of <001> recrystallization texture in non-equiatomic Fe-Ni-Co-Al-based high entropy alloys by combination of annealing and Cr addition	40
Abstract.....	40
2.1 Introduction	41
2.2 Experimental Procedures.....	45
2.3 Results and Discussion	46
2.3.1 Texture evolution in NCACB	46
2.3.2 Grain growth in NCACB	50
2.3.2.1 Normal and abnormal grain growth in NCACB	51
2.3.2.2 Zener’s model comparison	52

2.3.2.3 Effect of grain growth on texture evolution in NCACB	56
2.3.3 Comparison of texture evolution in NCAB, NCATB and NCACB	58
2.3.4 Effect of recrystallization texture and relative grain size on the mechanical properties of NCACB	63
2.4 Conclusion	64
References	66

Chapter 3 Design of Non-Equiatomic High Entropy Alloys with Heterogeneous Lamella Structure Towards Strength-Ductility Synergy	72
Abstract	72
3.1 Introduction	73
3.2 Experimental Procedures	74
3.3 Results and Discussion	75
3.3.1 Microstructure evolution and formation of heterogeneous lamella structure	75
3.3.2 Mechanical properties of NCACB	83
3.3.3 Back-stress determined by geometrically necessary dislocations (GND) and LUR cyclic tensile test	86
3.4 Conclusions	90
References	92

Chapter 4 Non-Equiatomic FeNiCoAl-Based High Entropy Alloys With Multiscale Heterogeneous Lamella Structure For Strength And Ductility	96
Abstract	96
4.1 Introduction	97
4.2 Experimental Procedures	100
4.3 Experimental Results	101
4.3.1 Microstructure evolution in HEA-NCATB	101
4.3.2 Heterogeneous lamella, fine-grained and coarse-grained structures in HEA-NCATB	103
4.3.3 Mechanical properties	107
4.4 Discussion	108
4.4.1 Formation of heterogeneous lamella structure in HEA-NCATB	108
4.4.2 Back-stress calculation	112
4.4.3 GND Density Analysis for HL-HEA-1200	116
4.4.4 Ductility improvement through twinned induced plasticity (TWIP)	119
4.5 Conclusions	121
References	124

Chapter 5 Multifunctional Non-equiatomic High Entropy Alloys	130
Abstract	130
5.1 Introduction	131

5.2 Experimental Procedures	135
5.3 Results and Discussion	137
5.3.1 Growth of γ' precipitates during aging	137
5.3.2 Martensite morphology under different aging conditions	140
5.3.3 Recrystallization texture evolution	144
5.3.4 Mechanical Properties	146
5.3.4.1 Mechanical properties at room temperature	146
5.3.4.2 Mechanical properties at cryogenic conditions	149
5.3.5 High-damping property	152
5.4 Conclusions	153
References	155
Chapter 6 Grain Boundary Precipitation of Ta and NiAl in Superelastic FeNiCoAlTaB Alloy	159
Abstract	159
6.1 Introduction	160
6.2 Experimental Procedures	162
6.3 Results	164
6.3.1 Microstructure Evolution before Aging	164
6.3.2 Precipitation of Ta and NiAl along Grain Boundaries of NCATB	165
6.3.3 Development of Low-angle Boundaries in NCATB	171
6.3.4 Mechanical Properties	174
6.4 Discussion	175
6.4.1 Effect of LABs on the precipitation of Ta and NiAl along the grain boundaries	175
6.4.2 Precipitation Behavior of different phases along grain boundaries in NCATB	176
6.4.3 Effect of grain boundaries on the martensitic transformation	179
6.5 Conclusions	180
References	182
Chapter 7 Conclusions	186
Chapter 8 Directions for future work	190

LIST OF ABBREVIATIONS

HEA: High Entropy Alloy

HL Structure: Heterogeneous Lamella Structure

SMA: Shape Memory Alloy

SME: Shape Memory Effect

NCACB: A non-equiatomic high entropy alloy comprising of iron (Fe), nickel (Ni), cobalt (Co), aluminum (Al), chromium (Cr) and boron (B), which is being investigated in this dissertation

NCATB: A non-equiatomic high entropy alloy comprising of iron (Fe), nickel (Ni), cobalt (Co), aluminum (Al), tantalum (Ta) and boron (B), which is being investigated in this dissertation. The specific content of each element may change in different chapters.

SEM: Scanning electron microscopy

EDS: Energy dispersive spectroscopy

EBSD: Electron backscatter diffraction

XRD: X-ray diffractometer

FCC: Face centered cubic

BCT: Body centered tetragonal

BSE: Back-scatter electron

TEM: Transmission electron microscopy

LUR: Loading-unloading-reloading cyclic tensile test

LIST OF FIGURES

Figure 1.1: Schematic diagram showing the compositional space of conventional alloys, equiatomic HEAs and non-equiatomic HEAs. [12].....	4
Figure 1.2: Summary of deformation mechanisms in different HEAs showing that tuning deformation mechanisms is the crucial factor to develop strong and ductile non-equiatomic HEAs.[12].....	4
Figure 1.3: (a) Tensile stress-strain curves obtained at room temperature in the NCATB alloy (A to C) with strong recrystallization texture as shown in (b) EBSD quasi-colored orientation mapping of NCATB with RIT of 98.5%, and (c) EBSD inverse pole figures with times random corresponding to (b). [44].	8
Figure 1.4: Schematic diagram of high-angle boundary, low-angle boundary and twin boundary [41]......	9
Figure 1.5: Optical microstructure of a Cu-Al-Mn-based shape memory alloy wire with a bamboo-like structure [47]......	9
Figure 1.6: Stress near triple junction after the upper grain has transformed to martensite. The contours show stresses at the wire surface ((a) and (b)), interior ((c) and (d)), and sample midplane ((e) and (f)). The images on the left show tensile stresses and images on the right show von Mises stresses. [55].	10
Figure 1.7: Gradient nanograined structure. After a surface mechanical grinding treatment to copper, grain sizes about 20 nm in the topmost treated surface and increase gradually to the microscale with depth [56].	11
Figure 1.8: EBSD image quality map overlaid with grain boundaries in the cross section of a bimodal grained Cu sample with a harmonic structure. [65].....	12
Figure 1.9: TEM image of Cu with bimodal grains, showing 25 vol% micrometer-sized grains randomly embedded among ultrafine grains [68].....	13
Figure 1.10: (a) EBSD image of HL Ti after partial recrystallization. (b) EBSD image of recrystallized grains larger than 1 μm [59].	14
Figure 1.11: Schematic diagram of lamella structure with elongated soft coarse-grained domains embedded in an ultrafine-grained matrix [72].	16

Figure 1.12: Mechanical properties and strain hardening of HL Ti. (A) Tensile engineering stress-strain (SS) curves in HL Ti, CG Ti and UFG Ti. (B) Tensile true SS curves in HL Ti, CG Ti and UFG Ti. (C) Strain hardening rate VS true strain of HL Ti [59]. 16

Figure 1.13: Bauschinger effect and back stress of HL Ti. (A) LUR stress-strain curves of HL Ti and CG Ti. (B) Hysteresis loop for HL Ti [59]. 17

Figure 1.14: Schematic diagram for the calculation of back-stress. 17

Figure 1.15: (A) Schematic diagram of the piling-up of geometrically necessary dislocations. (B) Plastic strain and strain gradient as a function of distance from the domain interface. (C) The effective stress as a function of distance from the domain interface [72].
..... 19

Figure 1.16: Schematic diagram of geometrically necessary dislocations (GNDs). If each grain of a polycrystal, shown at (a), deforms in a uniform manner, overlap and voids appear (b). These can be corrected by introducing GNDs, as shown in (c) and (d) [75]. 20

Figure 1.17: Bain correspondence in the martensitic transformation of F.C.C to B.C.T [78].
..... 22

Figure 1.18: Schematic diagram (NiTi as an example) of the process of shape memory effect and superelasticity. Af: Austenite finish temperature, Mf : Martensite finish temperature [88]. 24

Figure 1.19: Schematic images showing three types of the deformation mode in SMAs. (a) Formation of M plate and subsequent thickening by applied stress. (b) Movement of the boundary between M variants by applied stress. (c) Transformation from one M structure to another M structure by applied stress. M-martensite [92]. 25

Figure 2.1: EBSD IPF maps for NCACB samples after cold rolling (CR) with different RITs and annealing at 1200°C. (A) CR90-1200°C-15-min; (B) CR90-1200°C-30-min; (C) CR90-1200°C-60-min; (D) CR95-1200°C-15-min; (E) CR95-1200°C-30-min; (F) CR95-1200°C-60-min. 47

Figure 2.2: EBSD IPF maps for NCACB samples after cold rolling with different RITs and annealing at 1300°C. (A) CR90-1300°C-15-min; (B) CR90-1300°C-30-min; (C) CR90-1300°C-60-min; (D) CR95-1300°C-15-min; (E) CR95-1300°C-30-min; (F) CR95-1300°C-60-min. RD- Rolling Direction, TD-Transverse Direction. 48

Figure 2.3: The development of intensity of <001> recrystallization texture with different

annealing times in NCACB specimen with RIT of 90% and 95%. 49

Figure 2.4: (A) Grain size development ($\ln(d)$) with annealing time ($\ln(T)$) in NCACB with RIT of 90% and 95%; (B) Relative grain size (d/t) development with annealing time in NCACB with RIT of 90% and 95%, d -grain size, t -thickness of the sample, and T -annealing time. 50

Figure 2.5: SEM (BSE) images for the microstructure evolution of NCACB with RIT of 90% at different annealing conditions. (A) 1150°C-60-min, (B) 1175°C-60-min, (C) 1200°C-5-min, (D) 1200°C-7.5-min, (E) 1200°C-10-min. 54

Figure 2.6: XRD pattern for NCACB (CR90) after annealing at 1150°C for 1h. γ (FCC) matrix and NiAl (B2) β phase peaks are labeled with black and red, respectively. 55

Figure 2.7: EBSD inverse pole figure (IPF) maps for NCAB and NCATB samples with different reduction in thickness (RIT) annealed at 1300°C for 30-min. (A) NCAB-CR90; (B) NCAB-CR95; (C) NCATB-CR90; (D) NCATB-CR95; (E) NCATB-CR97. RD - Roll Direction, TD- Transverse Direction. 58

Figure 2.8: Development of texture intensity with RIT in NCATB. Red circle- NCACB, green circle - Tanaka et al. [40] (NCATB, CR98.5), blue circle - Omori et al. [41] 59

Figure 2.9: Development of fraction of the low-angle boundaries in annealed NCATB and NCACB samples with different reduction in thickness. 61

Figure 2.10: (A) EBSD IPFX map for NCATB with RIT of 97% annealed at 1300°C for 30-min; (B) Corresponding statistics for the misorientation between grains in Fig. 2.10(A). 62

Figure 2.11: (A) True Stress-Strain curves for CG-HEA-1200 and CG-HEA-1300; (B) Corresponding strain hardening rate curves for CG-HEA-1200 and CG-HEA-1300. 63

Figure 3.1: (A) SEM (BSE) image for NCACB after cold rolling (RIT=90%), RD-Rolling Direction, TD- Transverse Direction; (B) EBSD IPFX map for NCACB in the transverse direction after annealing at 1150°C for 1h; (C) Grain area map corresponding to Fig. 3.1(B). 77

Figure 3.2: (A) SEM (BSE) image for NCACB after arc-melting. The grain structure and compositions of the as-cast specimen indicate the presence of NiAl (B2) precipitates between the solid solution FCC phase dendrites; (B) EDS mapping for as-cast

NCACB. 78

Figure 3.3: (A) SEM (BSE) image for NCACB. Large grains, up to 500 μm diameter, are apparent in NCACB after homogenization, hot rolling and air cooling. Some NiAl (B2) precipitates can also be observed along the grain boundaries (B). 79

Figure 3.4: (A) EBSD IPFX Mapping for NCACB after annealing at 1150 $^{\circ}\text{C}$ for 1 h, which shows clear separation of grain size in fine grained and coarse grained lamella as well as its random texture; (B) Grain area map corresponding to Fig. 3.4(A) shows three order of magnitudes difference in term of grain area (unit: μm^2). 79

Figure 3.5: (A) XRD pattern for NCACB after annealing at 1150 $^{\circ}\text{C}$ for 1h; (B) EDS Mapping for NCACB after annealing at 1150 $^{\circ}\text{C}$ for 1h. 81

Figure 3.6: SEM (BSE) images for NCACB (RIT=90% in cold rolling) after annealing (A) at 1150 $^{\circ}\text{C}$ for 1 h; (B) the HL structure still exists after 1175 $^{\circ}\text{C}$ 1 h; (C) the HL structure is produced after annealing at 1200 $^{\circ}\text{C}$ for 5 min; (D) at 1200 $^{\circ}\text{C}$ for 7.5 min and (E) at 1200 $^{\circ}\text{C}$ for 10 min; (F) at 1000 $^{\circ}\text{C}$ for 1 h. 82

Figure 3.7: Tensile behavior of NCACB with four different grain structures. (A) Tensile engineering SS curves; (B) Tensile true SS curves; (C) Strain hardening rate curves; (D) Comparison of mechanical properties between HL NCACB HEA and other materials with similar structures. 84

Figure 3.8: EBSD IPFX maps for (A) FG-HEA 1000; (B) HL-HEA 1150; (C) CG HEA 1200; (D) CG-HEA 1300; (E) EBSD IPFX for HL-HEA 1150 after tensile test. 85

Figure 3.9: (A) Grain average GND density map in logarithmic scale; (B) Grain average GND density (m^{-2}) plotted against grain area (μm^2) with each data point colored according to the order of magnitude of grain average GND density; (C) True SS curves for LUR cyclic tensile tests of HL-1150; (D) Back-stress of HL-1150. 89

Figure 3.10: (A) Total GND density distribution map in logarithmic scale (color bar: 13.2-15.2 [unit: $\log_{10}(\text{m}^{-2})$]); (B) Area fraction distribution plot of GND data shown in (A) with 20 bins. 90

Figure 3.11: Loading-unloading-reloading (LUR) cyclic tensile tests for fine grain (FG), coarse grain (CG) and heterogeneous lamella (HL) NCACB HEAs. 90

Figure 4.1: (a) SEM image for HEA-NCATB specimen after cold rolling with reduction in thickness of 90%; (b) EBSD Band Contrast (BC) image for the enlarged red square area in

(a). RD – Rolling Direction, ND – Normal Direction. 101

Figure 4.2. (a) SEM (BSE) image for HEA-NCATB after annealing and quenching; (b) EDS Mapping for HEA-NCATB before cold rolling. Coarse grains with average grain size over 400 μm are formed in Fig. 4.2(a). 102

Figure 4.3: EBSD IPFX for two kinds of HL structure formed in HEA-NCATB after annealing. (a1) EBSD IPF for HEA-NCATB after annealing at 1050°C for 30min; (a2) grain area map corresponding to (a1); (b1) EBSD IPFX for HEA-NCATB after annealing at 1200°C for 10min; (b2) grain area map corresponding to (b1). 102

Figure 4.4: Schematic diagrams and EBSD IPFX for two kinds of HL structure in HEA-NCATB. (a1) the HL structure composed of CG band and FG band. (a2) EBSD IPFX of enlarged area in Fig. 4.3(a1). (b1) the HL structure composed of FG band UFG band; (b2) EBSD IPFX of enlarged area in Fig. 4.3(b1). 104

Figure 4.5:(a) EBSD phase map for HEA-NCATB after annealing at 1075°C for 1h, red – FCC (austenite) iron, blue – (B2) NiAl; (b) EDS Mapping for the matrix and the precipitates in HEA-NCATB after annealing at 1075°C for 1h ; (c) XRD pattern for NCATB after annealing at 1075°C for 1h. 105

Figure 4.6: EBSD phase maps for HEA-NCATB. (a) 1050°C 30min; (b) 1300°C 5min; (c) 1300°C 30min. Red - FCC Fe (austenite), Blue – NiAl (B2 structure). For HL-HEA-1050, NiAl (B2) are distributed along the grain boundaries in the FG area, as shown in Fig. 4.6(a). 106

Figure 4.7: SEM(BSE) images for NCATB-HEA after cold rolling and annealing for 30min. (a) 1200°C, (b) 1225°C, (c) 1250°C, (d) 1275°C, (e) 1300°C. NiAl (B2) precipitates are pointed out by red circles. 106

Figure 4.8 XRD patterns for NCATB-HEA after cold rolling and annealing for 30min. (a) 1200°C, (b) 1225°C, (c) 1250°C, (d) 1275°C, (e) 1300°C. NiAl (B2) phase is pointed out by red letter. 106

Figure 4.9: Tensile behavior of NCATB with five different grain structures. (a) Tensile engineering stress-strain curves; (b) tensile true stress-strain curves; (c) strain hardening rate curves; (d) comparison of mechanical properties between HL-NCATB-HEA and other materials with similar structures. 108

Figure 4.10: EBSD IPFX images for HEA-NCATB. (a) after cold rolling with RIT of 90%; (b) after annealing at 1050°C for 10min; (c) phase map corresponding to the black square

area in (b). Red – FCC Fe (austenite), Blue – NiAl (B2 structure). RD – Rolling Direction, ND- Normal Direction. 110

Figure 4.11: (a) EBSD IPFX for HL-HEA-1050; (b) corresponding recrystallization and recovery figure for (a). Blue – Recrystallized Grains; Yellow – Recovery Grains; Red – NiAl (B2) precipitates. TD – Transverse Direction; RD – Rolling Direction. 111

Figure 4.12: LUR cyclic tensile true stress-strain curves for HEA-NCATB specimens. (a)CG1-HEA-1300; (b) HL-HEA-1050; (c) HL-HEA-1200. (d) schematic diagram for the calculation of back-stress; (e) Back-stress for HL-HEA-1050 and HL-HEA-1200. Red – Normal tensile SS curves; Blue – LUR cyclic tensile test SS curves. 113

Figure 4.13: GND Calculation result for HL-HEA-1200 after tensile test. (a) Grain area map for HL-HEA-1200 after tensile test; (b) grain average GND density map in logarithmic scale (color bar: 14 – 15 [unit: $\log_{10}(m^{-2})$]). 119

Figure 4.14: (a) EBSD BC image for HL-HEA-1200 after tensile test with elongation over 40%. EBSD IPFs (b1), (c1) and (d1) for the selected areas in (a). Corresponding statistics figures of misorientation versus distance (b2), (c2) and (d2) for the black square areas in (b1), (c1) and (d1), respectively. 119

Figure 4.15: Overview of strengthening mechanisms in the current non-equiatomic NCATB HEA with heterogeneous lamella structure to achieve the synergy of high strength and high ductility. 120

Figure 5.1: TEM bright field (BF) images for NCATB-HEA specimens aged at 700 °C for different times. (A) 1 hour; (B) 5 hours; (C) 10 hours; (D) 24 hours; (E) 48 hours; (F) 72 hours; (G) 96 hours. 137

Figure 5.2: (A) TEM bright field (BF) image for NCATB-HEA sample aged at 700°C for 10 hours; (B) Corresponding Selected Area Diffraction (SAD) (FTT) pattern for 2(A). Zone Axis [001]. 139

Figure 5.3: TEM HAADF image and EDS Mapping for NCATB-HEA specimen aged at 700 °C for 72 hours. 139

Figure 5.4: Optical microscope images for NCATB-HEA aged at 700 °C for (A) 48 hours, (B) 72 hours and (C) 96 hours. EBSD Inverse Pole Figures (IPF) for HEA-NCATB aged for (D) 48 hours, (E) 72 hours and (F) 96 hours. Lenticular, butterfly and lath-like martensites are shown with arrows. 141

Figure 5.5: In-situ optical microscope images for NCATB-HEA aged at 700 °C for different times. (A) 5 hours (cooling to -172 °C); (B) 10 hours (cooling to -165 °C); (C) 24 hours (cooling to -148 °C).	143
Figure 5.6: A series of in-situ optical microscope images showing thermal-induced thin-plate martensites for a complete martensitic transformation occurred in NCATB-HEA aged at 700 °C for different times. (A) 5 hours; (B) 10 hours; (C) 24 hours.	143
Figure 5.7: Development of γ' size and martensite start (M_s) temperature with aging time for NCATB-HEA aged at 700 °C. Morphology of martensites with related γ' precipitates corresponding to different aging times are shown.	144
Figure 5.8: EBSD Inverse Pole Figures (IPFX) for NCATB-HEA samples after annealing at 1300 °C for 30 minutes with different reduction (RIT) in thickness in the cold-rolling step. (A) RIT=90%; (B) RIT=95.5%; (C) RIT=97.2%. RD – Rolling Direction; TD – Transverse Direction.	145
Figure 5.9: Development of times random (texture intensity) in the recrystallized NCATB-HEA with reduction in thickness.	146
Figure 5.10: (Vickers) Microhardenss development in aged NCATB-HEA with different aging times (1-96 hours) and temperatures (500 °C , 600 °C and 700 °C).	147
Figure 5.11. (A) Tensile stress-strain curves at room temperature for HEA-NCATB specimens with RIT of 90%, 95.3%, 97% and 97.5%. (B) Comparison of yield stress in various superelastic alloys. 1. HEA-NCATB; 2. NiTi; [53][54] 3. Fe-Mn-Al-Ni; [55] 4. Cu-Al-Ni; [50] 5. Mg-Sc; [56] 6. Ti-Nb-Ta. [52]	148
Figure 5.12: (A) Compression stress-strain curve for NCATB-HEA after aging at 700 °C for 96 hours; (B) Tensile stress-strain curve for NCATB-HEA before aging.	149
Figure 5.13: A series of images for bending test in liquid nitrogen. (A) Setup for the bending test. The diameter of the curvature is $D=30$ mm; (B) Samples are totally rinsed in the liquid nitrogen and deformed to U shape during the test; (C) After bending test, samples are taken out from the liquid nitrogen.	150
Figure 5.14. Absorbed energy in one superelastic cycle as a function of applied tensile strain for NCATB-HEA (aged at 700 °C for 5 hours), NiTi,[53][54] Cu-Al-Ni [50] and Fe-Mn-Al-Ni. [55]	153
Figure 6.1: (a) SEM (BSE) image and (b) EDS Mapping results of NCATB after arc-	

melting.	164
Figure 6.2: (a) SEM (BSE) image and (b) EDS Mapping results of NCATB after hot rolling.	165
Figure 6.3: (a) SEM(BSE) images for grain boundaries of NCATB aged at 600°C for various times; (b) BSE images for grain boundaries of NCATB aged at 700°C for various times.	167
Figure 6.4. (a) TEM bright-field image for a grain boundary of NCATB after aging at 700°C for 96h; (b) Selected area diffraction pattern for the red-circle area in Fig. 4(a). Zone-Axis is close to [001].	167
Figure 6.5: HAADF image and EDS maps for the grain boundary area of NCATB aged at 700°C for 96h.	169
Figure 6.6: Optical microscope image (a1), SEM (SE image) (a2) and SEM (BSE image) (a3) for NCATB (600°C, 48h); Optical microscope image (b1), SEM (SE image) (b2) and SEM (BSE image) (b3) images for NCATB (600°C, 72h).	171
Figure 6.7: EBSD IPFX images for NCATB after cold-rolling with RIT of (a) 90%, (b) 95% and (c) 97%, and subsequent solutionization at 1300°C for 30min. RD – Rolling Direction.	173
Figure 6.8: Development of fraction of LABs and Times Random (Texture Intensity) with RIT. Squares – Fraction of LABs, Triangle – Times Random.	173
Figure 6.9: Stress-Strain curves of aged NCATB (600°C, 72h) with RIT of (a) 90%; (b) 95.5%; (c) 97.2% after cyclic tensile test.	174
Figure 6.10: (a) EBSD rolling direction inverse pole figure image for NCATB (cold rolled RIT97) aged at 600°C for 72h; 6.10(b1) and (b2) SEM(BSE) images of corresponding enlarged areas for the yellow frame in (a).	175
Figure 6.11: Schematic diagram for the accumulation process of Ta (black lines and oval) and β -NiAl (B2) phase (green ovals), pink line--- HABs(>15°), blue line--- LABs (<15°).	178
Figure 6.12: A series of in-situ optical microscope images of NCATB (RIT90, aged at 700°C for 10h) during thermal cycling process.	179

LIST OF TABLES

Table 1.1: Features of plate, lenticular, butterfly and lath martensite [80]	22
Table 2.1: ΔS , ΔH_{MIX} and VEC values for NCAB, NCACB, and NCATB.....	45
Table 2.2: Summary of calculated results using Zener's model.....	56
Table 4.1: Summary of grain radii (R_c) calculated from Zener's model.....	112
Table 5.1: Size of γ' precipitates in NCATB-HEA aged at 700 °C for 1 to 96 hrs. ·	138
Table 6.1: Statistics of Ta appearing in triple-junction area	167
Table 6.2: Statistics of NiAl(B2) appearing along grain boundaries	168
Table 6.3. Values of ΔH^{mix} (kJ/mol) calculated by Miedema's model for atomic pairs between the elements.	169

ACKNOWLEDGEMENTS

First of all, I would like to thank my advisor, Professor Kenneth Vecchio, who has taught me what it means to be a scientist and a leader. He has always been an incredible inspiration, showing me that nothing is impossible with the right amount of optimism, persistence, enthusiasm and talent.

I also would like to thank the members of my dissertation committee, Professor Renkun Chen, Professor Jian Luo, Professor Marc Meyers, and Professor Kesong Yang, for their time and insightful comments.

From the day I joined Dr. Vecchio's group, the other members including Laura Andersen, Scott Olson, Steven McCloskey, Tyler Harrington, Sumin Shin, Yu Wang, Cameron McElfresh, William Mellor, Haoren Wang, Chaoyi Zhu, Mojtaba Samiee, Kevin Kaufman, Olivia Dippo, Xiao Liu, Chunhuan Guo and Eduardo Marin, have inspired me to be a better engineer and scientist through their hard work and creativity. Here I also would like to thank the two outstanding lab technicians Wayne Neison and Sabine Faulhaber, for their great help in training and setting up equipment. Specially, I would like to appreciate my outstanding partner Chaoyi Zhu for his significant and invaluable help in my extremely challenging PhD project. The great help from Tyler Harrington in solving experimental problems is also sincerely appreciated. For the several years in the same office, I am grateful to Chaoyi Zhu, Haoren Wang and Sumin Shin for their assistance not

only in the academic field, but also in my life. The day-to-day interaction with them has made my life at UC San Diego enjoyable and has taught me a great deal about even more than materials science and engineering.

Fruitful discussions with Professor R. James (University of Minnesota), Professor Y. Sutou and Professor K. Ando (Tohoku University), and Professor Marc Meyers and Professor Jian Luo (UC San Diego) in my PhD career are really appreciated. I also would like to thank Zezhou Li of Professor Marc Meyers's group for his help in some of my experiments.

Last, but certainly not least, I would like to thank my family. My parents, my grandma, my uncles and my aunts keep in touch with me during my PhD career in the USA, and keep reminding me that no matter where you go, there is always a place you can find support. Without the support not only physically, but also mentally from my parents, it is impossible for me to complete this dissertation.

Chapter 2, in full, is a reprint of the material as it appears in *Journal of Alloys and Compounds* 768 (2018): 277-286, Elsevier. Cheng Zhang, Chaoyi Zhu, Sumin Shin, Kenneth Vecchio. The dissertation author was the primary investigator and author of this paper.

Chapter 3, in full, is a reprint of the material as it appears in *Scripta Materialia* 154 (2018): 78-82, Elsevier. Cheng Zhang, Chaoyi Zhu, Tyler Harrington, and Kenneth Vecchio. The dissertation author was the primary investigator and author of this paper.

Chapter 4, in part, has been submitted for publication of the material as it may appear in *Materials Science and Engineering A*, 2018, Elsevier. Cheng Zhang, Chaoyi Zhu, and Kenneth Vecchio. The dissertation author was the primary investigator and author of this paper.

Chapter 5, in part, has been submitted for publication of the material as it may appear in *Advanced Engineering Materials*, 2018, Wiley-VCH. Cheng Zhang, Chaoyi Zhu, Tyler Harrington, Lee Casalena, Haoren Wang, Sumin Shin, Kenneth S. Vecchio. The dissertation author was the primary investigator and author of this paper.

Chapter 6, in part, has been submitted for publication of the material as it may appear in *Materials Science and Engineering A*, 2018, Elsevier. Cheng Zhang, Chaoyi Zhu, Sumin Shin, Lee Casalena, Kenneth Vecchio. The dissertation author was the primary investigator and author of this paper.

VITA

- 2012 Bachelor of Engineering, University of Science and Technology Beijing
- 2013 Master of Science, University of California San Diego
- 2018 Doctor of Philosophy, University of California San Diego

PUBLICATIONS

1. Fu, J. X., **Zhang, C.**, Hwang, W. S., Liao, Y. T., & Lin, Y. T. (2012). Exploration of biomass char for CO₂ reduction in RHF process for steel production. *International Journal of Greenhouse Gas Control*, 8, 143-149.
2. Shin, S., **Zhang, C.**, & Vecchio, K. S. (2017). Phase stability dependence of deformation mode correlated mechanical properties and elastic properties in Ti-Nb gum metal. *Materials Science and Engineering: A*, 702, 173-183.
3. **Zhang, C.**, Zhu, C., Harrington, T., & Vecchio, K. (2018). Design of non-equiatomic high entropy alloys with heterogeneous lamella structure towards strength-ductility synergy. *Scripta Materialia*, 154, 78-82.
4. **Zhang, C.**, Zhu, C., Shin, S., & Vecchio, K. (2018). Enhancement of < 001 > recrystallization texture in non-equiatomic Fe-Ni-Co-Al-based high entropy alloys by combination of annealing and Cr addition. *Journal of Alloys and Compounds*, 768, 277-286.
5. **Zhang, C.**, Zhu, C., Shin, S., Lee, C., Vecchio, K. S. Grain Boundary Precipitation of

Tantalum and NiAl in Superelastic FeNiCoAlTaB Alloy. Submitted to Materials Science and Engineering A.

6. **Zhang, C.**, Zhu, C., Vecchio, K. S. Non-Equiatomic FeNiCoAl-Based High Entropy Alloys With Multiscale Heterogeneous Lamella Structure For Strength And Ductility. Submitted to Materials Science and Engineering A.

7. **Zhang, C.**, Zhu, C., Harrington, T., Lee, C., Wang, H., Shin, S., Vecchio, K. S. Multifunctional Non-equiatomic High Entropy Alloys. Submitted to Advanced Engineering Materials.

FIELDS OF STUDY

Major Field: Materials Science and Engineering

Studies in FeNiCoAl-based shape memory and superelastic alloys

Studies in microstructure (texture and grain boundary) development in FeNiCoAl-based alloys

Studies in design of multiscale heterogeneous lamella (HL) structures in non-equiatomic high entropy alloys (HEAs) for synergy of high strength and high ductility

Studies in design of multifunctional non-equiatomic HEAs through controlling the morphology of martensites

Studies in formation of twin in Ti-Nb-based gum metal

Professor Kenneth S. Vecchio

ABSTRACT OF DISSERTATION

Microstructure Investigation of Non-equiatomic FeNiCoAl-Based
High Entropy Alloys

by

Cheng Zhang

Doctor of Philosophy in Materials Science and Engineering

University of California San Diego, 2018

Professor Kenneth S. Vecchio, Chair

High entropy alloys (HEAs) are a new class of metallic materials with at least four principal elements. Recently, intensive studies in HEAs have led to the discovery of a

number of attractive properties. The concept of non-equiatomic HEAs has greatly expanded the compositional space for HEA design, and work on these compositions has achieved unparalleled properties. In the development of traditional structural metals and alloys, the properties are essentially determined by the microstructure achieved via processing. For this reason, it is of great importance to explore the relationship between properties and microstructures in HEAs.

In the non-equiatomic FeNiCoAl-based HEAs, Cr is effective on the enhancement of $\langle 001 \rangle$ recrystallization texture through proper thermomechanical processing, and the ductility of specimens is improved with strong recrystallization texture.

Design of heterogeneous lamella structure in non-equiatomic HEAs towards synergy of high strength and ductility is successfully made. This precipitation-controlled method for tuning the microstructure of non-equiatomic FeNiCoAl-based HEAs provides an opportunity to modify mechanical properties within a strength and ductility window perhaps more effectively than a large number of existing metals and alloys. The heterogeneous lamella HEA has demonstrated better mechanical properties over fine grained and coarse grained HEAs due to the back-stress strengthening mechanism.

A new class of non-equiatomic FeNiCoAlTaB (HEA) is introduced, which exhibits tunable properties from cryogenic/ambient superelasticity to ultra-high strength through controlling the nature or type of martensite. This alloy system can help to expand the application domain of HEAs, for example into high-damping applications, robust actuators,

space exploration and other structural material applications.

For the precipitation behavior of tantalum (Ta) and NiAl along grain boundaries of polycrystalline FeNiCoAlTaB superelastic alloy, it is found that Ta precipitates at grain boundary triple-junctions first, then along grain boundaries, and acts as nuclei for β -NiAl phase formation. The superelasticity can be improved through suppressing the precipitation of Ta and NiAl along grain boundaries.

Chapter 1 Introduction

1.1 High Entropy Alloys and Non-equiatomic High Entropy Alloys

High Entropy Alloys (HEAs) are a new class of metallic materials with at least four equiatomic or near-equiatomic elements, and they were first independently discovered by Yeh *et al.* [1] and Cantor *et al.* [2] in 2004. During the time of exploration, most studies have been focused on one of the original concepts of HEAs for alloy design, which utilizes an equiatomic ratio of multiple principal elements to obtain the maximum configurational entropy [1, 3]. Based on Boltzmann's hypothesis in the relationship between entropy and system complexity, the configurational entropy change per mole, ΔS_{mix} , during the formation of a random solid solution with N components can be expressed in the following equation [3]:

$$\Delta S_{\text{mix}} = -R \sum_i C_i \ln C_i \quad (1.1.1)$$

where R (=8.31 J/K·mol) is the gas constant, and C_i is the molar content of the i th component. For the equiatomic HEAs, the configuration entropy of mixing reaches its maximum, and Eq. (1) can be expressed as follows:

$$\Delta S_{\text{mix}} = R \ln N \quad (1.1.2)$$

In the original concept, Yeh *et al.* define HEAs as those composed of five or more principal elements in equimolar ratio. In order to extend the scope of alloy design, HEAs may contain principal elements with the concentration of each element being between 5 and 35 at. % [1]. Apart from the original definition in the guidance for alloy design, in 2008, Zhang *et al.* put forward a two-parameter empirical rule to guide the design of HEAs [4],

that is, $-15 \text{ kJ/mol} < \Delta H_{\text{mix}} < 5 \text{ kJ/mol}$ and $0 < \delta < 5$, in which ΔH_{mix} and δ can be calculated from the following equations:

$$\Delta H_{\text{mix}} = 4 \sum_{i=1, i \neq j}^n \Delta H_{ij} C_i C_j \quad (1.1.3)$$

where ΔH_{mix} is the mixing enthalpy for the equiatomic alloy of i th and j th elements based on Miedema's model [5].

$$\delta = 100\% \sqrt{\sum_{i=1}^n C_i (1 - r_i / \sum_{j=1}^n C_j C_j)^2} \quad (1.1.4)$$

where r_i is the atomic radius of the i th element.

Another parameter that may be taken into account for alloy design of HEAs is the valence electron concentration (VEC). Guo *et al.* found that the weighted average of the VEC plays an important role in determining fcc or bcc structure of solid solution HEAs [6]. The VEC of HEAs can be calculated through the following equation [7]:

$$\text{VEC} = \sum_{i=1}^n C_i (\text{VEC})_i \quad (1.1.5)$$

where $(\text{VEC})_i$ is the valence electron configuration of the i th element. For fcc HEAs, the VEC is in the range 8.5 ± 1.0 . For bcc HEAs, the VEC is between 4.3 and 5.7. For hcp HEAs, the VEC is 2.8 ± 0.2 . Through controlling the values of VEC, Chen *et al.* proposed a method for designing HEAs with a combination of high strength and high ductility [8]. In this dissertation, to simplify the calculation of standards for HEAs, Eq. (1), (3) and (5) are employed to determine whether alloys are HEAs or not.

Based on the original concept of HEAs, some attractive properties of HEAs have been discovered. However, this design concept limits the compositional space and excludes

non-equiatomic candidates with potentially outstanding properties and potentially more commercially viable. Meanwhile, an increasing number of studies have shown that formation of single-phase solid solutions in HEAs shows weak dependence on maximization of the configurational entropy through equiatomic ratios of elements [9-12]. The concept “non-equiatomic High Entropy Alloys” (Non-equiatomic HEAs), first put forward by Raabe and his colleagues [13, 14], has greatly expanded the compositional space for HEA design, and work on these compositions has achieved unparalleled mechanical properties [13-15]. For example, the non-equiatomic $\text{Fe}_{49.5}\text{Mn}_{30}\text{Co}_{10}\text{Cr}_{10}\text{C}_{0.5}$ HEA with various deformation mechanisms, including substitution solid solution, interstitial solid solution, dual-phase, dislocations, grain boundaries, transformation induced plasticity (TRIP), twinning induced plasticity (TWIP), stacking faults, and nano-precipitation, can overcome the strength-ductility trade-off and show a synergy of high strength and high ductility [14]. The non-equiatomic HEA concept provides possibilities for the unification of various strengthening and toughening mechanisms, enabling great improvement of strain-hardening capacity and strength-ductility combinations.

During the initial time of exploration for HEAs, four core effects of HEAs, namely, high entropy effect, lattice distortion, sluggish diffusion and cocktail effect, were put forward by several researchers [1, 16, 17]. In a recent critical review paper, Miracle and Senkov [18] proposed that the ‘entropy effect’ is not supported by the present data, but it has nevertheless made an enduring contribution by inspiring a clearer understanding of the

importance of configurational entropy on phase stability. The ‘sluggish diffusion’ hypothesis is also not supported by available data, but it motivates re-evaluation of a classical concept of metallic diffusion. Additional work is needed to address a third ‘core effect’ on lattice distortion. The final ‘core effect’, known as the ‘cocktail’ effect, is not a hypothesis and requires no proof.

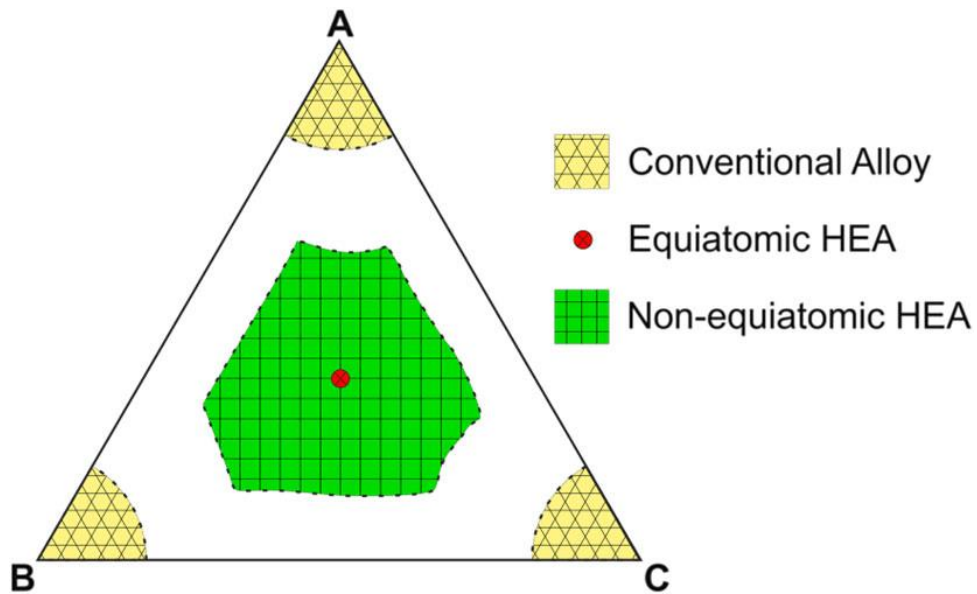


Figure 1.1 Schematic diagram showing the compositional space of conventional alloys, equiatomic HEAs and non-equiatomic HEAs. [12]

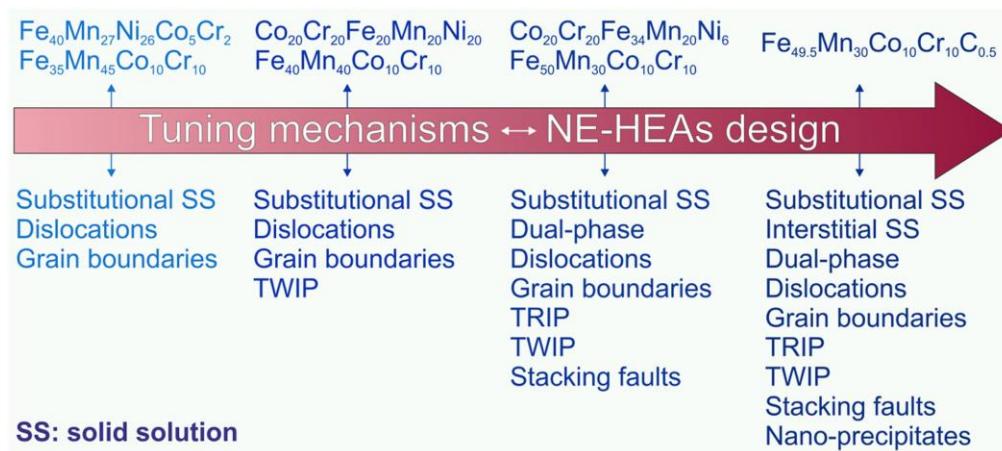


Figure 1.2 Summary of deformation mechanisms in different HEAs showing that tuning deformation mechanisms is the crucial factor to develop strong and ductile non-equiatomic HEAs.[12]

Recently, intensive studies in HEAs have led to the discovery of a number of attractive properties, such as good mechanical properties at cryogenic temperature [19-21], formation of nanotwins in thin films [22], irradiation responses [23], superconductivity [24], and refractory properties [25]. The newly-designed eutectic HEAs and high entropy superalloys (HESAs) greatly expand the application fields of HEAs, especially in the directly cast and high-temperature areas [26-28]. For the fabrication of HEAs, apart from conventional arc melting and induction melting, some special fabrication methods are also employed to produce HEA specimens, including carbothermal shock synthesis of HEA nanoparticles [29], selective laser melting (SLM) or additive manufacture [30-32], rapid solidification [33], and spark plasma sintering (SPS) [34]. With the use of in-situ TEM or SEM, the dislocation behavior and deformation mechanisms in HEAs have been investigated [35-37]. Furthermore, the high stability of structure in the CrMnFeCoNi HEA after high-strain rate deformation during the dynamic study suggests a high ballistic resistance for HEAs [38]. Grain boundary strengthening has recently been employed to the HEAs with addition of a small amount of boron [39]. The various properties of HEAs cited here mainly benefit from the diversity of microstructures [18].

1.2. Microstructure and Related Property

In the development of traditional metals and alloys, the properties are essentially determined by the microstructure, and modification of mechanical properties through controlled microstructure design has succeeded in many studies [40-43]. For example, the

strong recrystallization texture in Fe-Ni-Co-Al-based superelastic alloys [44-46] as shown in Fig. 1.3, bamboo-like or oligocrystal structure in Cu-based shape memory alloys [40, 47-51] as shown in Fig. 1.5 and Fig. 1.6, and gradient structures in nano-scale metals [52, 53] as presented in Fig. 1.7.

Crystalline solids are usually composed of a large number of grains separated by grain boundaries. In general, grain boundaries are classified in terms of the misorientation between two adjacent grains into high-angle grain boundaries with misorientation angles larger than 15° , and low-angle grain boundaries with misorientation smaller than 15° . The structure of some low-angle grain boundaries can be described as an array of dislocations. The excess energy of low-angle grain boundaries increases monotonically with the misorientation angle, that is, the higher misorientation angle, the higher energy of grain boundary. The twin boundary energy is usually an order of magnitude smaller than the energy of the conventional high-angle grain boundaries. Schematic diagrams of a high-angle boundary, a low-angle boundary and a twin boundary are shown in Fig. 1.4 [41]. For the FeNiCoAlTaB (hereafter named as NCATB) superelastic alloy, the strong $\{035\}\langle 001\rangle$ recrystallization texture can effectively increase the fraction of low-angle grain boundaries, which can suppress the precipitation of NiAl (B2) phase along the grain boundaries. Once NiAl precipitates are formed along the high-angle grain boundaries, the specimen will be extremely brittle due to the serious stress concentration introduced and the low ductility of NiAl, and no superelasticity can be achieved. NCATB specimens

with strong recrystallization texture can show a very large superelastic strain over 13% with a high fraction of low-angle grain boundaries. Therefore, the precipitation of NiAl (B2) phase is mainly determined by the energy of the grain boundaries. In this way, the nature and distribution of grain boundaries are key factors for achieving superelasticity in NCATB.

Grain size affects the mechanical properties of polycrystalline alloys as given by the Hall-Petch relation [54], which can be expressed as:

$$\sigma_y = \sigma_f + k_y * d^{-1/2} \quad (1.2.1)$$

where σ_y is the yield stress, σ_f is a friction stress (constant), k_y is the strengthening coefficient, and d is the grain size. The Hall-Petch relation is a consequence of dislocation pile-ups in polycrystals. As the number of grains increases and grain diameter becomes smaller, dislocations within each grain can travel a smaller distance before they encounter the grain boundary, at which point their movement is significantly limited (dislocation pileup). It is for this reason that fine-grained materials possess a higher strength. While in grains with a diameter less than 100nm, dislocation pile-up are hard to achieve, and therefore, the Hall-Petch relation may no longer be suitable for describing the plastic flow [41].

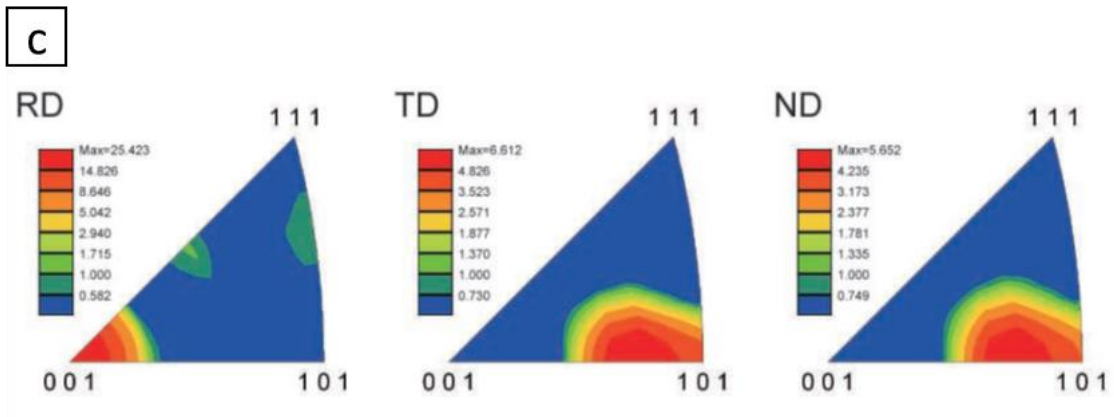
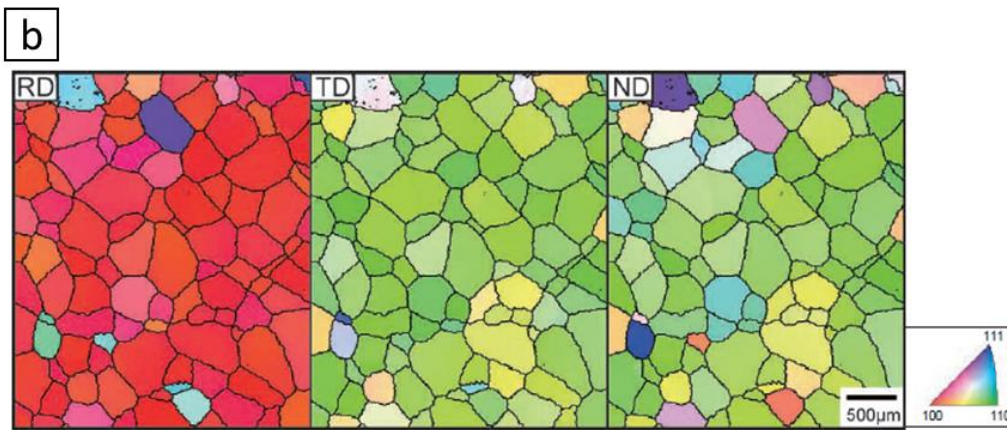
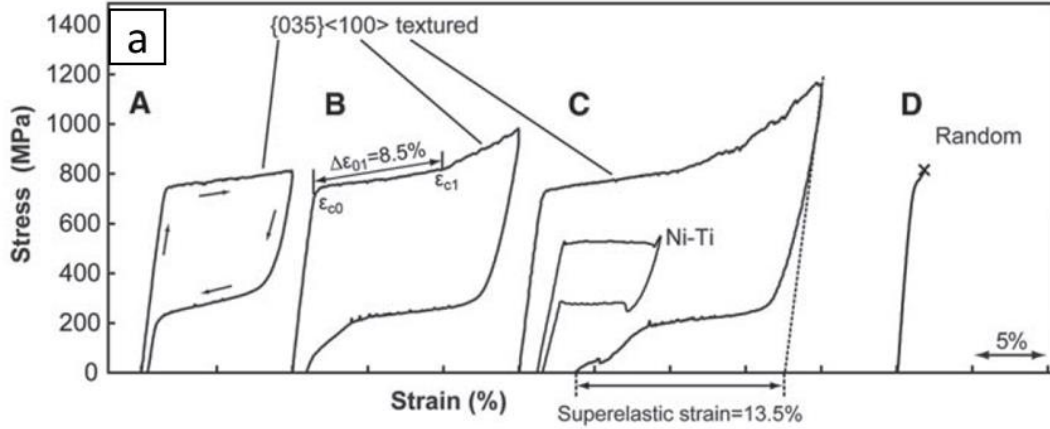


Figure 1.3 (a) Tensile stress-strain curves obtained at room temperature in the NCATB alloy (A to C) with strong recrystallization texture as shown in (b) EBSD quasi-colored orientation mapping of NCATB with RIT of 98.5%, and (c) EBSD inverse pole figures with times random corresponding to (b). RD: rolling direction; TD: transverse direction; ND: normal direction [44].

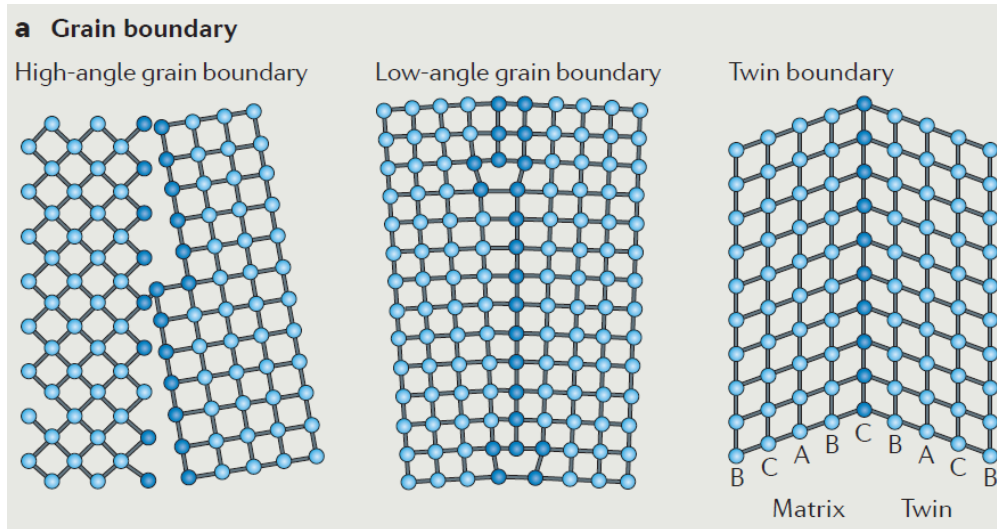


Figure 1.4 Schematic diagram of high-angle boundary, low-angle boundary and twin boundary [41].

However, for metal and alloys with the shape of thin sheet or wire, the relative grain size (d/t , d -grain size, t -thickness of the sheet or the diameter of the wire) also affects the mechanical properties. Sutou *et al.* found that the maximum pseudoelastic strain increased with increasing d/t [47]. This result can be explained from the standpoint of constraints between grains, depending on grain structure such as a fine equiaxed grain structure, a columnar-like grain structure and a fully columnar grain structure. The fully columnar grain structure is shown in Fig.1.5. Based on this research, Ueland *et al.* [55] further showed that transformation induced stress concentrations are more severe around triple junctions than around grain boundaries. Their finite element modeling also provides an estimate for constraint effects on martensitic transformation yielding higher stresses near triple junctions than near grain boundaries, as can be seen in Fig.1.6.



Figure 1.5 Optical microstructure of a Cu-Al-Mn-based shape memory alloy wire with a bamboo-like structure [47].

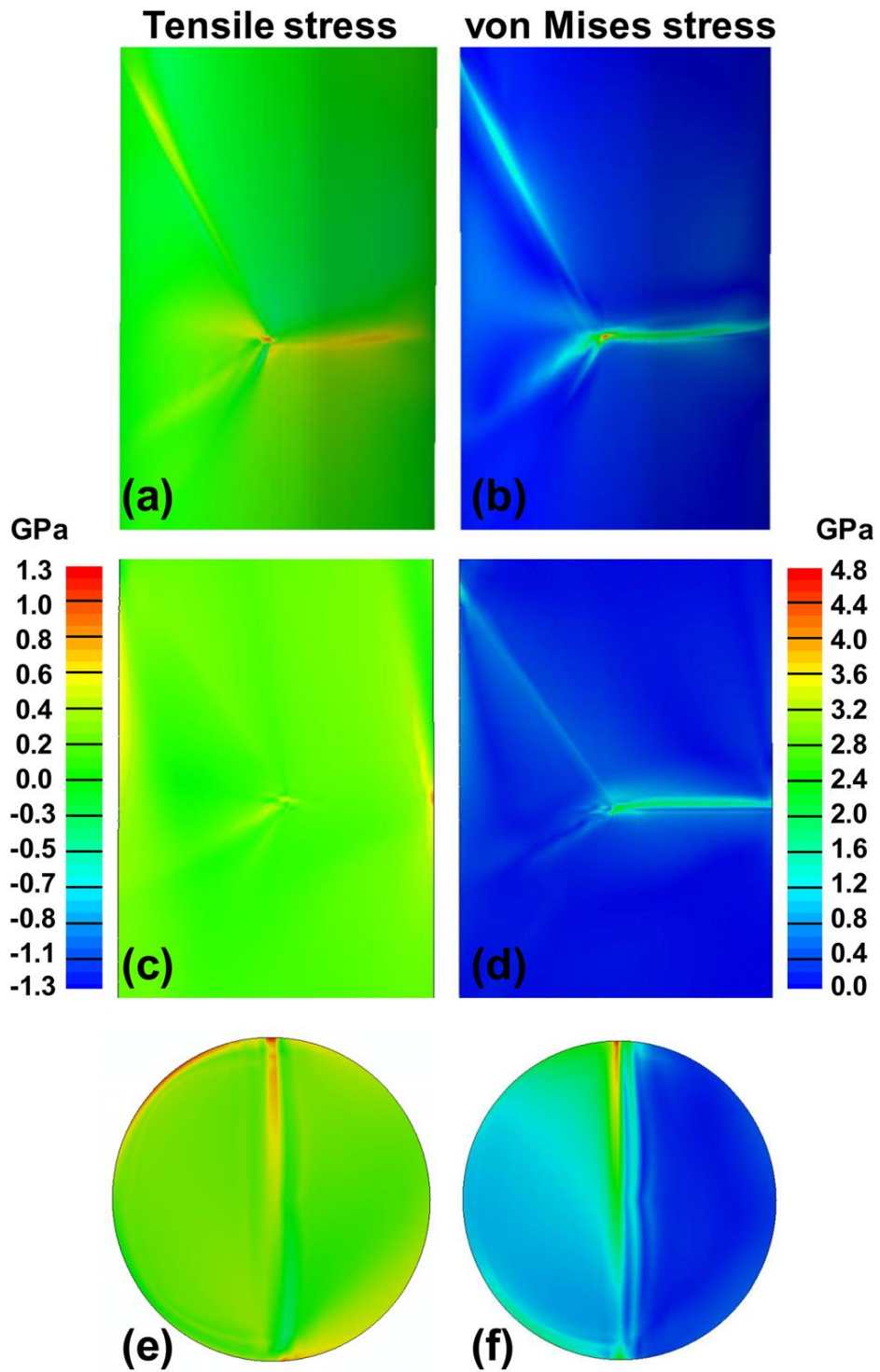


Figure 1.6 Stress near triple junction after the upper grain has transformed to martensite. The contours show stresses at the wire surface ((a) and (b)), interior ((c) and (d)), and sample midplane ((e) and (f)). The images on the left show tensile stresses and images on the right show von Mises stresses. The scale bar on the left corresponds to the tensile stresses and the scale bar on the right corresponds to the von Mises stresses [55].

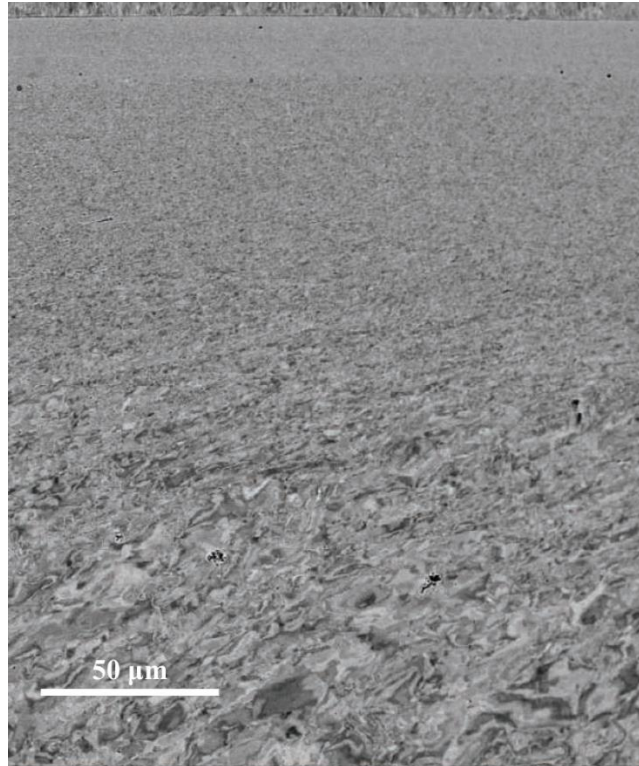


Figure 1.7 Gradient nanogained structure. After a surface mechanical grinding treatment to copper, grain sizes about 20 nm in the topmost treated surface and increase gradually to the microscale with depth [56].

For the gradient architecture in nanogained materials as shown in Fig. 1.7 [56], a layer of nanoscale-grained materials adheres to a ductile coarse-grained substrate of the same material; between them is positioned a transition layer with a gradient in grain size. For the fabrication of gradient structure, surface mechanical attrition treatment (SMAT) and surface mechanical grinding treatment (SMGT) are the two typical methods [57, 58]. For normal nanogained materials, the tensile brittleness of nanogained metals originates from the superposition of strain localization and early necking, owing to the lack of work-hardening. While for the gradient-structured materials with gradual spatially varying grain sizes, it is elastically homogeneous but plastically exhibits a gradient, which results in the

delocalization of strains and work-hardening from the coarse-grained substrate. When a gradient-grained specimen is strained, deformation in coarse grains starts first and smaller grains deform at higher loads. With an increasing applied load, plastic deformation propagates from coarse-grained areas to finer and finer grains progressively, until it reaches the topmost nanogained layer. Intergranular stress between neighboring grains of different sizes is effectively released and strain localization is suppressed, enabling the nanogained skin to undertake plastic deformation concurrently with the other part of the sample [56].

Recently, apart from the gradient structures, heterogeneous lamella structures, bimodal structures, and harmonic structures have been fabricated to overcome strength-ductility trade-off in some pure metals like Ti and Cu [41, 52, 59] , steels [53, 60, 61], aluminum alloys [62, 63], and CoCrNi medium entropy alloys [64] over a wide range of length scale [42].

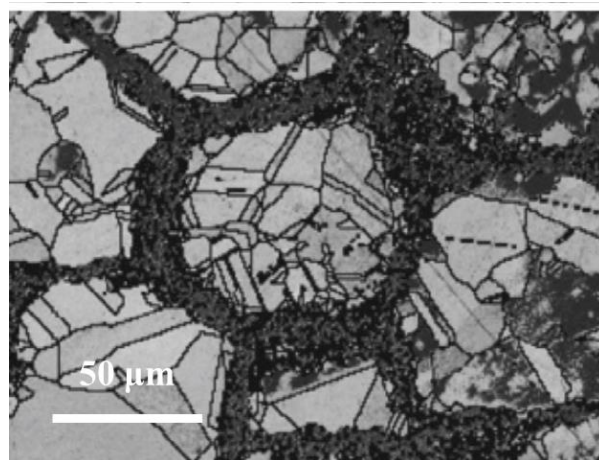


Figure 1.8 EBSD image quality map overlaid with grain boundaries in the cross section of a bimodal grained Cu sample with a harmonic structure. It was produced by consolidation of powders with a core-shell microstructure wherein the coarse-grained inner part of the powder is surrounded by a severely deformed layer with submicron sized grains [65].

Harmonic structure. Prior to sintering via processes like hot pressing or spark plasma sintering (SPS), powders with different sizes are mixed and severely deformed [65-67]. High strength and large elongation obtained in this structure can be attributed to the extension of uniform tensile strain, which results from the continuous network of ultrafine-grained areas encompassing coarse-grained areas [42].

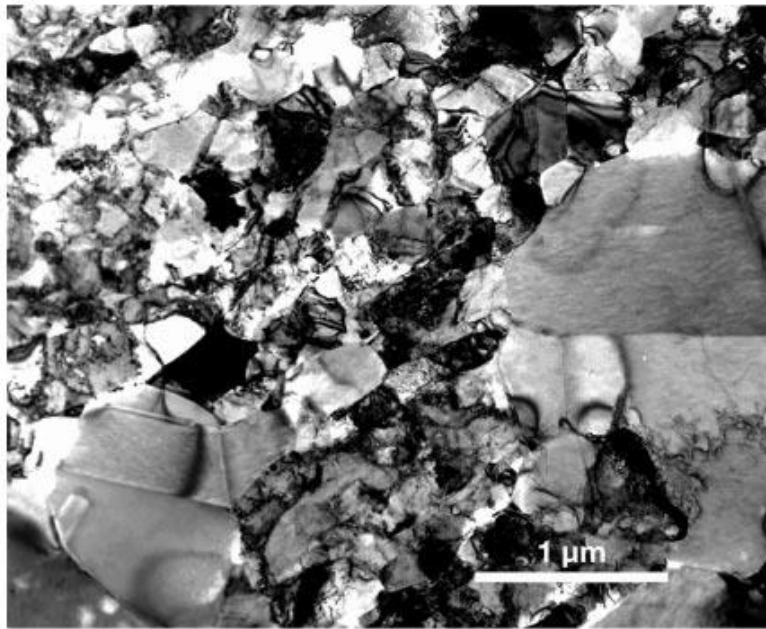


Figure 1.9 TEM image of Cu with bimodal grains, showing 25 vol% micrometer-sized grains randomly embedded among ultrafine grains [68]

Bimodal Structure. Two methods can be employed to fabricate bimodal structure in metals and alloys. One is cryogenic rolling with the subsequent secondary recrystallization, which helps to achieve a good strength-ductility synergy in Cu [68]. The other is the use of powder metallurgy, which employs particles with different sizes through hot pressing or SPS [62, 69, 70]. Wang *et al.* suggest that the additional work hardening capacity of bimodal grains is mainly due to dislocation accumulation resulting from an

excessively large number of geometrically necessary dislocations (GNDs) that form to accommodate the large strain gradient across the ultrafine-coarse grain boundaries [68].

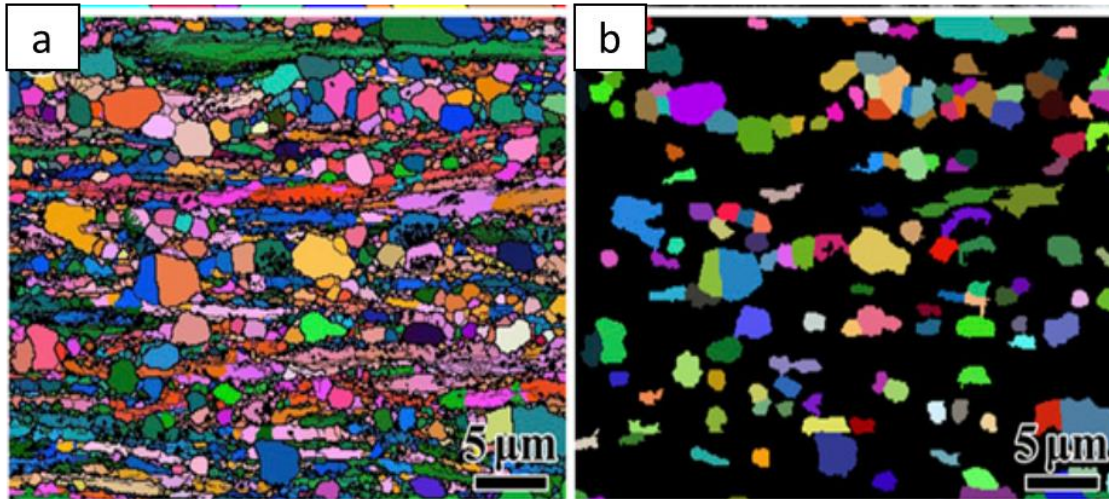


Figure 1.10 (a) EBSD image of HL Ti after partial recrystallization. (b) EBSD image of recrystallized grains larger than 1 μm [59]

Heterogeneous Lamella (HL) Structure. Inspired by the bimodal structure, Wu and his colleagues [59] first developed the heterogeneous lamella (HL) structure in pure Ti through asymmetric rolling and partial recrystallization. Due to the high back-stress, the specimen can show strength as high as ultrafine-grained Ti and elongation as large as coarse-grained Ti. Among gradient structures, harmonic structures, bimodal structures and HL structures, HL structures are the only ones that can be fabricated through conventional metallurgical method. Therefore, HL structures are the most practical and most economic among those described above. In the next section, the formation of HL structure and its strengthening mechanism will be discussed in detail.

1.2.1 Heterogeneous lamella structure and related properties

Since Wu *et al.* [59] first reported the heterogeneous lamella (HL) structure in pure Ti that can overcome strength-ductility trade-off, significantly more research has been conducted in this field [71]. The schematic diagram of HL structure is shown in Fig.1.11. from Ref. [72], where fine-grained lamellae with lower hardness are heterogeneously distributed in the ultrafine-grained lamella matrix having higher hardness. To some degree, HL structures can be treated as a special type of bimodal structure. Meanwhile, HL structured materials show superior mechanical properties to the conventional bimodal-structure materials due to the following advantages:

- (a) The formation of lamella. Tanaka and Mori [73] reported that high strain hardening can benefit more from the disc- or needle-shape inclusions than that from spherical inclusions. Meanwhile, if the orientation of the elongated inclusions is parallel to the loading direction, higher strain hardening rate can be achieved. For HL structures, both the presence of lamellae and the orientation of these bands satisfy the conditions that can produce high strain hardening rates.
- (b) The soft lamellae are fully surrounded by hard lamella matrix. The complete constraint of the coarse-grained lamellae by the fine-grained lamella matrix makes it more effective to constrain the plastic deformation of soft lamellae, which leads to producing higher back-stress than common bimodal structure.
- (c) The high density of interfaces between soft lamellae and hard lamellae. In this case, the

pile-up and accumulation of dislocations results in the enhancement of back-stress hardening and dislocation hardening.

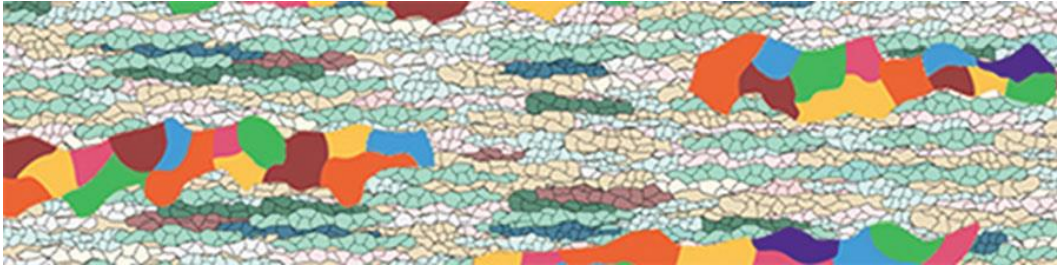


Figure 1.11 Schematic diagram of lamella structure with elongated soft coarse-grained domains embedded in an ultrafine-grained matrix [72].

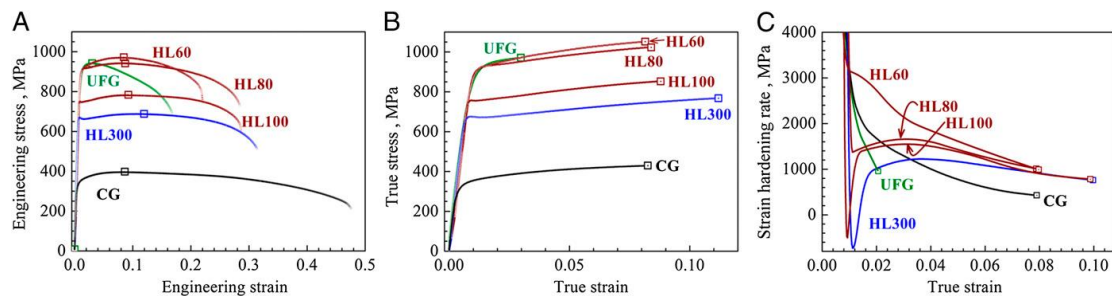


Figure 1.12 Mechanical properties and strain hardening of HL Ti. (A) Tensile engineering stress-strain (SS) curves in HL Ti, CG Ti and UFG Ti. (B) Tensile true SS curves in HL Ti, CG Ti and UFG Ti. (C) Strain hardening rate VS true strain of HL Ti [59].

Fig. 1.12 shows the mechanical properties of HL Ti, and it is found that HL Ti is as strong as ultrafine-grained (UFG) Ti and as ductile as coarse-grained (CG) Ti. Wu *et al.* [59] found that the HL Ti specimens derive the high ductility from the high strain-hardening rate. Since these CG lamellas are surrounded and constrained by FG lamellae with higher yield strength, dislocations in the coarse grains accumulate and are blocked by the fine grains. Consequently, long-range back-stresses are induced, which resist the slipping of dislocation in the GC lamella. With increasing applied load, the fine grains begin to

deform plastically, and hence the overall strength is increased by the back-stress.

Experimentally, “Loading-Unloading-Reloading” (LUR) cyclic tensile tests can be conducted for the HL specimens to show the Bauschinger effect and calculation of the back-stresses. During the “unloading-reloading” process, the hysteresis loop is characteristic of the Bauschinger effect; the larger the hysteresis loop, the stronger the Bauschinger effect.

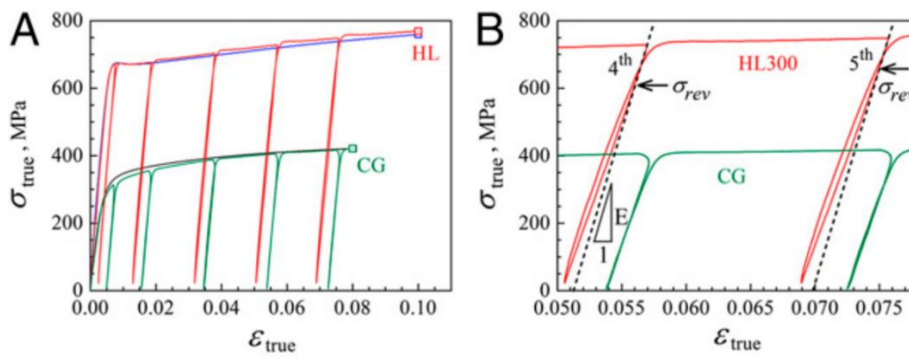


Figure 1.13 Bauschinger effect and back stress of HL Ti. (A) LUR stress-strain curves of HL Ti and CG Ti. (B) Hysteresis loop for HL Ti [59].

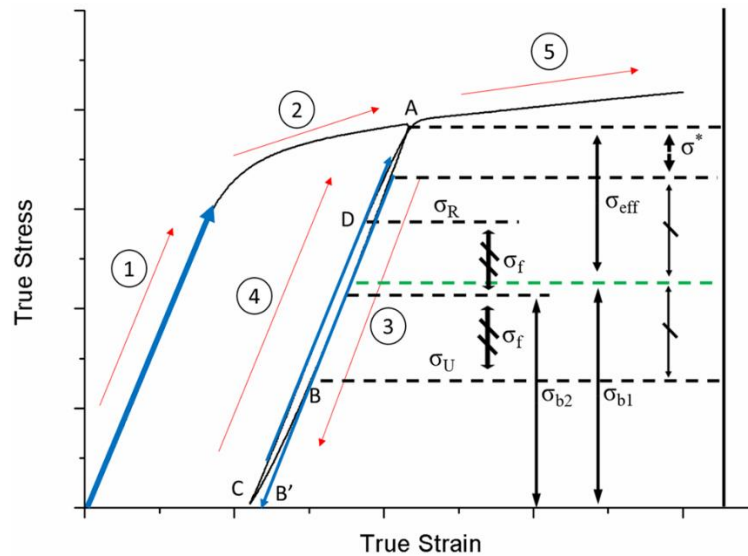


Figure 1.14 Schematic diagram for the calculation of back-stress. σ_{b1} is the back-stress, σ_n is the flow stress, σ_{eff} is the effective stress, σ^* is the thermal part of the flow stress σ_n , and σ_U is the yield stress in the unloading step. σ_{b2} is the back-stress, σ_f is the friction stress, and σ_R is the yield stress in the reloading process.

Recently, Wu and his colleagues [74] proposed a method for calculating the back-stress. They assume that the friction stress is a constant during the unloading-reloading process, and the back-stress is stable with loading before the unloading yield point B (labeled in Fig. 1.14). The equations are shown as follows:

$$\sigma_{b2} = \sigma_U + \sigma_f \quad (1.2.2)$$

$$\sigma_R = \sigma_{b2} + \sigma_f \quad (1.2.3)$$

where σ_{b2} is the back-stress, σ_f is the friction stress, and σ_R is the yield stress in the reloading process. By solving the above two equations, the back-stress and the friction stress can be expressed as:

$$\sigma_{b2} = (\sigma_R + \sigma_U)/2 \quad (1.2.4)$$

$$\sigma_f = (\sigma_R - \sigma_U)/2 \quad (1.2.5)$$

In this method, since the back-stress is induced by geometrically necessary dislocations (GNDs), and the density of GNDs remains stable before the yield point of the unloading process, the back-stress is approximately constant. Meanwhile, this method employs the same criteria for defining unloading yield and reloading yield, which leads to the same deviation of the effective Young's modulus. Therefore, we employ this method for back-stress calculation in the current study.

The back-stress is closely related to the plastic strain gradient. In Fig. 1.15(A), the strain is zero at the interface of the domain (namely, pile-up head), and the strain is increased to seven Burgers vector at the dislocation source. Fig. 1.15(B) and 1.15(C) show

that the pile-up of GNDs produces strain gradients as well as stress gradients. Therefore, if strain gradients appear, the pile-up of GNDs and corresponding back-stress will also exist [72].

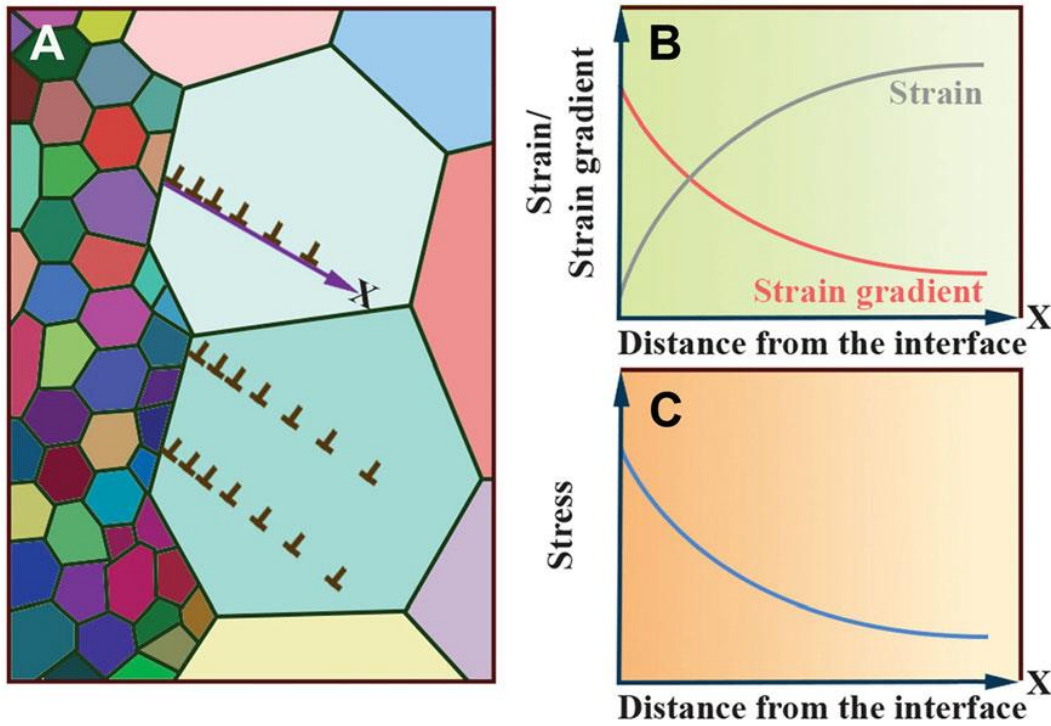


Figure 1.15 (A) Schematic diagram of the piling-up of geometrically necessary dislocations. (B) Plastic strain and strain gradient as a function of distance from the domain interface. (C) The effective stress as a function of distance from the domain interface [72].

For the geometrically necessary dislocations (GNDs), Ashby [75] first systematically defined them and compared GNDs with the statistically stored dislocations (SSDs). In a two-phase alloy, when one component deforms plastically more than the other, the gradients of deformation will build up with a wavelength about equal to the spacing between phases. In this way, the gradients of deformation imposed by the microstructure require that dislocations be stored. In other words, dislocations are stored to accommodate

the deformation gradients, and so as to allow compatible deformation of the two phases. These dislocations is named as geometrically necessary dislocation (GND) because they are required to achieve the shape changes associated with plasticity. The accumulation of SSDs is likely a result of chance encounters in the crystal resulting in mutual trapping, and they are determined by the material itself instead of associated with shape changes in the microstructure. The schematic diagram of GNDs is shown in Fig. 1.16 [75].

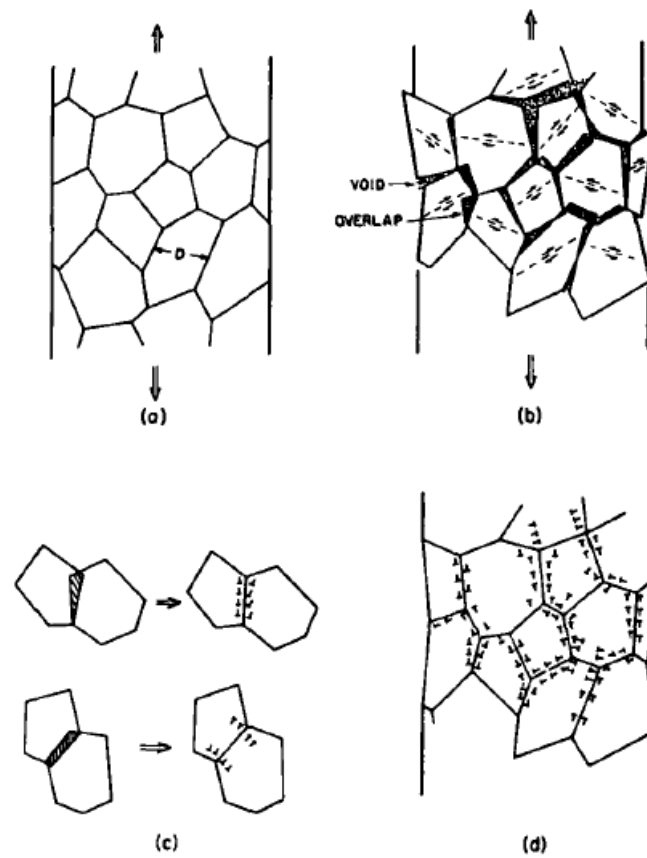


Figure 1.16 Schematic diagram of geometrically necessary dislocations (GNDs). If each grain of a polycrystal, shown at (a), deforms in a uniform manner, overlap and voids appear (b). These can be corrected by introducing GNDs, as shown in (c) and (d) [75].

The accumulation of GNDs can be described in a general way by the following

equation:

$$\rho^G = (1/\lambda^G) * 4\gamma/b \quad (1.2.6)$$

where ρ^G is density of GNDs, λ^G is the geometric distance, b is the Burgers vector, and λ is the shear strain. In polycrystals, or structures composed of two primary phases, λ^G is proportional to the grain size, or phase separation [75].

1.3 Martensite and Shape Memory Alloys

1.3.1 Introduction to martensite and martensitic transformation

Martensite, which forms as the result of a diffusionless phase transformation, plays an important role in the mechanical properties of various materials, especially ferrous alloys [76, 77]. The martensitic transformation always occurs from a higher symmetry phase to a lower symmetry phase. In Fe-Ni alloys, the martensite start temperature (M_s) of the FCC→BCT/BCC transformation is known to decrease with increasing Ni concentration, which can affect the resultant martensite morphology. The classical Bain correspondence can be employed to describe the martensitic transformation from FCC to BCT, as shown in Fig. 1.17 [78]. In Fe-Ni alloys, four morphologies of α' martensite can form: lath, butterfly, lenticular, and thin plate. Among these four, lath martensite forms at the highest temperature and thin plate martensite forms at the lowest temperature [76-80]. In addition, with decreasing M_s temperature, the substructure of martensite changes from dislocations (lath martensite) to completely twinned (thin plate martensite). The

above features of martensites in Fe-Ni alloys can be summarized in Table 1.1 [80, 81]. For lath martensite in ferrous alloys, the typical low-energy dislocation structure, characterized by the alternating misorientation change across the lath boundaries and a high dislocation density, leads to enhanced strength, which was the basis for development of high-strength alloy steels [81, 82]. Similarly, thin plate martensite, especially the thermoelastic type, is the basis for the shape memory effect in ferrous shape memory alloys [77]. For butterfly and lenticular morphologies, the substructure comprises a mixture of dislocations and twins [80, 83, 84].

Table 1.1 Features of plate, lenticular, butterfly and lath martensite [80]

Martensite type	Plate	Lenticular	Butterfly	Lath
Shape				
Ni concentration in Fe-Ni alloy	High			Low
Formation temperature	Low			High
Substructure	Twins	Twins + dislocations	Twins + dislocations	Dislocations
Crystal orientation relationship	G-T	G-T, N-W or K-S	K-S or N-W	K-S
Habit plane	$\{3\ 10\ 15\}_\gamma$	$\{3\ 10\ 15\}_\gamma$ or $\{2\ 5\ 9\}_\gamma$	$\{2\ 2\ 5\}_\gamma$	$\{5\ 5\ 7\}_\gamma$ or $\{1\ 1\ 1\}_\gamma$

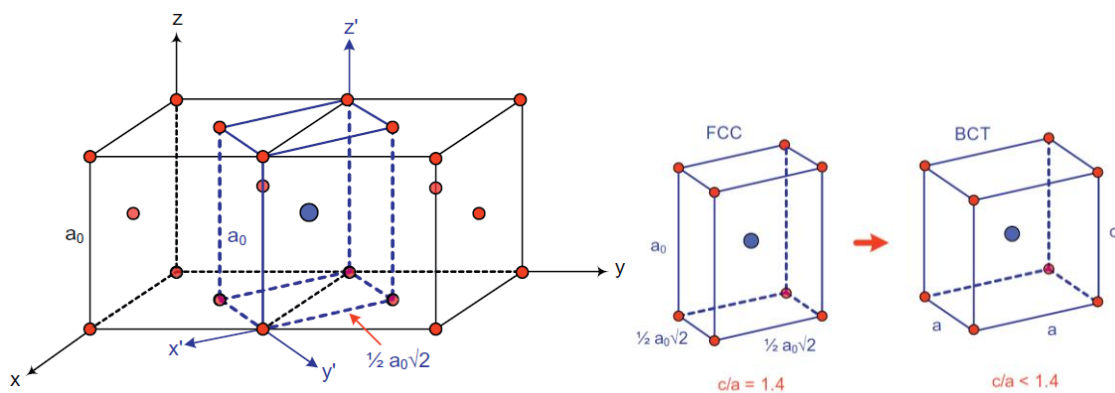


Figure 1.17 Bain correspondence in the martensitic transformation of FCC to BCT [78].

1.3.2 Shape memory alloys and superelastic alloys

Shape memory alloys (to be abbreviated SMA hereafter) are special materials with fascinating properties that are characterized by the shape memory effect (SME) and superelasticity (SE) [77]. In general, elastic strain of conventional metals and their alloys is usually limited to 0.5%, while many SMAs, such as Ni-Ti and Cu-based SMAs, can exhibit a large reversible strain of more than several percent due to SE [44, 85]. Because of the unique property SMAs are being utilized for various applications such as damping materials, sensor materials, pipe coupling, various actuators in electric appliances, automobile applications, space exploration and medical implants and guidewire etc. [44, 77].

The shape memory effect (SME) was first observed in a Au-47.5 at% Cd alloy by Chang and Read [86], and it was publicized with the discovery in Ni-Ti alloys by Buehler *et al.* [87] in the 1960s. The SME is a phenomenon such that even though a specimen is deformed in the low temperature phase, it recovers to its original shape by the reverse transformation upon heating to a critical temperature (A_f : reverse transformation finish temperature). Here, SME occurs when specimens are deformed below M_f (martensite finish temperature) or at temperatures between M_f and A_s (reverse transformation start temperature), above which the martensite becomes unstable [1]. Superelasticity is another unique property of SMAs at a higher temperature, which is associated with a large nonlinear recoverable strain upon loading and unloading. When a stress is applied to an

SMA, a phase transition is induced, most commonly from austenite with a higher symmetry to martensite with a lower symmetry. When this applied stress is removed, the specimen fully recovers its original shape. SE appears only when the temperature is high enough for austenite to become more stable than martensite [77]. Fig. 1.18 shows SME and SE in NiTi [88].

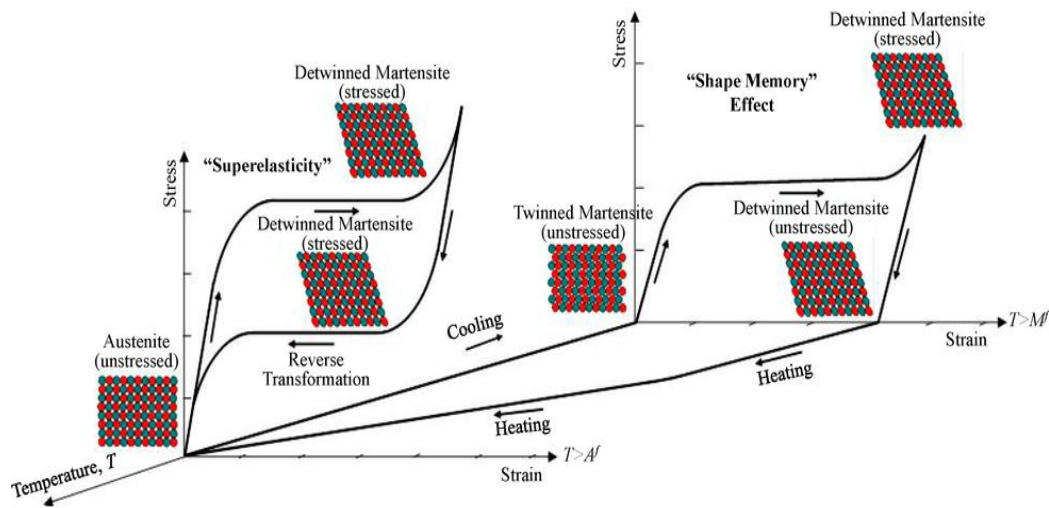


Figure 1.18 Schematic diagram (NiTi as an example) of the process of shape memory effect and superelasticity. Af: Austenite finish temperature, Mf : Martensite finish temperature [88].

Due to the excellent SME and SE, Ni-Ti alloys (also named as Nitinol) are practically utilized in engineering and medical fields [89]. However, reduced productivity and the high expense of fabrication caused by the low cold-workability restrict and limit the application of these materials. By contrast, ferrous SMAs are commercially more attractive than the Ni-Ti based SMAs because of their much better workability and lower cost [2]. Many efforts have been made to develop ferrous SMAs since the first ferrous SMA alloy (Fe-25 at%Pt) was discovered by Wayman [90].

In ferrous SMAs, an FCC austenite (γ) is transformed to three kinds of martensites with different crystal structures: (1) γ/α' (BCC or BCT) in Fe-C and Fe-Ni alloys, (2) γ/ϵ (HCP) in Fe-Cr-Ni and Fe-high Mn alloys, (3) γ/FCT in Fe-Pd and Fe-Pt alloys. Among the above three kinds of ferrous martensites, α' is the most common. Here, this review focuses on the development of ferrous SMAs with α' martensite. Although five kinds of morphologies have been discovered in α' martensite, the thin plate martensite is the only one that may exhibit a perfect SME [1]; this martensite has a highly smooth and planar interface, and transformation twins in this martensite extend completely from one interface to the other. In addition, the shape strain is accommodated elastically, and the interface of this martensite stays mobile and thus a martensite plate becomes thick gradually during cooling and becomes thin during heating by the movement of interface [77, 91]. Fig. 1.19 exhibits the three deformation modes in SMA when an external stress is applied [92].

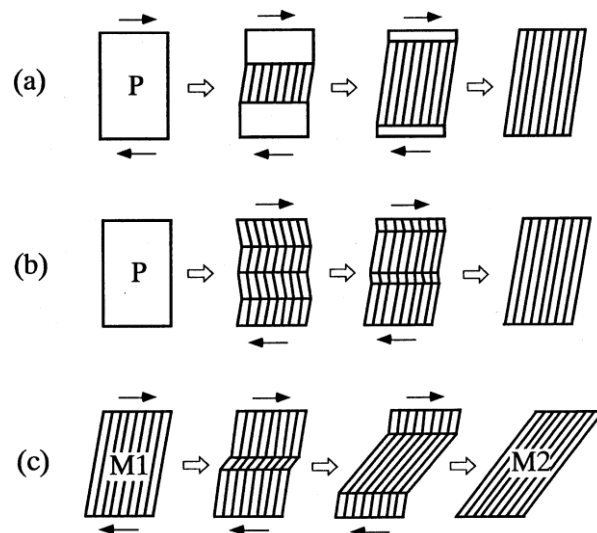


Figure 1.19 Schematic pictures showing three types of the deformation mode in SMAs. (a) Formation of martensite plate and subsequent thickening by applied stress. (b) Movement of the boundary between martensite variants by applied stress. (c) Transformation from one martensite structure to another martensite structure by applied stress [92].

In order to exhibit SME and SE, thin plate α' martensite should be thermoelastic. The criteria for thermoelastic transformation can be summarized as: (1) a small critical driving force and a small hysteresis, (2) reversibility of the motion of the interface between martensite and parent phase, (3) the shape strain is accommodated elastically and the stored energy is available to contribute a part of the driving force for the reverse transformation [92]. However, most existing ferrous SMAs show no/poor SME due to non-thermoelastic martensitic transformation with a large thermal hysteresis (several hundred degrees) [77]. A critical breakthrough was made when T. Maki and others succeeded in obtaining a thermoelastic transformation in an ausaged Fe-Ni-Ti-Co polycrystalline alloy [93].

Another significant breakthrough was made recently in 2010, when Y. Tanaka *et al.* discovered a ferrous polycrystalline, high-strength, shape-memory alloy exhibiting a superelastic strain of more than 13%, with a tensile strength above 1 gigapascal [2]. This ferrous alloy with a composition of Fe-28Ni-17Co-11.5Al-2.5Ta-0.05B (at. %)(NCATB) shows a large superelastic strain at room temperature due to a thermoelastic γ/α' transformation, and it is mechanically strengthened by fine and coherent precipitates of a γ' -(Ni,Fe,Co)₃(Al,Ta) phase with a L1₂ structure due to aging and a strong recrystallization {035}<100> texture (Fig. 1.2) obtained by thermomechanical treatment.

Martensite morphology in ferrous alloys, especially the formation of α' thin plate martensite, can be manipulated through the addition of certain elements and appropriate strengthening mechanisms. With the addition of Co to the Fe-Ni system, Shibata *et al.*

[94] found that the volume change accompanying the martensitic transformation decreases due to the Invar effect, and lath and/or lenticular martensite (primarily determined by the Ni content) can be observed in Fe-Ni-Co alloys with different compositions. In the Fe-Ni-Ti and Fe-Ni-Si alloys, only lenticular martensite forms and, consequently, these alloys systems demonstrate low hardness [95-97]. By adding Co to the Fe-Ni-Ti and Fe-Ni-Si alloys, the hardness of both is greatly enhanced, and the shape memory effect can be achieved due to the formation of thin plate martensite [93, 98]. Therefore, the addition of Co not only contributes to the increased hardness of the austenitic matrix, but also favors the formation of the thin plate martensite responsible for the shape memory effect.

Moreover, Ohtsuka *et al.* [99] have found that the addition of Al is effective in driving the formation of the γ' -Ni₃Al (L1₂) phase for precipitation strengthening in Fe-Ni-Co-based alloys. As a result, the addition of Co and Al contributes to the increase of tetragonality (increase in c/a ratio) in martensite and the hardness of the austenite matrix.

In the Fe-Ni-Co-Al system, strong γ' formers are introduced to effectively make use of the γ' phase for precipitation strengthening. Ishida [100] and Jia [101] demonstrated that Ta, Nb, Ti, Mo, V and W are strong γ' formers. Among the above elements, Tanaka *et al.* [102] showed that Ta and Nb are the two strongest since they increase the hardness of the austenite matrix to the greatest extent after aging. For the resulting γ'' -Ni₃Nb (DO₂₂) and γ' -Ni₃Ta (L1₂) precipitate phases, the lattice misfit between the γ'' -Ni₃Nb and the fcc austenite matrix should be the larger of the two [103]. Jiang *et al.* [104] have found that

new ultra-strong steel can be obtained via the method aiming at minimizing lattice misfit between the precipitates and the matrix. Therefore, Ta is chosen as the strong γ' former in the current study, as it maximizes γ' precipitate formation and minimizes lattice misfit.

1.4 Research objectives and outline of dissertation

The basic concept of high entropy alloys (HEAs) and some properties of HEAs have been introduced in the previous sections, and some typical heterogeneous structures that can overcome strength-ductility trade-off in materials were also presented. However, to date, studies in tuning the mechanical properties of HEAs through controlling the microstructures are rarely reported. Therefore, it is of great importance to investigate the microstructure in HEAs to control and improve the properties of HEAs. On the other hand, the current research essentially focuses on the mechanical properties of HEAs, very limited studies have been reported to explore the multifunctional properties and expand the application fields of these new alloys. Therefore, it is also necessary to explore the multifunctional properties of HEAs.

In order to address the issues outlined in the preceding paragraphs, the work in the current dissertation is organized as follows:

- In Chapter 2, the recrystallization texture in the non-equiatomic FeNiCoAl-based HEAs is investigated in various thermomechanical processing conditions. The comparison of the texture intensity in FeNiCoAl-based alloys with different addition of elements is presented. The optimal annealing condition is also determined in the

study. Additionally, the relationship between ductility and texture is discussed in this chapter.

- In Chapter 3, a newly-developed method used for the design of heterogeneous lamella (HL) structure in the non-equiatomic HEAs towards synergy of high strength and ductility is introduced. A back-stress strengthening mechanism, unique to deformation of heterogeneous microstructures, is verified through electron backscatter diffraction enabled geometrically necessary dislocation density analysis and LUR cyclic tensile tests.
- In Chapter 4, a new method based on conventional thermomechanical processing is proposed for design of non-equiatomic FeNiCoAlTaB (NCATB) HEA with multiscale HL structures to achieve outstanding mechanical properties. The function of shear bands formed in the cold rolling step will be explored for the formation of HL structures. Various strengthening mechanisms in HL NCATB HEA are discussed in this chapter.
- In Chapter 5, a new class of non-equiatomic FeNiCoAlTaB (NCATB) HEA is introduced, which exhibits tunable properties from cryogenic/ambient superelasticity to ultra-high strength through controlling the nature or type of martensite. This current alloy system can help to expand the application domain of HEAs, for example into high-damping applications, robust actuators, space exploration and other structural material applications.

- In Chapter 6, the precipitation behavior of tantalum (Ta) and NiAl along grain boundaries has been investigated in polycrystalline Fe-28.5Ni-17.5Co-11.5Al-2.5Ta-0.05B (NCATB) (at.%) alloy in order to understand their role in limiting its superelastic behavior. The relationship between fraction of low-angle boundaries and superelasticity is also explored in this chapter.
- In Chapter 7, the conclusions of this dissertation are presented.
- In Chapter 8, directions and some suggestions for the future work are provided.

References

- [1] J. Yeh, S. Chen, S. Lin, J. Gan, T. Chin, T. Shun, C. Tsau, S. Chang, Nanostructured high-entropy alloys with multiple principal elements: novel alloy design concepts and outcomes, *Adv. Eng. Mater.* 6 (2004) 299–303.
- [2] B. Cantor, I.T.H. Chang, P. Knight, A.J.B. Vincent, Microstructural development in equiatomic multicomponent alloys, *Mater. Sci. Eng. A.* 375 (2004) 213–218.
- [3] Y. Zhang, T.T. Zuo, Z. Tang, M.C. Gao, K.A. Dahmen, P.K. Liaw, Z.P. Lu, Microstructures and properties of high-entropy alloys, *Prog. Mater. Sci.* 61 (2014) 1–93.
- [4] Y. Zhang, Y.J. Zhou, J.P. Lin, G.L. Chen, P.K. Liaw, Solid-solution phase formation rules for multi-component alloys, *Adv. Eng. Mater.* 10 (2008) 534–538.
- [5] H. Bakker, Enthalpies in alloys, Miedema's semi-empirical model, *Trans. Tech. Publ.* (1998).
- [6] S. Guo, C. Ng, J. Lu, C.T. Liu, Effect of valence electron concentration on stability of fcc or bcc phase in high entropy alloys, *J. Appl. Phys.* 109 (2011) 103505.
- [7] Q.F. He, Z.Y. Ding, Y.F. Ye, Y. Yang, Design of high-entropy alloy: a perspective from nonideal mixing, *JOM.* 69 (2017) 2092–2098.
- [8] R. Chen, G. Qin, H. Zheng, L. Wang, Y. Su, Y. Chiu, H. Ding, J. Guo, H. Fu, Composition design of high entropy alloys using the valence electron concentration to balance strength and ductility, *Acta Mater.* 144 (2018) 129–137.
- [9] Y.P. Wang, B.S. Li, H.Z. Fu, Solid Solution or Intermetallics in a High-Entropy Alloy, *Adv. Eng. Mater.* 11 (2009) 641–644.
- [10] F. Otto, Y. Yang, H. Bei, E.P. George, Relative effects of enthalpy and entropy on the phase stability of equiatomic high-entropy alloys, *Acta Mater.* 61 (2013) 2628–2638.
- [11] C.C. Tasan, Y. Deng, K.G. Pradeep, M.J. Yao, H. Springer, D. Raabe, Composition dependence of phase stability, deformation mechanisms, and mechanical properties of the CoCrFeMnNi high-entropy alloy system, *Jom.* 66 (2014) 1993–2001.
- [12] Z. Li, D. Raabe, Strong and ductile non-equiatomically high-entropy alloys: design, processing, microstructure, and mechanical properties, *Jom.* 69 (2017) 2099–2106.
- [13] M.J. Yao, K.G. Pradeep, C.C. Tasan, D. Raabe, A novel, single phase, non-

equiatomic FeMnNiCoCr high-entropy alloy with exceptional phase stability and tensile ductility, *Scr. Mater.* 72 (2014) 5–8.

[14] Z. Li, K.G. Pradeep, Y. Deng, D. Raabe, C.C. Tasan, Metastable high-entropy dual-phase alloys overcome the strength–ductility trade-off, *Nature*. 534 (2016) 227.

[15] Z. Li, C.C. Tasan, K.G. Pradeep, D. Raabe, A TRIP-assisted dual-phase high-entropy alloy: grain size and phase fraction effects on deformation behavior, *Acta Mater.* 131 (2017) 323–335.

[16] Y. Jien-Wei, Recent progress in high entropy alloys, *Ann. Chim. Sci. Mat.* 31 (2006) 633–648.

[17] S. Ranganathan, Alloyed pleasures: multimetallic cocktails, *Curr. Sci.* 85 (2003) 1404–1406.

[18] D.B. Miracle, O.N. Senkov, A critical review of high entropy alloys and related concepts, *Acta Mater.* 122 (2017) 448–511.

[19] B. Gludovatz, A. Hohenwarter, D. Catoor, E.H. Chang, E.P. George, R.O. Ritchie, A fracture-resistant high-entropy alloy for cryogenic applications, *Science* (80-.). 345 (2014) 1153–1158.

[20] D. Li, C. Li, T. Feng, Y. Zhang, G. Sha, J.J. Lewandowski, P.K. Liaw, Y. Zhang, High-entropy Al 0.3 CoCrFeNi alloy fibers with high tensile strength and ductility at ambient and cryogenic temperatures, *Acta Mater.* 123 (2017) 285–294.

[21] E.D. Tabachnikova, A. V Podolskiy, M.O. Laktionova, N.A. Bereznaiia, M.A. Tikhonovsky, A.S. Tortika, Mechanical properties of the CoCrFeNiMnVx high entropy alloys in temperature range 4.2–300 K, *J. Alloys Compd.* 698 (2017) 501–509.

[22] X.B. Feng, W. Fu, J.Y. Zhang, J.T. Zhao, J. Li, K. Wu, G. Liu, J. Sun, Effects of nanotwins on the mechanical properties of Al_xCoCrFeNi high entropy alloy thin films, *Scr. Mater.* 139 (2017) 71–76.

[23] T. Yang, S. Xia, W. Guo, R. Hu, J.D. Poplawsky, G. Sha, Y. Fang, Z. Yan, C. Wang, C. Li, Effects of temperature on the irradiation responses of Al 0.1 CoCrFeNi high entropy alloy, *Scr. Mater.* 144 (2018) 31–35.

[24] S. Vrtnik, P. Koželj, A. Meden, S. Maiti, W. Steurer, M. Feuerbacher, J. Dolinšek, Superconductivity in thermally annealed Ta-Nb-Hf-Zr-Ti high-entropy alloys, *J. Alloys*

Compd. 695 (2017) 3530–3540.

[25] H.W. Yao, J.W. Qiao, J.A. Hawk, H.F. Zhou, M.W. Chen, M.C. Gao, Mechanical properties of refractory high-entropy alloys: Experiments and modeling, *J. Alloys Compd.* 696 (2017) 1139–1150.

[26] Y. Lu, X. Gao, L. Jiang, Z. Chen, T. Wang, J. Jie, H. Kang, Y. Zhang, S. Guo, H. Ruan, Directly cast bulk eutectic and near-eutectic high entropy alloys with balanced strength and ductility in a wide temperature range, *Acta Mater.* 124 (2017) 143–150.

[27] C. Ai, F. He, M. Guo, J. Zhou, Z. Wang, Z. Yuan, Y. Guo, Y. Liu, L. Liu, Alloy design, micromechanical and macromechanical properties of CoCrFeNiTa_x eutectic high entropy alloys, *J. Alloys Compd.* 735 (2018) 2653–2662.

[28] J. Chen, X. Zhou, W. Wang, B. Liu, Y. Lv, W. Yang, D. Xu, Y. Liu, A review on fundamental of high entropy alloys with promising high-temperature properties, *J. Alloys Compd.* (2018).

[29] Y. Yao, Z. Huang, P. Xie, S.D. Lacey, R.J. Jacob, H. Xie, F. Chen, A. Nie, T. Pu, M. Rehwoldt, Carbothermal shock synthesis of high-entropy-alloy nanoparticles, *Science* (80-.). 359 (2018) 1489–1494.

[30] R. Wang, K. Zhang, C. Davies, X. Wu, Evolution of microstructure, mechanical and corrosion properties of AlCoCrFeNi high-entropy alloy prepared by direct laser fabrication, *J. Alloys Compd.* 694 (2017) 971–981.

[31] R. Li, P. Niu, T. Yuan, P. Cao, C. Chen, K. Zhou, Selective laser melting of an equiatomic CoCrFeMnNi high-entropy alloy: Processability, non-equilibrium microstructure and mechanical property, *J. Alloys Compd.* 746 (2018) 125–134.

[32] J. Joseph, N. Stanford, P. Hodgson, D.M. Fabijanic, Tension/compression asymmetry in additive manufactured face centered cubic high entropy alloy, *Scr. Mater.* 129 (2017) 30–34.

[33] X. Qiu, Microstructure, hardness and corrosion resistance of Al₂CoCrCuFeNiTi_x high-entropy alloy coatings prepared by rapid solidification, *J. Alloys Compd.* 735 (2018) 359–364.

[34] S.-H. Joo, H. Kato, M.J. Jang, J. Moon, E.B. Kim, S.-J. Hong, H.S. Kim, Structure and properties of ultrafine-grained CoCrFeMnNi high-entropy alloys produced by mechanical alloying and spark plasma sintering, *J. Alloys Compd.* 698 (2017) 591–604.

- [35] X.D. Xu, P. Liu, Z. Tang, A. Hirata, S.X. Song, T.G. Nieh, P.K. Liaw, C.T. Liu, M.W. Chen, Transmission electron microscopy characterization of dislocation structure in a face-centered cubic high-entropy alloy Al_{0.1}CoCrFeNi, *Acta Mater.* 144 (2018) 107–115.
- [36] Q. Lin, X. An, H. Liu, Q. Tang, P. Dai, X. Liao, In-situ high-resolution transmission electron microscopy investigation of grain boundary dislocation activities in a nanocrystalline CrMnFeCoNi high-entropy alloy, *J. Alloys Compd.* 709 (2017) 802–807.
- [37] M. Wang, Z. Li, D. Raabe, In-situ SEM observation of phase transformation and twinning mechanisms in an interstitial high-entropy alloy, *Acta Mater.* 147 (2018) 236–246.
- [38] Z. Li, S. Zhao, S.M. Alotaibi, Y. Liu, B. Wang, M.A. Meyers, Adiabatic shear localization in the CrMnFeCoNi high-entropy alloy, *Acta Mater.* 151 (2018) 424–431.
- [39] J.B. Seol, J.W. Bae, Z. Li, J.C. Han, J.G. Kim, D. Raabe, H.S. Kim, Boron doped ultrastrong and ductile high-entropy alloys, *Acta Mater.* (2018).
- [40] S.M. Ueland, Y. Chen, C.A. Schuh, Oligocrystalline shape memory alloys, *Adv. Funct. Mater.* 22 (2012) 2094–2099.
- [41] K. Lu, Stabilizing nanostructures in metals using grain and twin boundary architectures, *Nat. Rev. Mater.* 1 (2016) 16019.
- [42] E. Ma, T. Zhu, Towards strength–ductility synergy through the design of heterogeneous nanostructures in metals, *Mater. Today.* 20 (2017) 323–331.
- [43] J.-L. Zhang, C.C. Tasan, M.J. Lai, D. Yan, D. Raabe, Partial recrystallization of gum metal to achieve enhanced strength and ductility, *Acta Mater.* 135 (2017) 400–410.
- [44] Y. Tanaka, Y. Himuro, R. Kainuma, Y. Sutou, T. Omori, K. Ishida, Ferrous polycrystalline shape-memory alloy showing huge superelasticity, *Science* (80-.). 327 (2010) 1488–1490.
- [45] T. Omori, S. Abe, Y. Tanaka, D.Y. Lee, K. Ishida, R. Kainuma, Thermoelastic martensitic transformation and superelasticity in Fe–Ni–Co–Al–Nb–B polycrystalline alloy, *Scr. Mater.* 69 (2013) 812–815.

- [46] D. Lee, T. Omori, R. Kainuma, Ductility enhancement and superelasticity in Fe–Ni–Co–Al–Ti–B polycrystalline alloy, *J. Alloys Compd.* 617 (2014) 120–123.
- [47] Y. Sutou, T. Omori, K. Yamauchi, N. Ono, R. Kainuma, K. Ishida, Effect of grain size and texture on pseudoelasticity in Cu–Al–Mn-based shape memory wire, *Acta Mater.* 53 (2005) 4121–4133.
- [48] Y. Sutou, N. Koeda, T. Omori, R. Kainuma, K. Ishida, Effects of aging on stress-induced martensitic transformation in ductile Cu–Al–Mn-based shape memory alloys, *Acta Mater.* 57 (2009) 5759–5770.
- [49] Y. Sutou, T. Omori, R. Kainuma, K. Ishida, Grain size dependence of pseudoelasticity in polycrystalline Cu–Al–Mn-based shape memory sheets, *Acta Mater.* 61 (2013) 3842–3850.
- [50] Y. Chen, X. Zhang, D.C. Dunand, C.A. Schuh, Shape memory and superelasticity in polycrystalline Cu–Al–Ni microwires, *Appl. Phys. Lett.* 95 (2009) 171906.
- [51] Y. Chen, C.A. Schuh, Size effects in shape memory alloy microwires, *Acta Mater.* 59 (2011) 537–553.
- [52] T.H. Fang, W.L. Li, N.R. Tao, K. Lu, Revealing extraordinary intrinsic tensile plasticity in gradient nano-grained copper, *Science* (80-.). 331 (2011) 1587–1590.
- [53] X. Wu, P. Jiang, L. Chen, F. Yuan, Y.T. Zhu, Extraordinary strain hardening by gradient structure, *Proc. Natl. Acad. Sci.* 111 (2014) 7197–7201.
- [54] N. Hansen, Hall–Petch relation and boundary strengthening, *Scr. Mater.* 51 (2004) 801–806.
- [55] S.M. Ueland, C.A. Schuh, Grain boundary and triple junction constraints during martensitic transformation in shape memory alloys, *J. Appl. Phys.* 114 (2013) 53503.
- [56] K. Lu, Making strong nanomaterials ductile with gradients, *Science* (80-.). 345 (2014) 1455–1456.
- [57] K. Lu, J. Lu, Nanostructured surface layer on metallic materials induced by surface mechanical attrition treatment, *Mater. Sci. Eng. A.* 375 (2004) 38–45.
- [58] W.L. Li, N.R. Tao, K. Lu, Fabrication of a gradient nano-micro-structured surface layer on bulk copper by means of a surface mechanical grinding treatment, *Scr. Mater.* 59

(2008) 546–549.

[59] X. Wu, M. Yang, F. Yuan, G. Wu, Y. Wei, X. Huang, Y. Zhu, Heterogeneous lamella structure unites ultrafine-grain strength with coarse-grain ductility, *Proc. Natl. Acad. Sci.* 112 (2015) 14501–14505.

[60] X.L. Wu, M.X. Yang, F.P. Yuan, L. Chen, Y.T. Zhu, Combining gradient structure and TRIP effect to produce austenite stainless steel with high strength and ductility, *Acta Mater.* 112 (2016) 337–346.

[61] Y. Li, Y. Lu, W. Li, M. Khedr, H. Liu, X. Jin, Hierarchical microstructure design of a bimodal grained twinning-induced plasticity steel with excellent cryogenic mechanical properties, *Acta Mater.* (2018).

[62] A. Magee, L. Ladani, T.D. Topping, E.J. Lavernia, Effects of tensile test parameters on the mechanical properties of a bimodal Al–Mg alloy, *Acta Mater.* 60 (2012) 5838–5849.

[63] K. Huang, K. Zhang, K. Marthinsen, R.E. Logé, Controlling grain structure and texture in Al–Mn from the competition between precipitation and recrystallization, *Acta Mater.* 141 (2017) 360–373.

[64] M. Yang, D. Yan, F. Yuan, P. Jiang, E. Ma, X. Wu, Dynamically reinforced heterogeneous grain structure prolongs ductility in a medium-entropy alloy with gigapascal yield strength, *Proc. Natl. Acad. Sci.* (2018) 201807817.

[65] C. Sawangrat, S. Kato, D. Orlov, K. Ameyama, Harmonic-structured copper: performance and proof of fabrication concept based on severe plastic deformation of powders, *J. Mater. Sci.* 49 (2014) 6579–6585.

[66] T. Sekiguchi, K. Ono, H. Fujiwara, K. Ameyama, New microstructure design for commercially pure titanium with outstanding mechanical properties by mechanical milling and hot roll sintering, *Mater. Trans.* 51 (2010) 39–45.

[67] D. Orlov, H. Fujiwara, K. Ameyama, Obtaining copper with harmonic structure for the optimal balance of structure-performance relationship, *Mater. Trans.* 54 (2013) 1549–1553.

[68] Y. Wang, M. Chen, F. Zhou, E. Ma, High tensile ductility in a nanostructured metal, *Nature.* 419 (2002) 912.

- [69] D. Witkin, Z. Lee, R. Rodriguez, S. Nutt, E. Lavernia, Al–Mg alloy engineered with bimodal grain size for high strength and increased ductility, *Scr. Mater.* 49 (2003) 297–302.
- [70] G.J. Fan, H. Choo, P.K. Liaw, E.J. Lavernia, Plastic deformation and fracture of ultrafine-grained Al–Mg alloys with a bimodal grain size distribution, *Acta Mater.* 54 (2006) 1759–1766.
- [71] C. Zhang, C. Zhu, T. Harrington, K. Vecchio, Design of non-equiaxed high entropy alloys with heterogeneous lamella structure towards strength-ductility synergy, *Scr. Mater.* 154 (2018) 78–82.
- [72] X. Wu, Y. Zhu, Heterogeneous materials: a new class of materials with unprecedented mechanical properties, *Mater. Res. Lett.* 5 (2017) 527–532.
- [73] K. Tanaka, T. Mori, The hardening of crystals by non-deforming particles and fibres, *Acta Metall.* 18 (1970) 931–941.
- [74] M. Yang, Y. Pan, F. Yuan, Y. Zhu, X. Wu, Back stress strengthening and strain hardening in gradient structure, *Mater. Res. Lett.* 4 (2016) 145–151.
- [75] M.F. Ashby, The deformation of plastically non-homogeneous materials, *Philos. Mag.* 21 (1970) 399–424.
- [76] Z. Nishiyama, *Martensitic transformation*, Elsevier, 2012.
- [77] K. Otsuka, C.M. Wayman, *Shape memory materials*, Cambridge university press, 1999.
- [78] J. Ma, B.C. Hornbuckle, I. Karaman, G.B. Thompson, Z.P. Luo, Y.I. Chumlyakov, The effect of nanoprecipitates on the superelastic properties of FeNiCoAlTa shape memory alloy single crystals, *Acta Mater.* 61 (2013) 3445–3455.
- [79] T. Maki, Microstructure and mechanical behaviour of ferrous martensite, in: *Mater. Sci. Forum*, Trans Tech Publ, 1990: pp. 157–168.
- [80] H. Sato, S. Zaefferer, A study on the formation mechanisms of butterfly-type martensite in Fe–30% Ni alloy using EBSD-based orientation microscopy, *Acta Mater.* 57 (2009) 1931–1937.
- [81] G. Krauss, A.R. Marder, The morphology of martensite in iron alloys, *Metall.*

Trans. 2 (1971) 2343.

[82] S. Morito, X. Huang, T. Furuhashi, T. Maki, N. Hansen, The morphology and crystallography of lath martensite in alloy steels, *Acta Mater.* 54 (2006) 5323–5331.

[83] H. Kitahara, R. Ueji, M. Ueda, N. Tsuji, Y. Minamino, Crystallographic analysis of plate martensite in Fe–28.5 at.% Ni by FE-SEM/EBSD, *Mater. Charact.* 54 (2005) 378–386.

[84] A. Shibata, S. Morito, T. Furuhashi, T. Maki, Local orientation change inside lenticular martensite plate in Fe–33Ni alloy, *Scr. Mater.* 53 (2005) 597–602.

[85] J. Ma, I. Karaman, Expanding the repertoire of shape memory alloys, *Science* (80-.). 327 (2010) 1468–1469.

[86] L.C. Chang, T.A. Read, Plastic deformation and diffusionless phase changes in metals—the gold-cadmium beta phase, *JOM.* 3 (1951) 47–52.

[87] W.J. Buehler, J. V Gilfrich, R.C. Wiley, Effect of low-temperature phase changes on the mechanical properties of alloys near composition TiNi, *J. Appl. Phys.* 34 (1963) 1475–1477.

[88] J. Seo, Y.C. Kim, J.W. Hu, Pilot study for investigating the cyclic behavior of slit damper systems with recentering shape memory alloy (SMA) bending bars used for seismic restrainers, *Appl. Sci.* 5 (2015) 187–208.

[89] K. Otsuka, X. Ren, Physical metallurgy of Ti–Ni-based shape memory alloys, *Prog. Mater. Sci.* 50 (2005) 511–678.

[90] C.M. Wayman, On memory effects related to martensitic transformations and observations in β -brass and Fe₃Pt, *Scr. Metall.* 5 (1971) 489–492.

[91] S. Kajiwara, T. Kikuchi, Reversible movement of the austenite-martensite interface and dislocation structures in reverse-transformed austenite in Fe-Ni-C alloys, *Philos. Mag. A.* 48 (1983) 509–526.

[92] S. Kajiwara, Characteristic features of shape memory effect and related transformation behavior in Fe-based alloys, *Mater. Sci. Eng. A.* 273 (1999) 67–88.

[93] T. Maki, K. Kobayashi, M. Minato, I. Tamura, Thermoelastic martensite in an ausaged Fe–Ni–Ti–Co alloy, *Scr. Metall.* 18 (1984) 1105–1109.

- [94] A. Shibata, H. Yonezawa, K. Yabuuchi, S. Morito, T. Furuhashi, T. Maki, Relation between martensite morphology and volume change accompanying fcc to bcc martensitic transformation in Fe–Ni–Co alloys, *Mater. Sci. Eng. A*. 438 (2006) 241–245.
- [95] J.K. Abraham, J.S. Pascover, The transformation and structure of Fe-Ni-Ti alloys (Precipitation influence on martensite formation kinetics and structure of Fe-Ni-Ti alloys), *Metall. Soc. AIME, Trans.* 245 (1969) 759–768.
- [96] Y. Himuro, O. Ikeda, R. Kainuma, K. Ishida, Effect of ausaging on the morphology of martensite in an Fe-25% Ni-7.5% Si alloy, *Le J. Phys. IV*. 11 (2001) Pr8-205.
- [97] Y. Himuro, R. Kainuma, K. Ishida, Martensitic Transformation and Shape Memory Effect in Ausaged Fe–Ni–Si Alloys, *ISIJ Int.* 42 (2002) 184–190.
- [98] Y. Tanaka, Y. Himuro, T. Omori, Y. Sutou, R. Kainuma, K. Ishida, Martensitic transformation and shape memory effect in ausaged Fe–Ni–Si–Co alloys, *Mater. Sci. Eng. A*. 438 (2006) 1030–1035.
- [99] H. Ohtsuka, S. Kajiwara, Effects of carbon content and ausaging on $\gamma \leftrightarrow \alpha'$ transformation behavior and reverse-transformed structure in Fe-Ni-Co-Al-C alloys, *Metall. Mater. Trans. A*. 25 (1994) 63–71.
- [100] K. Ishida, R. Kainuma, N. Ueno, T. Nishizawa, Ductility enhancement in NiAl (B2)-base alloys by microstructural control, *Metall. Trans. A*. 22 (1991) 441–446.
- [101] C.C. Jia, K. Ishida, T. Nishizawa, Partition of alloying elements between γ (A1), γ' (L1₂), and β (B2) phases in Ni-Al base systems, *Metall. Mater. Trans. A*. 25 (1994) 473–485.
- [102] Y. Tanaka, R. Kainuma, T. Omori, K. Ishida, Alloy Design for Fe-Ni-Co-Al-based Superelastic Alloys, *Mater. Today Proc.* 2 (2015) S485–S492.
- [103] F.C. Campbell, *Elements of metallurgy and engineering alloys*, ASM International, 2008.
- [104] S. Jiang, H. Wang, Y. Wu, X. Liu, H. Chen, M. Yao, B. Gault, D. Ponge, D. Raabe, A. Hirata, Ultrastrong steel via minimal lattice misfit and high-density nanoprecipitation, *Nature*. 544 (2017) 460.

Chapter 2

Enhancement of <001> recrystallization texture in non-equiatomic Fe-Ni-Co-Al-based high entropy alloys by combination of annealing and Cr addition

Chapter 2 is the part of published paper in Journal of Alloys and Compounds.

Cheng Zhang, Chaoyi Zhu, Sumin Shin, Kenneth Vecchio. “Enhancement of <001> recrystallization texture in non-equiatomic Fe-Ni-Co-Al-based high entropy alloys by combination of annealing and Cr addition” Journal of Alloys and Compounds 768 (2018): 277-286. Elsevier.

Abstract

In Chapter 2, formation of strong <001> recrystallization texture in new non-equiatomic Fe-Ni-Co-Al-based high entropy alloys has been investigated. Optimal annealing temperature and time to obtain strong <001> texture is subsequently determined through microstructure and recrystallization texture study of cold-rolled NCACB (34.95Fe-27.5Ni-17.5Co-11.5Al-8.5Cr-0.05B at.%) at 1200°C and 1300°C for different annealing times. It has also been found that the recrystallization texture is influenced by grain growth and the relative grain size (d/t , d -grain size, t -sheet thickness). Furthermore, contribution of chemical composition to <001> texture has been examined in two additional cold-rolled non-equiatomic high entropy alloys, NCAB (Fe-27.5Ni-17.5Co-

11.5Al-0.05B at.%) and NCATB (Fe-27.5Ni-17.5Co-11.5Al-2.5Ta-0.05B at.%), under the same optimal annealing condition used for NCACB. Comparison of texture intensity of NCAB, NCATB, and NCACB demonstrates that Cr is very effective in the formation of strong $\langle 001 \rangle$ recrystallization texture of Fe-Ni-Co-Al-based alloys. Based on low-angle boundary statistics, it is hypothesized that decrease in stacking fault energy is responsible for the enhanced recrystallization texture in NCACB. Additionally, it is demonstrated employing a Zener-type model for the pinning of grain boundaries by second-phase particles, that precipitated NiAl particles facilitate the abnormal grain growth in NCACB. The tensile tests results show that strong recrystallization texture and bamboo-like structure improve the ductility of NCACB.

2.1 Introduction

High entropy alloys (HEAs) are a new class of metallic materials with four or more equiatomic or near-equiatomic elements [1]. During the period of exploration, most studies have been focused on one of the original concepts of HEAs for alloy design, which utilizes an equiatomic ratio of multiple principal elements to obtain the maximum configurational entropy [1-3]. However, traditional HEA design concepts limit the compositional space and excludes non-equiatomic candidates with potentially outstanding properties and higher commercial viability. The concept of non-equiatomic HEAs, first put forward by Raabe and his colleagues [4,5], has greatly expanded the compositional space for HEA design,

and work on these compositions has achieved unparalleled mechanical properties [5-7].

Recently, intensive studies in HEAs have led to the discovery of a number of attractive properties, such as good mechanical properties at cryogenic temperature [8-10], formation of nanotwins in thin films [11], irradiation responses [12], superconductivity [13], and refractory properties [14]. The newly-designed eutectic HEAs and high entropy superalloys (HESAs) greatly expand the application fields of HEAs, especially in the directly cast and high-temperature areas [15-17]. For the fabrication of HEAs, apart from conventional arc melting and induction melting, some special fabrication methods are also employed to produce HEA materials, including carbothermal shock synthesis of HEA nanoparticles [18], selective laser melting (SLM) or additive manufacture [19-21], rapid solidification [22], and spark plasma sintering (SPS) [23]. With the use of in-situ TEM or transmission SEM (tSEM), the dislocation behavior and deformation mechanisms in HEAs have been investigated [24-26]. Furthermore, the high structural stability in the CrMnFeCoNi HEA after high-strain rate deformation suggests potential for high ballistic resistance for HEAs [27]. Grain boundary strengthening has recently been employed to HEAs with addition of a small amount of boron [28]. The various properties of HEAs cited here mainly benefit from the diversity of microstructures.

In the development of traditional structural metals and alloys, the properties are essentially determined by the microstructure achieved via processing. For this reason, it is of great importance to explore the relationship between properties and microstructures

in HEAs. Apart from fine-grained structure, recent studies show that bimodal/hierarchical structure, heterogeneous lamellar structure, and partial recrystallization structure can lead to a combination of high strength and high ductility [29-31]. Since microstructure and texture affect the mechanical properties of HEAs, some studies have been carried out to investigate the microstructure and texture evolution in the equiatomic CoCrFeMnNi/FeCrCuMnNi HEA during the thermomechanical processing with variants including plastic strain, grain size, heating rate and cryo-rolling [32-35]. However, no strong recrystallization texture is formed in the temperature range between 700°C and 1200°C. For some HEAs, mechanical properties can be tailored through varying the microstructure, especially the texture and the grain size [6, 31, 36]. A recent study in the CoCrFeMnNi HEA shows that twinning facilitates the transition from the Cu-type to the Brass-type texture during cold rolling deformation, while annealing twinning leads to a strong modification of the texture formed during recrystallization [36]. However, research in texture evolution of non-equiatomic HEAs is unexplored, and the effect of strong recrystallization texture on the mechanical properties of HEAs is not clear. Therefore, it is of great interest to systematically determine the evolution of recrystallization texture in non-equiatomic HEA and its synergetic effect on improved mechanical properties.

Grain size affects the mechanical properties of polycrystalline alloys due to the Hall-Petch relation. However, for metal and alloys with a thin sheet form, the relative grain size (d/t , d -grain size, t -thickness of the sheet) also affects the mechanical properties. Sutou

et al. [37] found that superelastic strain of Cu-based polycrystalline shape memory alloys with relative grain size over 1 can be greatly increased due to the reduction of grain constraint [38]. Additionally, Lee et al. [39] found that the increasing fraction of low-angle grain boundaries (LAGB) improves the ductility in Fe-Ni-Co-Al-based alloys due to their effect on suppressing the precipitation of NiAl along the grain boundaries [40,41]. However, the relative grain size and the fraction of LAGBs have not been studied in HEAs. In the equiatomic or near equiatomic FeNiCoAl_x($x=0-0.5$)Cr HEAs, NiAl (B2) phase and/or Ni₃Al-type (L1₂) γ' can be employed to strengthen the matrix through various aging treatments [42-44] at the expense of significant loss of ductility. Therefore, it is worthwhile exploring the development of LAGBs in the newly-designed non-equiatomic FeNiCoAlCrB-HEA to improve mechanical properties by suppressing the formation of precipitation phases along grain boundaries, without altering the chemical composition.

To improve our understanding of the recrystallization texture developed in non-equiatomic Fe-Ni-Co-Al-based HEAs, samples with different alloying elements (Ta/Cr) are studied through a series of different reductions in thickness (RIT) under various annealing conditions. Meanwhile, grain growth and its effect on the texture development is discussed. The fraction of LAGBs in non-equiatomic Fe-Ni-Co-Al-based HEAs are calculated and compared to related materials. The influence of texture and bamboo-like structure in the mechanical properties of non-equiatomic HEAs is also examined and discussed.

2.2 Experimental Procedures

Three non-equiatomic alloys, NCAB (43.45Fe-28Ni-17Co-11.5Al-0.05B), NCATB (40.95Fe- 28Ni-17Co-11.5Al-2.5Ta-0.05B) and NCACB (34.95Fe-28Ni-17Co-11.5Al-8.5Cr-0.05B) (all at.%) were prepared through arc-melting under an argon atmosphere with raw materials as follows: Fe (99.95%), Ni (99.9%), Co (99.9%), Al (99.9%), Ta (99.9%), Cr (99.9%) and Ni₂B (99%). The related data including configurational entropy (ΔS), mixing enthalpy (ΔH_{mix}) and valence electron concentration (VEC) of these three alloys are listed in Table 2.1 [45, 46]. Values of ΔH_{mix} and VEC of these samples are in the range of fcc HEAs. Therefore, NCAB, NCACB, and NCATB in the current study can be regarded as non-equiatomic HEAs.

Table 2.1 ΔS , ΔH_{MIX} and VEC values for NCAB, NCACB, and NCATB

	ΔS	ΔH_{mix} (kJ/mol)	VEC
NCAB	1.29R	-7.8	8.1
NCACB	1.52R	-8.5	8.0
NCATB	1.38R	-9.6	8.1

During the process of arc-melting, each ingot was flipped and re-melted eight times to ensure homogeneity. After arc-melting, ingots with an original thickness of about 10 mm were processed through hot rolling (1250°C, reduction in thickness (RIT) is 20-30%), cold rolling (RIT \geq 90%) and annealing (1300°C, 30 mins). For NCATB specimens, induction heat-treatment under the argon atmosphere was carried out for homogenization

before hot rolling. For NCACB samples, they were annealed, after cold rolling, at 1200°C and 1300°C for 15-min, 30-min and 60-min. Then, their homogenization as a function of time and temperature was examined. After cold rolling and annealing, electron backscatter diffraction (EBSD) was employed to detect the texture development in these three alloys. Since samples with RIT over 90% were very thin, they were carefully ground and polished using standard metallographic techniques followed by vibratory polishing to obtain high-quality surface finish for EBSD. A Rigaku X-ray diffractometer (rotating anode type and Cu K α radiation) and FEI Quanta 600 SEM equipped with a Bruker XFlash 6160 EDS/EBSD detector were used. Quasi-static tensile tests were carried out at room temperature, with the tensile direction parallel to the rolling direction with a sample gauge-length of 20 mm, gauge-width of 2 mm and thickness between 0.4 mm and 0.5 mm.

2.3 Results and Discussion

2.3.1 Texture evolution in NCACB

Fig. 2.1(A)-(F) present a series of EBSD images along rolling direction in NCACB samples that are annealed at 1200°C for 15-min, 30-min and 60-min respectively. Fig. 2.1(A) shows the random orientation of grains, indicating that no strong recrystallization texture is formed the sample subject to annealing at 1200°C for 15 minutes. It is also found that there exists large variation in the grain structure, i.e. bimodal structure. When annealing time increases to 60-min, the heterogeneity in grain size still exists with no

obvious recrystallization texture. For the NCACB (CR95) sample annealed at 1200°C, as shown in Fig. 2.1(D), the orientation of grains is also random with a large variation in grain size at annealing time of 15-min. However, the fraction of grains along [001] becomes larger when annealing time increases to 30-min, indicating texture enhancement. When the annealing time increases to 60-min, the orientation distribution of grains shows even stronger [001] texture without obvious bimodality of the grain structure. Based on the above observations, no strong recrystallization texture can be formed in CR90 samples when annealed at 1200°C, whereas [001] texture is formed in CR95 samples under 60-min annealing.

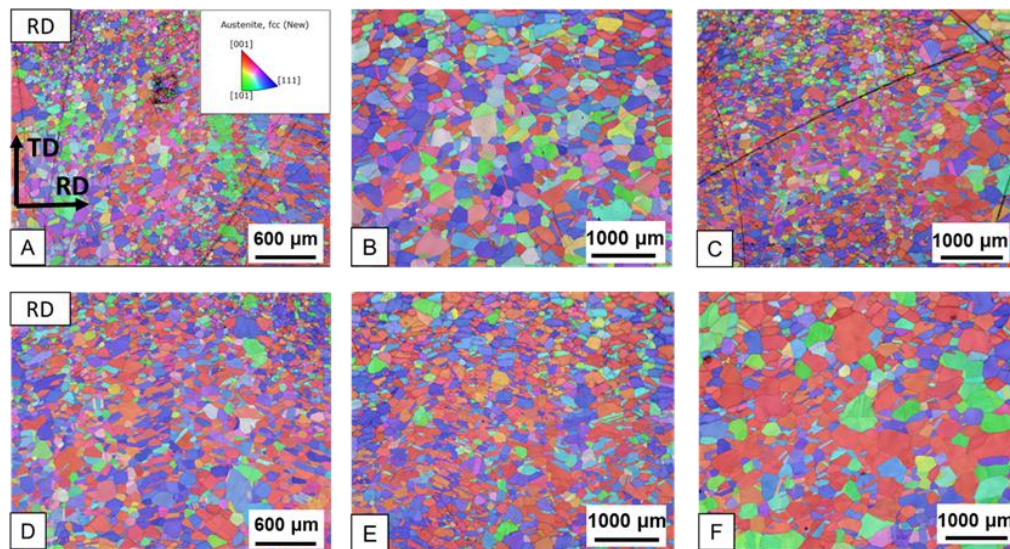


Figure 2.1. EBSD Inverse Pole Figure (IPF) maps for NCACB samples after cold rolling (CR) with different reduction in thickness (RIT) and annealing at 1200°C. (A) CR90-1200°C-15-min; (B) CR90-1200°C-30-min; (C) CR90-1200°C-60-min; (D) CR95-1200°C-15-min; (E) CR95-1200°C-30-min; (F) CR95-1200°C-60-min. RD- Rolling Direction, TD-Transverse Direction.

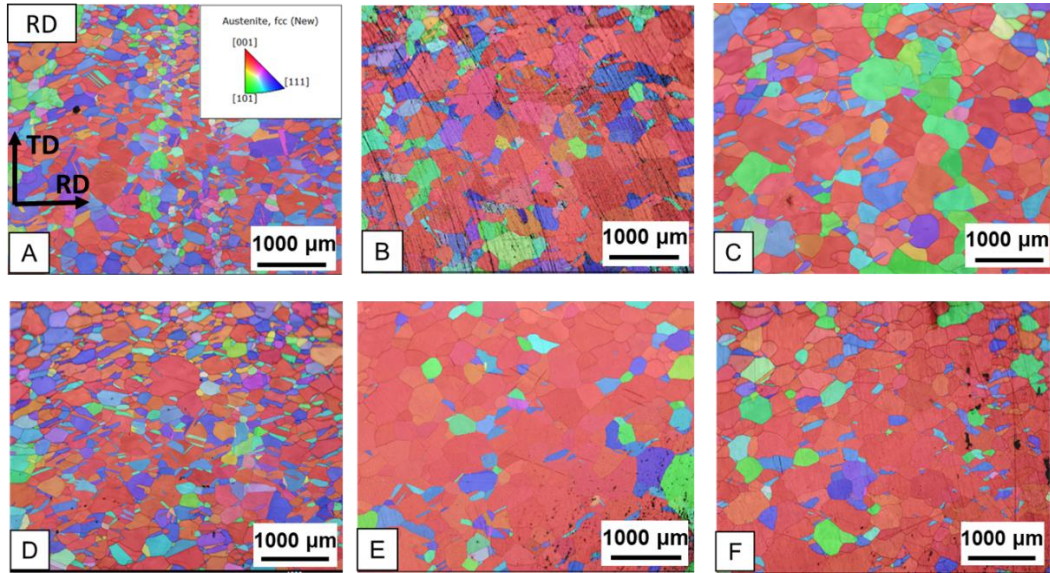


Figure 2.2. EBSD Inverse Pole Figure (IPF) maps for NCACB samples after cold rolling with different reduction in thickness and annealing at 1300°C. (A) CR90-1300°C-15-min; (B) CR90-1300°C-30-min; (C) CR90-1300°C-60-min; (D) CR95-1300°C-15-min; (E) CR95-1300°C-30-min; (F) CR95-1300°C-60-min. RD- Rolling Direction, TD-Transverse Direction.

The development of recrystallization texture in NCACB annealed at 1300°C is shown in Fig. 2.2. Grains shown in Fig. 2.2(A) in the middle have a much smaller size compared with grains in the surrounding regions, which demonstrates significant heterogeneity in grain size distribution. Fig. 2.2(B) shows enhanced texture and equiaxed grain structure when annealed for 30-min. Under 60-min annealing, no obvious enhancement in texture is observed in Fig. 2.2(C). For the NCACB (CR95) sample annealed at 1300°C for 15-min, the size distribution of grains is quite uniform with slight [001] recrystallization texture. In Fig. 2.2(E), a strong [001] recrystallization texture is observed when the annealing time is 30-min. With an annealing time of 60-min, no obvious change in the texture intensity can be seen in Fig. 2.2(F) compared with texture in Fig. 2.2(E). Based on the above experimental results, annealing at 1300°C promotes the

formation of a stronger [001] recrystallization texture.

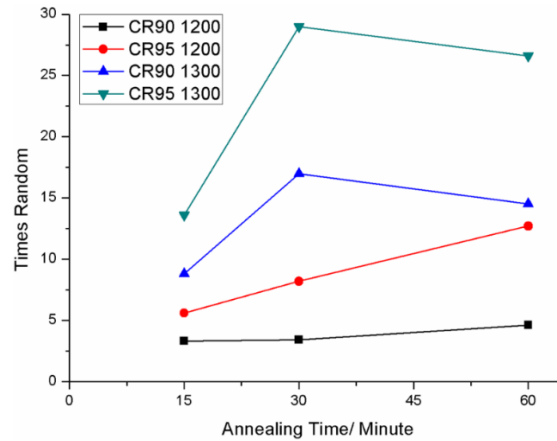


Figure 2.3. The development of intensity of <001> recrystallization texture with different annealing times in NCACB specimen with RIT of 90% and 95%.

In order to evaluate the variation in texture intensity quantitatively, the ‘times random’ parameter is employed [40]. The value of times random can be obtained from the orientation distribution function (ODF) using the MTEX software [47]. In general, measured texture with a times random value over 10 is regarded as a strong texture. Times random values between 5 and 10 are regarded as medium texture. Times random values less than 5 are a weak texture. Fig. 2.3 presents the times random values of the recrystallization texture for NCACB with RIT of 90% and 95%, indicating that the intensity of texture remains relatively constant with a times random value of around 3, i.e. weak texture when CR90 samples are annealed at 1200°C. However, for the CR95 sample annealed at 1200°C, the intensity of texture increases from a medium to a strong texture with increase in annealing time. Furthermore, the texture is significantly influenced by the annealing temperature, indicating that the times random value is increased by increasing

annealing temperature from 1200°C to 1300°C in the CR90 samples. A medium texture can be obtained with an annealing time of 15-min. When the annealing time increases to 30-min, a strong texture with a times random value over 15 can be achieved. However, there is a small decrease in the intensity of texture when the annealing time reaches 60-min. For CR95 samples annealed at 1300°C, Fig. 2.3 shows that a strong texture is formed after annealing for 15-min and 30-min. Similarly, the intensity of texture decreases slightly when the annealing time is extended to 60-min. Therefore, the optimal annealing condition obtained in this study for the formation of strong recrystallization texture in NCACB samples is determined to have an annealing temperature at 1300°C and an annealing time for 30-min. Additionally, the plotted results shown in Fig. 2.3 are generally in agreement with the texture evolution exhibited in Figs. 2.1 and 2.2.

2.3.2 Grain growth in NCACB

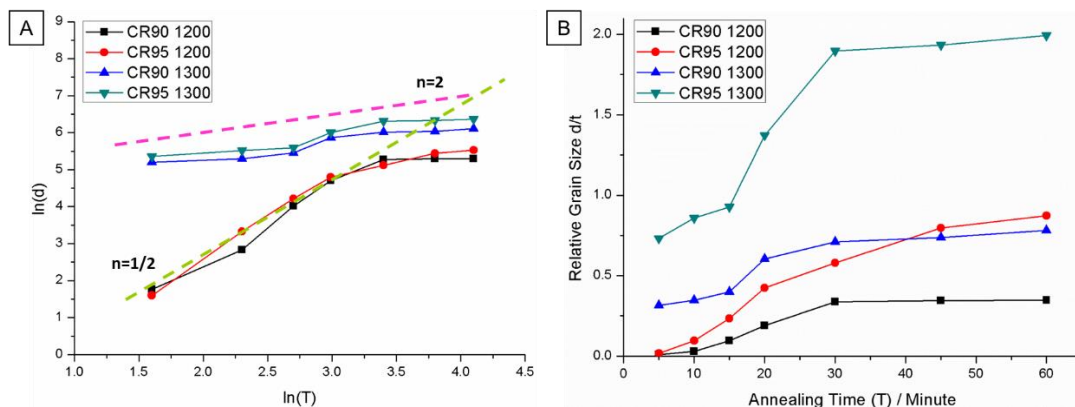


Figure 2.4. (A) Grain size development ($\ln(d)$) with annealing time ($\ln(T)$) in NCACB with RIT of 90% and 95%; (B) Relative grain size (d/t) development with annealing time in NCACB with RIT of 90% and 95%, d -grain size, t -thickness of the sample, and T -annealing time.

As mentioned previously, the mechanical properties of polycrystalline alloys are

affected by relative grain size to thickness ratio. Therefore, statistics of average grain size at different annealing conditions are required to study this effect. A method used by Toth et al. [48] for calculating the average grain size is employed here. Fig. 2.4 present the relationship between grain size (d) and annealing time (T) ($T=5, 10, 15, 20, 30, 45, 60$ -min) [2.4(A)], and relative grain size and annealing time in [2.4(B)]. In Fig. 2.4(A), the grain size increases rapidly in the first 30-min, followed by a much slower increase in grain size with annealing time approaching 60-min, for specimens annealed at 1200°C. Meanwhile, higher annealing temperatures (e.g., 1300°C) results in a more constant slow grain growth rate. For NCACB (CR95), although the grain size increases with annealing up to one hour when annealed at 1200°C, the relative grain size (d/t) is still below 1 as shown in Fig. 2.4(B). When the annealing temperature increases to 1300°C with a heating time of 15-min, the relative grain size is close to 1. The relative grain size approaches 2 when the annealing time is 30-min, but the increase in the relative grain size during the period from 30-min to 1h is limited.

2.3.2.1 Normal and abnormal grain growth in NCACB

As shown in Fig. 2.1, a large difference in the distribution of grain size exists in some NCACB samples after annealing. The grain growth mechanism is determined in the following analysis to have a better understanding of grain growth in NCACB. A classical kinetic approach to describing the gradual coarsening phenomenon has been suggested by

Burke and Turnbull [49, 50]. The equation is shown as:

$$d^n - d_0^n = kT \quad (2.1)$$

$$k = k_0 \exp(-Q/RT) \quad (2.2)$$

where d is the current average grain size, d_0 is the initial grain size, n is the grain growth exponent, k is the rate constant, and T is time. If d is much larger than d_0 , then equation (1) can be transformed to:

$$d^n = kT \quad (2.3)$$

$$n \cdot \ln(d) = \ln(k) + \ln(T) \quad (2.4)$$

$$\ln(d) = (1/n) \cdot \ln(T) + (1/n) \cdot \ln(k) \quad (2.5)$$

For normal grain growth, n is around 2. By comparing the slope ($1/n$), it is feasible to determine the type of grain growth. Fig. 2.4(A) also shows the normal grain growth line with $n=2$ and abnormal grain growth line with $n=1/2$ [51]. It is found that in the initial stage of grain growth with annealing time less than 30-min at 1200°C, the growth of grains is close to the abnormal type. When the annealing time is over 30-min, the grain growth of specimens is close to normal grain growth. As for the CR90 and CR95 samples annealed at 1300°C, the normal grain growth line fits the apparent grain growth mechanism.

2.3.2.2 Zener's model comparison

The calculated results in Section 2.3.2.1 confirm that abnormal grain growth occurs in the recrystallization of these alloys. Microstructure evolution of NCACB, through a

series of heat-treatment conditions, is undertaken to understand the mechanism for abnormal grain growth. The microstructure of NCACB (CR90, 1150°C 60-min) is shown in Fig. 2.5(A). It is found that a bimodal-type or heterogeneous lamella structure forms in the sample. No second-phase particles are found along the grain boundaries of large grains, while second-phase particles are observed along the boundaries of small grains. XRD result (Fig. 2.6) shows that these particles are NiAl (B2) β phase particles embedded in a matrix of the γ (FCC) phase. When the temperature is increased to 1175°C, the bimodal-type structure remains, but with reduced bimodality, as shown in Fig. 2.5(B). It is observed that the size of small grains increases with increasing annealing temperature from 1150°C to 1175°C, whereas the fraction of NiAl particles becomes smaller. When the annealing temperature reaches 1200°C, a bimodal-type structure is observed after 5-min. Increasing the annealing time to 7.5-min, the number of NiAl particles along grain boundaries drastically decrease, as shown in Fig. 2.5(D3). No NiAl particles can be found for an annealing time of 10-min in Fig. 2.5(E3), indicating that B2 particles are completely dissolved into the γ (FCC) matrix.

The classic approach to determine the role that the pinning particles play on the grain growth is to employ Zener's equation [51, 52]:

$$R_c = 4r / 3f \quad (2.6)$$

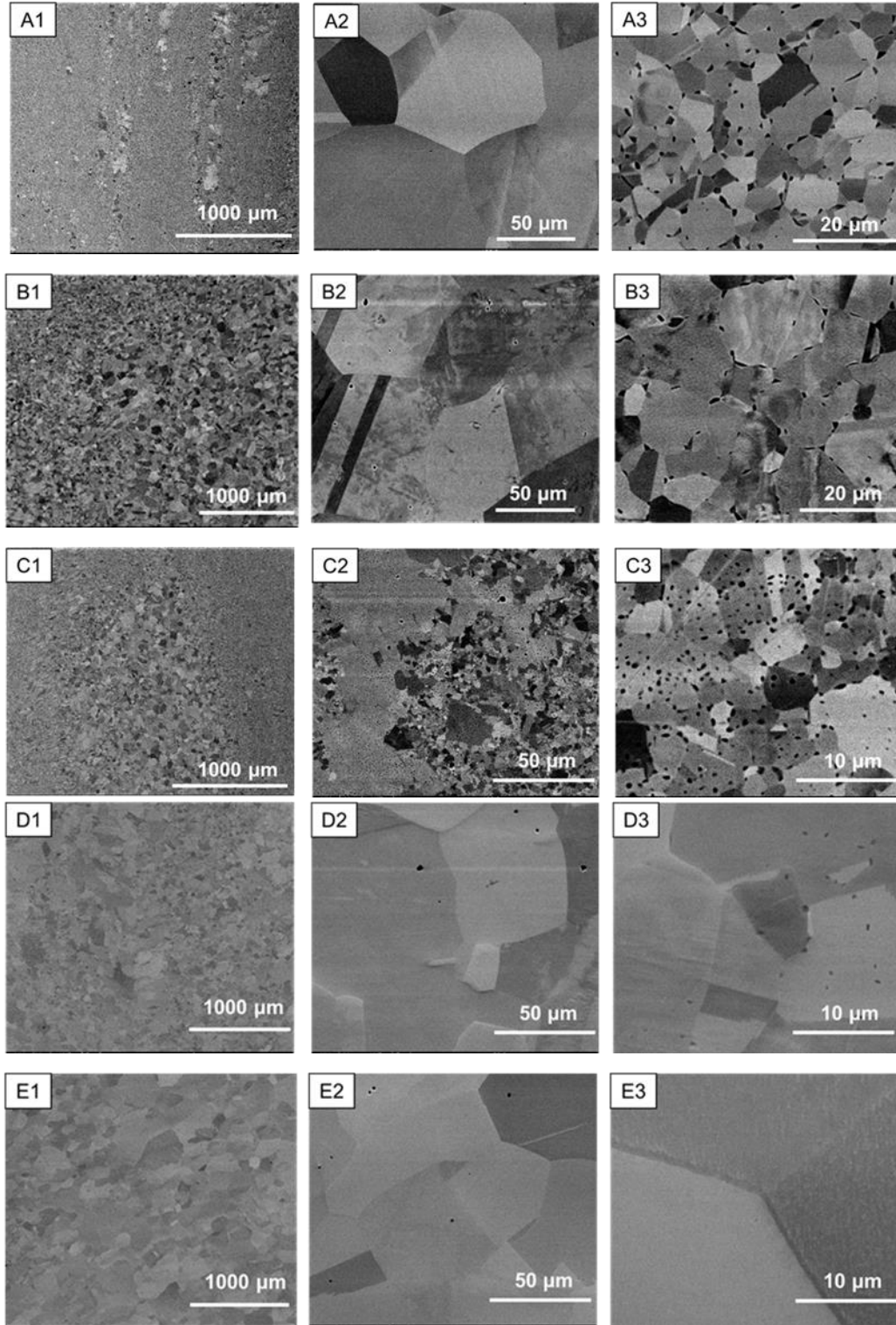


Figure 2.5. SEM (BSE) images for the microstructure evolution of NCACB with RIT of 90% at different annealing conditions. (A) 1150°C-60-min, (B) 1175°C-60-min, (C) 1200°C-5-min, (D) 1200°C-7.5-min, (E) 1200°C-10-min.

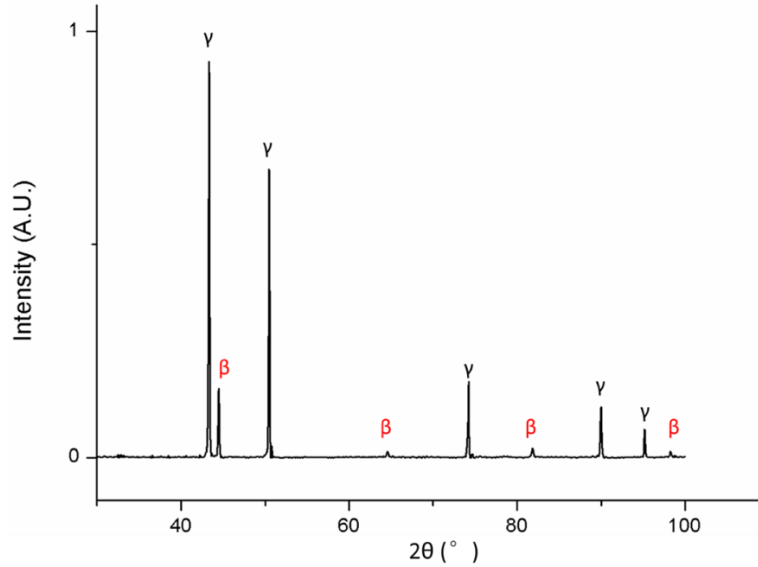


Figure 2.6. XRD pattern for NCACB (CR90) after annealing at 1150°C for 1h. γ (FCC) matrix and NiAl (B2) β phase peaks are labeled with black and red, respectively.

where R_c is the limited grain radius, r is the radius of the particles, and f is the volume fraction of particles. The limited grain radius of the NCACB samples annealed at 1150°C, 1175°C and 1200°C are summarized in Table 2.2. The calculated R_c agrees with those observed experimentally. For example, the calculated R_c with an annealing temperature of 1150°C and 1175°C is 19.5 μm and 40.1 μm , respectively, and the comparable size of small grains is about 10 μm and 20 μm in Fig. 2.5(A3) and 2.5(B3), respectively. The size of the small grains is all within the range of the calculated R_c values. Therefore, the precipitated NiAl particles are responsible for the abnormal grain growth in NCACB.

Table 2.2. Summary of calculated results using Zener's model

Temperature (°C)	Time (s)	Particle Size (μm)	Particle Volume	
			Fraction	R_c (μm)
1150	3600	0.8	0.028	19.5
1175	3600	1.5	0.025	40.1
1200	300	0.54	0.051	7.1
1200	450	0.24	0.002	60.2

2.3.2.3 Effect of grain growth on texture evolution in NCACB

During the process of grain growth, large grains along [001] grow at the expense of the small neighboring grains, i.e. Ostwald ripening. If the small grains are in a different orientation compared with the larger grains, the intensity of texture would be consequently increased. As shown in the previous section, the texture intensity of NCACB samples annealed at 1300°C is much higher than that of samples annealed at 1200°C. Based on the experimental results in section 2.3.2.2, NiAl β -phase particles affect the texture development by controlling grain growth. For samples annealed at 1200°C, it takes about 10-min for NiAl particles to dissolve into the matrix as shown in Fig. 2.5(E). During this period, grains with fewer particles or larger deformation would grow much faster than those surrounded by many particles. Samples annealed at 1300°C require a much shorter time for NiAl particles to be dissolved into the matrix. Consequently, no obvious bimodal-type structure is observed. Meanwhile, even though the grains with high-angle boundaries grow faster in the very early stage, their grain size reaches the thickness of the sheet very quickly and further growth is restrained by the thickness of the sheet. Therefore, abnormal grain growth occurring at the early stage is due to the Zener pinning effect from NiAl particles; when NiAl particles are dissolved in the matrix, the grain growth quickly becomes normal-type grain growth.

For NCACB (CR95) annealed at 1300°C, the grains grow very fast in the early stage due to the high temperature. However, Fig. 2.4(B) shows that the grains grow much

slower from 30-min to 60-min. The reason can be explained as follows.

When the grain is columnar, the pressure difference along grain boundary can be expressed as [50,53,54]:

$$\Delta P = \sigma / r \quad (2.7)$$

where σ is the interfacial tension, and r is the radius of the curvature. When the interface is spherical, the radius of the curvature would be twice that of the columnar grain.

The pressure difference along the grain boundary can be expressed as:

$$\Delta P = 2\sigma / r \quad (2.8)$$

When the relative grain size is around 2, the shape of the grain boundary and the radius of the curvature would be greatly changed. In other words, the shape of the grains transforms from spherical to columnar, meaning that the radius of the curvature is reduced to half of the spherical case. Consequently, this leads to the decrease of the driving force for the grain boundary migration, slowing down grain growth.

The above results can be used to explain the small decrease in texture intensity in samples that are annealed at 1300°C during the period from 30-min to 60-min. In the process of grain growth, the grains with high-angle boundaries migrate faster than those with low-angle boundaries. The increasing relative grain size would limit the growth of grains especially when the grain size reaches the thickness of the sheet. At this point, grains with high-angle boundaries grow faster than those with low-angle boundaries along the direction of the strong texture, thus leading to a decrease of texture intensity. In this

situation, the thickness of the sheet strongly limits the growth of the grains, so the decrease in texture intensity is quite small.

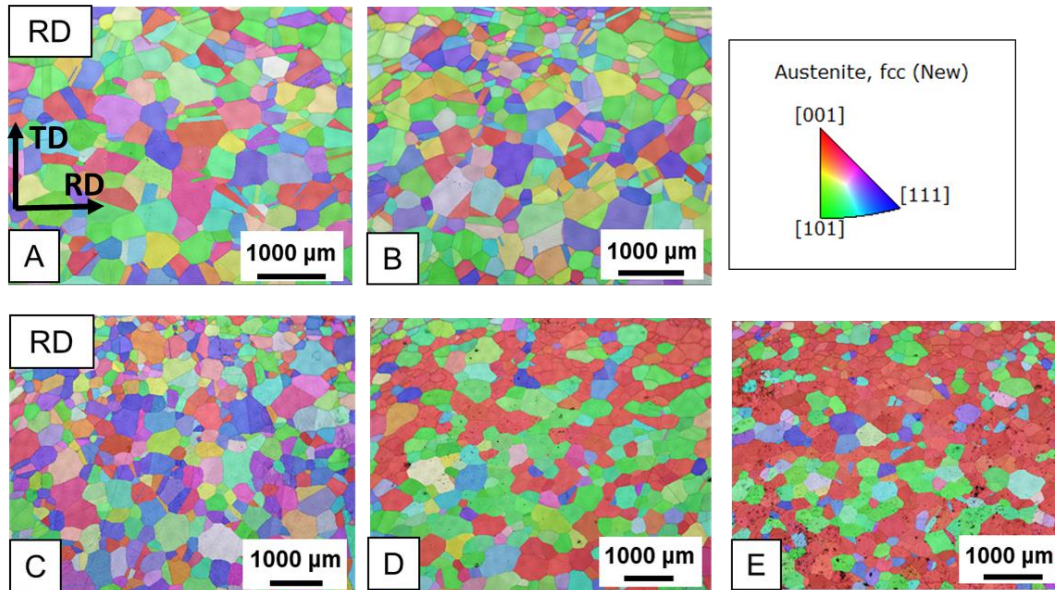


Figure 2.7. EBSD inverse pole figure (IPF) maps for NCAB and NCATB samples with different reduction in thickness (RIT) annealed at 1300°C for 30-min. (A) NCAB-CR90; (B) NCAB-CR95; (C) NCATB-CR90; (D) NCATB-CR95; (E) NCATB-CR97. RD - Roll Direction, TD- Transverse Direction.

2.3.3 Comparison of texture evolution in NCAB, NCATB and NCACB

Since the optimal annealing condition for NCACB is determined in Section 2.3.1, two additional Fe-Ni-Co-Al-based non-equiatom HEAs are examined for comparison using the same cold-rolling and annealing conditions. Fig. 2.7(A-E) present the EBSD inverse pole figure maps for annealed NCAB and NCATB samples. For annealed NCAB samples with RIT of 90% and 95%, the orientation of grains is random with no obvious recrystallization texture in Figs. 2.7(A) and 2.7(B). In Fig. 2.7(C), no recrystallization texture is present for the NCATB CR90 sample. When RIT is 95%, the fraction of grains

with orientation along [001] becomes larger, forming some degree of recrystallization texture in Fig. 2.7(D). When RIT reaches 97%, as shown in Fig. 2.7(E), the orientation of grains become more uniform in the [001] direction. In comparison, the NCACB samples (in Fig. 2.2(B) and 2.2(E)) show the strongest recrystallization texture under the same conditions among the three samples. Very recently, Lee [55] found that strong recrystallization texture can be achieved through slow heating rate in the polycrystalline FeNiCoAlTiB alloy with RIT is 90%. This discovery may offer a new way for obtaining strong recrystallization texture in NCACB.

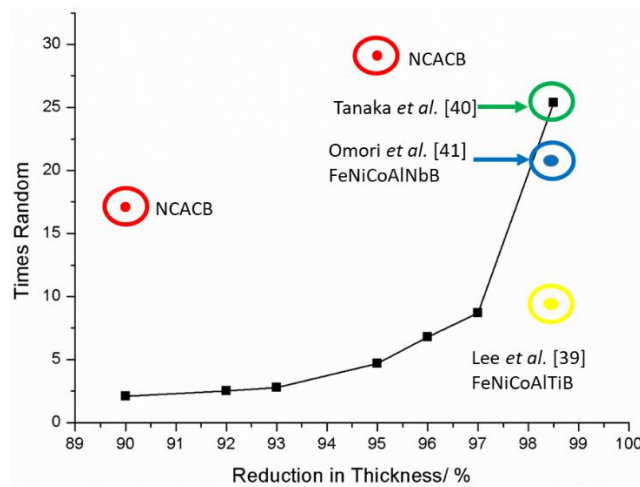


Figure 2.8. Development of texture intensity with RIT in NCATB. Red circle- NCACB, green circle - Tanaka et al. [40] (NCATB, CR98.5), blue circle - Omori et al. [41] (FeNiCoAlNbB, CR98.5), yellow circle - Lee et al. [39] (FeNiCoAlTiB, CR98.5).

Fig. 2.8 presents the development of texture intensity with RIT in non-equiatomic FeNiCoAl-based alloys. Based on the comparison results, NCACB can achieve a stronger recrystallization texture than NCATB under the same condition (CR90 and CR95, annealing at 1300°C for 30min). The texture intensity of NCACB with RIT of 95% is even higher than that obtained in FeNiCoAlNbB (RIT=98%) and FeNiCoAlTiB (RIT=98%),

respectively. Therefore, the addition of Cr is effective in the formation of strong recrystallization texture in Fe-Ni-Co-Al-based alloys. It is hypothesized that this is due to the difference in stacking fault energy among these alloys. Smallman and Green [56] have found that the stacking fault energy affects the type of rolling texture, and the transition of texture is associated with the difficulty of cross-slip. The lower the SFE, the more difficult it is for dislocations containing stacking faults to cross-slip. Therefore, lower SFE hinders the texture transition. A recent study about the SFE in HEA shows that the increase in the concentration of Ni leads to the increase in the SFE of the HEA system due to the high SFE of Ni [57], while the addition of Co helps to reduce the SFE of the HEA system [57]. By comparing the SFE of FeNiCoCr with that of FeNiCoCrAl0.1, the addition of Al increases the SFE with about 10% [58]. Based on the SFE values of recent studies in HEAs [57][58][59], the higher concentration of Ni and Al in the current non-equiatomically NCACB HEA should make the SFE much higher than that in the equiatomically FeNiCoCrMn HEA. Additionally, for NCATB, NCACB and FeNiCoAlTiB alloys, the directions of the main recrystallization textures are all along [001] direction. While for FeNiCoAlNbB, the recrystallization texture is along [101] in Omori's work [41] and along [001] in Fu's study [60]. Li et al. [61] calculated the stacking fault energy of iron-based shape memory alloys and found that the addition of Cr would decrease the stacking fault energy. However, the contribution of Ta, Nb, or Ti to the stacking fault energy of this alloy system has not been evaluated. Further research in the stacking fault energy of Fe-

Ni-Co-Al-based alloys should yield guidance on tuning the recrystallization texture.

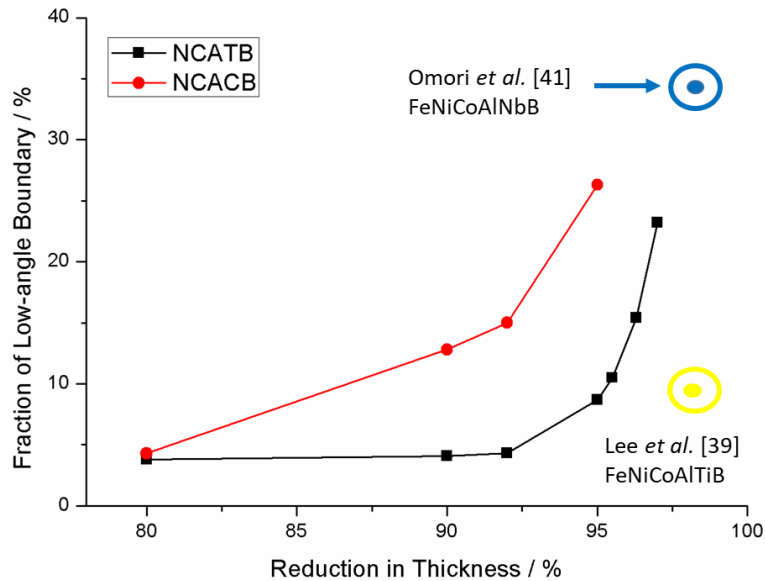


Figure 2.9. Development of fraction of the low-angle boundaries in annealed NCATB and NCACB samples with different reduction in thickness.

For Fe-Ni-Co-Al-based polycrystalline alloys to show good ductility, it is very important to increase the fraction of low-angle boundaries to make the specimen behave similar to the single crystals [39]. Therefore, it is necessary to determine the fraction of low-angle boundaries in NCACB. Fig. 2.9 shows the development of the fraction of the low-angle boundary with increasing RIT. It is obvious that the fraction of low-angle boundaries in NCACB is much higher than that in NCATB under the same conditions. It can also be seen that the fraction of low-angle boundaries in NCACB (CR95) is higher than that in NCATB (CR97), indicating that it is easier for NCACB to achieve a higher fraction of low-angle boundaries than NCATB. For FeNiCoAlNbB (CR98.5) [41], the fraction of low-angle boundaries can reach over 30%, while the fraction of low-angle boundaries is only about 10% for FeNiCoAlTiB (CR98.5) [39]. Difference in the fraction of the low-

angle boundary may also be due to the difference in the stacking fault energy, but further study is required.

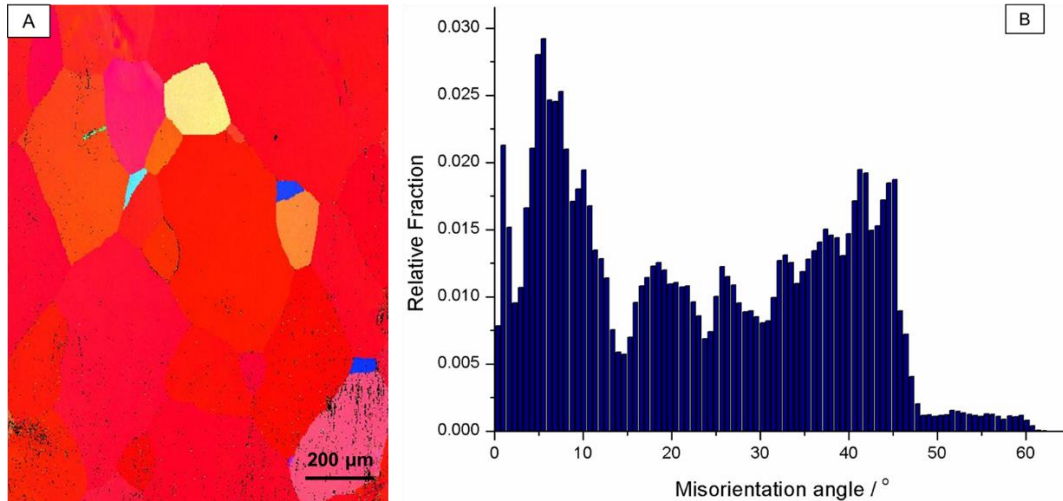


Figure 2.10. (A) EBSD IPFX map for NCATB with RIT of 97% annealed at 1300°C for 30-min; (B) Corresponding statistics for the misorientation between grains in Fig. 2.10(A).

Furthermore, the statistics of the fraction of low-angle boundaries can be biased depending on the scan area. Tanaka et al. [40] found that the fraction of low-angle boundaries in NCATB (CR98.5) can reach almost 60%. If the selected area is larger, the result may be slightly lower. For example, Fig. 2.10(A) shows the EBSD IPF map for NCATB (CR97, 1300°C, 30-min) with higher magnification than that in Fig. 2.7(E), and Fig. 2.10(B) is the corresponding statistics figure of the misorientation between grains in Fig. 2.10(A). Fig. 2.10(B) shows that the fraction of low-angle boundaries in Fig. 2.10(A) is over 40%, while in Fig. 2.7(E) it is less than 30%. For FeNiCoAlNbB (CR98.5) alloy, the fraction of low-angle boundaries in Omori's study [41] is about 35%, while in Fu's research [60] it is over 50% with fewer grains. Therefore, the number of grains selected

in the scan area affects the measured fraction of low-angle boundaries. Overall, the more grains included in the analysis, the more representative the result is of bulk texture.

2.3.4 Effect of recrystallization texture and relative grain size on the mechanical properties of NCACB

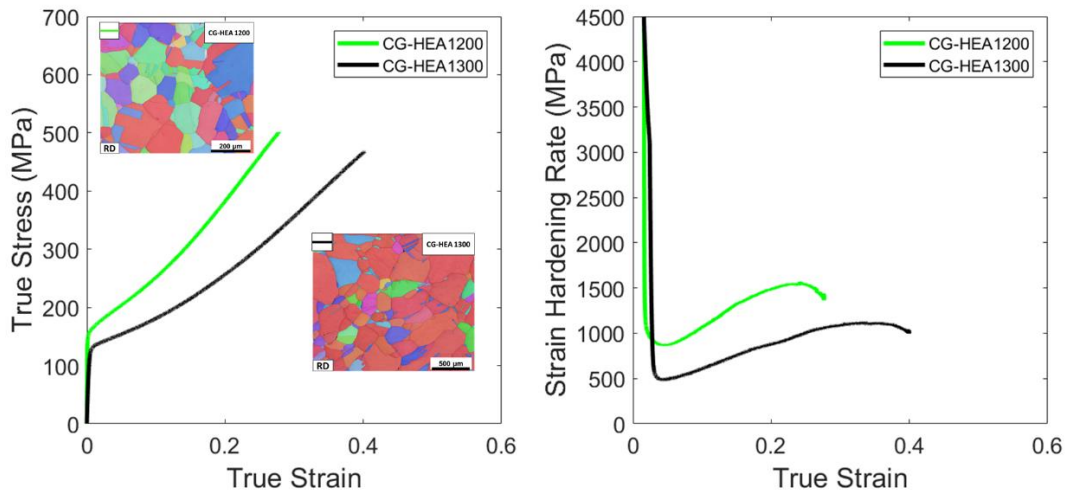


Figure 2.11. (A) True Stress-Strain curves for CG-HEA-1200 and CG-HEA-1300; (B) Corresponding strain hardening rate curves for CG-HEA-1200 and CG-HEA-1300.

Fig. 2.11 show tensile properties of two cold-rolled and annealed NCACB (RIT=90%) with distinct microstructures. Coarse-grained NCACB after annealing at 1200°C for 20min is denoted CG-HEA-1200 with an average grain size of 140 μm, and coarse-grained NCACB after annealing at 1300°C for 30min is denoted CG-HEA 1300 with an average grain size of 420 μm. The higher ductility in CG-HEA-1300 is due to the relatively large grain size (grain size/thickness) and strong texture that lead to the formation of a bamboo-like or oligocrystal structure, which effectively reduces the grain constraint

and the deformation mimics that of a single crystal [37][38]. On the other hand, CG-HEA-1200 undergoes significant heterogeneous deformation as misfit strains of differently orientated grain (random texture) induce plastic strain gradients as well as residual stresses, hence lower ductility. The strain hardening rate of both specimens first decreases, and then increases at higher strains. This phenomena was verified here to be due to stress-induced twins formed during the tensile test which effectively reduce the slip distance, thereby increasing the stress necessary for further slip to occur.

2.4 Conclusion

The recrystallization texture evolution is studied in Fe-Ni-Co-Al-based non-equiatomic high entropy alloys. Important results are summarized as follows:

1. For cold-rolled NCACB, the optimal annealing condition for obtaining strong recrystallization texture is at 1300°C for 30-min.
2. Abnormal grain growth occurred at the early stage is due to the Zener pinning effect resulting from the presence of precipitated NiAl particles. When NiAl particles are dissolved in the matrix, the grain growth turns back to normal growth.
3. The grain growth affects the texture evolution of NCACB. The experimental results show that recrystallization texture formed at 1300°C is much stronger than that formed at 1200°C with the same RIT, especially for the CR90. The increase in times random values can be attributed to the decrease of grain boundaries, i.e. Ostwald ripening

effect.

4. Among cold-rolled NCAB, NCATB, and NCACB, NCACB shows the strongest texture under the same annealing condition (1300°C 30-min). It is also found that Cr is effective in the formation of strong recrystallization texture in Fe-Ni-Co-Al-based alloys, hypothetically, due to decreased stacking fault energy. The enhancement of <001> recrystallization texture in Fe-Ni-Co-Al-based alloys can be achieved using optimal annealing condition with the addition of Cr.

5. Non-biased statistics of the fraction of low-angle boundaries can be achieved with selection of as many grains as possible. A higher fraction of low-angle boundaries (~30%) can be obtained in NCACB (CR95) than FeNiCoAlTiB (CR98.5), comparable to that obtained in NCATB (CR97) and FeNiCoAlNbB (CR98.5).

6. High ductility can be achieved in NCACB with strong recrystallization texture and large relative grain size because the bamboo-like structure effectively reduces the grain constraint and the deformation mimics that of a single crystal.

Acknowledgement

Chapter 2, in full, is a reprint of the material as it appears in *Journal of Alloys and Compounds* 768 (2018): 277-286, Elsevier. Cheng Zhang, Chaoyi Zhu, Sumin Shin, Kenneth Vecchio. The dissertation author was the primary investigator and author of this paper.

The current authors would like to thank Tyler Harrington, Eduardo Marin, Haoren Wang, Zezhou Li, Sabine Faulhaber and Wayne Neilson for help on experiments.

Reference

- [1] J. Yeh, S. Chen, S. Lin, J. Gan, T. Chin, T. Shun, C. Tsau, S. Chang, Nanostructured high - entropy alloys with multiple principal elements: novel alloy design concepts and outcomes, *Adv. Eng. Mater.* 6 (2004) 299–303.
- [2] Y. Zhang, T.T. Zuo, Z. Tang, M.C. Gao, K.A. Dahmen, P.K. Liaw, Z.P. Lu, Microstructures and properties of high-entropy alloys, *Prog. Mater. Sci.* 61 (2014) 1–93.
- [3] D.B. Miracle, O.N. Senkov, A critical review of high entropy alloys and related concepts, *Acta Mater.* 122 (2017) 448–511.
- [4] M.J. Yao, K.G. Pradeep, C.C. Tasan, D. Raabe, A novel, single phase, non-equiatomic FeMnNiCoCr high-entropy alloy with exceptional phase stability and tensile ductility, *Scr. Mater.* 72 (2014) 5–8.
- [5] Z. Li, K.G. Pradeep, Y. Deng, D. Raabe, C.C. Tasan, Metastable high-entropy dual-phase alloys overcome the strength–ductility trade-off, *Nature.* 534 (2016) 227.
- [6] Z. Li, C.C. Tasan, K.G. Pradeep, D. Raabe, A TRIP-assisted dual-phase high-entropy alloy: grain size and phase fraction effects on deformation behavior, *Acta Mater.* 131 (2017) 323–335.
- [7] Z. Li, F. Körmann, B. Grabowski, J. Neugebauer, D. Raabe, Ab initio assisted design of quinary dual-phase high-entropy alloys with transformation-induced plasticity, *Acta Mater.* 136 (2017) 262–270.
- [8] B. Gludovatz, A. Hohenwarter, D. Catoor, E.H. Chang, E.P. George, R.O. Ritchie, A fracture-resistant high-entropy alloy for cryogenic applications, *Science* (80-.). 345 (2014) 1153–1158.
- [9] D. Li, C. Li, T. Feng, Y. Zhang, G. Sha, J.J. Lewandowski, P.K. Liaw, Y. Zhang, High-entropy Al 0.3 CoCrFeNi alloy fibers with high tensile strength and ductility at ambient

and cryogenic temperatures, *Acta Mater.* 123 (2017) 285–294.

[10] E.D. Tabachnikova, A. V Podolskiy, M.O. Laktionova, N.A. Bereznaia, M.A. Tikhonovsky, A.S. Tortika, Mechanical properties of the CoCrFeNiMnVx high entropy alloys in temperature range 4.2–300 K, *J. Alloys Compd.* 698 (2017) 501–509.

[11] X.B. Feng, W. Fu, J.Y. Zhang, J.T. Zhao, J. Li, K. Wu, G. Liu, J. Sun, Effects of nanotwins on the mechanical properties of AlxCoCrFeNi high entropy alloy thin films, *Scr. Mater.* 139 (2017) 71–76.

[12] T. Yang, S. Xia, W. Guo, R. Hu, J.D. Poplawsky, G. Sha, Y. Fang, Z. Yan, C. Wang, C. Li, Effects of temperature on the irradiation responses of Al 0.1 CoCrFeNi high entropy alloy, *Scr. Mater.* 144 (2018) 31–35.

[13] S. Vrtnik, P. Koželj, A. Meden, S. Maiti, W. Steurer, M. Feuerbacher, J. Dolinšek, Superconductivity in thermally annealed Ta-Nb-Hf-Zr-Ti high-entropy alloys, *J. Alloys Compd.* 695 (2017) 3530–3540.

[14] H.W. Yao, J.W. Qiao, J.A. Hawk, H.F. Zhou, M.W. Chen, M.C. Gao, Mechanical properties of refractory high-entropy alloys: Experiments and modeling, *J. Alloys Compd.* 696 (2017) 1139–1150.

[15] Y. Lu, X. Gao, L. Jiang, Z. Chen, T. Wang, J. Jie, H. Kang, Y. Zhang, S. Guo, H. Ruan, Directly cast bulk eutectic and near-eutectic high entropy alloys with balanced strength and ductility in a wide temperature range, *Acta Mater.* 124 (2017) 143–150.

[16] C. Ai, F. He, M. Guo, J. Zhou, Z. Wang, Z. Yuan, Y. Guo, Y. Liu, L. Liu, Alloy design, micromechanical and macromechanical properties of CoCrFeNiTa x eutectic high entropy alloys, *J. Alloys Compd.* 735 (2018) 2653–2662.

[17] J. Chen, X. Zhou, W. Wang, B. Liu, Y. Lv, W. Yang, D. Xu, Y. Liu, A review on fundamental of high entropy alloys with promising high-temperature properties, *J. Alloys Compd.* 760 (2018) 15–30.

[18] Y. Yao, Z. Huang, P. Xie, S.D. Lacey, R.J. Jacob, H. Xie, F. Chen, A. Nie, T. Pu, M. Rehwoldt, Carbothermal shock synthesis of high-entropy-alloy nanoparticles, *Science*, 359 (2018) 1489–1494.

[19] R. Wang, K. Zhang, C. Davies, X. Wu, Evolution of microstructure, mechanical and corrosion properties of AlCoCrFeNi high-entropy alloy prepared by direct laser fabrication, *J. Alloys Compd.* 694 (2017) 971–981.

- [20] R. Li, P. Niu, T. Yuan, P. Cao, C. Chen, K. Zhou, Selective laser melting of an equiatomic CoCrFeMnNi high-entropy alloy: Processability, non-equilibrium microstructure and mechanical property, *J. Alloys Compd.* 746 (2018) 125–134.
- [21] J. Joseph, N. Stanford, P. Hodgson, D.M. Fabijanic, Tension/compression asymmetry in additive manufactured face centered cubic high entropy alloy, *Scr. Mater.* 129 (2017) 30–34.
- [22] X. Qiu, Microstructure, hardness and corrosion resistance of Al₂CoCrCuFeNiTi_x high-entropy alloy coatings prepared by rapid solidification, *J. Alloys Compd.* 735 (2018) 359–364.
- [23] S.-H. Joo, H. Kato, M.J. Jang, J. Moon, E.B. Kim, S.-J. Hong, H.S. Kim, Structure and properties of ultrafine-grained CoCrFeMnNi high-entropy alloys produced by mechanical alloying and spark plasma sintering, *J. Alloys Compd.* 698 (2017) 591–604.
- [24] X.D. Xu, P. Liu, Z. Tang, A. Hirata, S.X. Song, T.G. Nieh, P.K. Liaw, C.T. Liu, M.W. Chen, Transmission electron microscopy characterization of dislocation structure in a face-centered cubic high-entropy alloy Al_{0.1}CoCrFeNi, *Acta Mater.* 144 (2018) 107–115.
- [25] Q. Lin, X. An, H. Liu, Q. Tang, P. Dai, X. Liao, In-situ high-resolution transmission electron microscopy investigation of grain boundary dislocation activities in a nanocrystalline CrMnFeCoNi high-entropy alloy, *J. Alloys Compd.* 709 (2017) 802–807.
- [26] M. Wang, Z. Li, D. Raabe, In-situ SEM observation of phase transformation and twinning mechanisms in an interstitial high-entropy alloy, *Acta Mater.* 147 (2018) 236–246.
- [27] Z. Li, S. Zhao, S.M. Alotaibi, Y. Liu, B. Wang, M.A. Meyers, Adiabatic shear localization in the CrMnFeCoNi high-entropy alloy, *Acta Mater.* 151 (2018) 424–431.
- [28] J.B. Seol, J.W. Bae, Z. Li, J.C. Han, J.G. Kim, D. Raabe, H.S. Kim, Boron doped ultrastrong and ductile high-entropy alloys, *Acta Mater.* 151 (2018) 366–376.
- [29] Y. Zhou, X. Jin, L. Zhang, X. Du, B. Li, A hierarchical nanostructured Fe₃₄Cr₃₄Ni₁₄Al₁₄Co₄ high-entropy alloy with good compressive mechanical properties, *Mater. Sci. Eng. A.* 716 (2018) 235–239.
- [30] C. Zhang, C. Zhu, T. Harrington, K. Vecchio, Design of non-equiatomic high entropy alloys with heterogeneous lamella structure towards strength-ductility synergy, *Scr.*

Mater. 154 (2018) 78–82.

[31] J.W. Bae, J. Moon, M.J. Jang, D. Yim, D. Kim, S. Lee, H.S. Kim, Trade-off between tensile property and formability by partial recrystallization of CrMnFeCoNi high-entropy alloy, Mater. Sci. Eng. A. 703 (2017) 324–330.

[32] P.P. Bhattacharjee, G.D. Sathiaraj, M. Zaid, J.R. Gatti, C. Lee, C.-W. Tsai, J.-W. Yeh, Microstructure and texture evolution during annealing of equiatomic CoCrFeMnNi high-entropy alloy, J. Alloys Compd. 587 (2014) 544–552.

[33] G.D. Sathiaraj, P.P. Bhattacharjee, Effect of starting grain size on the evolution of microstructure and texture during thermo-mechanical processing of CoCrFeMnNi high entropy alloy, J. Alloys Compd. 647 (2015) 82–96.

[34] G.D. Sathiaraj, C.W. Tsai, J.W. Yeh, M. Jahazi, P.P. Bhattacharjee, The effect of heating rate on microstructure and texture formation during annealing of heavily cold-rolled equiatomic CoCrFeMnNi high entropy alloy, J. Alloys Compd. 688 (2016) 752–761.

[35] A. Shabani, M.R. Toroghinejad, A. Shafyei, P. Cavaliere, Effect of cold-rolling on microstructure, texture and mechanical properties of an equiatomic FeCrCuMnNi high entropy alloy, Materialia. (2018) in press.

[36] C. Haase, L.A. Barrales-Mora, Influence of deformation and annealing twinning on the microstructure and texture evolution of face-centered cubic high-entropy alloys, Acta Mater. 150 (2018) 88–103.

[37] Y. Sutou, T. Omori, K. Yamauchi, N. Ono, R. Kainuma, K. Ishida, Effect of grain size and texture on pseudoelasticity in Cu–Al–Mn-based shape memory wire, Acta Mater. 53 (2005) 4121–4133.

[38] S.M. Ueland, Y. Chen, C.A. Schuh, Oligocrystalline shape memory alloys, Adv. Funct. Mater. 22 (2012) 2094–2099.

[39] D. Lee, T. Omori, R. Kainuma, Ductility enhancement and superelasticity in Fe–Ni–Co–Al–Ti–B polycrystalline alloy, J. Alloys Compd. 617 (2014) 120–123.

[40] Y. Tanaka, Y. Himuro, R. Kainuma, Y. Sutou, T. Omori, K. Ishida, Ferrous polycrystalline shape-memory alloy showing huge superelasticity, Science, 327 (2010) 1488–1490.

[41] T. Omori, S. Abe, Y. Tanaka, D.Y. Lee, K. Ishida, R. Kainuma, Thermoelastic

martensitic transformation and superelasticity in Fe–Ni–Co–Al–Nb–B polycrystalline alloy, *Scr. Mater.* 69 (2013) 812–815.

[42] Y. Ma, Q. Wang, B.B. Jiang, C.L. Li, J.M. Hao, X.N. Li, C. Dong, T.G. Nieh, Controlled formation of coherent cuboidal nanoprecipitates in body-centered cubic high-entropy alloys based on Al₂ (Ni, Co, Fe, Cr) 14 compositions, *Acta Mater.* 147 (2018) 213–225.

[43] T. Guo, J. Li, J. Wang, W.Y. Wang, Y. Liu, X. Luo, H. Kou, E. Beaugnon, Microstructure and properties of bulk Al_{0.5}CoCrFeNi high-entropy alloy by cold rolling and subsequent annealing, *Mater. Sci. Eng. A.* 729 (2018) 141–148.

[44] S. Niu, H. Kou, T. Guo, Y. Zhang, J. Wang, J. Li, Strengthening of nanoprecipitations in an annealed Al_{0.5}CoCrFeNi high entropy alloy, *Mater. Sci. Eng. A.* 671 (2016) 82–86.

[45] S. Guo, C. Ng, J. Lu, C.T. Liu, Effect of valence electron concentration on stability of fcc or bcc phase in high entropy alloys, *J. Appl. Phys.* 109 (2011) 103505.

[46] Y. Zhang, Y.J. Zhou, J.P. Lin, G.L. Chen, P.K. Liaw, Solid-solution phase formation rules for multi-component alloys, *Adv. Eng. Mater.* 10 (2008) 534–538.

[47] F. Bachmann, R. Hielscher, H. Schaeben, Texture Analysis with MTEX – Free and Open Source Software Toolbox, *Solid State Phenom.* 160 (2010) 63–68.

[48] L.S. Toth, S. Biswas, C. Gu, B. Beausir, Notes on representing grain size distributions obtained by electron backscatter diffraction, *Mater. Charact.* 84 (2013) 67–71.

[49] J.E. Burke, D. Turnbull, Recrystallization and grain growth, *Prog. Met. Phys.* 3 (1952) 220–292.

[50] D. Raabe, Recovery and recrystallization: phenomena, physics, models, simulation, in: *Phys. Metall.*, Fifth Ed., Elsevier, (2015) pp. 2291–2397.

[51] M. Hillert, On the theory of normal and abnormal grain growth, *Acta Metall.* 13 (1965) 227–238.

[52] J.J. Bhattacharyya, S.R. Agnew, G. Muralidharan, Texture enhancement during grain growth of magnesium alloy AZ31B, *Acta Mater.* 86 (2015) 80–94.

[53] F.J. Humphreys, A unified theory of recovery, recrystallization and grain growth,

based on the stability and growth of cellular microstructures—I. The basic model, *Acta Mater.* 45 (1997) 4231–4240.

[54] J.M. Feppon, W.B. Hutchinson, On the growth of grains, *Acta Mater.* 50 (2002) 3293–3300.

[55] D. Lee, T. Omori, K. Han, Y. Hayakawa, R. Kainuma, Effect of Thermomechanical Processing on Texture and Superelasticity in Fe–Ni–Co–Al–Ti–B Alloy, *Shape Mem. Superelasticity*, 4-1 (2018) 102–111.

[56] R.E. Smallman, D. Green, The dependence of rolling texture on stacking fault energy, *Acta Metall.* 12 (1964) 145–154.

[57] S.F. Liu, Y. Wu, H.T. Wang, J.Y. He, J.B. Liu, C.X. Chen, X.J. Liu, H. Wang, Z.P. Lu, Stacking fault energy of face-centered-cubic high entropy alloys, *Intermetallics*. 93 (2018) 269–273.

[58] J. Liu, C. Chen, Y. Xu, S. Wu, G. Wang, H. Wang, Y. Fang, L. Meng, Deformation twinning behaviors of the low stacking fault energy high-entropy alloy: an in-situ TEM study, *Scr. Mater.* 137 (2017) 9–12.

[59] Y.H. Zhang, Y. Zhuang, A. Hu, J.J. Kai, C.T. Liu, The origin of negative stacking fault energies and nano-twin formation in face-centered cubic high entropy alloys, *Scr. Mater.* 130 (2017) 96–99.

[60] H. Fu, H. Zhao, S. Song, Z. Zhang, J. Xie, Evolution of the cold-rolling and recrystallization textures in FeNiCoAlNbB shape memory alloy, *J. Alloys Compd.* 686 (2016) 1008–1016.

[61] J.C. Li, W. Zheng, Q. Jiang, Stacking fault energy of iron-base shape memory alloys, *Mater. Lett.* 38 (1999) 275–277.

Chapter 3

Design of Non-Equiatomic High Entropy Alloys with Heterogeneous Lamella Structure Towards Strength-Ductility Synergy

Chapter 3 is the part of the paper published in Scripta Materialia.

Cheng Zhang, Chaoyi Zhu, Tyler Harrington, and Kenneth Vecchio. "Design of non-equiatomic high entropy alloys with heterogeneous lamella structure towards strength-ductility synergy." Scripta Materialia 154 (2018): 78-82. Elsevier.

Abstract

A non-equiatomic FeNiCoAlCrB (NCACB) high entropy alloy (HEA) with a heterogeneous lamella (HL) structure is fabricated through conventional thermomechanical processing. In the HL microstructure, fine-grain regions result from inhibited grain growth due to Zener pinning of boundaries by NiAl (B2) precipitates, while coarse-grained regions originate from grain growth within large deformation bands in the absence of precipitates. A back-stress strengthening mechanism, unique to deformation of heterogeneous microstructures, is verified through electron backscatter diffraction enabled geometrically necessary dislocation density analysis. This mechanism gives rise to the combination of both high strength and high ductility in HL-NCACB-HEA.

3.1 Introduction

Owing to attractive engineering properties, high entropy alloys (HEAs) have drawn great attention over the past decade [1-5]. During this time of exploration, most studies have been focused on one of the original concepts of HEAs for alloy design, which utilizes an equiatomic ratio of multiple principal elements to obtain the maximum configurational entropy [1]. However, this design concept limits the compositional space and excludes non-equiatomic candidates with potentially outstanding properties and potentially more commercially viable. The concept of non-equiatomic HEAs, first put forward by Raabe and his colleagues [6-10], has greatly expanded the compositional space for HEA design, and work on these compositions has achieved unparalleled mechanical properties [6]. On the other hand, in the development of traditional metals and alloys, modification of mechanical properties through controlled microstructure design has succeeded in many studies. Heterogeneous lamella structures, bimodal structures, and gradient structures have been fabricated in pure Ti/Cu, steels and aluminum alloys over a wide range of length scales to overcome the strength-ductility trade-off [11-22]. For the fabrication of these microstructures, powder metallurgy with different size particles, surface mechanical attrition treatment (SMAT) techniques and asymmetrical rolling with subsequent annealing are typically employed [11-22]. Nevertheless, to these authors' knowledge, an effective method for the fabrication of a heterogeneous lamella structure in non-equiatomic HEAs has never been reported. In this study, a method using precipitation (NiAl) controlled

development of non-equiatomic HEAs with heterogeneous lamella structure has been devised. It is a reliable and reproducible method to manufacture a novel, heterogeneous lamella, non-equiatomic, $\text{Fe}_{34.95}\text{Ni}_{27.5}\text{Co}_{17.5}\text{Al}_{11.5}\text{Cr}_{8.5}\text{B}_{0.05}$ (at. %) (NCACB) HEA with high strength and high ductility. This composition can be regarded as a non-equiatomic HEA because the composition is clearly non-equiatomic, but has a Valence Electron Configuration (VEC) value of 8.0 (in the range of FCC-HEA, $7.5 < \text{VEC} < 9.5$) [23], has a mixing enthalpy (ΔH) of -8.5 kJ/mol (in the range of HEA, $-15 \text{ kJ/mol} < \Delta H < 5 \text{ kJ/mol}$) [24], and has a configurational entropy (ΔS) value of $1.52R$ [1].

3.2 Experimental Procedures

NCACB ingots were prepared through arc-melting under an argon atmosphere with raw materials as follows: Fe (99.95%), Ni (99.9%), Co (99.9%), Al (99.9%), Cr (99.9%), and Ni₂B (99%). Each ingot was flipped and re-melted eight times to ensure homogeneity. Next, each NCACB ingot with an original thickness of ~10 mm was processed through homogenization (1300°C, 3h), hot rolling (1250°C, reduction in thickness (RIT) of ~30%), cold rolling (RIT ~90%), annealing at 1000-1300°C for various times and water quenched. Depending on the annealing conditions, distinct microstructures can be achieved, e.g. fine grain (FG), coarse grain (CG) and heterogeneous lamella (HL) microstructures.

Microstructure characterization was performed in a Thermo-Fisher (formerly FEI) Apreo FEG-SEM equipped with Oxford Instruments EDS and EBSD-Symmetry detectors.

Thin samples rolled to a RIT = 90% were cut to standard dog-bone tensile shapes, and metallographic samples were ground and polished using standard metallographic techniques, followed by vibratory polishing. Quasi-static tensile tests were carried out at room temperature, with the tensile direction parallel to the rolling direction [gauge dimensions: $20 \times 2 \times 0.5$ (mm)]. After tensile tests, the geometrically necessary dislocation (GND) density in the deformed HL NCACB was calculated from EBSD orientation data using an in-house Matlab code developed by Zhu et al. [25, 26].

3.3 Results and Discussion

3.3.1 Microstructure evolution and formation of heterogeneous lamella structure

Fig. 3.1(A) shows the large deformation bands found in NCACB after cold rolling to a RIT of 90%. These deformation bands were previously reported in cold rolling (RIT=90%) of polycrystalline nickel with an initial average grain size of $500\mu\text{m}$ [27], but were not formed when the initial average grain size was between $80\text{-}100\mu\text{m}$ [28]. Hence, we conclude that each observable deformation band corresponds to one initial large grain in the NCACB sample prior to cold rolling (refer to Fig. 3.2 and Fig. 3.3 for the microstructure evolution prior to cold rolling). Similar phenomena have been observed in aluminum alloys with different grain sizes at large strains [29-31]. As for small grains, microbands are found across the entire microstructure [28, 29, 31-33], which leads to subdivision of grains instead of the formation of large deformation bands. Overall, highly

heterogeneous deformation during cold rolling leads to subdivision of small grains with NiAl particles along sub-grain/grain boundaries, and elongation of large grains into deformation bands. The unique heterogeneous microstructure for NCACB over a large region is shown in Fig. 3.1(B) & (C) after annealing at 1150°C for 1h to a RIT of 90% in the cold rolling step. At higher magnifications, coarse and fine grains are present in bands as more clearly shown in Fig. 3.4(A) & 3.8(B). Fine grain and coarse grain regions differ in size by almost three to four orders of magnitude are shown in Fig. 3.4(B), therefore this alloy is referred to as HL (heterogeneous lamella microstructure)-HEA (type of alloy)-1150 (annealing temperature). This microstructure was reproduced consistently under these processing conditions and is not a unique anomaly.

To understand the formation mechanism of the heterogeneous lamella (HL) structure, a microstructure evolution study of NCACB through a series of heat-treatment conditions was undertaken. While secondary phase precipitates are observed along the boundaries of fine grains that are composed of Ni and Al according to EDS analysis (Fig. 3.5(B)), no secondary phase is found along the grain boundaries in the coarse-grained regions. Combined EDS mapping and XRD in Fig. 3.5 further confirm that these particles are NiAl (B2) β phase particles embedded in a matrix of the γ (FCC) phase. Therefore, NiAl precipitates are formed prior to the heat treatment since no additional NiAl has precipitated out along coarse grain boundaries during the annealing step at 1150°C. Consequently, large deformed bands preferably grow into a coarse-grained region as grain boundaries

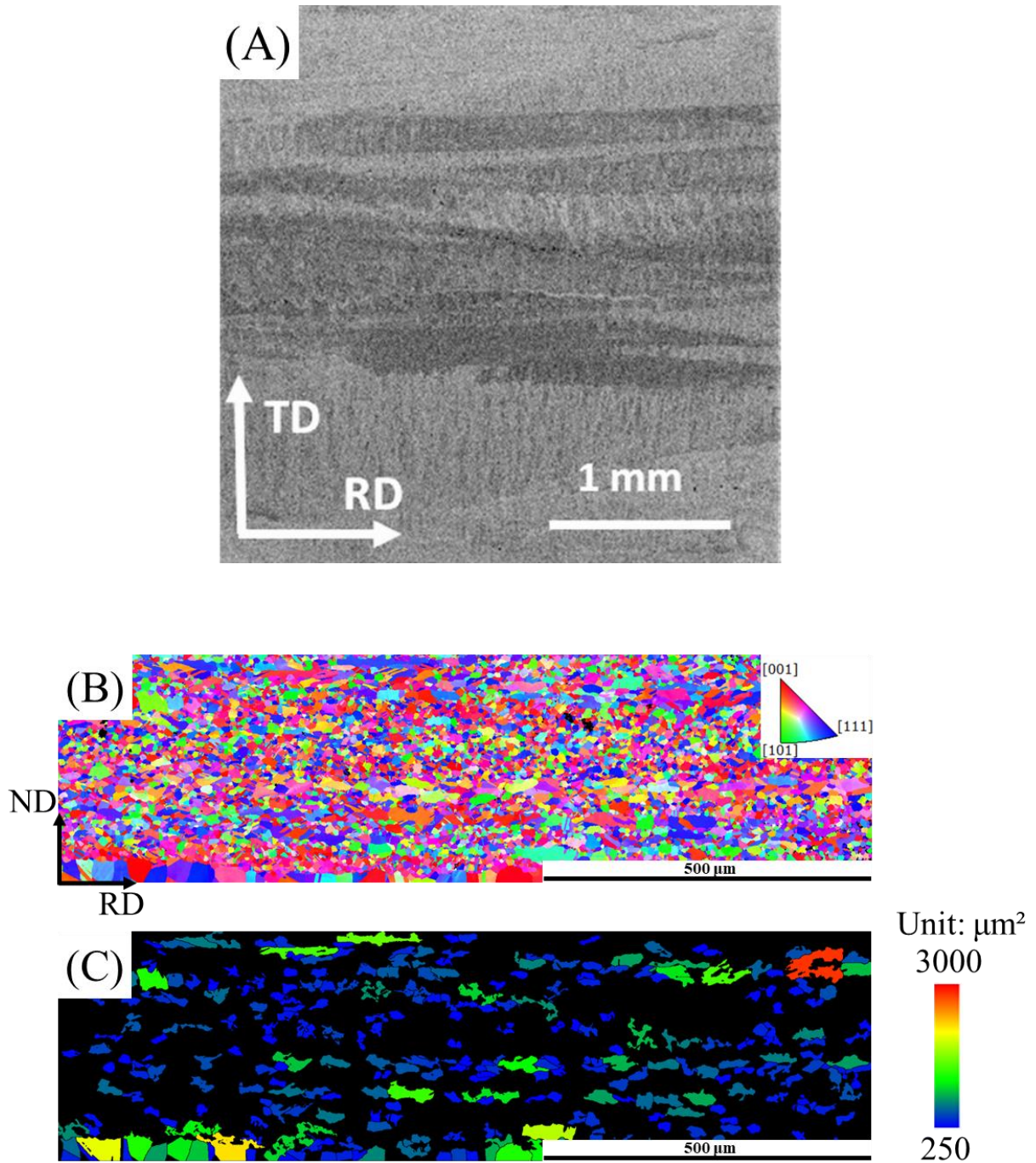


Figure 3.1: (A) SEM (BSE) image for NCACB after cold rolling (RIT=90%), RD-Rolling Direction, TD-Transverse Direction; (B) EBSD IPFX map for NCACB in the transverse direction after annealing at 1150°C for 1h; (C) Grain area map corresponding to Fig. 3.1(B).

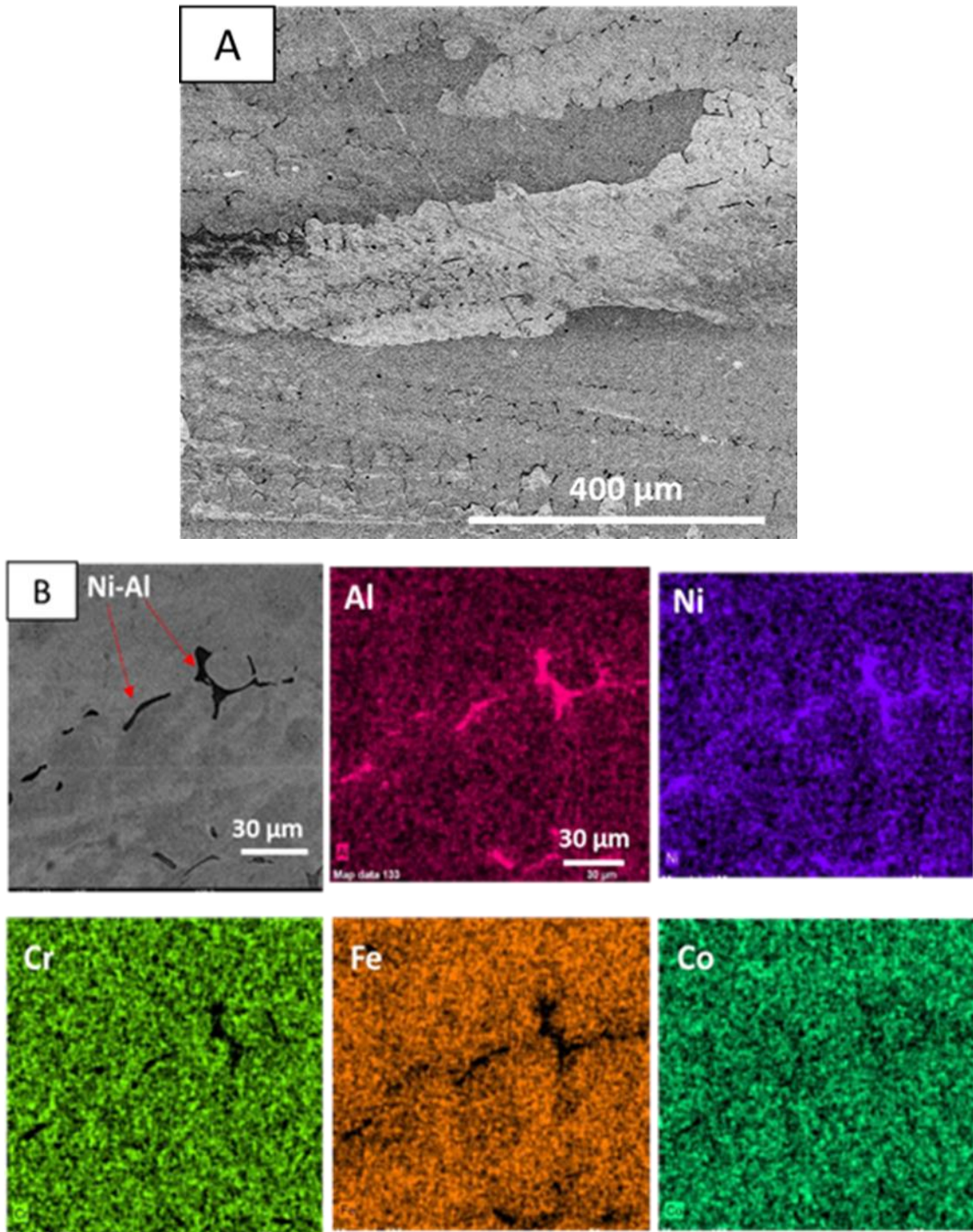


Figure 3.2: (A) SEM (BSE) image for NCACB after arc-melting. The grain structure and compositions of the as-cast specimen indicate the presence of NiAl (B2) precipitates between the solid solution FCC phase dendrites, similar to what has been found in an Al_{0.5}CoCrFeNi HEA after arc-melting ; (B) EDS mapping for as-cast NCACB.

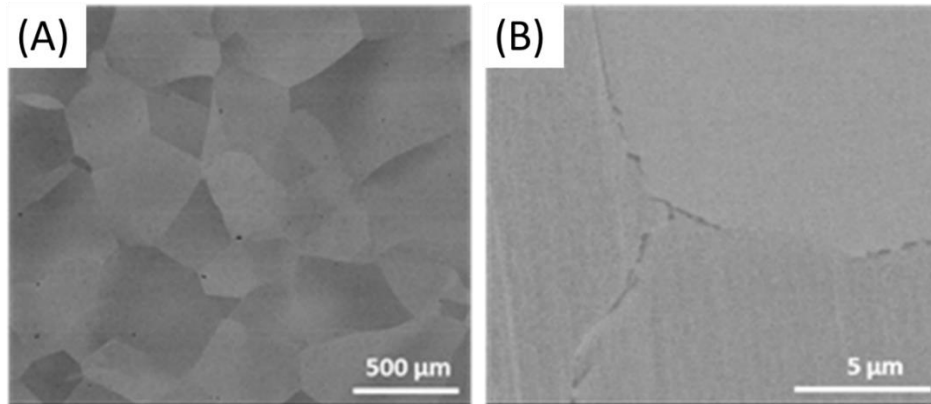


Figure 3.3: (A) SEM (BSE) image for NCACB. Large grains, up to 500 μm diameter, are apparent in NCACB after homogenization, hot rolling and air cooling. Some NiAl (B2) precipitates can also be observed along the grain boundaries (B).

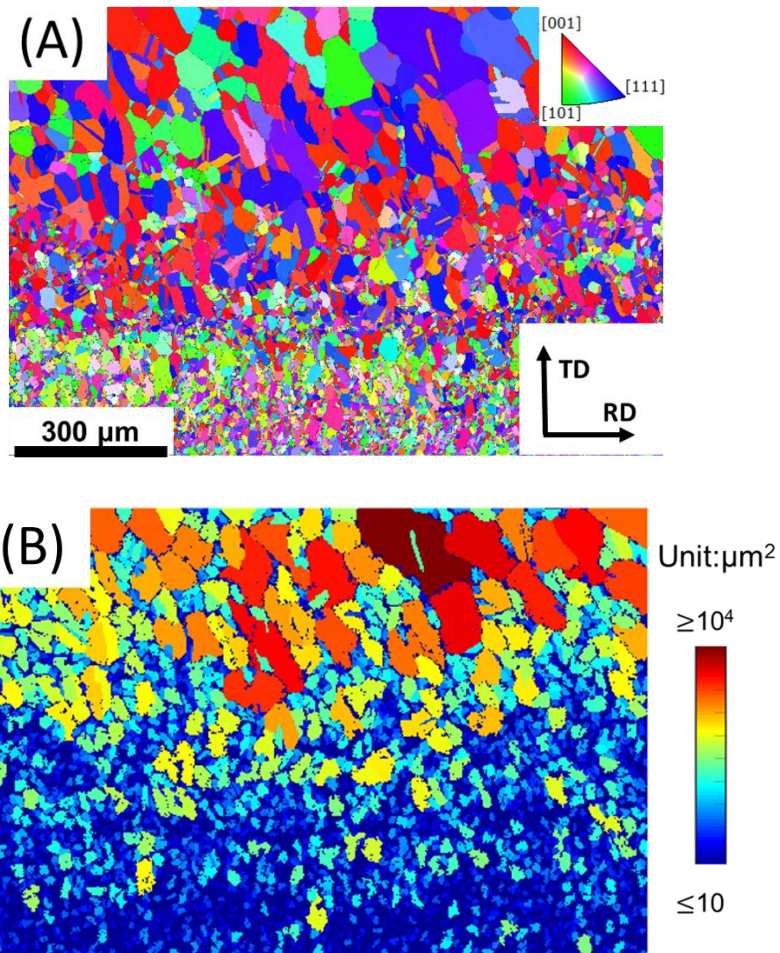


Figure 3.4: (A) EBSD IPFX Mapping for NCACB after annealing at 1150 $^{\circ}\text{C}$ for 1 h, which shows clear separation of grain size in fine grained and coarse grained lamella as well as its random texture; (B) Grain area map corresponding to Fig. 3.4(A) shows three orders of magnitude difference in term of grain area (unit: μm^2).

quickly sweep across the deform band without resistance from particle pinning. SEM images of NCACB (CR90, 1150°C 60-min) at different magnifications are shown in Fig. 3.6(A), which clearly indicate the presence of the HL structure. Small NiAl precipitates distributed outside the large deformation bands not only act as the nuclei for the recrystallization [34, 35], but also suppress grain growth due to Zener pinning of the boundaries.

For Zener's pinning effect, it can be calculated by the following equation:

$$R_c = \frac{4r}{3f} \quad (1)$$

Where R_c is the limited grain radius, r is the radius of the particles, and f is the volume fraction of particles. The limited grain radii of the NCACB samples annealed at 1000 °C, 1150 °C, 1175 °C and 1200 °C are 9.6µm, 19.5 µm, 45.1 µm and 7.1 µm and 60.2 µm, respectively. It is found that the calculated R_c is in agreement with those observed experimentally. For example, the calculated R_c values with annealing temperature of 1000 °C and 1150 °C are 9.6 µm and 19.5 µm, respectively. In comparison, sizes of small grains are about 2.4 µm and 4.7 µm in Fig. 3.6 (F3) and (A3), respectively. Therefore, the size of the small grains are all within the range of the calculated R_c values.

As the temperature is further increased to 1200°C, no NiAl precipitates are observed along grain boundaries for an annealing time of 10 min, as shown in Fig. 3.6(E3), indicating that these B2 particles are completely dissolved into the γ matrix. However, NCACB annealed at 1000°C for 1h, as shown in Fig. 3.6(F), does not exhibit the HL structure. As

NiAl particles precipitate out within large deformation bands at 1000°C, the pinning effect restricts grain growth over the entire sample to produce a fine grain microstructure with an average grain size of 4.7µm, hence the term: FG-HEA 1000. Based on the above study on annealing conditions, 1150°C is a temperature low enough to prevent NiAl outside deformation bands from dissolving into the matrix, and yet high enough to suppress precipitation within large deformation bands. Consequently, this condition leads to fast grain growth within the large deformation bands and suppression of grain growth outside the large deformation bands, i.e. formation of heterogeneous lamella structure in NCACB.

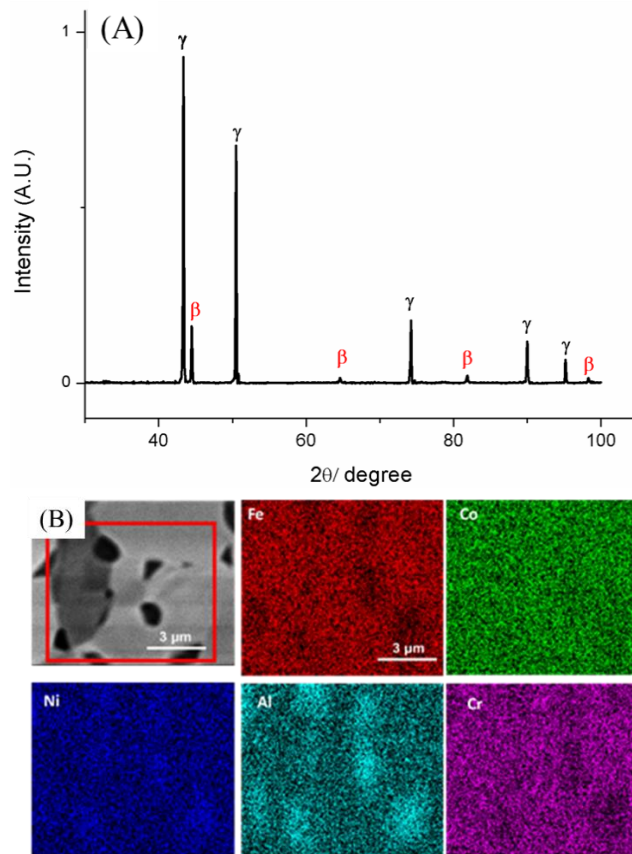


Figure 3.5: (A) XRD pattern for NCACB after annealing at 1150°C for 1h; (B) EDS Mapping for NCACB after annealing at 1150°C for 1h.

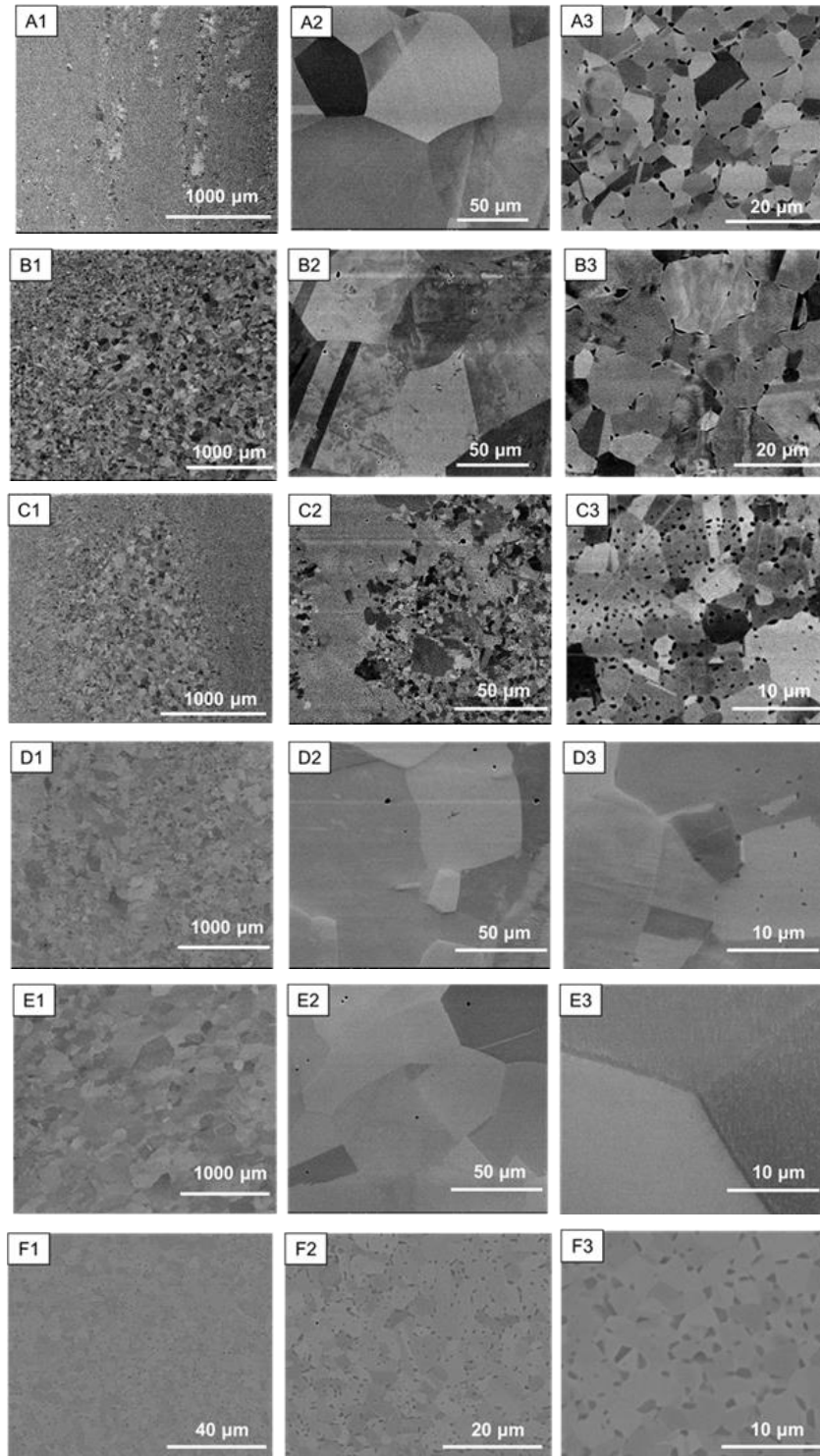


Figure 3.6: SEM (BSE) images for NCACB (RIT=90% in cold rolling) after annealing (A) at 1150 °C for 1 h to produce a HL structure; (B) the HL structure still exists after 1175 °C 1 h; (C) the HL structure is produced after annealing at 1200 °C for 5 min; (D) at 1200 °C for 7.5 min and (E) at 1200 °C for 10 min; (F) fine grain structure after annealing at 1000 °C for 1 h.

3.3.2 Mechanical properties of NCACB

Fig. 3.7(A)-(C) show tensile properties of four NCACB with distinct microstructures, and the comparison between NCACB HEA and other existing materials. The microstructure of these four NCACB samples are presented in Supplementary Fig. 3.8(A-D): FG-HEA 1000 with average grain size of $4.7\mu\text{m}$, HL-HEA 1150, CG-HEA 1200 with average grain size of $140\mu\text{m}$, and CG-HEA 1300 with average grain size of $400\mu\text{m}$. In Fig. 3.7(A), HL-HEA 1150 sample can achieve an ultimate tensile strength (UTS) of 690 MPa with total elongation of 34%, which gives the best combination of strength and ductility. The ultra-high ductility in CG-HEA 1300 is due to the relatively large grain size (grain size/thickness) and strong texture that lead to the formation of a bamboo-like or oligocrystal structure, which effectively reduces the grain constraint and the deformation mimics that of a single crystal [36-40]. On the other hand, CG-HEA 1200 undergoes significant heterogeneous deformation as misfit strains of differently orientated grain (random texture) induce plastic strain gradients as well as residual stresses, hence lower ductility. The ultra-high strength in FG-HEA 1000 can be attributed to smaller grain size, i.e. Hall-Petch effect and presence of larger fraction of precipitates, i.e. precipitation strengthening; the latter of which compromises the overall ductility of the material. In comparison with CG-HEA 1200, whose grain size is close to those in the coarse-grained bands of HL-HEA 1150, the HL sample shows nearly twice the UTS, while maintaining the same ductility. When comparing with FG-HEA 1000, the HL sample exhibits slightly

lower strength, with significantly enhanced ductility. Moreover, Fig. 3.7(B-C) includes true stress-strain curves and strain hardening rate curves for these four NCACB samples, which shows significant strain hardening in HL and FG samples. In Fig. 3.7(D), some metals fabricated through microstructure design are presented here for comparison to this work in the UTS versus total elongation plot. Many of these materials compromise either ductility or strength to achieve their target properties. By comparison, the mechanical properties of NCACB HEA can be better tuned through the microstructure design over the range (blue ellipse) of high strength and high ductility, especially the HL-HEA sample. In the following part, a study is carried out to specifically investigate deformation mechanisms of the HL-HEA, which can help explain its exceptional properties.

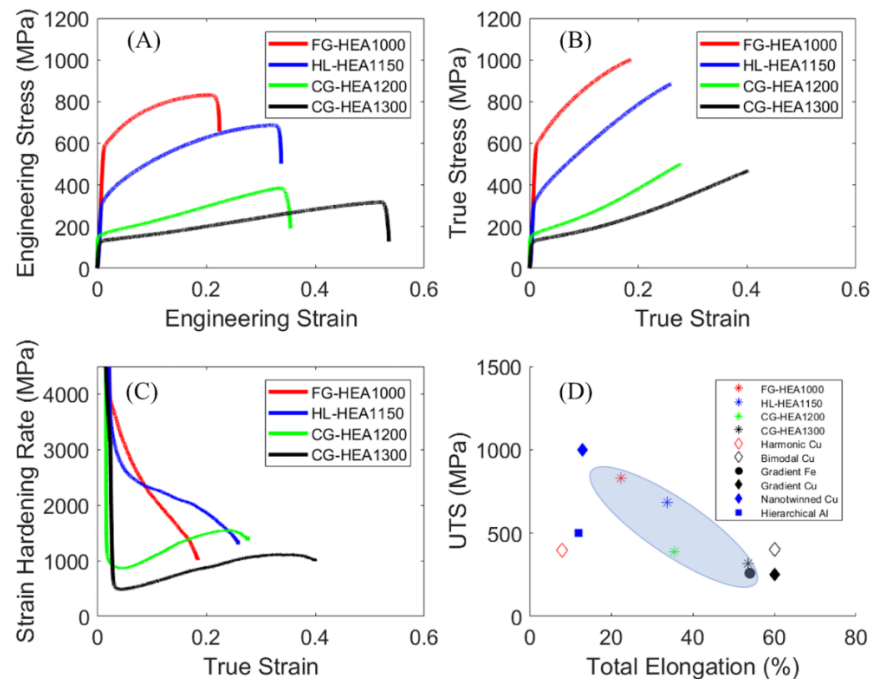


Figure 3.7: Tensile behavior of NCACB with four different grain structures. (A) Tensile engineering stress-strain curves; (B) Tensile true SS curves; (C) Strain hardening rate curves; (D) Comparison of mechanical properties between HL NCACB HEA and other materials with similar structures (harmonic Cu [55], bimodal Cu [21], gradient Fe [12], gradient Cu [20], nanotwinned Cu [56] and hierarchical Al [22]).

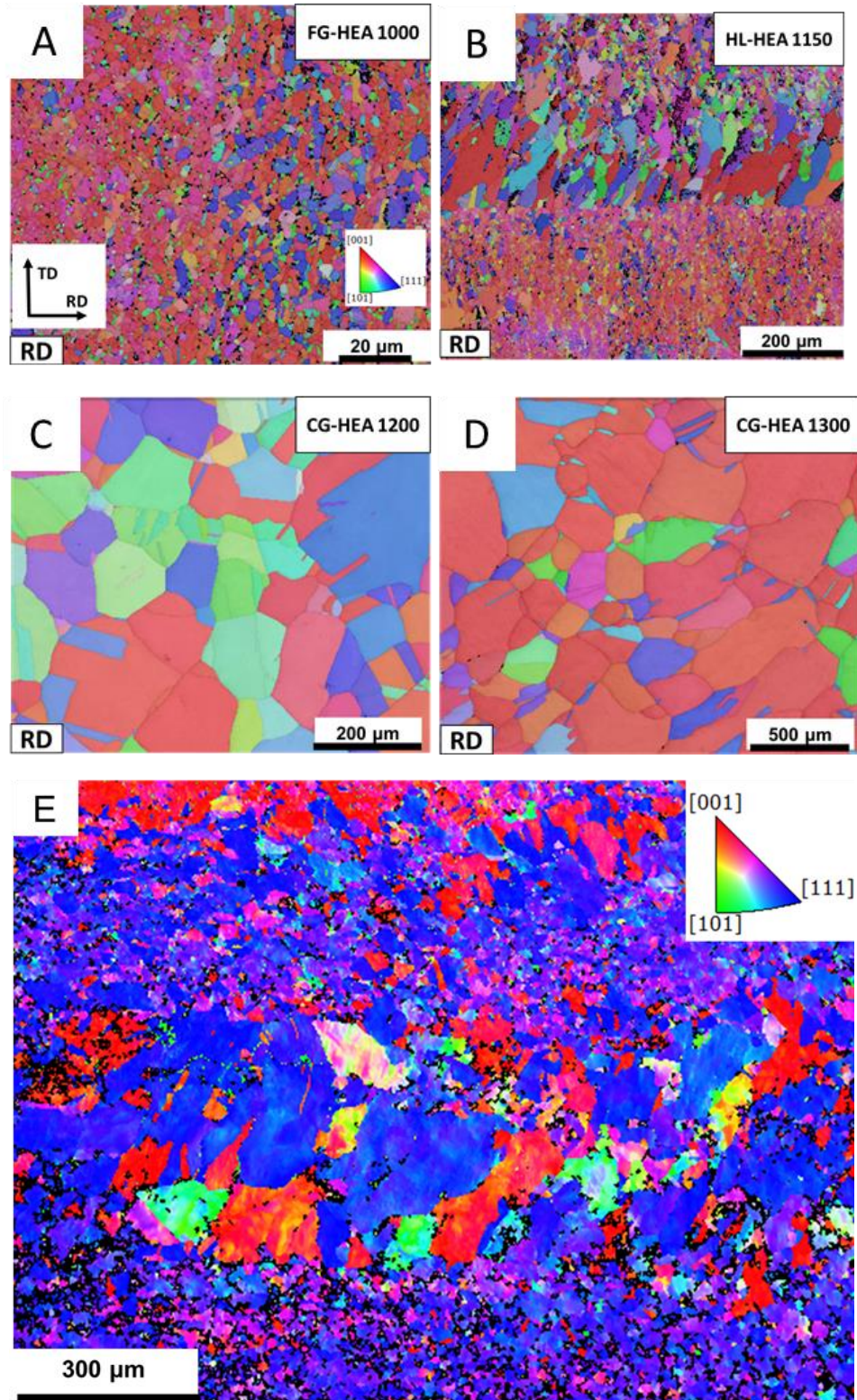


Figure 3.8: EBSD IPFX maps for (A) FG-HEA 1000; (B) HL-HEA 1150; (C) CG HEA 1200; (D) CG-HEA 1300; (E) EBSD IPFX for HL-HEA 1150 after tensile test.

3.3.3 Back-stress determined by geometrically necessary dislocations (GND) and LUR cyclic tensile test

Heterogeneous lamella structured materials overcome the strength-ductility trade-off by means of enhancing the strain hardening ability [41] to avert early necking [42]. At the onset of plasticity, coarse grained lamellae yield first, while the fine grained lamellae remain mostly elastic; this is effectively a local Hall-Petch phenomenon [43]. Since, due to higher resolved shear stresses generated by more dislocation pile-ups over a larger grain diameter [44], coarse-grained lamellae reach the critical resolved shear stress faster than the fine-grained regions. Thus, coarse grains will eventually carry more plastic strain than fine grains in the later deformation stages, i.e. strain partitioning. To maintain compatibility across the CG-(soft)/FG-(hard) interface under the rigid plastic material assumption, the coarse grains must deform heterogeneously to avoid formation of voids and material overlap [45], which generates strain gradients [46]. Furthermore, accommodation of the plastic strain gradient is through multiplication and storage of geometrically necessary dislocations (GND) [47-49] instead of the more randomly distributed statistically stored dislocations (SSD) [45]. Pile-ups of GNDs across the microstructure are believed to be responsible for generating long-range back-stresses that resists forward dislocation motion and leads to the Bauschinger effect and pronounced strain hardening [12]. Loading-unloading-reloading (LUR) cyclic tensile tests are carried out to calculate the back-stress as shown in Fig. 3.9(C-D). All the LUR cyclic tensile tests

results can be found in Fig. 3.11. Details of back-stress calculation can be referred to Ref. [12]. However, very few studies have been carried out to measure the distribution of the GND density and relate the distribution of GNDs to the heterogeneous microstructure. Hence, a quantitative analysis of the GND distribution will not only provide insight into the failure of this material, but also experimentally verify the local back-stress strengthening mechanism. Recent advances in EBSD allow fast and accurate characterization of many aspects of materials, e.g. crystal orientation, texture, microstructure, etc. [50, 51]. Moreover, the EBSD-based GND density measurement is established based on crystal orientation data [52, 53]. By constructing the Nye dislocation density tensor using measured disorientation gradients, dislocation density values related to a specific type of dislocation are computed. In this study, the typical $\langle 110 \rangle \{111\}$ dislocation configurations in FCC are assumed: 6 screw and 12 edge dislocations [26, 49]. Using the EBSD orientation data obtained from Supplementary Fig. 3.8(E), the GND density map of a CG-FG interface near the point of failure is plotted as shown in Supplementary Fig. 3.10(A). The logarithmic color scale utilized in plotting the GND map reveals notable heterogeneity of deformation across the CG-FG interface, particularly in the coarse-grained lamella. GND hot spots are most commonly found near geometric constraints such as triple junctions and grain boundaries. The step size of $0.8 \mu\text{m}$ establishes a noise floor to be around 1.2×10^{13} dislocations/ m^2 , which is below the majority of the data points, as shown by the distribution plot in Supplementary Fig. 3.10(B). The

area fraction distribution is a slightly left-skewed normal distribution due to the sampling of very few large grains with large GND ‘cold-spots’ in the grain interiors. To probe the dependence of the GND density on the size of the individual grains, grains are first indexed using a misorientation threshold of 5° to separate them from the deformation texture. Next, the area of each grain is approximated by the number of pixels of a given grain times the size of the pixel in square micrometers. The grain average GND density is readily computed as the geometric mean of the GND density values obtained from each pixel of a specified grain. In Fig. 3.9(B), it can be found that the grain average GND density versus grain area data is separated into two distinct regions above and below $\sim 2.3 \times 10^{14}$ dislocations/m². Then, each data point in Fig. 3.9(B) has its grain average GND density value distributed over the corresponding grain and produces a map as in Fig. 3.9(A). It can be found that the high-density data ($> 2.3 \times 10^{14} \text{ m}^{-2}$) lies primarily within the FG region, whereas the low-density data ($< 2.3 \times 10^{14} \text{ m}^{-2}$) resides mostly in the CG region. This means that the residual stresses are overall higher in the FG region and on average lower in the CG region. Therefore, potential failure is more likely to initiate from the FG region and then traverse through the CG-FG interface, and eventually lead to failure of the entire sample. Most interesting in this analysis is the discovery of a layer of high-density grains immediately adjacent to the CG side of the CG-FG interface, and a layer of low-density grains on the FG side of the CG-FG interface. The high-density layer is the ‘compatibility layer’, which restores compatibility in plastic strain near the CG-FG interface through

generating large amount of GNDs. In other words, the CG region homogenizes the otherwise highly heterogeneous plastic strain distribution in the FG region by activating multi-slip along the interface [54]. Since the ‘compatibility layer’ carries more plastic strain gradients on the interface, this results in the formation of a low-density ‘transition layer’ with relatively uniform plastic strain into the high residual stress FG region. A more comprehensive study regarding generation of back-stress would involve plastic strain analysis using DIC coupled with crystal plasticity finite element methods, which is the subject of future work.

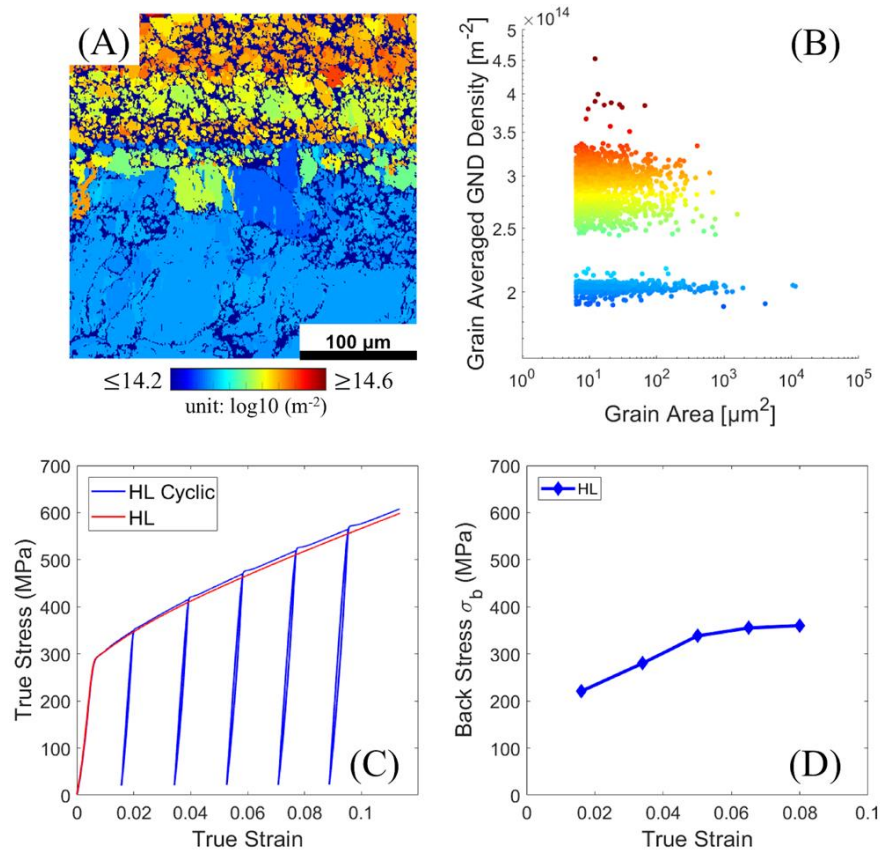


Figure 3.9 (A) Grain average GND density map in logarithmic scale (color bar: 14.2-14.6 [unit: $\log_{10}(\text{m}^{-2})$]); (B) Grain average GND density (m^{-2}) plotted against grain area (μm^2) with each data point colored according to the order of magnitude of grain average GND density (color bar: 14.2-14.6 [unit: $\log_{10}(\text{m}^{-2})$]); (C) True SS curves for LUR cyclic tensile tests of HL-1150; (D) Back-stress of HL-1150.

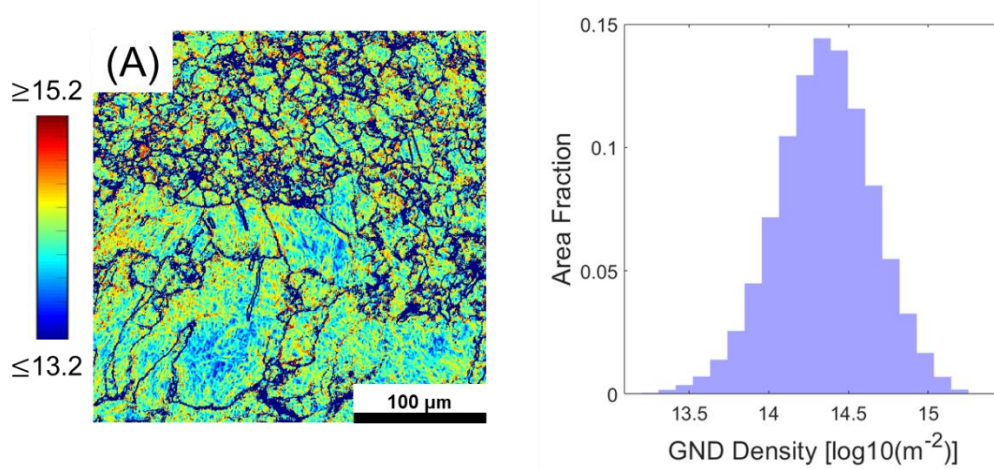


Figure 3.10: (A) Total GND density distribution map in logarithmic scale (color bar: 13.2-15.2 [unit: $\log_{10}(\text{m}^{-2})$]); (B) Area fraction distribution plot of GND data shown in (A) with 20 bins.

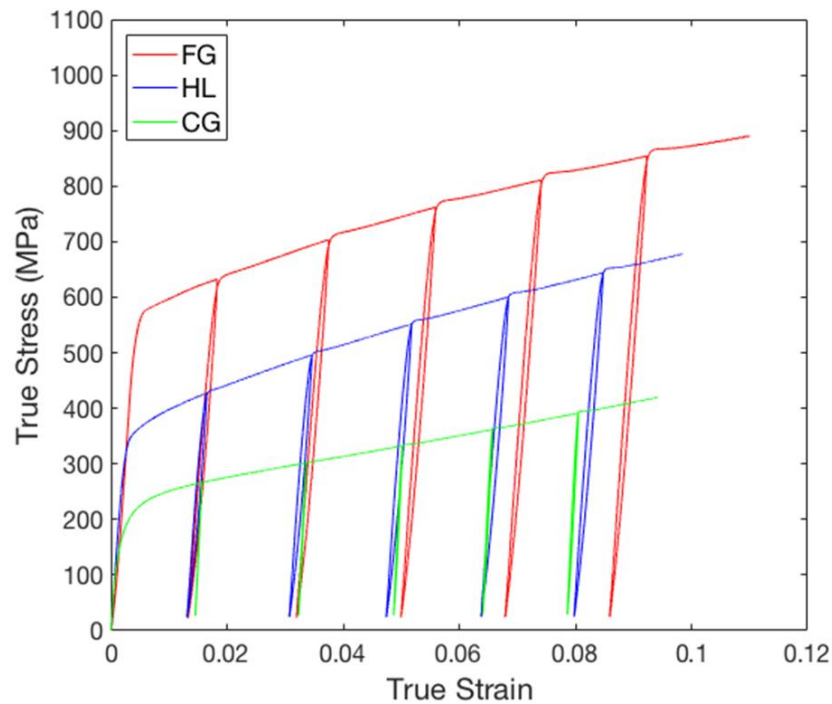


Figure 3.11: Loading-unloading-reloading (LUR) cyclic tensile tests for fine grain (FG), coarse grain (CG) and heterogeneous lamella (HL) NCACB HEAs.

3.4 Conclusion

In summary, a precipitation-controlled method for tuning the microstructure of non-

equiatomic FeNiCoAlCrB (NCACB) high entropy alloy is proposed, which provides an opportunity to modify mechanical properties within a strength and ductility window perhaps more effectively than a large number of existing metals and alloys. In this study, the heterogeneous lamella HEA has demonstrated better mechanical properties over fine grained and coarse grained HEAs due to the back-stress strengthening mechanism.

Acknowledgement

Chapter 3 is the part of the paper published in *Scripta Materialia*. Cheng Zhang, Chaoyi Zhu, Tyler Harrington, and Kenneth Vecchio. "Design of non-equiatomic high entropy alloys with heterogeneous lamella structure towards strength-ductility synergy." *Scripta Materialia* 154 (2018): 78-82. The dissertation author was the primary investigator and author of this paper.

The current authors would like to thank Zezhou Li, Sumin Shin, Sabine Faulhaber, Wayne Neilson and Mojtaba Samiee for help on experiments.

References

- [1] J.W. Yeh, S.K. Chen, S.J. Lin, J.Y. Gan, T.S. Chin, T.T. Shun, C.H. Tsau, S.Y. Chang, *Adv. Eng. Mater.* 6(5) (2004) 299.
- [2] B. Cantor, I. Chang, P. Knight, A. Vincent, *Mater. Sci. Eng. A* 375 (2004) 213.
- [3] Y. Zhang, T.T. Zuo, Z. Tang, M.C. Gao, K.A. Dahmen, P.K. Liaw, Z.P. Lu, *Prog. Mater Sci.* 61 (2014) 1.
- [4] B. Gludovatz, A. Hohenwarter, D. Catoor, E.H. Chang, E.P. George, R.O. Ritchie, *Science* 345(6201) (2014) 1153.
- [5] D. Miracle, O. Senkov, *Acta Mater.* 122 (2017) 448.
- [6] Z. Li, K.G. Pradeep, Y. Deng, D. Raabe, C.C. Tasan, *Nature* 534(7606) (2016) 227.
- [7] F. Otto, A. Dlouhý, K.G. Pradeep, M. Kuběnová, D. Raabe, G. Eggeler, E.P. George, *Acta Mater.* 112 (2016) 40.
- [8] C.C. Tasan, Y. Deng, K.G. Pradeep, M. Yao, H. Springer, D. Raabe, *JOM* 66(10) (2014) 1993.
- [9] Z. Li, C.C. Tasan, K.G. Pradeep, D. Raabe, *Acta Mater.* 131 (2017) 323.
- [10] M. Yao, K. Pradeep, C. Tasan, D. Raabe, *Scr. Mater.* 72 (2014) 5.
- [11] E. Ma, T. Zhu, *Mater. Today* 20(6) (2017) 323.
- [12] X. Wu, M. Yang, F. Yuan, G. Wu, Y. Wei, X. Huang, Y. Zhu, *Proc. Natl. Acad. Sci.* 112(47) (2015) 14501.
- [13] X. Wu, P. Jiang, L. Chen, F. Yuan, Y.T. Zhu, *Proc. Natl. Acad. Sci.* 111(20) (2014) 7197.
- [14] A. Magee, L. Ladani, T.D. Topping, E.J. Lavernia, *Acta Mater.* 60(16) (2012) 5838.
- [15] D. Witkin, Z. Lee, R. Rodriguez, S. Nutt, E. Lavernia, *Scr. Mater.* 49(4) (2003) 297.
- [16] H. Azizi-Alizamini, M. Militzer, W. Poole, *Scr. Mater.* 57(12) (2007) 1065.

- [17] Z. Zhang, S.K. Vajpai, D. Orlov, K. Ameyama, *Mater. Sci. Eng., A* 598 (2014) 106.
- [18] G. Fan, H. Choo, P. Liaw, E. Lavernia, *Acta Mater.* 54(7) (2006) 1759.
- [19] X. Wu, M. Yang, F. Yuan, L. Chen, Y. Zhu, *Acta Mater.* 112 (2016) 337.
- [20] T. Fang, W. Li, N. Tao, K. Lu, *Science* 331(6024) (2011) 1587.
- [21] Y. Wang, M. Chen, F. Zhou, E. Ma, *Nature* 419(6910) (2002) 912.
- [22] P.V. Liddicoat, X.-Z. Liao, Y. Zhao, Y. Zhu, M.Y. Murashkin, E.J. Lavernia, R.Z. Valiev, S.P. Ringer, *Nat. Commun.* 1 (2010) 63.
- [23] S. Guo, C. Ng, J. Lu, C. Liu, *J. Appl. Phys.* 109(10) (2011) 103505.
- [24] Y. Zhang, Y.J. Zhou, J.P. Lin, G.L. Chen, P.K. Liaw, *Adv. Eng. Mater.* 10(6) (2008) 534.
- [25] C. Zhu, V. Livescu, T. Harrington, O. Dippo, G.T. Gray III, K.S. Vecchio, *Int. J. Plast.* 92 (2017) 148.
- [26] C. Zhu, T. Harrington, V. Livescu, G.T. Gray III, K.S. Vecchio, *Acta Mater.* 118 (2016) 383.
- [27] H. Chen, A. Godfrey, N. Hansen, J. Xie, Q. Liu, *Mater. Sci. Eng., A* 483 (2008) 157.
- [28] D.A. Hughes, N. Hansen, *Acta Mater.* 48(11) (2000) 2985.
- [29] S. Bellier, R. Doherty, *Acta Metall.* 25(5) (1977) 521.
- [30] G. Rosen, D.J. Jensen, D. Hughes, N. Hansen, *Acta Metall.* 43(7) (1995) 2563.
- [31] J. Zhang, M. Ma, W. Liu, *Mater. Sci. Eng., A* 690 (2017) 233.
- [32] N. Hansen, D. Juul Jensen, *Mater. Sci. Technol.* 27(8) (2011) 1229.
- [33] B. Bay, N. Hansen, D. Hughes, D. Kuhlmann-Wilsdorf, *Acta Metall.* 40(2) (1992) 205.

- [34] F. Humphreys, *Acta Metall.* 25(11) (1977) 1323.
- [35] O. Mishin, A. Godfrey, D.J. Jensen, N. Hansen, *Acta Mater.* 61(14) (2013) 5354.
- [36] Y. Sutou, N. Koeda, T. Omori, R. Kainuma, K. Ishida, *Acta Mater.* 57(19) (2009) 5759.
- [37] Y. Sutou, T. Omori, K. Yamauchi, N. Ono, R. Kainuma, K. Ishida, *Acta Mater.* 53(15) (2005) 4121.
- [38] Y. Chen, X. Zhang, D.C. Dunand, C.A. Schuh, *Appl. Phys. Lett.* 95(17) (2009) 171906.
- [39] S.M. Ueland, Y. Chen, C.A. Schuh, *Adv. Funct. Mater.* 22(10) (2012) 2094.
- [40] Y. Chen, C.A. Schuh, *Acta Mater.* 59(2) (2011) 537.
- [41] X. Wu, Y. Zhu, *Mater. Res. Lett.* 5(8) (2017) 527.
- [42] E. Hart, *Acta Metall.* 15(2) (1967) 351.
- [43] N. Hansen, *Scr. Mater.* 51(8) (2004) 801.
- [44] J. Eshelby, F. Frank, F. Nabarro, *Philos. Mag.* 42(327) (1951) 351.
- [45] M. Ashby, *Philos. Mag.* 21(170) (1970) 399.
- [46] H.K. Park, K. Ameyama, J. Yoo, H. Hwang, H.S. Kim, *Mater. Res. Lett.* 6(5) (2018) 261.
- [47] J.F. Nye, *Acta Metall.* 1(2) (1953) 153.
- [48] E. Kroner, *Continuum Theory of Dislocations and Self-Stresses*, Springer, 1958.
- [49] E. Demir, D. Raabe, N. Zaafarani, S. Zaeferrer, *Acta Mater.* 57(2) (2009) 559.
- [50] K. Lassen, *Mater. Sci. Technol.* 12(10) (1996) 837.
- [51] B.L. Adams, S.I. Wright, K. Kunze, *Metall. Mater. Trans. A* 24(4) (1993) 819.
- [52] S. Sun, B. Adams, W. King, *Philosophical Magazine A* 80(1) (2000) 9.

- [53] B. El-Dasher, B. Adams, A. Rollett, *Scr. Mater.* 48(2) (2003) 141.
- [54] R. Yuan, I.J. Beyerlein, C. Zhou, *Mater. Res. Lett.* 5(4) (2017) 251.
- [55] D. Orlov, H. Fujiwara, K. Ameyama, *Mater. Trans.* 54(9) (2013) 1549.
- [56] L. Lu, Y. Shen, X. Chen, L. Qian, K. Lu, *Science* 304(5669) (2004) 422.

Chapter 4

Non-Equiatomic FeNiCoAl-Based High Entropy Alloys With Multiscale Heterogeneous Lamella Structure For Strength And Ductility

Chapter 4 is the part of material that is submitted for publication in Materials Science and Engineering A.

Cheng Zhang, Chaoyi Zhu, and Kenneth Vecchio. “Non-Equiatomic FeNiCoAl-Based High Entropy Alloys With Multiscale Heterogeneous Lamella Structure For Strength And Ductility”. Submitted to Materials Science and Engineering A. (2018). Elsevier.

Abstract

A new method based on conventional thermomechanical processing is proposed for design of non-equiatomic FeNiCoAlTaB (NCATB) high entropy alloy (HEA) with multiscale heterogeneous lamella (HL) structures to achieve outstanding mechanical properties. Two kinds of microstructures are produced in this study: 1) specimens annealed at 1050°C exhibit 1050 HL structure composed of fine grains and ultrafine grains, which exhibits a combination of high strength (UTS ~1050 MPa) and good ductility (elongation ~23%); and 2) specimens annealed at 1200°C which exhibit 1200 HL structure composed of fine grains and coarse grains, which demonstrates excellent synergy of good strength (UTS ~890 MPa) and exceptional ductility (elongation ~43%). It has been shown that shear

bands formed in the cold rolling step are responsible for the fine-grain area in both specimens. Additionally, precipitation of NiAl (B2) particles also affects the formation of HL structures due to Zener pinning effect. The back-stress strengthening mechanism, responsible for high strength and ductility, is verified through combined “loading-unloading-reloading” (LUR) cyclic tensile tests and electron backscatter diffraction (EBSD) based geometrically necessary dislocation (GND) density analysis.

4.1 Introduction

High entropy alloys (HEAs) are a new class of metallic materials with at least four equiatomic or near-equiatomic elements, which are independently discovered by Yeh [1] and Cantor [2]. During the time of exploration into HEAs, most studies have been concentrated on one of the original concepts of HEAs for alloy design, which utilizes an equiatomic ratio of multiple principal elements to achieve the maximum configuration entropy [1-4]. However, the conventional HEA design concept limits the compositional space and excludes non-equiatomic candidates with potentially outstanding properties and higher commercial viability. The concept of non-equiatomic HEAs, first put forward by Raabe and his colleagues [5,6], has significantly expanded the compositional space for HEA design, and research in these compositions has obtained unparalleled mechanical properties [7-10]. Recently, extensive studies in HEAs have led to the discovery of many attractive properties, such as good mechanical properties at cryogenic temperature [11,12],

enhanced irradiation responses [13,14], and high ballistic resistance [15]. Apart from conventional arc melting and induction melting, some special fabrication methods are employed, including carbothermal shock synthesis of HEA nanoparticles [16], selective laser melting (SLM) or additive manufacturing [17,18], and spark plasma sintering (SPS) [19] for the fabrication of HEAs. The attractive properties of HEAs in different application fields mainly benefit from the diversity of microstructures, which is the focus of this study.

In the development of traditional metals and alloys, the requisite properties are essentially determined by the microstructure, and modification of mechanical properties through controlled microstructure design has succeeded in many studies [e.g., 20-23]. Recently, heterogeneous lamella structures, bimodal structures, and gradient structures have been fabricated to overcome the strength-ductility trade-off in some pure metals like Ti and Cu [21,24,25], steels [26-28], aluminum alloys [29,30], and CoCrNi medium entropy alloys [31] over a wide range of length scales. The key benefit of having a heterogeneous lamella (HL) structure is to enhance the strain hardening ability [21,32] in order to prevent early necking [33]. Due to the bimodality of the microstructure, a local Hall-Petch effect is present [34], which leads to strain partitioning [21,35]. Under the rigid plastic material assumption, materials in high strain [coarse grained (CG)] and low strain [fine grained (FG)] regions are ‘connected’ through introduction of significant number of geometrically necessary dislocations (GNDs) that accommodate the strain

gradients to avoid formation of voids and material overlaps [36]. Pile-ups of GNDs across the CG/FG interface are believed to be responsible for generating long-range back-stresses that leads to the Bauschinger effect and enhanced strain hardening [24,37]. Macroscopically, the magnitude of the back-stress can be extracted from loading-unloading-reloading (LUR) experiments [24,38]. In addition, indirect analysis involving quantification of GND density mapping could also provide insight into the back-stress strengthening mechanism [39]. In this study, LUR experiments and local GND density mapping are both carried out to provide comprehensive analysis of the strengthening mechanism.

For the fabrication of these heterogeneous-grained structures, a number of different approaches have been utilized, including: powder metallurgy with different size particles [40], the surface mechanical attrition treatment (SMAT) technique [41,42], and asymmetrical rolling with subsequent annealing [24,30,43,44]. The current authors recently reported a novel, heterogeneous lamella structure, non-equiatomc $\text{Fe}_{34.95}\text{Ni}_{27.5}\text{Co}_{17.5}\text{Al}_{11.5}\text{Cr}_{8.5}\text{B}_{0.05}$ (at. %) (NCACB) HEA with high strength and ductility, fabricated using conventional thermomechanical treatments [39]. To improve the solid-solution strengthening capacity of the alloy, Ta with a much larger atomic radius than Cr is used here in the current non-equiatomc $\text{Fe}_{42.26}\text{Ni}_{27.5}\text{Co}_{17.5}\text{Al}_{10.5}\text{Ta}_{2.2}\text{B}_{0.04}$ (at. %) [referred to here as: (NCATB)] HEA. Moreover, a small amount of boron (~70 ppm by weight) is added to strengthen the grain boundaries due to the cohesion effect [45]. Herein, a newly-

designed non-equiatomic HEA-NCATB with multiscale heterogeneous lamella structure is reported that exhibits higher strength and ductility than the previously studied HL-HEA-NCACB [39]. A detailed and in-depth analysis for this new alloy HEA-NCATB is provided in this study, including alloy design, synthesis, and characterization.

4.2 Experimental Procedures

NCATB ingots were prepared through arc-melting under an argon atmosphere with raw materials as follows: Fe (99.95%), Ni (99.9%), Co (99.9%), Al (99.9%), Ta (99.9%), and Ni₂B (99%). Each ingot was flipped and re-melted eight times to ensure homogeneity. Next, each as-cast NCATB ingot with an original thickness of ~10 mm was processed through induction heat-treatment and hot rolling (1250°C, reduction in thickness (RIT) of ~25%), first annealing (1300°C, 30min), cold rolling (RIT ~90%), second annealing at 1050-1300°C for various times and water quenching. Depending on the second annealing conditions, distinct microstructures can be achieved, e.g. fine grained (FG), coarse grained (CG), and the desired heterogeneous lamella (HL) structure.

Microstructure characterization was performed in a Thermo-Scientific Apreo FEG-SEM equipped with Oxford Instruments EDS and EBSD-Symmetry detectors. Thin samples cold rolled to a RIT = 90% were cut to standard dog-bone tensile shapes and ground and polished using standard metallographic techniques, followed by vibratory polishing. Quasi-static tensile tests were carried out at room temperature, with the tensile direction parallel to the rolling direction with a sample gauge-length of 20 mm, gauge-

width of 2.4 mm and thickness between 0.4 mm and 0.5 mm. After tensile testing, the geometrically necessary dislocation (GND) density in the deformed HL NCATB was calculated from EBSD orientation data using an in-house Matlab code developed by Zhu et al. [46,47]. The Loading-Unloading-Reloading (LUR) cyclic tensile tests were set up with Instron Profiler software. An extensometer was employed to measure the strain during the tensile test. The strain rate in the current tensile test is 5×10^{-4} /s.

4.3 Experimental Results

4.3.1 Microstructure evolution in HEA-NCATB

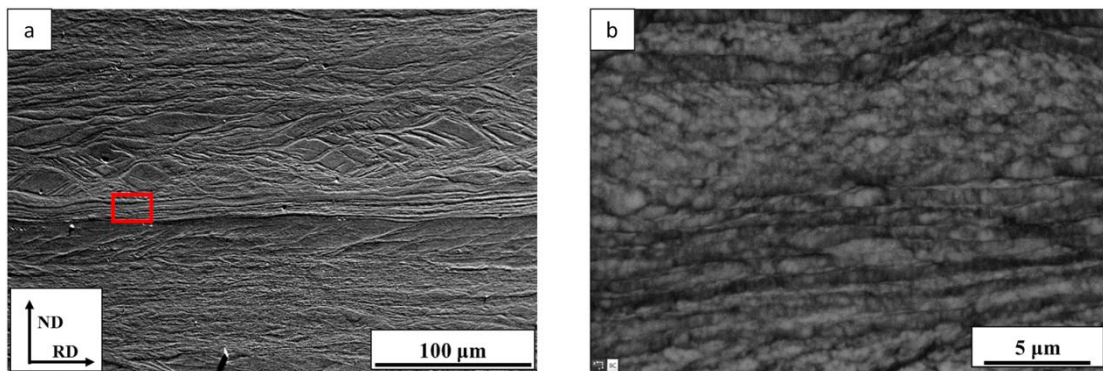


Figure 4.1. (a) SEM image for HEA-NCATB specimen after cold rolling with reduction in thickness of 90%; (b) EBSD Band Contrast (BC) image for the enlarged red square area in (a). RD – Rolling Direction, ND – Normal Direction.

Fig. 4.1 shows the grain structure after cold rolling with RIT of 90%. Large deformation bands can be observed in Fig. 4.1(a). Some shear bands with an angle around 40° along the rolling direction are also formed, which are usually observed in heavily deformed FCC metals or alloys with medium to high stacking fault energy [48-51]. Based on the width of these large deformation bands, each band should correspond to one initial

coarse grain in the NCATB sample after hot rolling and first annealing step. The microstructure evolution in HEA-NCATB before cold rolling is shown in Fig. 4.2. Fig. 4.1(b) depicts the EBSD band contrast (BC) image for the central part of the cold-rolled specimen. A well-developed structure of lamella bands (LBs) having a width of one cell block (CB) less than $1\mu\text{m}$ is formed, which is the typical characteristic of a large strain microstructure [49]. Apart from lamella bands, some microbands (MBs) and shear bands are also present, as seen in Fig. 4.1(a).

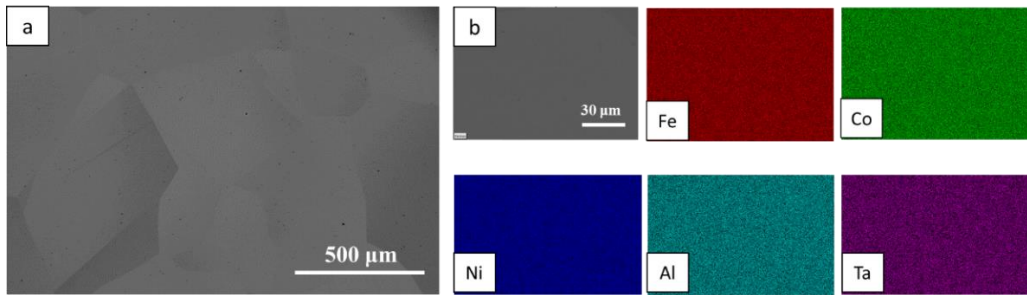


Figure 4.2. (a) SEM (BSE) image for HEA-NCATB specimen after first annealing and water quenching; (b) EDS Mapping for HEA-NCATB sample before cold rolling. Coarse grains with average grain size over $400\mu\text{m}$ are formed in Fig. 4.2(a).

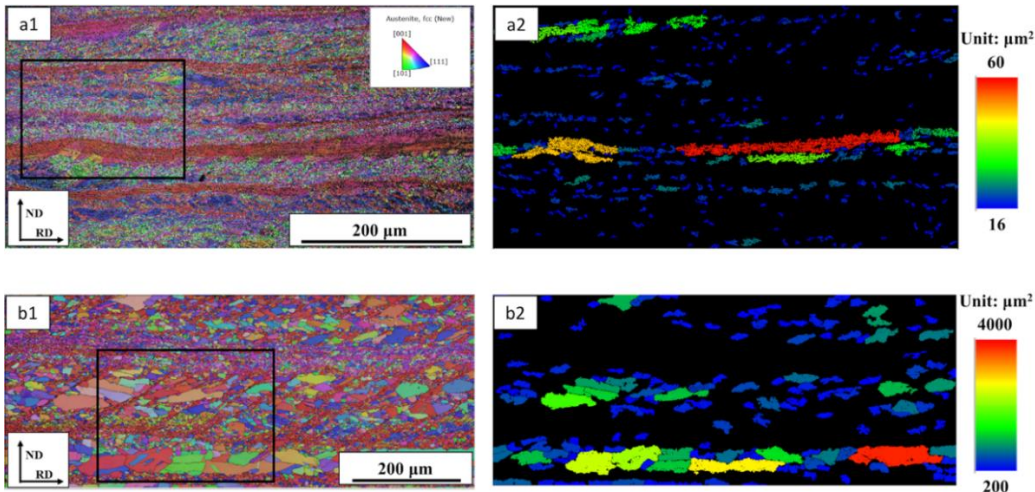


Figure 4.3. EBSD IPFX images for the two kinds of heterogeneous lamella structure formed in HEA-NCATB after annealing. (a1) EBSD (IPF) for HEA-NCATB after annealing at 1050°C for 30min (HL-HEA-1050); (a2) grain area map corresponding to Fig. (a1); (b1) EBSD IPFX image for HEA-NCATB after annealing at 1200°C for 10min (HL-HEA-1200); (b2) grain area map corresponding to (b1).

4.3.2 Heterogeneous lamella, fine-grained and coarse-grained structures in HEA-NCATB

Fig. 4.3(a1-a2) show the unique heterogeneous lamella (HL) structure of HEA-NCATB over a large region after annealing at 1050°C for 30min for a cold rolled sample with RIT of 90%. The formation of this kind of HL structure is due to partial recrystallization. Some grains with sizes between 2 μ m and 4 μ m are recrystallized first, and these grains can be considered as fine grains, while some ultrafine sub-grains with sizes less than 1 μ m within the deformation bands are still in the recovery state. The lamellae composed of ultrafine grains (misorientation between sub-grains is less than 10°) are presented in Fig. 4.3(a2). Therefore, this alloy is referred to as HL (heterogeneous lamella microstructure)-HEA-1050 (1050 °C annealing temperature).

Another unique HL structure containing fine grains and coarse grains is presented in Fig. 4.3(b1-b2). This structure is formed after HEA-NCATB is annealed at 1200°C for 10min with RIT of 90% in the cold rolling step. Hence, this alloy is named HL-HEA-1200 (1200°C annealing temperature). In Fig. 4.3(b1), it is found that grains are completely recrystallized. Coarse grains with size larger than 15 μ m are shown in Fig. 4.3(b2), and these bands composed of coarse grains are heterogeneously distributed in the specimen. In summary, the representative schematic Voronoi diagrams and EBSD IPF images for the two distinct heterogeneous lamella (HL) structures in HEA-NCATB are present in Fig. 4.4. The mechanism for the formation of HL structures will be discussed in the next section.

Fig. 4.5(a) shows EBSD phase map for the fine-grained (FG) structure in HEA-

NCATB after annealing at 1075°C for 1h. It is found that apart from the FCC austenite fine grains, some NiAl (B2) precipitates are formed along grain boundaries. The SEM image and EDS maps presented in Fig. 4.5(b) shows that these particles with size of approximately 1µm are mainly composed of Al and Ni. Further XRD result presented in Fig. 4.5(c) confirms that these are NiAl (B2) precipitates embedded at grain boundaries of the austenite FCC γ matrix. For HL-HEA-1050, NiAl (B2) particles are also distributed along the grain boundaries in the FG area, as shown in Fig. 4.6(a). For specimens annealed at 1300°C for 5min and 30min as shown in Fig. 4.6(b) and 4.6(c), no NiAl(B2) particles are found in the CG specimens. Similar to the HL structure formed in HL-HEA-NCACB [39], NiAl (B2) precipitates play an important role in the process for the formation of the HL structure.

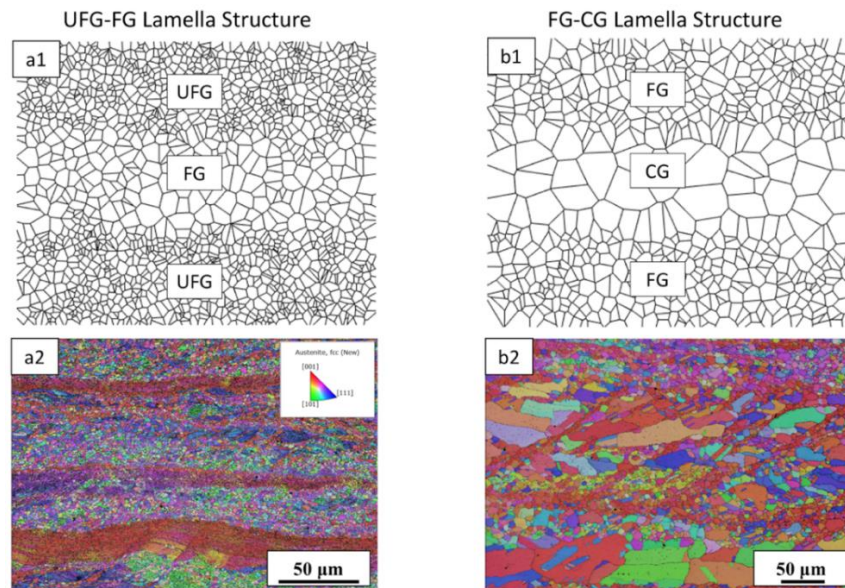


Figure 4.4. Schematic diagrams and EBSD IPFX images for the two kinds of HL structure in HEA-NCATB. (a1) Schematic diagram for the HL structure composed of CG band and FG band. (a2) EBSD IPFX image of enlarged area for the black square area in Fig. 4.3(a1). (b1) Schematic diagram for the HL structure composed of FG band and UFG band; (b2) EBSD IPFX image of enlarged area for the black square area in Fig. 4.3(b1).

The development of NiAl (B2) precipitates in the HEA-NCATB was studied through a series of heat-treatment conditions. Specifically, the cold-rolled HEA-NCATB samples were annealed at 1200°C, 1225°C, 1250°C, 1275°C and 1300°C for 30min. each. SEM (BSE) images in Fig. 4.7 show that NiAl (B2) precipitates can only be dissolved into the γ matrix when the annealing temperature is above 1250°C. The corresponding XRD result in Fig. 4.8 confirms that NiAl (B2) is completely dissolved into the austenite matrix when the annealing temperature reaches 1300°C. When comparing with the solvus temperature of NiAl in NCACB (1200°C) [39], the higher solvus temperature in NCATB (1300°C) is likely due to the addition of Ta with much higher melting point than Cr.

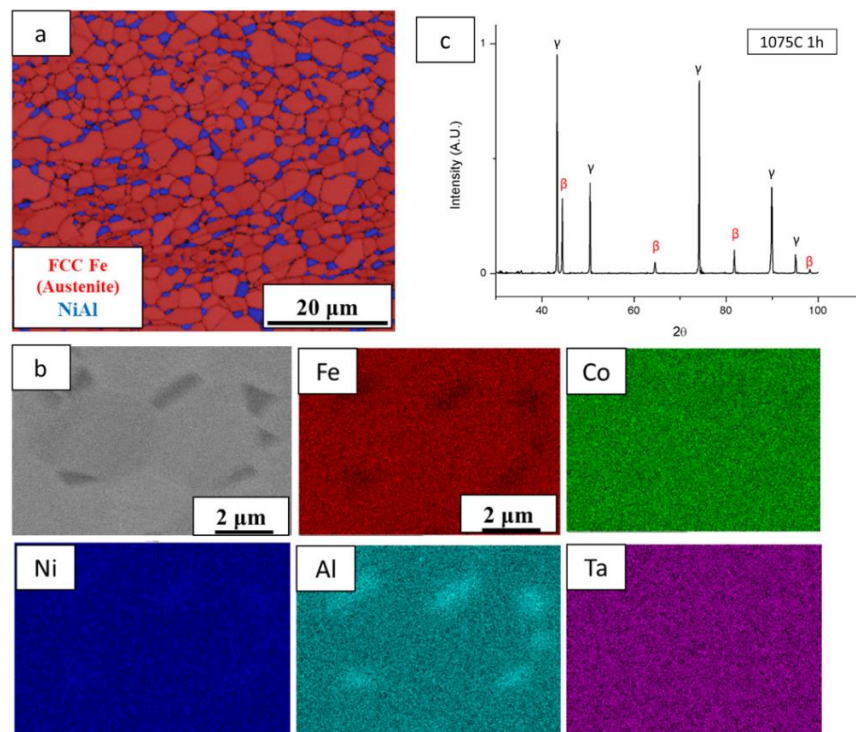


Figure 4.5. (a) EBSD phase map for HEA-NCATB after annealing at 1075°C for 1h, red – FCC (austenite) iron, blue – (B2) NiAl; (b) EDS Mapping for the matrix and the precipitates in HEA-NCATB after annealing at 1075°C for 1h ; (c) XRD pattern for NCATB after annealing at 1075°C for 1h.

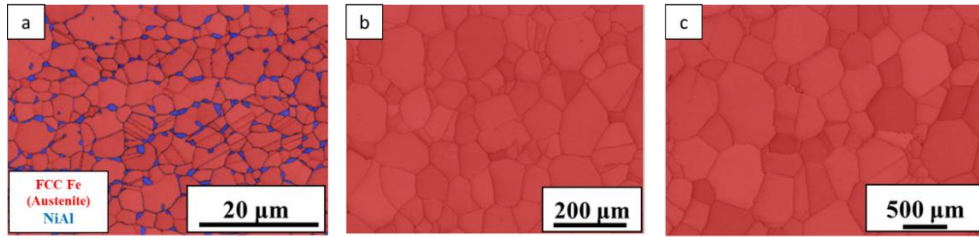


Figure 4.6 EBSD phase maps for HEA-NCATB. (a) 1050°C 30min; (b) 1300°C 5min; (c) 1300°C 30min. Red - FCC Fe (austenite), Blue – NiAl (B2 structure). For HL-HEA-1050, NiAl (B2) are distributed along the grain boundaries in the FG area, as shown in Fig. 4.6(a). For specimens annealed at 1300°C for 5min and 30min as shown in Fig. 4.6(b) & (c), no NiAl(B2) particles are found in the CG specimens.

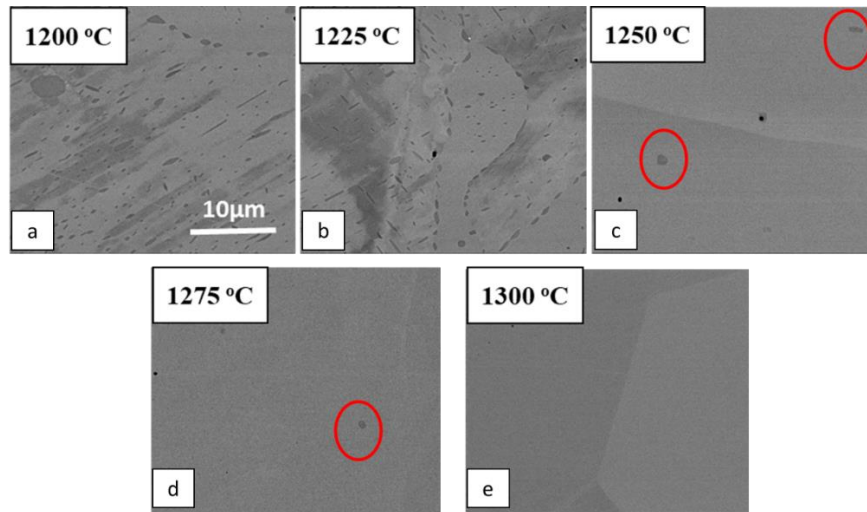


Figure 4.7 SEM(BSE) images for NCATB-HEA after cold rolling and annealing for 30min. (a) 1200°C, (b) 1225°C, (c) 1250°C, (d) 1275°C, (e) 1300°C. NiAl (B2) precipitates are pointed out by red circles.

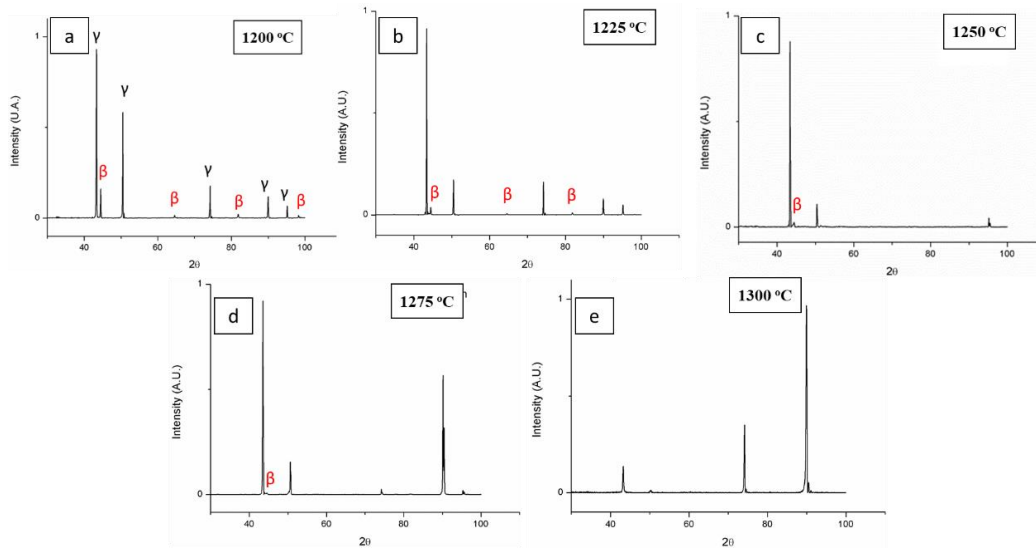


Figure 4.8 XRD patterns for NCATB-HEA after cold rolling and annealing for 30min. (a) 1200°C, (b) 1225°C, (c) 1250°C, (d) 1275°C, (e) 1300°C. NiAl (B2) phase is pointed out by red letter.

4.3.3 Mechanical properties

Fig. 4.9(a-c) shows the tensile properties of five different HEA-NCATB samples with distinctly different microstructures, and the comparison (Fig. 4.9(d)) of mechanical properties between these HEA-NCATB and other existing microstructurally-tailored materials (harmonic Cu [52], bimodal Cu [53], gradient Fe [26], gradient Cu [25], nanotwinned Cu [54], hierarchical Al [55] and HL-NCACB-HEA [39]). The microstructure of these five NCATB samples have already been presented in the previous sections: (fine grained) FG-HEA 1075 with average grain size of 3.6 μm , HL-HEA-1050 (UFG+FG), HL-HEA-1200 (FG+CG), (coarse grained) CG1-HEA 1300 with average grain size of approximately 100 μm , and CG2-HEA 1300 with average grain size of around 400 μm . In Fig. 4.9(a), HL-HEA-1050 sample can achieve an ultimate tensile strength (UTS) of 1050MPa with total elongation of 23%, and HL-HEA-1200 specimen can achieve a UTS of 890MPa with total elongation of 43.5%. These two specimens with HL structures show the best combination of strength and ductility. Fig. 4.9(b) and 4.9(c) show the true stress-strain curves and strain hardening rate curves for these five HEA-NCATB specimens, respectively. It is shown in Fig. 4.9(c) that significant strain hardening appears in the FG and HL samples. In Fig. 4.9(d), some metals and alloys fabricated through microstructure design or tailored microstructure approaches are presented here for comparison to the current study in the UTS versus total elongation plot. Most of these materials compromise either ductility or strength to achieve their target properties. By comparison,

the mechanical properties of HEA-NCATB can be better tuned through microstructure design over the range (red ellipse) of high strength and high ductility, especially the HL-HEA-NCATB samples. When compared with the previous HL-HEA-NCACB, the current HL-HEA-NCATB exhibits higher UTS and greater elongation. The increase in the strength of HEA-NCATB when compared with HEA-NCACB [39], is due to the larger size of Ta atoms which create a greater substitutional solid-solution strengthening effect than Cr in the current Fe-Ni-Co-Al-based alloy system.

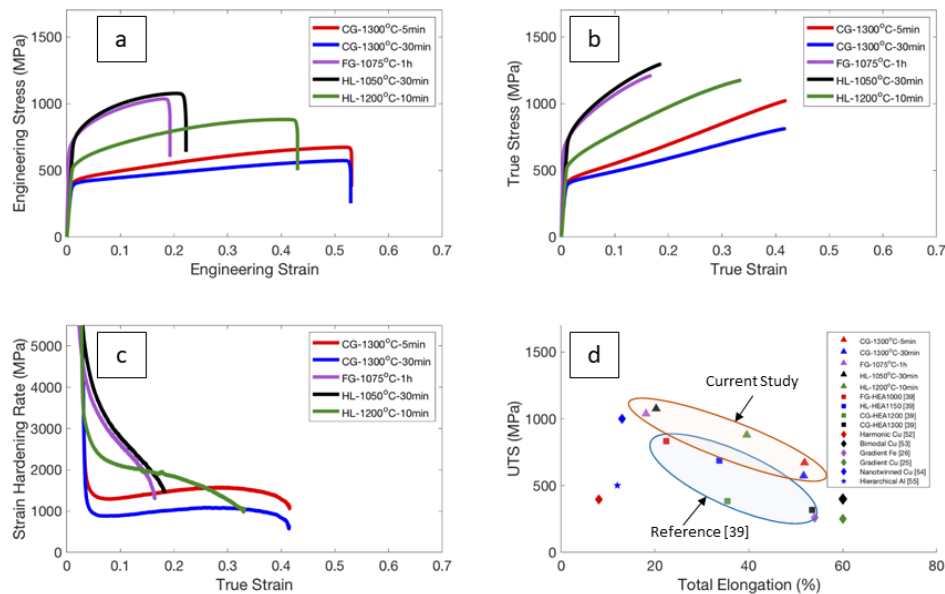


Figure 4.9. Tensile behavior of NCATB with five different grain structures. (a) Tensile engineering SS curves; (b) tensile true SS curves; (c) strain hardening rate curves; (d) comparison of mechanical properties between HL-NCATB-HEA and other materials with similar structures (harmonic Cu [52], bimodal Cu [53], gradient Fe [26], gradient Cu [25], nanotwinned Cu [54], hierarchical Al [55] and HL-NCACB-HEA [39]).

4.4 Discussion

4.4.1 Formation of heterogeneous lamella structure in HEA-NCATB

Since the HL-structured HEA-NCATB specimens exhibit a unique combination of

high strength and high ductility, it is of great interest to understand how this unique structure is formed and how it generates the improved properties. Fig. 4.10(a) shows EBSD IPF (X-direction) map for the cold-rolled specimen with RIT of 90%. After annealing at 1050°C for 10min, Fig. 4.10(b) reveals that grains first nucleate in the shear-bands that contain a high density of dislocations, while the central band of the specimen remains in the partially recovered state. The enlarged phase map in Fig. 4.10(c) shows that NiAl (B2) particles also precipitate within the shear bands due to the higher incidence of high angle boundaries. It has also been found that misorientation between cell blocks in the central band belongs to low-angle or medium angle boundaries ($< 15^\circ$), while the misorientation between microbands is high-angle boundaries ($>15^\circ$) [21,49]. Low-angle boundary is useful for suppression the precipitation of NiAl (B2) along the boundaries, which is also observed in some Fe-Ni-Co-Al-based superelastic alloys [56-58]. Therefore, the fraction of NiAl particles in the central band is much smaller than that within the shear bands. With increasing annealing time, an increasing number of grains transform from the recovered state to the recrystallization state, driven by the reduction in stored energy from the previous deformation step. As the annealing time approaches 30min, heterogeneous lamella structures composed of ultrafine grains and fine grains is formed as shown in Fig. 4.4(a2). By defining the misorientation between two recrystallized grains being larger than 10° , the recovery and recrystallization map as shown in Fig. 4.11 confirms that the ultrafine grains in the previous deformation bands are still in the recovered state,

not yet recrystallized.

For the HL-HEA-1200 specimen, the formation of heterogeneous structure is similar to that of the previous HL-HEA-NCACB study [39]. The grains first nucleate and recrystallize in the shear bands, while the grains in the deformation bands are still in the recovered state. With increasing annealing time, the growth of the first recrystallized grains in the shear bands are pinned by the precipitated NiAl particles along the grain boundaries. Meanwhile, the growth of the previous recovered grains becomes significantly fast without the precipitation of NiAl particles, thus leading to the formation of coarse-grained bands. In this way, FG+CG HL structure is formed in the HEA-NCATB-1200 samples, annealed at 1200°C for 10min.

The classic approach to quantify the role that the pinning particles play on grain growth is carried out using Zener's equation [59,60]:

$$R_c = \frac{4r}{3f} \quad (4.1)$$

where R_c is the limited grain radius, r is the radius of the particles, and f is the volume fraction of particles. The limited grain radii of the HEA-NCATB samples annealed at 1050°C, 1075°C, and 1200°C are summarized in Table 4.1. It is found that the calculated R_c is in agreement with those observed experimentally. For example, the calculated R_c values with annealing temperatures of 1050°C and 1200°C are 8.9 μm and 17.1 μm , respectively. For comparison, the sizes of fine grains are about 2.6 μm and 3.8 μm in Fig. 4.3(a1) and Fig. 4.3(b1), respectively. Therefore, the sizes of the fine grains are all within

the range of the calculated R_c values.

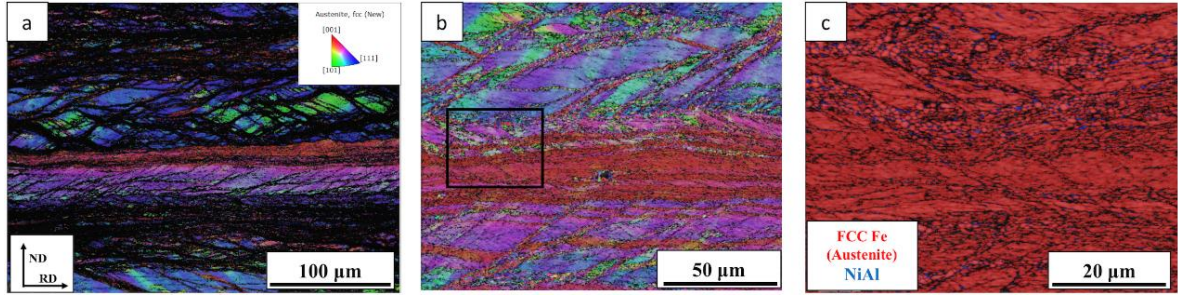


Figure 4.10 EBSD IPFX images for HEA-NCATB. (a) after cold rolling with RIT of 90%; (b) after annealing at 1050°C for 10min; (c) phase map corresponding to the black square area in (b). Red – FCC Fe (austenite), Blue – NiAl (B2 structure). RD – Rolling Direction, ND- Normal Direction.

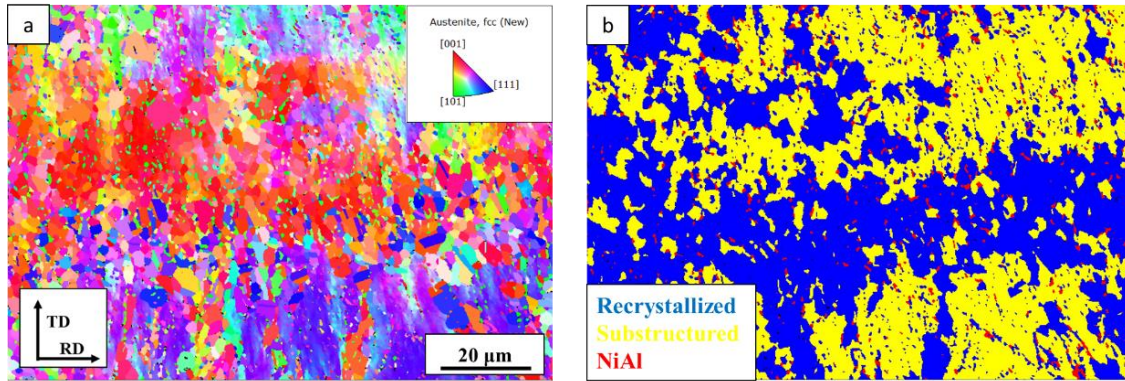


Figure 4.11. (a) EBSD IPFX image for HL-HEA-1050; (b) corresponding recrystallization and recovery figure for S3(a). Blue – Recrystallized Grains; Yellow – Recovery Grains; Red – NiAl (B2) precipitates. TD – Transverse Direction; RD – Rolling Direction. Precipitated NiAl particles mainly distribute in the recrystallized grain areas due to the high-angle boundaries with high energy.

Table 4.1: Summary of grain radii (R_c) calculated from Zener's model

Temperature (°C)	Time (s)	Particle Size (μm)	Particle Volume Fraction	R_c (μm)
1050	1800	0.90±0.068	0.067±0.005	8.96±0.03
1075	3600	1.04±0.097	0.102±0.097	6.79±0.34
1200	600	0.82±0.054	0.032±0.003	17.08±0.94

4.4.2 Back-stress calculation

Due to the heterogeneous lamella (HL) structure, high strength and ductility can be achieved in the HL-HEA-1050 and HL-HEA-1200. Here, HL-HEA-1200 is taken as an example. In the loading process, the CG lamella yields first during plastic deformation due to higher resolved shear stress from dislocation pile-ups [61]. Since these CG lamellas are surrounded and constrained by FG lamellae with higher yield strength, dislocations in the coarse grains accumulate and are blocked by the fine grains. Consequently, long-range back-stresses are induced, which resist the slipping of dislocation in the GC lamella. With increasing applied load, the fine grains begin to deform plastically, and hence the overall strength is increased by the back-stress.

Experimentally, “Loading-Unloading-Reloading” (LUR) cyclic tensile tests are conducted for the HL-HEA-NCATB specimens to show the Bauschinger effect and calculation of the back-stresses. Fig. 4.12(a-c) show the tensile LUR cyclic stress-strain curves for CG1-HEA-1300, HL-HEA-1050, and HL-HEA-1200, respectively. During the “unloading-reloading” process, the hysteresis loop is characteristic of Bauschinger effect; the larger the hysteresis loop, the stronger the Bauschinger effect [24]. In Fig. 4.12(a), no hysteresis loop is observed for the CG1-HEA-1300, indicating no back-stress is induced in this sample. For HL-HEA-1050 (4.12b) and HL-HEA-1200 (4.12c), increasingly larger hysteresis loops appear in both samples during the “unloading and reloading” process, demonstrating stronger Bauschinger effect with increasing numbers of

cycles.

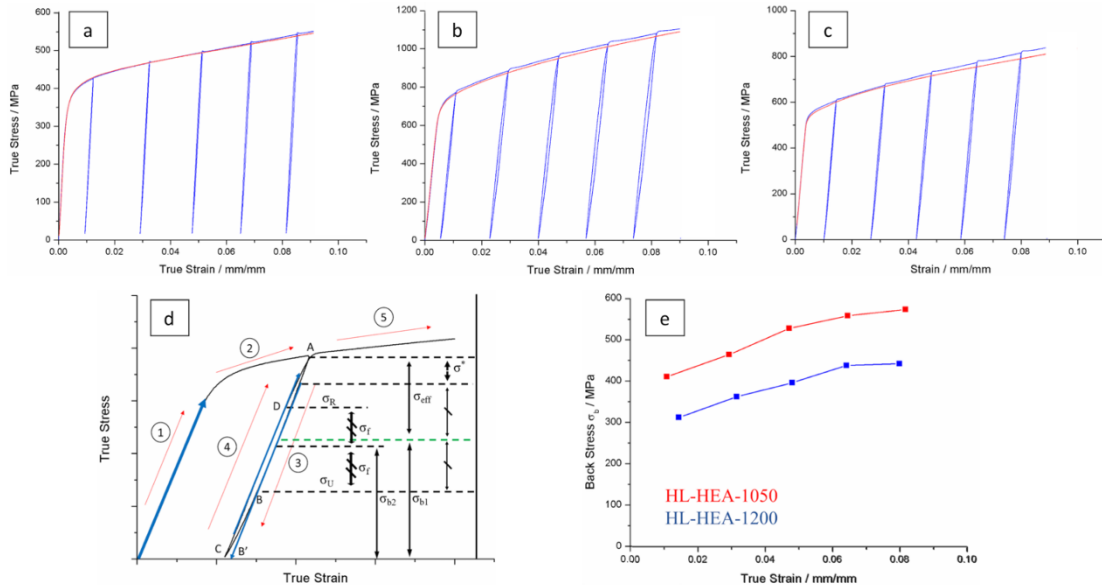


Figure 4.12. Loading-Unloading-Reloading (LUR) cyclic tensile true stress-strain curves for HEA-NCATB specimens. (a)CG1-HEA-1300; (b) HL-HEA-1050; (c) HL-HEA-1200. (d) schematic diagram for the calculation of back-stress; (e) Calculated back-stress for HL-HEA-1050 and HL-HEA-1200. Red – Normal tensile stress-strain curves; Blue – LUR cyclic tensile test SS curves.

The back-stresses can be calculated from LUR stress-strain curves. Fig. 4.12(d) is the schematic diagram for back-stress calculation. According to Dickson's equation that is modified from Cottrell's idea based on the stress partitioning [62,63], the partition in the unloading process can be expressed as:

$$\sigma_{b1} = \sigma_{fl} - \sigma_{eff} \quad (4.2)$$

$$\sigma_{eff} = (\sigma_{fl} - \sigma^* - \sigma_U)/2 + \sigma^* = (\sigma_{fl} - \sigma_U)/2 + \sigma^*/2 \quad (4.3)$$

where σ_{b1} is the back-stress, σ_{fl} is the flow stress, σ_{eff} is the effective stress, σ^* is the thermal part of the flow stress σ_{fl} , and σ_U is the yield stress in the unloading step. In this equation, the back-stress relates to the stress associated with a local strain process providing

long-range interactions with mobile dislocation. The effective stress is the local stress required for a dislocation to move (short-range interactions like friction stress and forest hardening) [62].

Recently, Wu and his colleagues [38] proposed another method for calculating the back-stress. They assume that the friction stress is a constant during the unloading-reloading process, and the back-stress is stable with loading before the unloading yield point B (labeled in Fig. 4.12d). The equations are shown as follows:

$$\sigma_{b2} = \sigma_U + \sigma_f \quad (4.4)$$

$$\sigma_R = \sigma_{b2} + \sigma_f \quad (4.5)$$

where σ_{b2} is the back-stress, σ_f is the friction stress, and σ_R is the yield stress in the reloading process. By solving the above two equations, the back-stress and the friction stress can be expressed as:

$$\sigma_{b2} = (\sigma_R + \sigma_U)/2 \quad (4.6)$$

$$\sigma_f = (\sigma_R - \sigma_U)/2 \quad (4.7)$$

In this method, since the back-stress is induced by geometrically necessary dislocations (GNDs), and the density of GNDs remains stable before the yield point of the unloading process, the back-stress is approximately constant. Meanwhile, this method employs the same criteria for defining unloading yield and reloading yield, which leads to the same deviation of the effective Young's modulus. Therefore, we employ the second method for back-stress calculation in the current study.

Fig. 4.12(e) presents the back-stress calculation results for the two HL-structure HEA-NCATB specimens. The back-stress in HL-HEA-1050 is higher than that in HL-HEA-1200, and higher back-stresses correspond to a stronger Bauschinger effect. For HL-HEA-1200, the back-stress is around 300MPa in the first LUR cycle, and it increases with increasing applied strain. The development of back-stress in HL-HEA-1200 is similar to that in the previously reported HL-HEA-NCACB specimen. In the reloading process, coarse-grained lamella with lower yield strength need to overcome this back-stress to initiate plasticity in addition to its own yield stress. The major increase in the yield stress in HL-HEA-1050 and HL-HEA-1200 is attributed to these high back-stresses. Additionally, the back-stress in HL-HEA-1050 is higher than that in HL-HEA-1200, indicating that the back-stress is also related to the Hall-Petch effect. Further research needs to be conducted to explore this phenomenon.

The Hall-Petch effect on the increase of the yield stress can be calculated following the equation [34]:

$$\sigma_y = \sigma_f + k_y * d^{-1/2} \quad (4.8)$$

where σ_y is the yield stress, σ_f is a friction stress (constant), k_y is the strengthening coefficient, and d is the grain size. By substituting the data of CG1-HEA-1300 ($\sigma_y=322$ MPa, $d=100 \mu\text{m}$) and CG2-HEA-1300 ($\sigma_y=300$ MPa, $d=400 \mu\text{m}$) to the equation (8), $\sigma_f = 277$ MPa and $k_y = 440 \text{ MPa} \cdot \mu\text{m}^{1/2}$ are obtained. Furthermore, equation (5) can be rewritten to estimate initial yield stress based on back-stress strengthening:

$$\sigma_y = \sigma_f (277 \text{ MPa}) + \sigma_b \quad (4.9)$$

Therefore, the contribution from the Hall-Petch effect is 250MPa for FG-HEA-1075 ($\sigma_y = 574 \text{ MPa}$) with grain size of $3.1\mu\text{m}$, and the precipitation strengthening from NiAl particles results in $574-250-277 = 47\text{MPa}$ (additional strength). For HL-HEA-1200 ($\sigma_y = 484\text{MPa}$), back-stress contribution towards initial yield strength due to heterogeneous microstructure is found to be $\sim 207\text{MPa}$, which agrees well with exponentially extrapolated result of the back-stress curve in Fig. 4.12(e) for HL-HEA-1200. Hence, the back-stress initially increases rapidly and then plateaus with increasing applied strain.

4.4.3 GND Density Analysis for HL-HEA-1200

While macroscopic mechanical tests, i.e. LUR tensile tests conducted in this study, have been used to support the concept of back-stress for improving strength and ductility, microscopic mapping of the back-stress is technically a challenging task. However, long-range back-stresses are essentially generated through pile-up of geometrically necessary dislocations (GNDs) across the CG/FG interface, which fortunately can be quantified through extracting the lattice orientation gradients obtained from electron backscatter diffraction measurement [39]. In a heterogeneous microstructure consisting of regions of fine grains and coarse grains, strain partitioning during deformation necessitates the presence of GNDs to maintain compatibility across the CG/FG interface. The design of heterogeneous lamella (HL) microstructure utilizes its ability to strain harden due to back-

stresses associated with GNDs. Therefore, the GND density map can be used to extract useful information regarding the back-stresses.

Here, GND density distribution has been examined in a deformed HL-HEA-1200 sample around the CG/FG interface using our in-house Matlab program [46,47,64], as shown in Fig. 4.13. The GND density is averaged for every grain in order to demonstrate the effect of grain structure on GND density distribution. The coarse grain region is formed by many ultrafine sub-grains, which collectively behaves as one large grain surrounded by many fine grains. In Fig. 4.13(a), the grain area ratio between fine grains and coarse grains range from one to four orders of magnitude differences, which represents a significant heterogeneity in the grain structure. Consequently, the distribution of local strain is highly heterogeneous, which results in a non-uniform GND density distribution as depicted in Fig. 4.13(b) showing the averaged GND density over each grain as a result of severe plastic deformation. The uniformity of the yellow color in the coarse grain region indicates an intermediate level GND density, whereas the surrounding fine grained region shows significant variation in the grain average GND density, from lower levels (blue shades) to much higher levels (red-brown shades). Therefore, the coarse grain region carries a relatively uniform strain with limited strain gradients along grain boundaries. Finer grains deform under much higher imposed geometric constraints, which could result in a higher strain gradient, i.e. GND density.

However, the overall deformation of the fine grain structure is very complicated. First, local plastic strain distribution around the CG/FG interface is a history dependent quantity, which is heterogeneously distributed. A similar study of the GND density distribution in HL microstructure even reveals presence of a low GND density ‘transition layer’ that connects the ‘compatibility layer’ with high plastic strain gradients with FG region [39]. In this study, the characteristic layers have not been clearly observed, but it is still clear the CG region contains relatively lower GND density overall compared to the adjacent FG region, as a result of strain partitioning. In addition, NiAl particles present in the microstructure might adversely disperse the plastic strain, which could lead to stress concentrations and early failure of the material. Hence, it is not surprising to see that some of the fine grains carry very low strain gradients, i.e. low GND density. Nevertheless, the heterogeneous microstructure does show significant heterogeneity in the distribution of GND density, which potentially correlates to back-stresses generated in this unique microstructure.

When compared with HL-HEA-1050, HL-HEA-1200 specimen exhibits much higher ductility. On one hand, the much smaller volume fraction of NiAl precipitates along the grain boundaries of HL-HEA-1200 reduce the probability of failure due to stress concentration. On the other hand, some stress-induced nano-scale twins are formed during the tensile test, which lead to the important TWIP effect: the effect of stress-induced twins on decreasing the dislocation mean free path to achieve a higher strain hardening rate

[28].

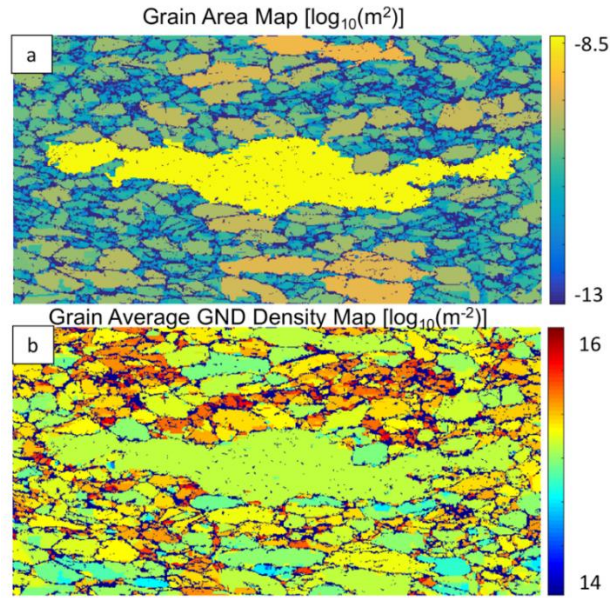


Figure 4.13. GND Calculation result for HL-HEA-1200 after tensile test. (a) Grain area map for HL-HEA-1200 after tensile test; (b) grain average GND density map in logarithmic scale (color bar: 14 – 15 [unit: log₁₀(m⁻²)]).

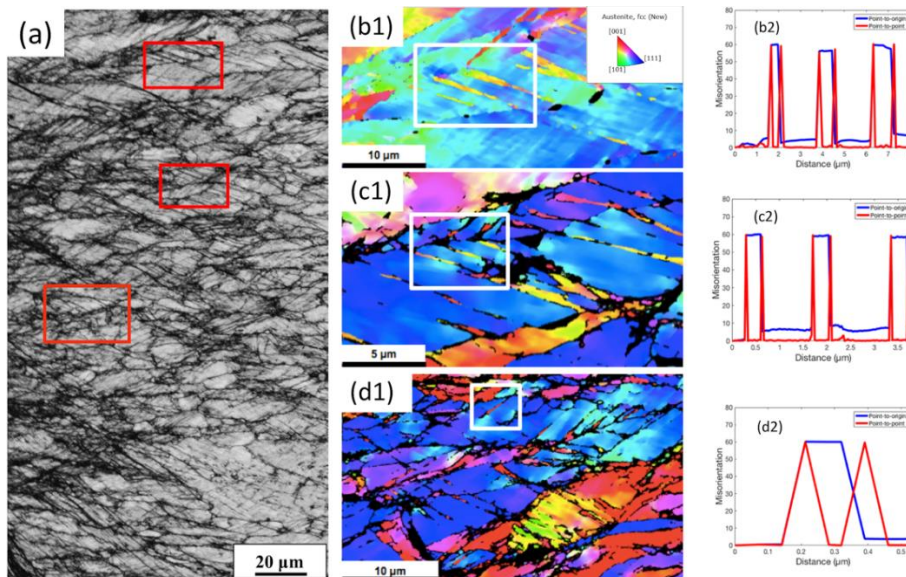


Figure 4.14. (a) EBSD BC image for HL-HEA-1200 after tensile test with elongation over 40%. EBSD IPFs (b1), (c1) and (d1) for the selected areas in (a). Corresponding statistics figures of misorientation versus distance (b2), (c2) and (d2) for the black square areas in (b1), (c1) and (d1), respectively.

4.4.4 Ductility improvement through twinned induced plasticity (TWIP)

Fig. 4.14(a) shows the microstructure of HL-HEA-1200 after tensile test with elongation over 40%. The EBSD IPFs in Fig. 4.14(b1-d1) from the selected areas in Fig. 4.14(a) show that some nano-scale twins appear, and the corresponding misorientation measurement results in Fig. 4.14(b2-d2) confirm that these fine bands are stress-induced twins. However, no observable nano-scale twins are found in the HL-HEA-1050 specimen after tensile test using the current characterization technique, although it is likely that nano-twins are also present in the HL-HEA-1050. Therefore, the stress-induced twins may help to increase the ductility of these HEA-NCATB, but the greater ductility of the HL-HEA-1200 is likely due to the reduction in NiAl particles at grain boundaries.

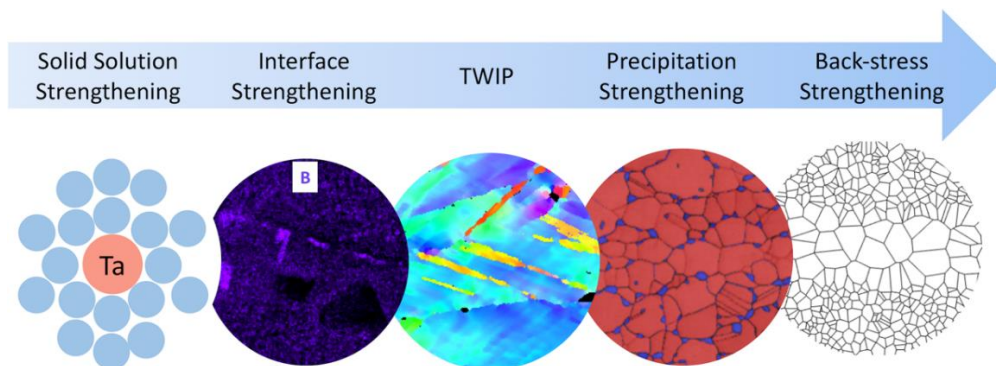


Figure 4.15. Overview of strengthening mechanisms in the current non-equiatomic NCATB HEA with heterogeneous lamella structure to achieve the synergy of high strength and high ductility.

For the current HEA-NCATB specimens, it has been found that the elongation increases with decreasing fraction of NiAl particles. Therefore, an optimized thermomechanical processing method is needed in the future to explore new compositions with even higher strength and ductility.

Based on the above results and discussions, the synergy of high strength and ductility in the current non-equiatomic NCATB HEA is attributed to the introduction of multiple deformation and strengthening mechanisms as depicted schematically in Fig. 4.15: solid solution strengthening (Ta addition), interface/grain boundary strengthening (small amount of boron addition, cohesion effect [45]), TWIP (formation of deformation twins), precipitation strengthening (the precipitation of NiAl particles), and back stress strengthening (UFG/FG, FG/CG). This alloy system and its processability highlights the unique opportunity to tailor microstructure to achieve unique combinations of strength and ductility.

4.5 Conclusion

In summary, a non-equiatomic FeNiCoAlTaB (NCATB) high entropy alloy (HEA) with two kinds of heterogeneous lamella (HL) structures showing a combination of high strength and high ductility is reported here. The following results of the current study are noteworthy:

(1) The specimen annealed at 1050°C exhibits an HL structure composed of fine grains and ultrafine grains, which exhibits a combination of high UTS (~1050MPa) and good ductility (elongation ~ 23%). The shear bands formed in the cold rolling step, which act as nucleation sites for fine grains, are responsible for the formation of fine-grain areas. The cell blocks with low-angle boundaries are responsible for the formation of ultrafine-

grain lamella. The NiAl(B2) precipitates suppress the growth of fine grains due to Zener pinning effect.

(2) The sample annealed at 1200°C exhibits a different HL structure composed of fine grains and coarse grains, which demonstrates the synergy of high UTS (~880 MPa) and high ductility (elongation ~43%). The fine grains prefer to nucleate within the shear bands, and their growth is suppressed by the precipitation of NiAl(B2) particles. The coarse grains form due to the absence of NiAl(B2) precipitates along their lower angle grain boundaries.

(3) The back-stress strengthening mechanism, unique to deformation of HL structures, is verified through “loading-unloading-reloading” (LUR) cyclic tensile test and geometrically necessary dislocation (GND) density analysis. For the LUR cyclic tensile test, a strong Bauschinger effect is observed in both HL-structure samples.

(4) NiAl(B2) precipitates play an important role in the formation of HL structures. Additionally, they also affect the ductility of the current alloys due to their effect creating stress concentrations. An optimized fraction of NiAl still needs to be explored.

(5) The current HEA-NCATB provides a new method for non-equiatomic FeNiCoAl-based HEAs design to achieve unique combinations of high strength and high ductility.

(6) The synergy of high strength and high ductility in the current non-equiatomic NCATB HEA can be attributed to the introduction of multiple deformation and

strengthening mechanisms: solid solution strengthening, interface/grain boundary strengthening, TWIP, precipitation strengthening, and back stress strengthening.

Acknowledgement

Chapter 4 is the part of material that is submitted for publication in Materials Science and Engineering A. Cheng Zhang, Chaoyi Zhu, and Kenneth Vecchio. “Non-Equiatomic FeNiCoAl-Based High Entropy Alloys With Multiscale Heterogeneous Lamella Structure For Strength And Ductility”. Submitted to Materials Science and Engineering A. (2018). Elsevier. The dissertation author was the primary investigator and author of this paper.

The current authors would like to thank Tyler Harrington, Haoren Wang, Sumin Shin, Kevin Kaufman, Sabine Faulhaber, Wayne Neilson (UC San Diego) and Dr. Chunhuan Guo (Harbin Engineering University) for help on experiments. We also appreciate Professor Y. Sutou and Professor K. Ando (Tohoku University) for fruitful discussion about the fabrication of samples.

References

- [1] J. Yeh, S. Chen, S. Lin, J. Gan, T. Chin, T. Shun, C. Tsau, S. Chang, Nanostructured high - entropy alloys with multiple principal elements: novel alloy design concepts and outcomes, *Adv. Eng. Mater.* 6 (2004) 299 - 303.
- [2] B. Cantor, I.T.H. Chang, P. Knight, A.J.B. Vincent, Microstructural development in equiatomic multicomponent alloys, *Mater. Sci. Eng. A.* 375 (2004) 213–218.
- [3] Y. Zhang, T.T. Zuo, Z. Tang, M.C. Gao, K.A. Dahmen, P.K. Liaw, Z.P. Lu, Microstructures and properties of high-entropy alloys, *Prog. Mater. Sci.* 61 (2014) 1–93.
- [4] D.B. Miracle, O.N. Senkov, A critical review of high entropy alloys and related concepts, *Acta Mater.* 122 (2017) 448–511.
- [5] M.J. Yao, K.G. Pradeep, C.C. Tasan, D. Raabe, A novel, single phase, non-equiatomic FeMnNiCoCr high-entropy alloy with exceptional phase stability and tensile ductility, *Scr. Mater.* 72 (2014) 5–8.
- [6] C.C. Tasan, Y. Deng, K.G. Pradeep, M.J. Yao, H. Springer, D. Raabe, Composition dependence of phase stability, deformation mechanisms, and mechanical properties of the CoCrFeMnNi high-entropy alloy system, *Jom.* 66 (2014) 1993–2001.
- [7] Z. Li, K.G. Pradeep, Y. Deng, D. Raabe, C.C. Tasan, Metastable high-entropy dual-phase alloys overcome the strength–ductility trade-off, *Nature.* 534 (2016) 227.
- [8] Z. Li, C.C. Tasan, K.G. Pradeep, D. Raabe, A TRIP-assisted dual-phase high-entropy alloy: grain size and phase fraction effects on deformation behavior, *Acta Mater.* 131 (2017) 323–335.
- [9] Z. Li, F. Körmann, B. Grabowski, J. Neugebauer, D. Raabe, Ab initio assisted design of quinary dual-phase high-entropy alloys with transformation-induced plasticity, *Acta Mater.* 136 (2017) 262–270.
- [10] Y. Zhou, X. Jin, L. Zhang, X. Du, B. Li, A hierarchical nanostructured Fe₃₄Cr₃₄Ni₁₄Al₁₄Co₄ high-entropy alloy with good compressive mechanical properties, *Mater. Sci. Eng. A.* 716 (2018) 235–239.
- [11] B. Gludovatz, A. Hohenwarter, D. Catoor, E.H. Chang, E.P. George, R.O. Ritchie, A fracture-resistant high-entropy alloy for cryogenic applications, *Science* (80-.). 345 (2014) 1153–1158.

- [12] D. Li, C. Li, T. Feng, Y. Zhang, G. Sha, J.J. Lewandowski, P.K. Liaw, Y. Zhang, High-entropy Al 0.3 CoCrFeNi alloy fibers with high tensile strength and ductility at ambient and cryogenic temperatures, *Acta Mater.* 123 (2017) 285–294.
- [13] T. Yang, S. Xia, W. Guo, R. Hu, J.D. Poplawsky, G. Sha, Y. Fang, Z. Yan, C. Wang, C. Li, Effects of temperature on the irradiation responses of Al 0.1 CoCrFeNi high entropy alloy, *Scr. Mater.* 144 (2018) 31–35.
- [14] S. Xia, Z. Wang, T.F. Yang, Y. Zhang, Irradiation behavior in high entropy alloys, *J. Iron Steel Res. Int.* 22 (2015) 879–884.
- [15] Z. Li, S. Zhao, S.M. Alotaibi, Y. Liu, B. Wang, M.A. Meyers, Adiabatic shear localization in the CrMnFeCoNi high-entropy alloy, *Acta Mater.* 151 (2018) 424–431.
- [16] Y. Yao, Z. Huang, P. Xie, S.D. Lacey, R.J. Jacob, H. Xie, F. Chen, A. Nie, T. Pu, M. Rehwoldt, Carbothermal shock synthesis of high-entropy-alloy nanoparticles, *Science* (80-.). 359 (2018) 1489–1494.
- [17] J. Joseph, N. Stanford, P. Hodgson, D.M. Fabijanic, Tension/compression asymmetry in additive manufactured face centered cubic high entropy alloy, *Scr. Mater.* 129 (2017) 30–34.
- [18] R. Li, P. Niu, T. Yuan, P. Cao, C. Chen, K. Zhou, Selective laser melting of an equiatomic CoCrFeMnNi high-entropy alloy: Processability, non-equilibrium microstructure and mechanical property, *J. Alloys Compd.* 746 (2018) 125–134.
- [19] S.-H. Joo, H. Kato, M.J. Jang, J. Moon, E.B. Kim, S.-J. Hong, H.S. Kim, Structure and properties of ultrafine-grained CoCrFeMnNi high-entropy alloys produced by mechanical alloying and spark plasma sintering, *J. Alloys Compd.* 698 (2017) 591–604.
- [20] S.M. Ueland, Y. Chen, C.A. Schuh, Oligocrystalline shape memory alloys, *Adv. Funct. Mater.* 22 (2012) 2094–2099.
- [21] K. Lu, Stabilizing nanostructures in metals using grain and twin boundary architectures, *Nat. Rev. Mater.* 1 (2016) 16019.
- [22] E. Ma, T. Zhu, Towards strength–ductility synergy through the design of heterogeneous nanostructures in metals, *Mater. Today.* 20 (2017) 323–331.
- [23] J.-L. Zhang, C.C. Tasan, M.J. Lai, D. Yan, D. Raabe, Partial recrystallization of

gum metal to achieve enhanced strength and ductility, *Acta Mater.* 135 (2017) 400–410.

[24] X. Wu, M. Yang, F. Yuan, G. Wu, Y. Wei, X. Huang, Y. Zhu, Heterogeneous lamella structure unites ultrafine-grain strength with coarse-grain ductility, *Proc. Natl. Acad. Sci.* 112 (2015) 14501–14505.

[25] T.H. Fang, W.L. Li, N.R. Tao, K. Lu, Revealing extraordinary intrinsic tensile plasticity in gradient nano-grained copper, *Science* (80-.). 331 (2011) 1587–1590.

[26] X. Wu, P. Jiang, L. Chen, F. Yuan, Y.T. Zhu, Extraordinary strain hardening by gradient structure, *Proc. Natl. Acad. Sci.* 111 (2014) 7197–7201.

[27] X.L. Wu, M.X. Yang, F.P. Yuan, L. Chen, Y.T. Zhu, Combining gradient structure and TRIP effect to produce austenite stainless steel with high strength and ductility, *Acta Mater.* 112 (2016) 337–346.

[28] Y. Li, Y. Lu, W. Li, M. Khedr, H. Liu, X. Jin, Hierarchical microstructure design of a bimodal grained twinning-induced plasticity steel with excellent cryogenic mechanical properties, *Acta Mater.* (2018).

[29] A. Magee, L. Ladani, T.D. Topping, E.J. Lavernia, Effects of tensile test parameters on the mechanical properties of a bimodal Al–Mg alloy, *Acta Mater.* 60 (2012) 5838–5849.

[30] K. Huang, K. Zhang, K. Marthinsen, R.E. Logé, Controlling grain structure and texture in Al–Mn from the competition between precipitation and recrystallization, *Acta Mater.* 141 (2017) 360–373.

[31] M. Yang, D. Yan, F. Yuan, P. Jiang, E. Ma, X. Wu, Dynamically reinforced heterogeneous grain structure prolongs ductility in a medium-entropy alloy with gigapascal yield strength, *Proc. Natl. Acad. Sci.* (2018) 201807817.

[32] X. Wu, Y. Zhu, Heterogeneous materials: a new class of materials with unprecedented mechanical properties, *Mater. Res. Lett.* 5 (2017) 527–532.

[33] E.W. Hart, Theory of the tensile test, *Acta Metall.* 15 (1967) 351–355.

[34] N. Hansen, Hall–Petch relation and boundary strengthening, *Scr. Mater.* 51 (2004) 801–806.

[35] H.K. Park, K. Ameyama, J. Yoo, H. Hwang, H.S. Kim, Additional hardening in

harmonic structured materials by strain partitioning and back stress, *Mater. Res. Lett.* 6 (2018) 261–267.

[36] M.F. Ashby, The deformation of plastically non-homogeneous materials, *Philos. Mag.* 21 (1970) 399–424.

[37] X. Liu, F. Yuan, Y. Zhu, X. Wu, Extraordinary Bauschinger effect in gradient structured copper, *Scr. Mater.* 150 (2018) 57–60.

[38] M. Yang, Y. Pan, F. Yuan, Y. Zhu, X. Wu, Back stress strengthening and strain hardening in gradient structure, *Mater. Res. Lett.* 4 (2016) 145–151.

[39] C. Zhang, C. Zhu, T. Harrington, K. Vecchio, Design of non-equiatomic high entropy alloys with heterogeneous lamella structure towards strength-ductility synergy, *Scr. Mater.* 154 (2018) 78–82. doi:10.1016/j.scriptamat.2018.05.020.

[40] Z. Fu, B.E. MacDonald, D. Zhang, B. Wu, W. Chen, J. Ivanisenko, H. Hahn, E.J. Lavernia, Fcc nanostructured TiFeCoNi alloy with multi-scale grains and enhanced plasticity, *Scr. Mater.* 143 (2018) 108–112.

[41] K. Lu, J. Lu, Nanostructured surface layer on metallic materials induced by surface mechanical attrition treatment, *Mater. Sci. Eng. A.* 375 (2004) 38–45.

[42] Y. Ma, F. Yuan, M. Yang, P. Jiang, E. Ma, X. Wu, Dynamic shear deformation of a CrCoNi medium-entropy alloy with heterogeneous grain structures, *Acta Mater.* 148 (2018) 407–418.

[43] J.W. Bae, J. Moon, M.J. Jang, D. Yim, D. Kim, S. Lee, H.S. Kim, Trade-off between tensile property and formability by partial recrystallization of CrMnFeCoNi high-entropy alloy, *Mater. Sci. Eng. A.* 703 (2017) 324–330.

[44] Y.H. Wang, J.M. Kang, Y. Peng, T.S. Wang, N. Hansen, X. Huang, Hall-Petch strengthening in Fe-34.5 Mn-0.04 C steel cold-rolled, partially recrystallized and fully recrystallized, *Scr. Mater.* 155 (2018) 41–45.

[45] J.B. Seol, J.W. Bae, Z. Li, J.C. Han, J.G. Kim, D. Raabe, H.S. Kim, Boron doped ultrastrong and ductile high-entropy alloys, *Acta Mater.* (2018).

[46] C. Zhu, V. Livescu, T. Harrington, O. Dippo, G.T. Gray, K.S. Vecchio, Investigation of the shear response and geometrically necessary dislocation densities in shear localization in high-purity titanium, *Int. J. Plast.* 92 (2017) 148–163.

- [47] C. Zhu, T. Harrington, V. Livescu, G.T. Gray, K.S. Vecchio, Determination of geometrically necessary dislocations in large shear strain localization in aluminum, *Acta Mater.* 118 (2016) 383–394.
- [48] H.S. Chen, A. Godfrey, N. Hansen, J.X. Xie, Q. Liu, Microstructure–grain orientation relationship in coarse grain nickel cold-rolled to large strain, *Mater. Sci. Eng. A.* 483 (2008) 157–160.
- [49] D.A. Hughes, N. Hansen, Microstructure and strength of nickel at large strains, *Acta Mater.* 48 (2000) 2985–3004.
- [50] S.P. Bellier, R.D. Doherty, The structure of deformed aluminium and its recrystallization—investigations with transmission Kossel diffraction, *Acta Metall.* 25 (1977) 521–538.
- [51] G.I. Rosen, D.J. Jensen, D.A. Hughes, N. Hansen, Microstructure and local crystallography of cold rolled aluminium, *Acta Metall. Mater.* 43 (1995) 2563–2579.
- [52] D. Orlov, H. Fujiwara, K. Ameyama, Obtaining copper with harmonic structure for the optimal balance of structure-performance relationship, *Mater. Trans.* 54 (2013) 1549–1553.
- [53] Y. Wang, M. Chen, F. Zhou, E. Ma, High tensile ductility in a nanostructured metal, *Nature.* 419 (2002) 912.
- [54] L. Lu, Y. Shen, X. Chen, L. Qian, K. Lu, Ultrahigh strength and high electrical conductivity in copper, *Science* (80-.). 304 (2004) 422–426.
- [55] P. V Liddicoat, X.-Z. Liao, Y. Zhao, Y. Zhu, M.Y. Murashkin, E.J. Lavernia, R.Z. Valiev, S.P. Ringer, Nanostructural hierarchy increases the strength of aluminium alloys, *Nat. Commun.* 1 (2010) 63.
- [56] Y. Tanaka, Y. Himuro, R. Kainuma, Y. Sutou, T. Omori, K. Ishida, Ferrous polycrystalline shape-memory alloy showing huge superelasticity, *Science* (80-.). 327 (2010) 1488–1490.
- [57] T. Omori, S. Abe, Y. Tanaka, D.Y. Lee, K. Ishida, R. Kainuma, Thermoelastic martensitic transformation and superelasticity in Fe–Ni–Co–Al–Nb–B polycrystalline alloy, *Scr. Mater.* 69 (2013) 812–815.

[58] D. Lee, T. Omori, R. Kainuma, Ductility enhancement and superelasticity in Fe–Ni–Co–Al–Ti–B polycrystalline alloy, *J. Alloys Compd.* 617 (2014) 120–123.

[59] M. Hillert, On the theory of normal and abnormal grain growth, *Acta Metall.* 13 (1965) 227–238.

[60] J.J. Bhattacharyya, S.R. Agnew, G. Muralidharan, Texture enhancement during grain growth of magnesium alloy AZ31B, *Acta Mater.* 86 (2015) 80–94.

[61] J.D. Eshelby, F.C. Frank, F.R.N. Nabarro, XLI. The equilibrium of linear arrays of dislocations., London, Edinburgh, Dublin *Philos. Mag. J. Sci.* 42 (1951) 351–364.

[62] X. Feaugas, On the origin of the tensile flow stress in the stainless steel AISI 316L at 300 K: back stress and effective stress, *Acta Mater.* 47 (1999) 3617–3632.

[63] J.I. Dickson, J. Boutin, L. Handfield, A comparison of two simple methods for measuring cyclic internal and effective stresses, *Mater. Sci. Eng.* 64 (1984) L7–L11.

[64] C. Zhu, T. Harrington, G.T. Gray, K.S. Vecchio, Dislocation-Type Evolution in Quasi-Statically Compressed Polycrystalline Nickel, *Acta Mater.* (2018).

Chapter 5

Multifunctional Non-equiatomic High Entropy Alloys

Chapter 5 is the part of material that is submitted for publication in Advanced Engineering Materials.

Cheng Zhang, Chaoyi Zhu, Tyler Harrington, Lee Casalena, Haoren Wang, Sumin Shin, Kenneth S. Vecchio. “Multifunctional Non-equiatomic High Entropy Alloys”. Submitted to Advanced Engineering Materials. (2018). Wiley-VCH.

Abstract

A new class of non-equiatomic FeNiCoAlTaB (NCATB) high entropy alloy (HEA) is introduced, which exhibits tunable properties from cryogenic/ambient superelasticity to ultra-high strength through controlling the nature or type of martensite. In the current NCATB-HEA alloy system, depending on the size of γ' -Ni₃Al (L1₂) precipitates, thin-plate, lenticular, butterfly and lath-like martensite can form. When thin-plate thermoelastic martensite is favored, a superelastic strain of about 0.025 (ambient) and ~0.01 (cryogenic) can be achieved with a high yield stress of ~800 MPa and a high-damping effect (10 times higher than Cu-Al-Ni superelastic alloy). While for butterfly and lath-like martensite dominated NCATB-HEA, an ultra-high yield stress of around 1.1 GPa can be achieved while no superelasticity is demonstrated. This current alloy system can help to expand the

application domain of HEAs, for example into high-damping applications, robust actuators, space exploration and other structural material applications.

5.1 Introduction

Owing to attractive engineering properties, such as high strength and high ductility at cryogenic temperatures and refractory properties, high entropy alloys (HEAs) have drawn great attention over the past decade.[1-5] During this time of exploration, most studies have been primarily focused the original concept of HEA design, which utilizes an equiatomic ratio of multiple principal elements to obtain the maximum configurational entropy.[1] However, this design concept limits the compositional space and excludes non-equiatomic candidates with potentially outstanding properties. The concept of non-equiatomic HEAs, first put forward by Raabe and his colleagues,[6-10] has greatly expanded the compositional space of HEA design, and work on these compositions has led to the development of materials with unparalleled mechanical properties.[6] In the non-equiatomic $\text{Fe}_{49.5}\text{Mn}_{30}\text{Co}_{10}\text{Cr}_{10}\text{C}_{0.5}$ HEA, the introduction of HCP martensite, due to the change of stacking fault energy, leads to transformation-induced plasticity (TRIP), which can make a significant contribution to the synergy of high strength and high ductility.[6]

Martensite, which forms as the result of a diffusionless phase transformation, plays an important role in the mechanical properties of various materials, especially ferrous alloys. In Fe-Ni alloys, the martensite start temperature (M_s) of the FCC \rightarrow BCT/BCC

transformation is known to decrease with increasing Ni concentration, which can affect the resultant martensite morphology. In Fe-Ni alloys, four morphologies of α' martensite can form: lath, butterfly, lenticular, and thin plate. Among these four, lath martensite forms at the highest temperature and thin plate martensite forms at the lowest temperature.[11-14] In addition, with decreasing M_s temperature, the substructure of martensite changes from dislocations (lath martensite) to completely twinned (thin plate martensite). For lath martensite in ferrous alloys, the typical low-energy dislocation structure, characterized by the alternating misorientation change across the lath boundaries and a high dislocation density, leads to enhanced strength, which was the basis for development of high-strength alloy steels.[15-17] Similarly, thin plate martensite, especially the thermoelastic type, is the basis for the shape memory effect in ferrous shape memory alloys.[14] For butterfly and lenticular morphologies, the substructure comprises a mixture of dislocations and twins.[13,18-20] These phenomena are well studied in ferrous alloys, however, research regarding the presence of a martensitic transformation in HEAs has rarely been reported. Further, the opportunity for tunable properties of HEAs through control of the nature of martensite is also unexplored to the knowledge of these authors.

Martensite morphology in ferrous alloys, especially the formation of α' thin plate martensite, can be manipulated through the addition of certain elements and appropriate strengthening mechanisms. With the addition of Co to the Fe-Ni system, Shibata et al. [21] found that the volume change accompanying the martensitic transformation decreases

due to the Invar effect, and lath and/or lenticular martensite (primarily determined by the Ni content) can be observed in Fe-Ni-Co alloys with different compositions. In the Fe-Ni-Ti and Fe-Ni-Si alloys, only lenticular martensite forms and, consequently, these alloys systems demonstrate low hardness.[22-24] By adding Co to the Fe-Ni-Ti and Fe-Ni-Si alloys, the hardness of both is greatly enhanced, and the shape memory effect can be achieved due to the formation of thin plate martensite.[25,26] Therefore, the addition of Co not only contributes to the increased hardness of the austenitic matrix, but also favors the formation of the thin plate martensite responsible for the shape memory effect.

Moreover, Ohtsuka et al. [27] have found that the addition of Al is effective in driving the formation of the γ' -Ni₃Al (L1₂) phase for precipitation strengthening in Fe-Ni-Co-based alloys. As a result, the addition of Co and Al contributes to the increase of tetragonality (increase in c/a ratio) in martensite and the hardness of the austenite matrix.

In the Fe-Ni-Co-Al system, strong γ' formers are introduced to effectively make use of the γ' phase for precipitation strengthening. Ishida[28] and Jia[29] demonstrated that Ta, Nb, Ti, Mo, V and W are strong γ' formers. Among the above elements, Tanaka et al.[30] showed that Ta and Nb are the two strongest since they increase the hardness of the austenite matrix to the greatest extent after aging. For the resulting γ'' -Ni₃Nb (DO₂₂) and γ' -Ni₃Ta (L1₂) precipitate phases, the lattice misfit between the γ'' -Ni₃Nb and the fcc austenite matrix should be the larger of the two.[31] Jiang et al.[32] have found that new ultra-strong steel can be obtained via the method aiming at minimizing lattice misfit

between the precipitates and the matrix. Therefore, Ta is chosen as the strong γ' former in the current study, as it maximizes γ' precipitate formation and minimizes lattice misfit.

Recently, several Fe-Ni-Co-Al-based ferrous shape memory alloys have been studied with additions of Ta, Nb or Ti. Among these ferrous alloys, the alloy with Ta addition shows the largest superelastic strain.[33-35] These studies also show that the addition of B is effective in suppressing the precipitation of β -NiAl (B2) phase along grain boundaries, which embrittles the material.[33-35] Ruhl and Cohen[36] have found that most of the B in the Fe-Ni-B alloys is formed as precipitated $(\text{Fe,Ni})_3\text{B}$, which may be related to grain boundary strengthening in the Fe-Ni-Co-Al-based alloy. In a recent study, Seol et al.[37] found that in the boron doped FeMnCrCoNi and $\text{Fe}_{40}\text{Mn}_{40}\text{Cr}_{10}\text{Co}_{10}$ high entropy alloys that boron decorates the grain boundaries and acts twofold; (1) through interface strengthening and (2) grain size reduction. Although boron is widely used for improving the ductility in L_{12} - Ni_3Al , L_{12} - Ni_3Si , B2-ordered FeAl and L_{10} TiAl, due to its cohesive effect on the grain boundaries, [38-43] precise control over the boron concentration is critical to exploit its beneficial effects. Based on previous research for taking advantage of cohesion effect from boron,[37-38] the amount of boron in the current study is 0.04 % (atomic percent), which is 70 ppm in weight percent.

Since the coherency between the precipitated γ' particles and the fcc austenite matrix is important for developing thermoelastic thin plate martensite, and the coherency is determined by the size of the γ' particles,[44] it is feasible to design the morphology of

martensite through controlling the size of γ' precipitates. Some previous studies show that aging can result in a change of the M_s temperature, and that M_s temperature is closely related to the morphology of martensite.[25,45-47] It is shown here to be feasible to control both the M_s temperature and the type of martensite formed of the non-equiatomic FeNiCoAlTaB (NCATB) HEA by controlling the aging time and temperature, and hence tailor properties and functionality.

5.2 Experimental Procedures

Fabrication of NCATB-HEA samples: NCATB (Fe-27.5Ni-16.5Co-10Al-2.2Ta-0.04B) (at. %) was prepared through arc-melting under an argon atmosphere with raw materials as follows: Fe (99.95%), Ni (99.9%), Co (99.9%), Al (99.9%), Ta (99.9%), and Ni₂B (99%). The ingot was flipped and re-melted eight times to ensure chemical homogeneity. After arc-melting, induction heat-treatment in an argon atmosphere was carried out for further homogenization before hot rolling. The NCATB samples with original thickness of about 12 mm, were processed through hot rolling (1250 °C, reduction in thickness (RIT) is about 20%), cold rolling (RIT \geq 90%), annealing (1300 °C, 30 mins) and aging at 500-700 °C for various times.

Detection of γ' Precipitates: To measure the size and composition of γ' particles, a Thermo Scientific Talos F200X S/TEM was used. Bright-field TEM images and Super-X EDS maps were collected at 200 kV for specimens aged in different conditions. For

electrochemical thin-foil preparation, the samples were first mechanically ground and polished down to a thickness of 0.15 mm by hand. The electron-transparent areas in the thin foils were achieved using twin-jet electro-polishing with the solution of 4% perchloric acid and 96% ethanol under an applied potential of 40 V at a temperature of around -15 °C.

Morphology of Martensites Detection and Martensite Start (M_s) Temperature Measurement: The morphologies of martensites were taken by a LEICA optical microscope that was equipped with cooling and heating apparatus. Some of M_s and A_f temperatures were measured with a Perkin Elmer Cryo-DSC with cooling and heating rate of 10 °C min⁻¹, while some other M_s temperatures were determined by recording the sample temperature while imaging under optical microscopy when surface relief started to occur.

Recrystallization Texture Detection: After cold rolling and annealing, a Thermo Scientific Apreo FE-SEM equipped with an Oxford Symmetry EBSD system was used to detect the texture development in NCATB. Since samples with RIT over 90% were very thin, they were carefully ground and polished using standard metallographic techniques followed by vibratory polishing in order to obtain high-quality EBSD images.

Mechanical Property Measurements: The microhardness after aging was evaluated by Vicker's hardness testing with a LECO Hardness Testing Machine. Load and loading time were 500 gf and 15 sec, respectively. A minimum of 10 data points were used for each measurement of the reported values.

Samples with high hardness over 400 Vickers after aging were chosen for the tensile

test and cyclic tensile test. In the tensile test at room temperature, the tensile direction was parallel to the rolling direction and the size of samples in the gauge-length were 20 mm x 1.0 mm x (0.2-0.3) mm. The strain rate in the current study was $5 \times 10^{-4} \text{ s}^{-1}$. NCATB sheet with dimensions of 60 mm x 8 mm x 0.30 mm was bent in the liquid nitrogen in comparison with a 304 stainless steel sheet and a 1095 spring steel sheet with the same size. The diameter of the curvature in the bending test is 30 mm.

5.3 Results and Discussion

5.3.1 Growth of γ' precipitates during aging

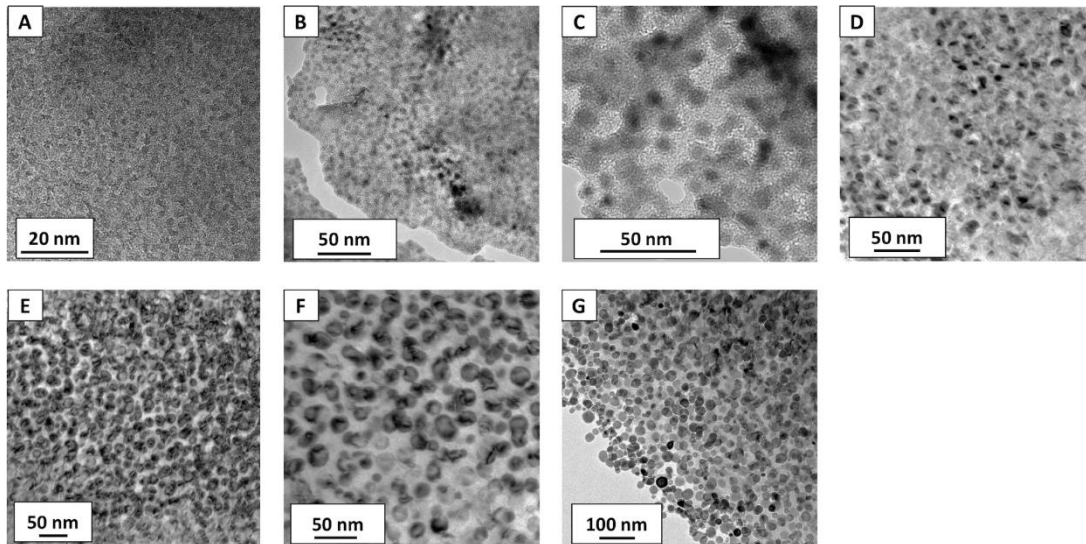


Figure 5.1. TEM bright field (BF) images for NCATB-HEA specimens aged at 700 °C for different times. (A) 1 hour; (B) 5 hours; (C) 10 hours; (D) 24 hours; (E) 48 hours; (F) 72 hours; (G) 96 hours.

Figure 5.1 shows the bright field TEM images of γ' nano-scale particles precipitated in NCATB-HEA aged at 700 °C for different times. The size of γ' particles increases with

increasing aging time. For specimens aged for 48 hours or longer, the size of γ' is ~20nm or slightly greater. While for samples aged for 10 hours or shorter, the size of γ' is less than 10nm. Although the size of γ' varies with aging time, the volume fraction of the precipitates remains almost constant. Hence, the coarsening process of γ' is likely through 'Ostwald Ripening' following the equation:

$$R^3 - R_0^3 = kt \quad (5.1)$$

where R is the mean radius of precipitates, R_0 is the initial mean radius, t is the aging time, and k is the growth rate constant that is related to temperature and interfacial energy. The statistically representative data of the mean radius of γ' particles in NCATB-HEA aged at 700 °C for different times are listed in Table 5.1.

Table 5.1. Size of γ' precipitates in NCATB-HEA aged at 700 °C for 1 to 96 hrs.

Aging Time (hrs)	1	5	10	24	48	72	96
Average Size (nm) [std-dev. <0.5nm]	5.1	6.7	9.3	12.3	19.6	21.8	25.2

For specimens aged at 700 °C ($t \leq 24$ hours), by employing Equation (1), the coarsening behavior of γ' precipitates can be described as:

$$R^3 - 4.2^3 = 75t \quad (5.2)$$

When $t > 24$ hours, the size of γ' particles increase significantly and deviates from the predictions of this Ostwald Ripening equation, indicating that there is loss of coherency between the precipitates and the matrix.

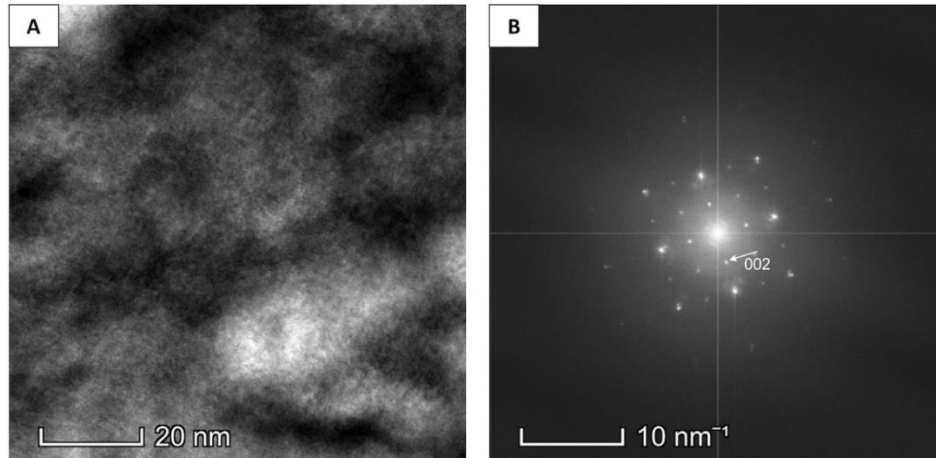


Figure 5.2. (A) TEM bright field (BF) image for NCATB-HEA sample aged at 700°C for 10 hours; (B) Corresponding Selected Area Diffraction (SAD) (FTT) pattern for 2(A). Zone Axis [001].

Figure 5.2 shows the bright field TEM image and the corresponding selected area electron diffraction (SAED) pattern for the specimen aged at 700 °C for 10 hours. The SAED pattern confirms that the γ' particles are present in a high-volume fraction and that they comprise the ordered L1₂ structure. The EDS mapping result of γ' particles in NCATB-HEA aged at 700 °C for 72 hours is shown in Figure 5.3. The enrichment of Ta in the γ' precipitates confirms that Ta is a strong γ' former. The main constituents of these γ' are Ni, Al, and Ta.

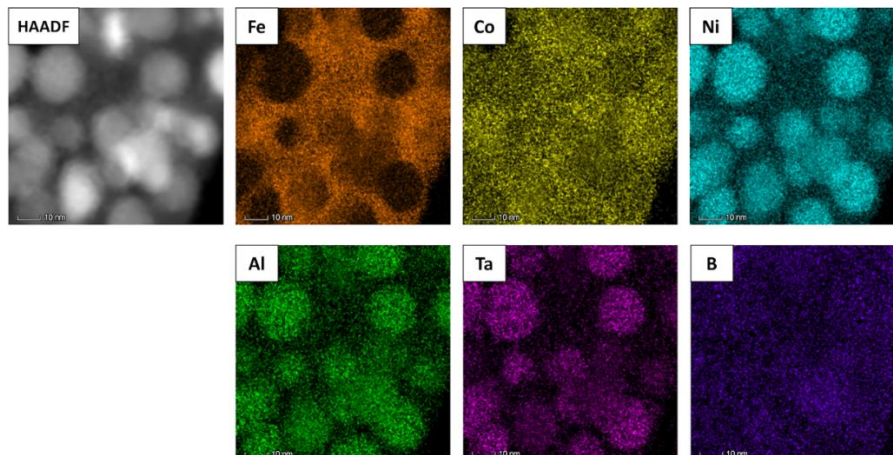


Figure 5.3. TEM HAADF image and EDS Mapping for NCATB-HEA specimen aged at 700 °C for 72 hours.

5.3.2 Martensite morphology under different aging conditions

Coherency between γ' precipitates and the γ matrix affects the morphology of the martensite in NCATB-HEA alloys. Figure 5.4 shows the microstructure of the NCATB-HEA via optical images and EBSD Inverse Pole Figure (IPF-X) maps showing martensite development in NCATB with aging time longer than 24 hours. For specimens aged at 700 °C for 96 hours, lath-like and butterfly martensite are observed. While in the sample aged for 48 hours and 72 hours, some lenticular martensite is seen, characterized by the appearance of mid-ribs, and some butterfly-like martensite can also be observed. Since lath-like martensite contains a high density of dislocations, high strength can be expected in these samples. In the current study, the specimen aged for 96 hours is chosen for compression testing. The formation of lath-like martensite can be explained as follows: On one hand, the continuous growth of γ' during the aging process leads to the loss of coherency between γ' precipitates and the γ matrix. Therefore, large γ' particles above some critical radius cannot suppress the formation of martensite, which leads to the increase of the martensite start (M_s) temperature. On the other hand, Ni_3Al -type γ' precipitates are mainly composed of Ni, Al, and Ta. During the aging step, the increase in Ni content in the γ' results in a decrease of Ni concentration in the matrix. Since the M_s temperature strongly depends on the Ni concentration, the reduction of Ni content in the matrix gives rise to the significant increase in the M_s temperature. Therefore, the combined effect of the coherency and the change in the chemical composition results in the

formation of martensite with different morphologies in the current material.

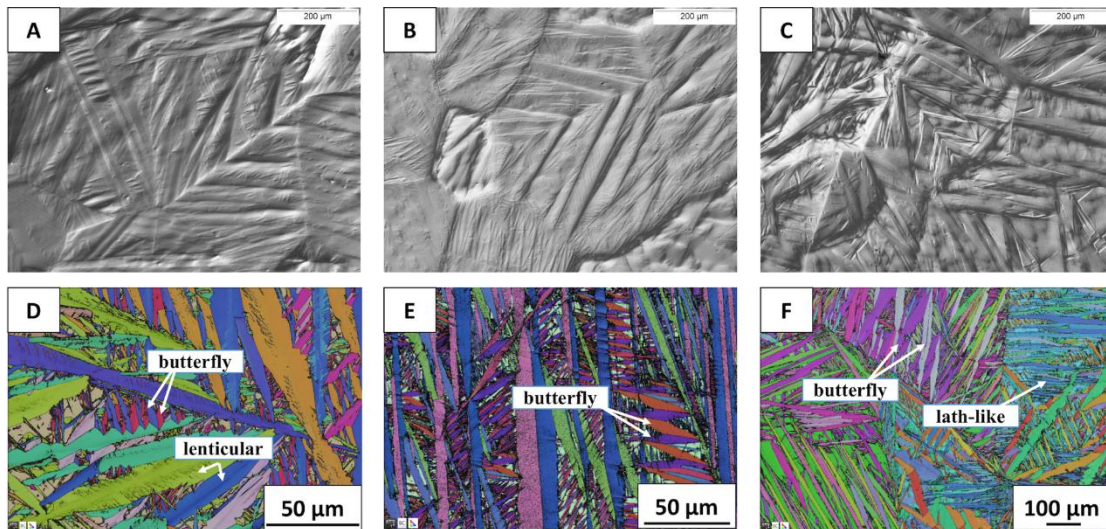


Figure 5.4. Optical microscope images for NCATB-HEA aged at 700 °C for (A) 48 hours, (B) 72 hours and (C) 96 hours. EBSD Inverse Pole Figures (IPF) for HEA-NCATB aged for (D) 48 hours, (E) 72 hours and (F) 96 hours. Lenticular, butterfly and lath-like martensites are shown with arrows.

Figure 5.5 presents the optical images of martensite in NCATB aged at 700 °C for 5 hours, 10 hours, and 24 hours. In all three samples, no lath-like martensite is formed. Instead, thin-plate martensite is formed at temperatures lower than -100°C. Figure 5.6 shows a series of in-situ images showing thin-plate martensite forming and reversing in a complete martensitic transformation (cooling-heating cycles) for NCATB-HEA samples. For the specimen aged for 5 hours, no retained martensite is observed after three cooling-heating cycles. This indicates that the martensitic transformation occurring in this sample is reversible, and the martensite is thermoelastic. For the sample aged for 10 hours, the martensitic transformation is also reversible and no retained martensite is observed after three cycles. However, for the specimen aged for 24 hours, some martensite remains after

three cooling-heating cycles, indicating that at least some of the thin-plate martensite is non-thermoelastic. During the cooling-heating cycle, one feature to be noted is that the temperature for martensite formation along the grain boundaries is about 30-40 °C higher than that for martensite formation in the interior portion of grains. This phenomenon is due to heterogeneous nucleation in the formation of martensite, where less energy is required for nucleation of martensite regions along grain boundaries.[11]

Figure 5.7 presents the development of the martensite start (M_s) temperatures of NCATB-HEA samples aged at 700 °C for different aging times, along with a summary of the morphology of martensite with the corresponding γ' size. For the specimen aged for 1 hour, even when the temperature is below -175°C, no martensite formation is observed through the in-situ cooling-heating experiments, and no phase transformation peak is found in the DSC curve, indicating that the M_s temperature lies somewhere below -175 °C. For the other samples of different aging times, the M_s temperature increases with increasing aging due to an increase in γ' size and loss in the coherency between particles and matrix. This supports the view that the coherent interfaces suppress the martensitic transformation. Therefore, it appears feasible to control the morphology of martensite through tracking the size of γ' particles in the current non-equiatomic NCATB-HEA. When the aging time is less than 10 hours, thermoelastic thin-plate martensite forms. With aging time approaching 24 hours, non-thermoelastic thin-plate martensite can be achieved. When aging time increases to 48 hours, lenticular martensite appears. A mixture of lenticular

and butterfly martensite is formed during the period from 48 hours to 72 hours. When the aging time increases to 96 hours, lath-like martensite appears, accompanied by some butterfly martensite. Therefore, the tailoring of martensite morphology through adjusting the size of γ' is successfully demonstrated in the current non-equiatomic NCATB-HEA.

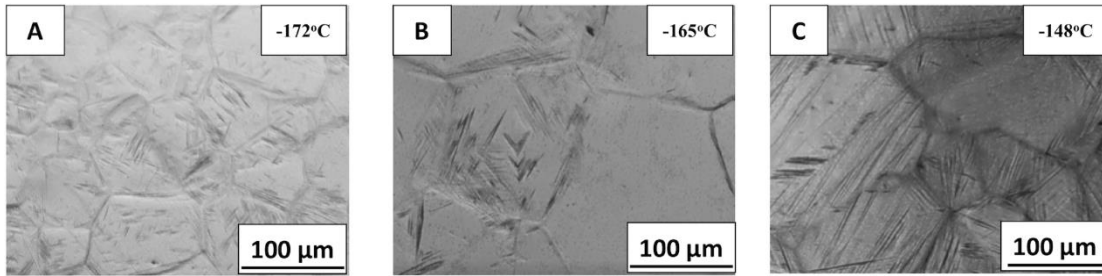


Figure 5.5. In-situ optical microscope images for NCATB-HEA aged at 700 °C for different times. (A) 5 hours (cooling to -172 °C); (B) 10 hours (cooling to -165 °C); (C) 24 hours (cooling to -148 °C).

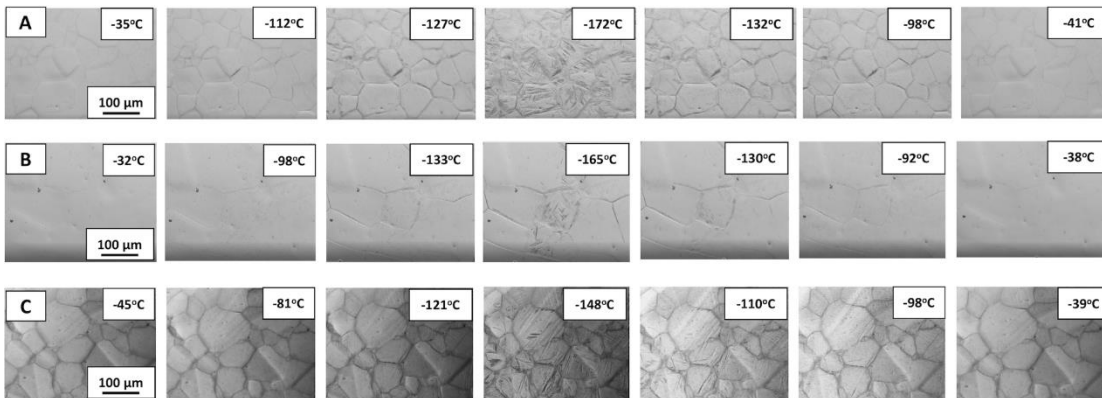


Figure 5.6. A series of in-situ optical microscope images showing thermal-induced thin-plate martensites for a complete martensitic transformation occurred in NCATB-HEA aged at 700 °C for different times. (A) 5 hours; (B) 10 hours; (C) 24 hours.

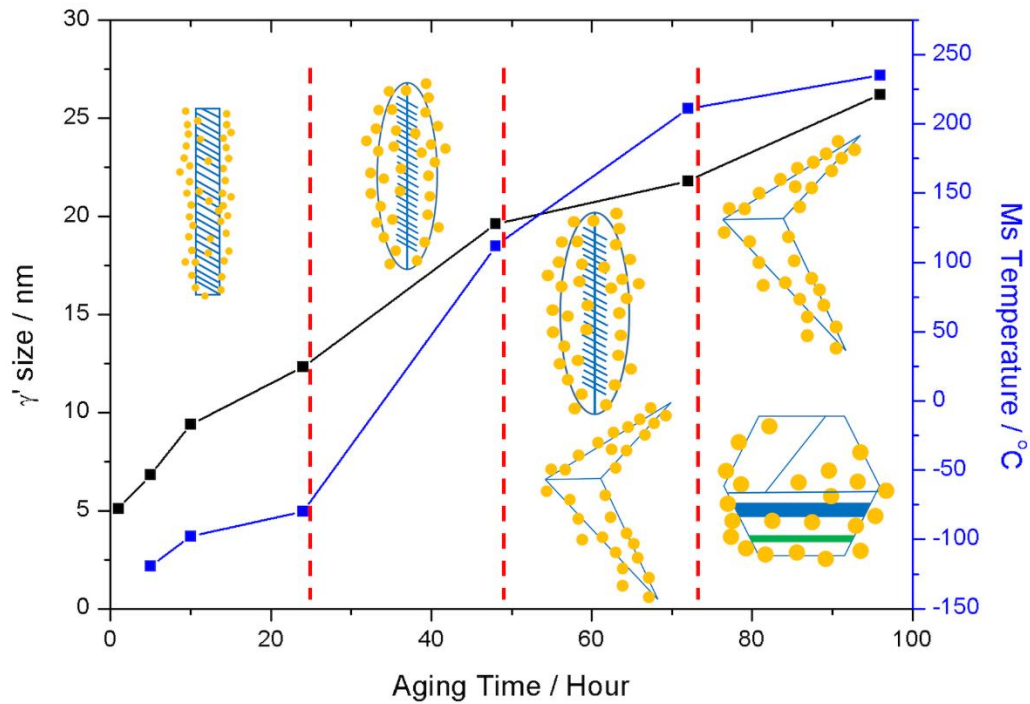


Figure 5.7. Development of γ' size and martensite start (Ms) temperature with aging time for NCATB-HEA aged at 700 °C. Morphology of martensites with related γ' precipitates corresponding to different aging times are shown.

5.3.3 Recrystallization texture evolution

Texture affects the superelasticity of polycrystalline alloys, especially the Fe-Ni-Co-Al-based polycrystalline alloys.[48] Figure 5.8 shows the EBSD IPF-X maps for NCATB-HEA samples with different reductions in thickness (RIT) after annealing at 1300 °C for 30 minutes. In Figure 5.8(A), the orientation of grains is random, which indicates that no recrystallization texture is formed. With more severe cold rolling, some recrystallization texture along $\langle 001 \rangle$ direction is formed in Figure 5.8(B), which is further enhanced with cold rolling over 97% as shown in Figure 5.8(C).

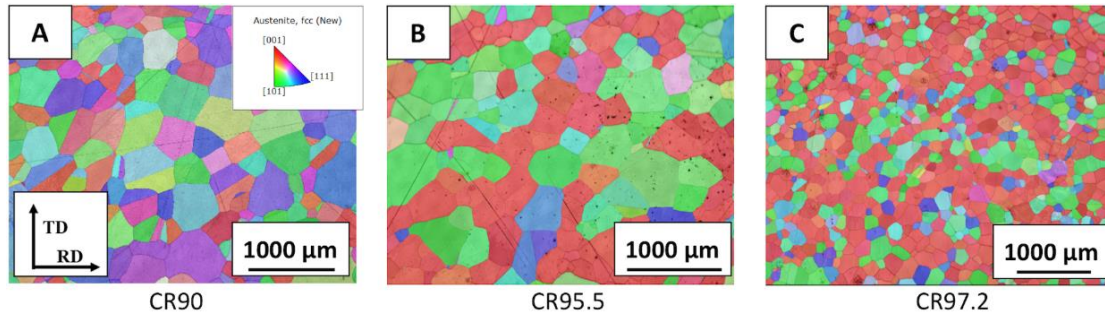


Figure 5.8. EBSD Inverse Pole Figures (IPFX) for NCATB-HEA samples after annealing at 1300 °C for 30 minutes with different reduction (RIT) in thickness in the cold-rolling step. (A) RIT=90%; (B) RIT=95.5%; (C) RIT=97.2%. RD – Rolling Direction; TD – Transverse Direction.

To evaluate the variation in texture intensity quantitatively, the ‘times random’ parameter is employed.[33] The value of times random can be obtained from the orientation distribution function (ODF) using the MTEX software.[49] In general, measured texture with a times random value over 10 is regarded as a strong texture. Times random values between 5 and 10 are regarded as medium texture. Times random values less than 5 are a weak texture. Figure 5.9 shows the relationship between texture intensity and reduction in thickness (RIT). The texture intensity significantly increases only if RIT is over 95%. Medium texture can be achieved when RIT is ~95%, and strong texture forms when RIT is over 97%.

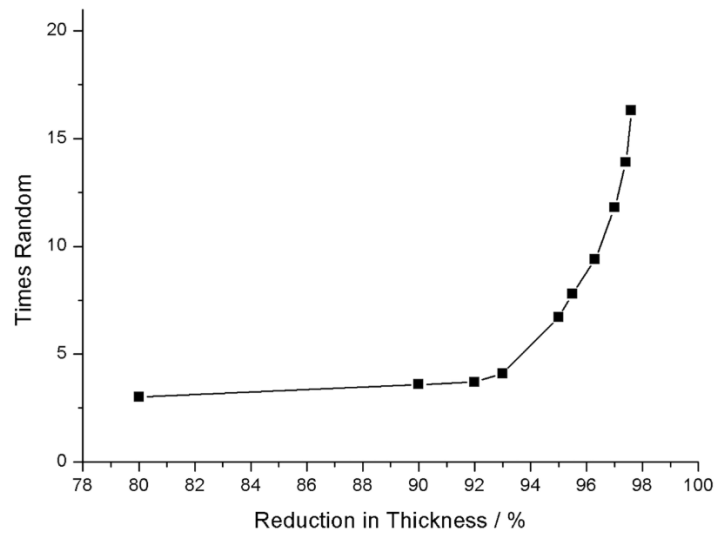


Figure 5.9. Development of times random (texture intensity) in the recrystallized NCATB-HEA with reduction in thickness.

5.3.4 Mechanical Properties

5.3.4.1 Mechanical properties at room temperature

To exhibit superelasticity, the martensitic transformation should be induced before slip occurs, so a high yield strength matrix is required.[14] In general, hardness is used to approximate the yield strength of materials. For the current study, microhardness testing is employed to measure the hardness of specimens after aging at different conditions; the results are presented in Figure 5.10. The hardness of aged specimens increases with increasing time at all three aging temperatures. By comparing the three hardness curves, for aging times less than 24 hours, the most significant increase can be achieved in the samples aged at 700 °C. For samples aged at 700 °C, high hardness (Vickers hardness > 400) can be obtained when aging time is over 5 hours. The highest hardness (Vickers

hardness around 600) is achieved when the aging time is 96 hours, which is likely due to the high dislocation density within the lath-like and butterfly martensite formed in this specimen.

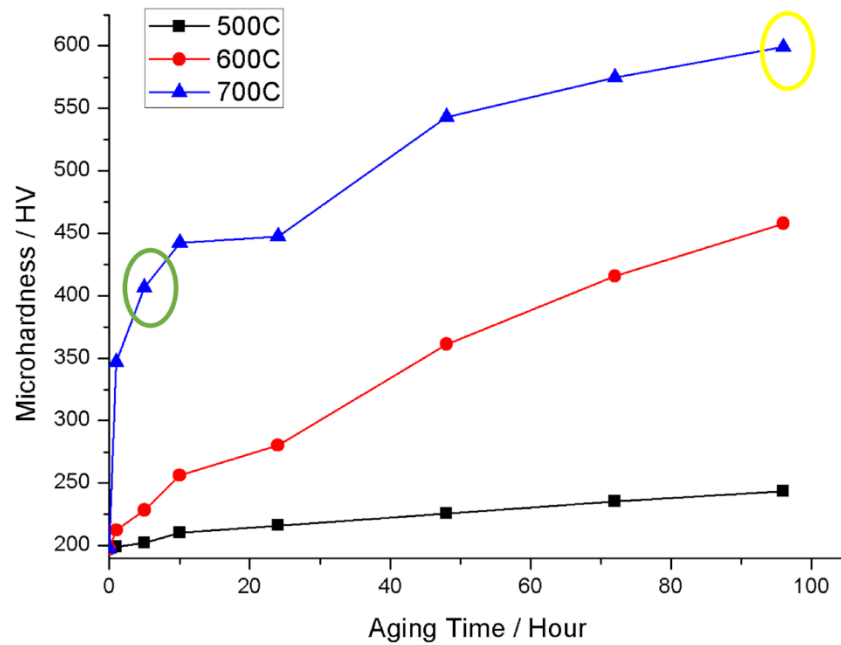


Figure 5.10. (Vickers) Microhardness development in aged NCATB-HEA with different aging times (1-96 hours) and temperatures (500 °C , 600 °C and 700 °C).

Considering that the size of γ' precipitates is less than 7nm and thermoelastic thin-plate martensite is achieved in the specimen aged at 700 °C for 5 hours, cyclic tensile testing is undertaken to examine the superelasticity in this sample. Figure 5.11(A) shows the cyclic tensile stress-strain curves obtained at room temperature for NCATB-HEA with different reductions in thickness. An oligocrystal or bamboo-like structure is employed for the testing specimens to reduce grain constraint and obtain good superelasticity.[50,51] The CR90 sample with randomly oriented grains exhibits no superelasticity, though the

yield stress is high. The CR95.3 specimen with medium-strength recrystallization texture shows a very small superelastic strain of 0.004. The CR97 sample with high-strength recrystallization texture exhibits a superelastic strain of 0.016. The CR97.5 sample with the strongest recrystallization texture shows the largest superelastic strain of 0.025, which is similar to that of the Ti-Nb-based superelastic alloys.[52] The comparison of yield stress in different alloy systems is presented in Figure 5.11(B).[50,53-56] The current non-equiatomic NCATB-HEA exhibits the highest yield stress among all the superelastic alloys. Furthermore, the yield stress of the current alloy is higher than that of most high-strength steels. Therefore, the NCATB-HEA material can be regarded as a high-strength superelastic alloy.

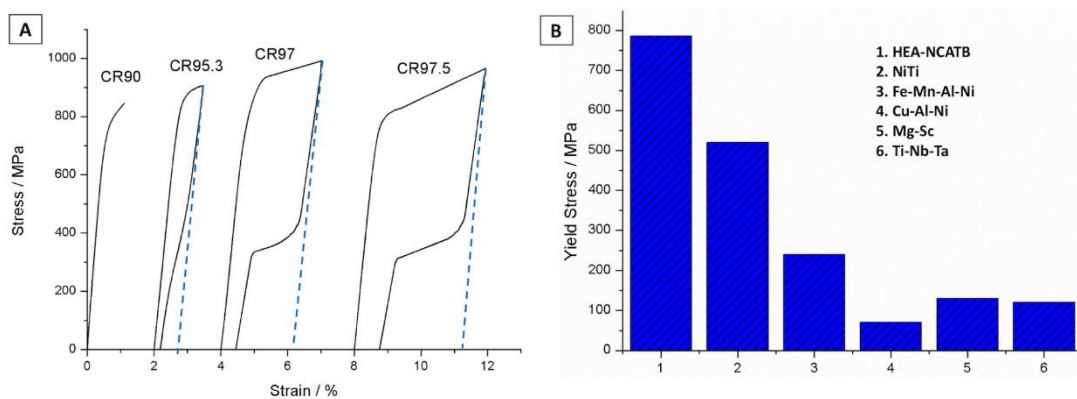


Figure 5.11. (A) Tensile stress-strain curves at room temperature for HEA-NCATB specimens with RIT of 90%, 95.3%, 97% and 97.5%. (B) Comparison of yield stress in various superelastic alloys. 1. HEA-NCATB; 2. NiTi; [53][54] 3. Fe-Mn-Al-Ni; [55] 4. Cu-Al-Ni; [50] 5. Mg-Sc; [56] 6. Ti-Nb-Ta. [52]

By controlling the size of γ' precipitates, not only is thermoelastic thin-plate martensite obtained, but also high-strength lath-like martensite. Figure 5.12(A) shows the compression stress-strain curve obtained at room temperature for NCATB aged at 700 °C

for 96 hours. Although an ultrahigh yield strength around 1.1 GPa is achieved, the ductility is limited. Figure 5.12(B) presents the tensile stress-strain curve achieved at room temperature for an NCATB specimen before aging. The solutionized NCATB-HEA sample shows an ultimate tensile strength (UTS) of about 580 MPa with a high elongation over 50%, which is similar to that of high-strength low-alloy steels (HSLA). Therefore, the present NCATB-HEA shows potential for application as a structural material.

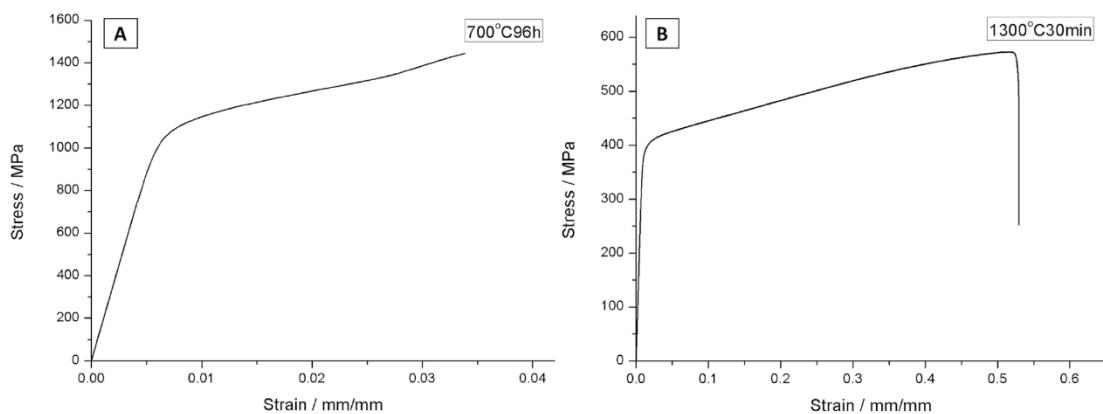


Figure 5.12. (A) Compression stress-strain curve for NCATB-HEA after aging at 700 °C for 96 hours; (B) Tensile stress-strain curve for NCATB-HEA before aging.

5.3.4.2 Mechanical properties at cryogenic conditions

Since thin-plate martensite is always formed at temperatures lower than -50 °C, it is of great interest to explore the potential applications of the current alloy at cryogenic conditions. 304 stainless steel (SS) is widely used at low temperature due to its good mechanical properties at cryogenic temperatures. In the current study, 304 SS and 1095 spring steel (with ultrahigh strength) are chosen for comparison with NCATB-HEA samples at extremely low temperature: identical sample geometries are used. The results

of the bending test in liquid nitrogen for NCATB-HEA with RIT of 96.5%, 304 stainless steel and 1095 spring steel sheets are shown in Figure 5.13. Before bending, all the specimens are straight, and the setup of bending test is present in Figure 5.13(A). After bending to 180° (bending into a U shape) in the liquid nitrogen as shown in Figure 5.13(B), the NCATB-HEA sample recovers to its original shape upon unloading, while some obvious plastic deformation is retained for both the 304 SS and 1095 spring steel sheet after removing the loading, as can be seen in Figure 5.13(C).

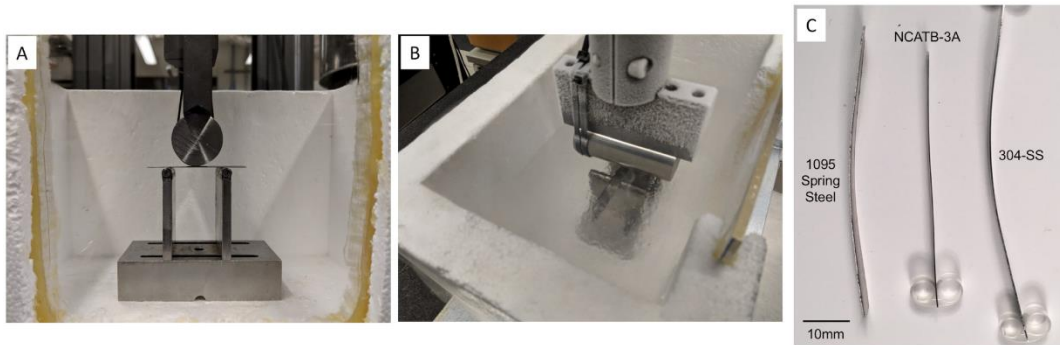


Figure 5.13. A series of images for bending test in liquid nitrogen. (A) Setup for the bending test. Before the test, samples are straight. The diameter of the curvature is $D=30$ mm; (B) Samples are totally rinsed in the liquid nitrogen and deformed to U shape during the test; (C) After bending test, samples are taken out from the liquid nitrogen. Only NCATB-HEA sample can completely recover to its original shape.

The following equation can be used to estimate the strain in the bending test:

$$\text{strain } (\epsilon) = t / D \quad (5.3)$$

where t is the thickness of the test sheet, D is the diameter of curvature.[57]

In the current study, $t = 0.30\text{mm}$, $D = 30\text{mm}$, and based on Equation (3), the strain $(\epsilon) = 0.01$. Therefore, the applied strain is estimated to be 0.01 in the bending test. The NCATB-HEA sample with medium-strength can completely recover to the original shape

in the liquid nitrogen upon unloading when the applied strain is approximately 0.01. This result shows that superelasticity can be achieved in the current non-equiatomic NCATB-HEA at cryogenic temperatures. Moreover, the NCATB-HEA specimen can recover to the original shape even after 20 loading-unloading cycles at cryogenic conditions ($T = 77$ K). If the yield strength were 1 GPa, and the material modulus is 200 GPa, then the elastic limit is 0.5% (or 0.005 strain). As such, the current U shape bend test achieves twice the elastic limit as recoverable strain and can therefore be classified as superelastic under cryogenic conditions.

The mechanism for the recoverable strain of NCATB-HEA in the liquid nitrogen is different from the superelastic strain obtained at room temperature. At ambient temperature, the specimen undergoes the diffusionless transformation from austenite to martensite with the temperature higher than austenite finish (A_f) temperature. While at cryogenic temperature, the transformation should be related to the rubber-like behavior, which takes place between two distinct morphologies of martensite.[14,58] Since the M_s temperature of the sample aged at 700 °C for 5 hours is around -120 °C, the specimen contains a high-volume fraction of thermal-induced thin-plate martensite at -196 °C. When the applied loading with strain over 0.01 is employed to the sample, the original thermal-induced thin-plate martensite will transform to another martensite morphology with a different lattice parameter. This is possibly due to the transition from planar-slip dislocation activity at room temperature to deformation by mechanical nanotwinning at cryogenic temperature.[4]

This rubber-like behavior at cryogenic temperatures in the NCATB-HEA qualifies this alloy as a promising candidate for material employed in the cryogenic condition of space.

5.3.5 High-damping property

In the superelastic cycle, due to the high yield stress and large stress hysteresis as shown in Figure 5.11(A), large energy absorption can be achieved. The amount of energy can be calculated as the area enclosed by the hysteresis loop in the stress-strain curves. Figure 5.14 shows the energy absorbed in a single superelastic ‘loading-unloading’ cycle for NCATB-HEA, in comparison to polycrystalline NiTi,[53] Cu-Al-Ni,[50] and Fe-Mn-Al-Ni alloys.[55] The largest energy absorbed by one superelastic cycle for NCATB-HEA with tensile strain of 0.04 is over 15 MJ m^{-3} , which is as large as that in the NiTi alloy with applied strain of 0.06, nearly 4 times larger than that in the Fe-Mn-Al-Ni alloy, and nearly 10 times larger than the Cu-Al-Ni alloy. NCATB-HEA alloy shows a great potential for high-damping materials, especially for the dampers in buildings and bridges.

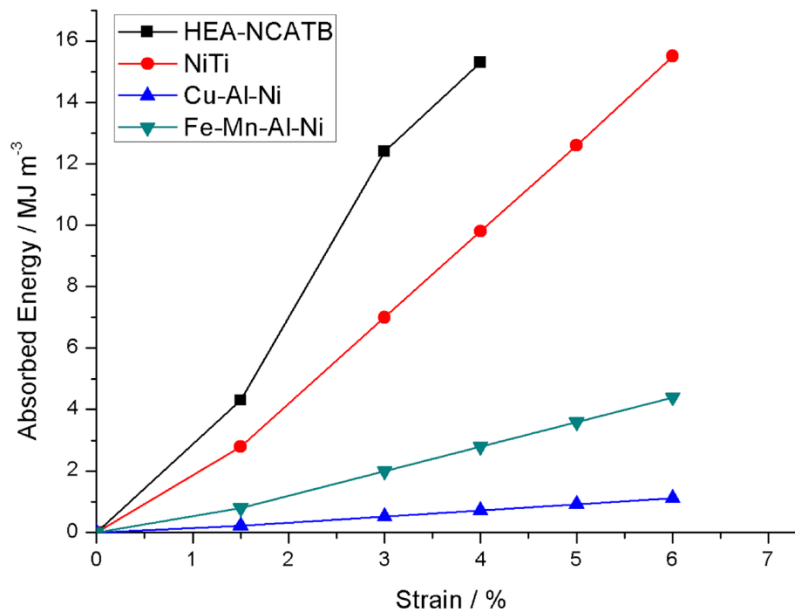


Figure 5.14. Absorbed energy in one superelastic cycle as a function of applied tensile strain for NCATB-HEA (aged at 700 °C for 5 hours), NiTi,[53][54] Cu-Al-Ni [50] and Fe-Mn-Al-Ni. [55]

5.4 Conclusion

In summary, the current study reports a new class of ferrous non-equiatomic FeNiCoAlTaB (NCATB) high entropy alloy (HEA) that possesses multifunctional properties through control of the martensite morphology. It is found that the size of γ' particles affects not only the coherency between the precipitates and the matrix, but also the martensite start (M_s) temperature and the morphology of martensite that is formed. With thin-plate thermoelastic martensite and a strong recrystallization texture, a superelastic strain of about 0.025 at ambient temperature can be achieved with a high yield stress around 800MPa. Meanwhile, large absorbed energy of approximately 15 MJ m⁻³ in one superelastic cycle can be obtained, which is approximately equivalent to that of the

more common NiTi superelastic alloy and about 10 times higher than that of a Cu-Al-Ni superelastic alloy. Furthermore, the NCATB-HEA can recover to the original shape with applied strain over 0.01 upon unloading in the cryogenic condition (~77 K). Additionally, with butterfly and lath-like martensite, an ultrahigh yield stress of around 1.1 GPa can be achieved in compression. The present non-equiatomc NCATB-HEA alloy system serves as a promising candidate material for many high strength or superelastic structural applications such as dampers, actuators and can be utilized under ambient or cryogenic conditions.

Acknowledgement

Chapter 5 is the part of material that is submitted for publication in *Advanced Engineering Materials*. Cheng Zhang, Chaoyi Zhu, Tyler Harrington, Lee Casalena, Haoren Wang, Sumin Shin, Kenneth S. Vecchio. “Multifunctional Non-equiatomc High Entropy Alloys”. Submitted to *Advanced Engineering Materials*. (2018). Wiley-VCH. The dissertation author was the primary investigator and author of this paper.

The current authors would like to thank Professor Richard James (University of Minnesota) for his useful suggestions for setting up the in-situ cooling-heating apparatus. We also appreciate Professor Y. Sutou and Professor K. Ando (Tohoku University) for fruitful discussion about the fabrication of samples. Additionally, we thank Wayne Neilson and Sabine Faulhaber (Department of NanoEngineering’s Materials Research Center at UC

San Diego) Cameron McElfresh and Mojtaba Samiee (UC San Diego), and Professor Chunhuan Guo (Harbin Engineering University) for their help in experiments.

Reference

- [1] J. Yeh, S. Chen, S. Lin, J. Gan, T. Chin, T. Shun, C. Tsau, S. Chang, *Adv. Eng. Mater.* **2004**, *6*, 299.
- [2] B. Cantor, I. T. H. Chang, P. Knight, A. J. B. Vincent, *Mater. Sci. Eng. A* **2004**, *375*, 213.
- [3] Y. Zhang, T. T. Zuo, Z. Tang, M. C. Gao, K. A. Dahmen, P. K. Liaw, Z. P. Lu, *Prog. Mater. Sci.* **2014**, *61*, 1.
- [4] B. Gludovatz, A. Hohenwarter, D. Catoor, E. H. Chang, E. P. George, R. O. Ritchie, *Science (80-.)*. **2014**, *345*, 1153.
- [5] D. B. Miracle, O. N. Senkov, *Acta Mater.* **2017**, *122*, 448.
- [6] Z. Li, K. G. Pradeep, Y. Deng, D. Raabe, C. C. Tasan, *Nature* **2016**, *534*, 227.
- [7] F. Otto, A. Dlouhý, K. G. Pradeep, M. Kuběnová, D. Raabe, G. Eggeler, E. P. George, *Acta Mater.* **2016**, *112*, 40.
- [8] C. C. Tasan, Y. Deng, K. G. Pradeep, M. J. Yao, H. Springer, D. Raabe, *Jom* **2014**, *66*, 1993.
- [9] Z. Li, C. C. Tasan, K. G. Pradeep, D. Raabe, *Acta Mater.* **2017**, *131*, 323.
- [10] M. J. Yao, K. G. Pradeep, C. C. Tasan, D. Raabe, *Scr. Mater.* **2014**, *72*, 5.
- [11] Z. Nishiyama, *Martensitic transformation*; Elsevier, 2012.
- [12] T. Maki, In *Materials Science Forum*; Trans Tech Publ, 1990; Vol. 56, pp. 157–168.

- [13] H. Sato, S. Zaefferer, *Acta Mater.* **2009**, *57*, 1931.
- [14] K. Otsuka, C. M. Wayman, *Shape memory materials*; Cambridge university press, 1999.
- [15] G. Krauss, A. R. Marder, *Metall. Trans.* **1971**, *2*, 2343.
- [16] J. W. Morris Jr, C. Kinney, K. Pytlewski, Y. Adachi, *Sci. Technol. Adv. Mater.* **2013**, *14*, 14208.
- [17] S. Morito, X. Huang, T. Furuhashi, T. Maki, N. Hansen, *Acta Mater.* **2006**, *54*, 5323.
- [18] H. Kitahara, R. Ueji, M. Ueda, N. Tsuji, Y. Minamino, *Mater. Charact.* **2005**, *54*, 378.
- [19] A. Shibata, S. Morito, T. Furuhashi, T. Maki, *Scr. Mater.* **2005**, *53*, 597.
- [20] N. Nakada, *Mater. Lett.* **2017**, *187*, 166.
- [21] A. Shibata, H. Yonezawa, K. Yabuuchi, S. Morito, T. Furuhashi, T. Maki, *Mater. Sci. Eng. A* **2006**, *438*, 241.
- [22] J. K. Abraham, J. S. Pascover, *Metall. Soc. AIME, Trans.* **1969**, *245*, 759.
- [23] Y. Himuro, O. Ikeda, R. Kainuma, K. Ishida, *Le J. Phys. IV* **2001**, *11*, Pr8.
- [24] Y. Himuro, R. Kainuma, K. Ishida, *ISIJ Int.* **2002**, *42*, 184.
- [25] T. Maki, K. Kobayashi, M. Minato, I. Tamura, *Scr. Metall.* **1984**, *18*, 1105.
- [26] Y. Tanaka, Y. Himuro, T. Omori, Y. Sutou, R. Kainuma, K. Ishida, *Mater. Sci. Eng. A* **2006**, *438*, 1030.
- [27] H. Ohtsuka, S. Kajiwara, *Metall. Mater. Trans. A* **1994**, *25*, 63.
- [28] K. Ishida, R. Kainuma, N. Ueno, T. Nishizawa, *Metall. Trans. A* **1991**, *22*, 441.
- [29] C. C. Jia, K. Ishida, T. Nishizawa, *Metall. Mater. Trans. A* **1994**, *25*, 473.
- [30] Y. Tanaka, R. Kainuma, T. Omori, K. Ishida, *Mater. Today Proc.* **2015**, *2*, S485.

- [31] F. C. Campbell, *Elements of metallurgy and engineering alloys*; ASM International, 2008.
- [32] S. Jiang, H. Wang, Y. Wu, X. Liu, H. Chen, M. Yao, B. Gault, D. Ponge, D. Raabe, A. Hirata, *Nature* **2017**, *544*, 460.
- [33] Y. Tanaka, Y. Himuro, R. Kainuma, Y. Sutou, T. Omori, K. Ishida, *Science (80-.)*. **2010**, *327*, 1488.
- [34] T. Omori, S. Abe, Y. Tanaka, D. Y. Lee, K. Ishida, R. Kainuma, *Scr. Mater.* **2013**, *69*, 812.
- [35] D. Lee, T. Omori, R. Kainuma, *J. Alloys Compd.* **2014**, *617*, 120.
- [36] R. C. Ruhl, M. Cohen, *TRANS MET SOC AIME* **1969**, *245*, 253.
- [37] J. B. Seol, J. W. Bae, Z. Li, J. C. Han, J. G. Kim, D. Raabe, H. S. Kim, *Acta Mater.* **2018**.
- [38] C. T. Liu, C. L. White, J. A. Horton, *Acta Metall.* **1985**, *33*, 213.
- [39] C. T. Liu, E. P. George, W. C. Oliver, *Intermetallics* **1996**, *4*, 77.
- [40] I. Baker, X. Li, H. Xiao, R. Carleton, E. P. George, *Intermetallics* **1998**, *6*, 177.
- [41] D. Hu, *Intermetallics* **2002**, *10*, 851.
- [42] R. Wu, A. J. Freeman, G. B. Olson, *Science (80-.)*. **1994**, *265*, 376.
- [43] D. Raabe, M. Herbig, S. Sandlöbes, Y. Li, D. Tytko, M. Kuzmina, D. Ponge, P.-P. Choi, *Curr. Opin. Solid State Mater. Sci.* **2014**, *18*, 253.
- [44] Y. Geng, D. Lee, X. Xu, M. Nagasako, M. Jin, X. Jin, T. Omori, R. Kainuma, *J. Alloys Compd.* **2015**, *628*, 287.
- [45] E. Hornbogen, W. Meyer, *Acta Met* **1967**, *15*, 584.
- [46] L. Jian, C. C. Chou, C. M. Wayman, *Mater. Chem. Phys.* **1993**, *34*, 14.
- [47] Y. Geng, M. Jin, W. Ren, W. Zhang, X. Jin, *J. Alloys Compd.* **2013**, *577*, S631.

- [48] K. Bhattacharya, R. V Kohn, *Acta Mater.* **1996**, *44*, 529.
- [49] F. Bachmann, R. Hielscher, H. Schaeben, *Solid State Phenom.* **2010**, *160*, 63.
- [50] S. M. Ueland, Y. Chen, C. A. Schuh, *Adv. Funct. Mater.* **2012**, *22*, 2094.
- [51] Y. Sutou, T. Omori, R. Kainuma, K. Ishida, *Acta Mater.* **2013**, *61*, 3842.
- [52] H. Y. Kim, T. Sasaki, K. Okutsu, J. I. Kim, T. Inamura, H. Hosoda, S. Miyazaki, *Acta Mater.* **2006**, *54*, 423.
- [53] L. Di Sarno, A. S. Elnashai, *Prog. Struct. Eng. Mater.* **2003**, *5*, 60.
- [54] R. DesRoches, M. Delemont, *Eng. Struct.* **2002**, *24*, 325.
- [55] T. Omori, K. Ando, M. Okano, X. Xu, Y. Tanaka, I. Ohnuma, R. Kainuma, K. Ishida, *Science (80-.)*. **2011**, *333*, 68.
- [56] Y. Ogawa, D. Ando, Y. Sutou, J. Koike, *Science (80-.)*. **2016**, *353*, 368.
- [57] Y. H. Wen, M. Yan, N. Li, *Scr. Mater.* **2004**, *50*, 441.
- [58] X. Ren, K. Otsuka, *Nature* **1997**, *389*, 579.

Chapter 6

Grain Boundary Precipitation of Ta and NiAl in Superelastic FeNiCoAlTaB Alloy

Chapter 6 is the part of material that is submitted for publication in Materials Science and Engineering A

Cheng Zhang, Chaoyi Zhu, Sumin Shin, Lee Casalena, Kenneth Vecchio. “Grain Boundary Precipitation of Tantalum and NiAl in Superelastic FeNiCoAlTaB Alloy”. Submitted to Materials Science and Engineering A. (2018). Elsevier.

Abstract

The precipitation behavior of tantalum (Ta) and NiAl along grain boundaries has been investigated in polycrystalline Fe-28.5Ni-17.5Co-11.5Al-2.5Ta-0.05B (NCATB) (at.%) alloy in order to understand their role in limiting its superelastic behavior. It is found that Ta precipitates at grain boundary triple-junctions first, then along grain boundaries, and acts as nuclei for β -NiAl phase formation. Small amounts of boron is also found distributed adjacent to the Ta precipitates. Consequently, the martensitic transformation associated with the superelastic response is promoted along grain boundaries by the Ta and β -NiAl precipitated there. Furthermore, increasing aging temperature facilitates the precipitation of Ta and β -NiAl along grain boundaries. Both the fraction of low-angle boundaries and the intensity of recrystallization texture are

significantly increased with increasing reduction in thickness of cold-rolled specimens over 95%, which is effective for the suppression of Ta and β -NiAl formation as their formation occurs primarily on high angle grain boundaries. As a result, the superelastic behavior of the FeNiCoAlTaB alloy is closely linked to the reduction in thickness, which increases the ratio of low angle to high angle boundaries, and hence the propensity for grain boundary failure associated with the grain boundary precipitates and grain boundary initiated martensitic transformation.

6.1 Introduction

Due to their low cost and excellent cold workability, ferrous superelastic alloys have been considered to be promising candidates for replacing superelastic Nitinol [1-7]. Recently, it has been reported that precipitation of Ni₃Al-type γ' (L1₂) phase can be employed to strengthen the γ matrix of Fe-Ni-Co-Al-X-B (X=Ti, Nb, and Ta) alloys based on the Kovar alloy (Fe-29Ni-17Co-0.3Mn-0.2Si-<0.01C) (wt.%) through thermomechanical processing. Considerable superelastic strains (4.2-13.5%) have been achieved in these ferrous polycrystalline alloys [8-11]. For reversible stress-induced martensite, the martensitic transformation should occur before slip, and therefore a strong slip-resistant austenite matrix is required. The introduction of γ' precipitates can effectively increase the strength of austenite matrix via enhanced slip resistance. However, the superelastic response of ferrous alloys strengthened by nanoscale γ' particles

is significantly limited by the precipitation of β -NiAl (B2) phase along the grain boundaries [9-14].

In the current Fe-Ni-Co-Al-Ta-B (hereafter referred to as NCATB) alloys, the addition of Ni stabilizes the austenite phase and Co is added to increase the matrix strength through solid solution strengthening. Al and Ta are used for facilitating the precipitation of γ' [15-23]. Boron is considered to contribute to strengthening of the grain boundaries. However, the distribution of boron in NCATB after aging is not clear yet. Although some work has been done in the single-crystal field of NCATB [24-27], very few studies have examined NCATB polycrystalline alloys in terms of superelastic response development because of the following reasons: 1) it is difficult to eliminate Ta segregation in NCATB starting from the as-cast condition to make it homogeneous; and 2) the formation of β -NiAl (B2) phase along the grain boundaries makes the sample extremely brittle, limiting formability. Therefore, it is very important to determine the precipitation behavior of these different phases along the grain boundaries in order to improve the superelastic response of polycrystalline NCATB.

From previous studies, FeNiCoAlTaB polycrystalline alloy, the CR90 sample (CR90 represents a reduction in thickness of 90% in the cold rolling step) exhibited no superelastic behavior, while CR98.5 sample, with very strong recrystallization texture, shows significant superelastic strain >13% [9]. Therefore, the strength of the recrystallization texture is very important for obtaining superelasticity in polycrystalline Fe-Ni-Co-Al-based

alloys. However, studies on the relationship between the recrystallization texture and the superelastic strain have not been detailed since the discovery of NCATB. Additionally, Lee et al. [11] have found that low-angle boundaries (LAB) affect superelasticity in the FeNiCoAlTi alloy due to their effect on suppressing the precipitation of NiAl along the grain boundaries. Hence, the fraction of LABs also plays an important role in superelasticity of FeNiCoAl-based alloys. Furthermore, to avoid severe stress concentration, bamboo-like or oligocrystal structure is usually employed with relative grain size (grain size/thickness) larger than 1 [28]. The bamboo-like structure can effectively reduce the grain constraint and mimics the response of a single crystal [29-31]. Therefore, in the current study, samples with relative grain size over 1 or bamboo-like structure are used in cyclic tensile tests.

In order to determine the role that grain boundaries play in limiting the extent of the superelastic response in NCATB alloys, the precipitation behavior of Ta and β -NiAl along the grain boundaries is investigated for various cold deformation and aging conditions. Additionally, the development of recrystallization texture, the fraction of LABs, and the improvement of superelasticity is further discussed in this study.

6.2 Experimental Procedures

NCATB (Fe-28Ni-17Co-11.5Al-2.5Ta-0.05B) (at.%) was prepared through arc-melting under an argon atmosphere with raw materials as follows: Fe (99.95%), Ni (99.9%),

Co (99.9%), Al (99.9%), Ta (99.9%), and Ni₂B (99%). After arc-melting, ingots with original thickness of approximately 12 mm were processed through induction heat-treatment, hot rolling (1250°C, reduction in thickness (RIT) is 20-30%), cold rolling (RIT \geq 90%), solutionization (1300°C, 30 min or 3h), and aging (600°C and 700°C, 1hr to 96hrs). After cold rolling and solutionization, EBSD was employed to detect low-angle boundaries and the texture development. All samples were carefully ground and polished using standard metallographic techniques followed by vibratory polishing in order to obtain high-quality EBSD images.

In the current research, a Thermo Scientific Quanta 600 SEM equipped with a Bruker XFlash 6160 EDS/EBSD detector was used for the EBSD analysis, and a Thermo Scientific Apreo EF-SEM was used for the higher resolution observations of the microstructure. A Thermo Scientific Talos F200X STEM equipped with Super-X EDS was employed to detect the composition near the grain boundaries after aging. In-situ martensitic transformation was imaged with a LEICA optical microscope equipped with cooling and heating apparatus, following the general protocols in reference [32]. For the cyclic tensile test at room temperature, the tensile direction was parallel to the rolling direction. The size of samples in the gauge-length were 20mm×1mm×0.2-0.3mm. The strain rate in the current study was 5×10^{-4} /s. For electrochemical preparation, the samples were first mechanically ground and polished by hand down to a thickness less than 0.15 mm. The electron-transparent areas in the thin foils were achieved using twin-jet electro-polishing

with the solution of 4% perchloric acid and 96% ethanol under an applied potential of 40V at a temperature around -15°C.

6.3 Results

6.3.1 Microstructure Evolution before Aging

In order to investigate the precipitation behavior of Ta and β -NiAl along the grain boundaries of NCATB, a homogeneous sample is required. The microstructure development of NCATB before aging is shown in Fig. 6.1. Due to the much heavier atomic mass, Ta is the brightest element in the back-scattered electron (BSE) mode among all the elements in the current alloy. Therefore, it is very easy to distinguish Ta from other elements in the BSE mode. After arc-melting, obvious Ta segregation is formed between dendrites, see Fig. 6.1(a). The EDS mapping results of the enlarged area in the as-cast NCATB are presented in Fig. 6.1(b), which shows two types of segregation after arc-melting: 1) Ta segregation and 2) precipitated β -NiAl (B2) phase. The Ta segregation is always surrounded by Ni and Al segregants in the as-cast specimen. Through induction heat-treatment and hot rolling, both Ta segregation and Ni-Al segregation are eliminated in NCATB specimen, as shown in Fig. 6.2(a), and the EDS Mapping results in Fig. 6.2(b) confirm that all the elements are uniformly distributed. The EDS maps were acquired on a similar sized region using the same acquisition parameters as Fig. 6.1(b).

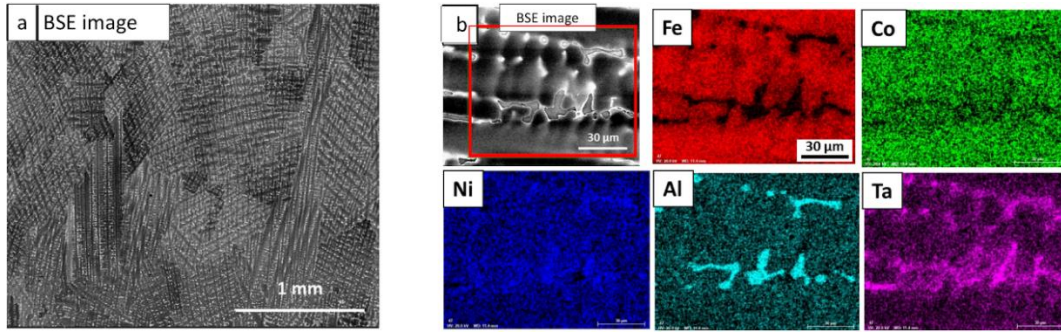


Figure 6.1. (a) SEM (BSE) image and (b) EDS Mapping of NCATB after arc-melting.

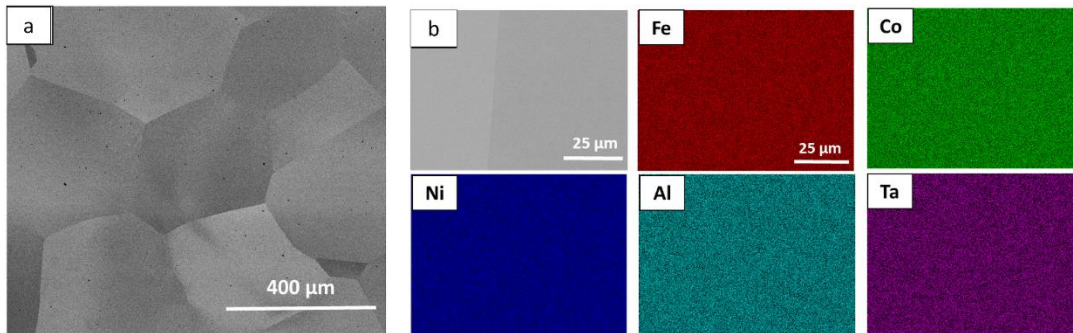


Figure 6.2. (a) SEM (BSE) image and (b) EDS Mapping of NCATB after hot rolling.

6.3.2 Precipitation of Ta and NiAl along Grain Boundaries of NCATB

The precipitation behavior of different phases along the grain boundaries of NCATB is studied through a series of aging conditions. The microstructure evolution of grain boundaries is shown in Fig. 6.3. Previous researchers typically employed only optical microscopy to observe precipitates along the grain boundaries in Fe-Ni-Co-Al-based alloys. Due to the limitation of the optical microscopy, β -NiAl (B2) was previously considered as the only precipitate phase along the grain boundaries in these NCATB alloys [9-12,14]. However, with the use of high-resolution SEM, not only β -NiAl (B2) phase, but also isolated Ta precipitates are observed along the grain boundaries. Fig. 3(a) presents the microstructure development of grain boundaries in NCATB aged at 600°C for various times.

For NCATB aged at 600°C for 1hr, neither Ta nor β -NiAl (B2) is observed along the grain boundaries. When the aging time is increased to 5hrs, some Ta begins to accumulate along the grain boundaries, particularly in the triple-junctions. However, no observable β -NiAl (B2) phase is formed along the grain boundaries until the aging time is increased to 10hrs. The location of NiAl suggests that NiAl prefers to be precipitate on the preexisting Ta. Given the structural similarity between Ta (bcc) [$a = 0.3306$ nm] and β -NiAl (ordered bcc, B2) [$a = 0.2880$ nm], and a lattice mismatch of <13%, this is not surprising. When the aging time is greater than 24hrs, increasing amounts of Ta and β -NiAl phases are formed along the grain boundaries. Meanwhile, the discrete Ta segregates gradually coalesce to form a continuous layer along the grain boundaries. The process of Ta and β -NiAl accumulation along the grain boundaries accelerates when the aging temperature is increased from 600°C to 700°C. Fig. 3(b) show the development of grain boundaries in NCATB aged at 700°C. It is found that even when the aging time is as short as 1hr, some Ta accumulates on grain boundaries. Moreover, some β -NiAl precipitates around and on the Ta particles. With increasingly longer aging time (10hrs), β -NiAl precipitates grow from the continuous line of Ta along the grain boundaries. Note that the image of NCATB aged at 700°C for 96h is taken by TEM, and a high volume density of γ' particles can be found within the grains. It is also found that the formation of β -NiAl phase leads to an asymmetric precipitation free zone (PFZ), absent of γ' particles in the near grain boundary region of the adjacent grain. A statistical analysis of presence

of Ta near triple-junction area and NiAl precipitates along the grain boundaries derived from extensive SEM imaging are recorded in Table 6.1 and Table 6.2, respectively. Fig. 6.4(a) shows the TEM bright-field image and the corresponding selected area diffraction (SAD) pattern for a grain boundary area of NCATB (700°C, 96h). The SAD pattern in Fig. 6.4(b) reveals (100)-type superlattice reflections, which confirms the presence of a distinct ordered B2 β -NiAl phase.

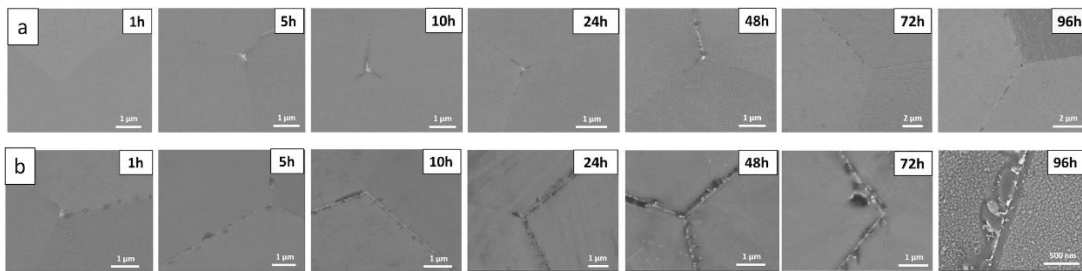


Figure 6.3. (a) BSE images for grain boundaries of NCATB aged at 600°C for various times; (b) BSE images for grain boundaries of NCATB aged at 700°C for various times.

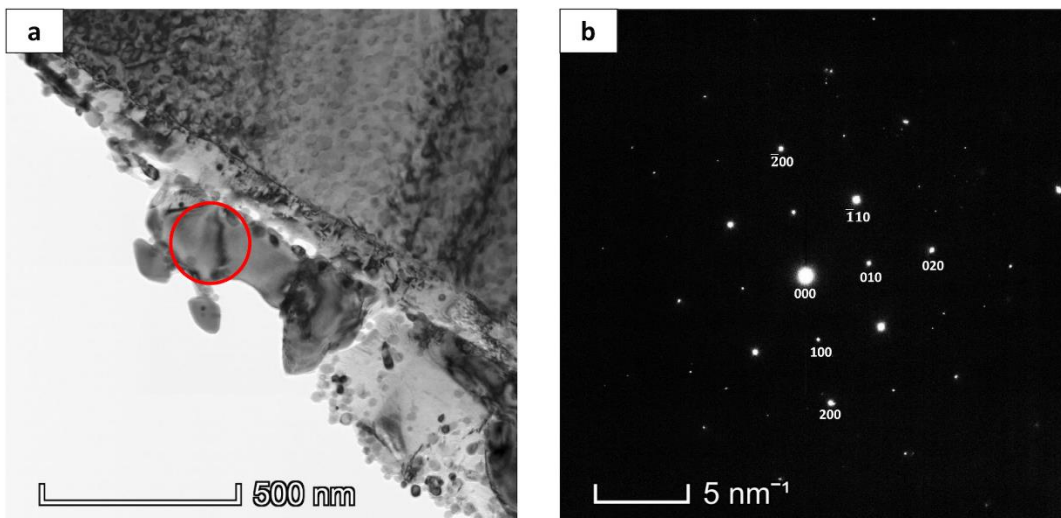


Figure 6.4. (a) TEM bright-field image for a grain boundary of NCATB after aging at 700°C for 96h; (b) Selected area diffraction pattern for the red-circle area in Fig. 4(a). Zone-Axis is close to [001].

Table 6.1: Statistics of Ta appearing in triple-junction area

	1h	5h	10h	24h	48h	72h	96h
600°C	0/15	8/15	10/15	14/15	15/15	15/15	15/15
700°C	12/15	14/15	15/15	15/15	15/15	15/15	15/15

Table 6.2: Statistics of NiAl(B2) appearing along grain boundaries

	1h	5h	10h	24h	48h	72h	96h
600°C	1/30	11/30	17/30	21/30	25/30	27/30	27/30
700°C	16/30	19/30	24/30	26/30	27/30	28/30	28/30

Fig. 6.5 present the STEM-EDS mapping results of NCATB aged at 700°C for 96h. The thin bright line with a thickness less than 50 nm along the grain boundary is confirmed to be Ta, and the small grains formed along the Ta layer is β -NiAl (B2) phase. In addition to Ta and β -NiAl, boron is also found to be distributed along the grain boundaries with Ta, indicating the possible formation of tantalum borides, however the structure of these Ta-rich regions could not be confirmed to be a specific Ta-boride structure. However, Ta₂B, which is tetragonal structure, has an a-lattice constant of 0.5778nm, almost an exact 2x multiple of that of NiAl, so close coincident site lattice matching is possible. In Table 6.3, the mixing enthalpy calculated by Miedema's model for atomic pairs between B-Al, B-Fe, B-Co, B-Ni, and B-Ta are 0 kJ/mol, -26 kJ/mol, -24 kJ/mol, -24 kJ/mol, and -54 kJ/mol, respectively [33]. The very negative mixing enthalpy contributes to the strong binding energy between the B-Ta atomic pairs, which may further suggest the formation of tantalum boride along the grain boundaries. The existence of Ta and boron along the grain boundaries will be further discussed in part 6.4.

Table 6.3. Values of ΔH^{mix} (kJ/mol) calculated by Miedema's model for atomic pairs between the elements.

Element	Al	Fe	Co	Ni	Ta	B
Al	-	-11	-19	-22	-19	0
Fe	-11	-	-1	-2	-15	-26
Co	-19	-1	-	0	-24	-24
Ni	-22	-2	0	-	-29	-24
Ta	-19	-15	-24	-29	-	-54
B	0	-26	-24	-24	-54	-

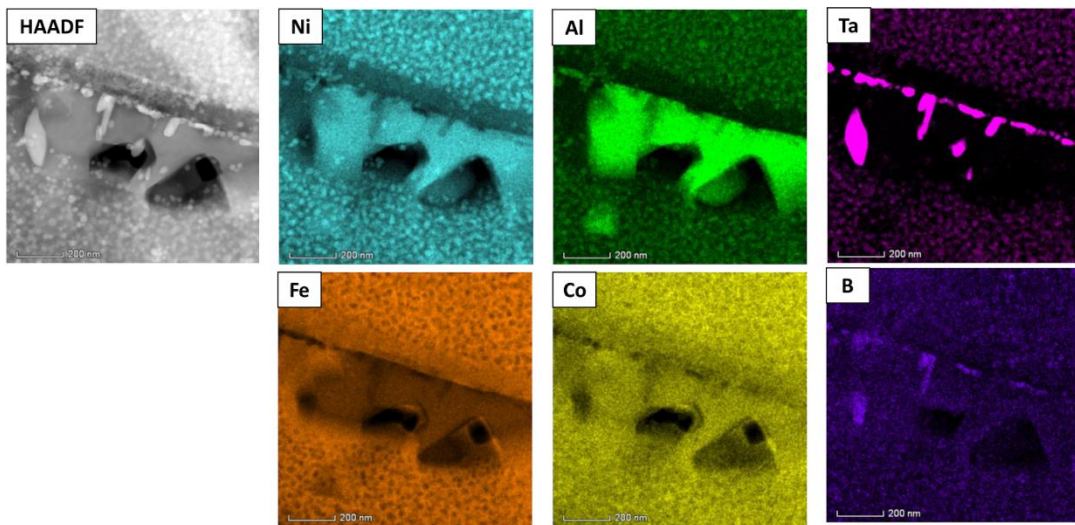


Figure. 6.5. HAADF image and EDS maps for the grain boundary area of NCATB aged at 700°C for 96h.

Fig. 6.6(a1) and Fig. 6.6(b1) show optical micrographs of heterogeneous NCATB after aging (without homogenization before or after hot rolling). In these figures, similar to previous studies, obvious β -NiAl precipitates along grain boundaries are observed in the optical microscope images. When SEM imaging is performed in the secondary electron (SE) mode, as shown in Fig. 6.6(a2) and Fig. 6.6(b2), numerous bright clusters are found along the grain boundaries. The BSE images in Fig. 6.6(a3) and Fig. 6.6(b3) strongly suggest that these bright clusters are segregated Ta, which has been confirmed by SEM-

EDS. The thickness of layers composed of Ta and β -NiAl along grain boundaries in the heterogeneous specimen is around $5\mu\text{m}$, which is much larger than those in the homogeneous sample. Additionally, at room temperature, some thermo-induced lenticular martensites are formed in the heterogeneous specimens after aging, while no martensites exist in the homogenous samples at the sample aging conditions. The formation of lenticular martensites can be explained as follows. On one hand, Ta is likely to be surrounded by β -NiAl due to the very negative enthalpy, which results in the reduction of Ni content in the matrix. Since the martensite start (M_s) temperature is very sensitive to the Ni concentration in the ferrous alloys, the reduction of Ni content leads to the increase of the M_s temperature [8]. On the other hand, Ta is a strong γ' former [13,23], and the undissolved Ta decreases Ta content in the matrix. Therefore, for the same limited aging time, the time for the precipitation of γ' is decreased due to the reduction of Ta in the matrix, whereas the time for the coarsening of γ' particles is increased. The increased time in the coarsening process of γ' leads to the transformation of the relationship between the precipitates and the matrix from the coherent type to the incoherent type [34]. The incoherency between γ' precipitates and FCC matrix increases the M_s temperature [8].

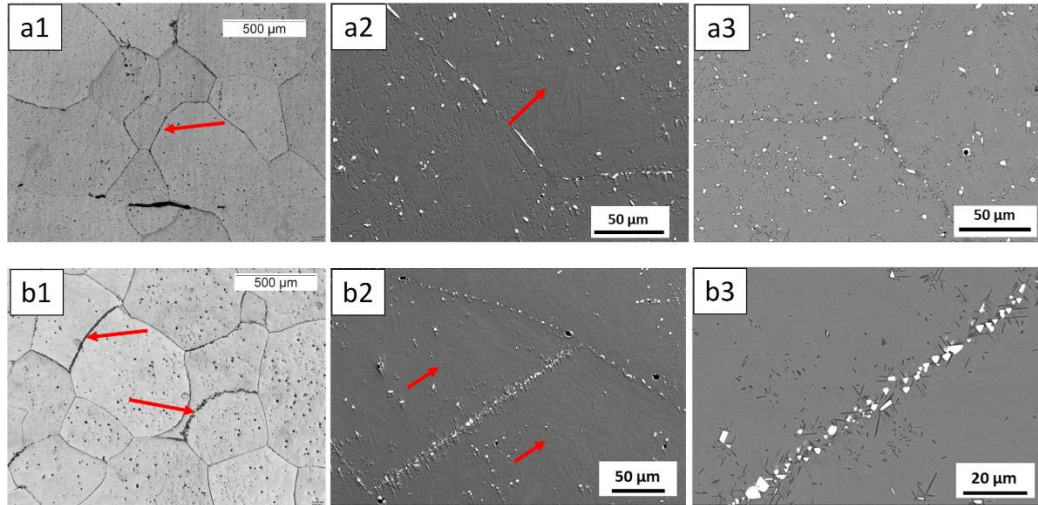


Figure. 6.6. Optical microscope image (a1), SEM (SE image) (a2) and SEM (BSE image) (a3) for NCATB (600°C, 48h); Optical microscope image (b1), SEM (SE image) (b2) and SEM (BSE image) (b3) images for NCATB (600°C, 72h).

6.3.3 Development of Low-angle Boundaries in NCATB

The development of low-angle boundaries (LABs) is studied due to its important role in suppressing the precipitation of β -NiAl along grain boundaries. It is known that the intensity of recrystallization texture affects the fraction of LABs in Fe-Ni-Co-Al-based polycrystalline superelastic alloys [11]. Therefore, the relationship between recrystallization texture and LABs is examined here. Fig. 6.7 shows the recrystallization texture development with reduction in thickness (RIT) from cold-rolling. The grains in red color are oriented along the $\langle 001 \rangle$ direction and the rolling direction. In Fig. 6.7, the larger the RIT, the greater the number grains that become aligned in the RD, which means that the texture intensity along the $\langle 001 \rangle$ direction increases with increasing RIT. The calculated ‘times random’ parameter is employed to describe, in a quantitative sense,

the texture intensity. The value of times random can be obtained from the orientation distribution function (ODF) using the MTEX software. In general, measured textures with times random values over 10 are regarded as a strong texture, times random values between 5 and 10 are regarded as a medium texture, times random values less than 5 as a weak texture. The development of the fraction of LABs and texture intensity with RIT is shown in Fig. 6.8; the correlation exhibited by both curves is quite strong. It is perhaps worth noting that only when the RIT is over 95%, does the fraction of LABs and texture intensity greatly increase. Strong texture and a high fraction of LABs can be achieved only in the case that RIT is over 97%. The large increase in the fraction of LABs and texture intensity induced by only 1% RIT between the current study and Tanaka's [9] still needs to be further explored. Lee [35] found that strong recrystallization texture can be achieved through application of a slow heating rate in the polycrystalline FeNiCoAlTiB alloy with 90% RIT, which offers a new way for obtaining strong recrystallization texture in NCATB. In a recent study, strong recrystallization texture along $\langle 001 \rangle$ can be formed with RIT of 95% in the polycrystalline FeNiCoAlCrB alloy, and it is suggested that medium or high stacking fault energy is responsible for the formation of strong recrystallization texture in the FeNiCoAl-based alloys [36,37].

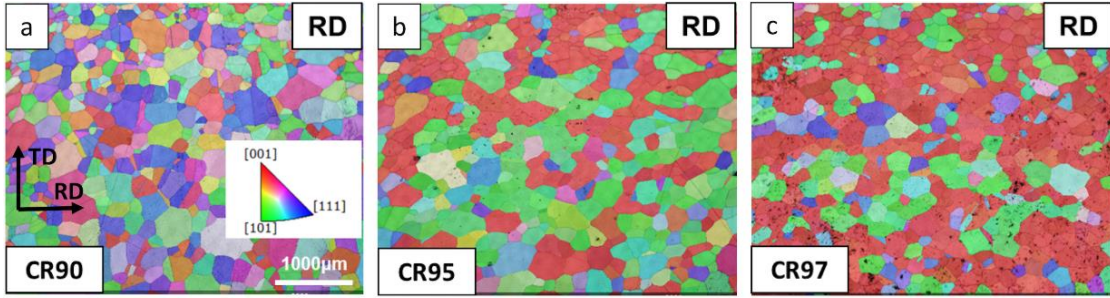


Figure. 6.7. EBSD IPFX images for NCATB after cold-rolling with RIT of (a) 90%, (b) 95% and (c) 97%, and subsequent solutionization at 1300°C for 30min. RD – Rolling Direction.

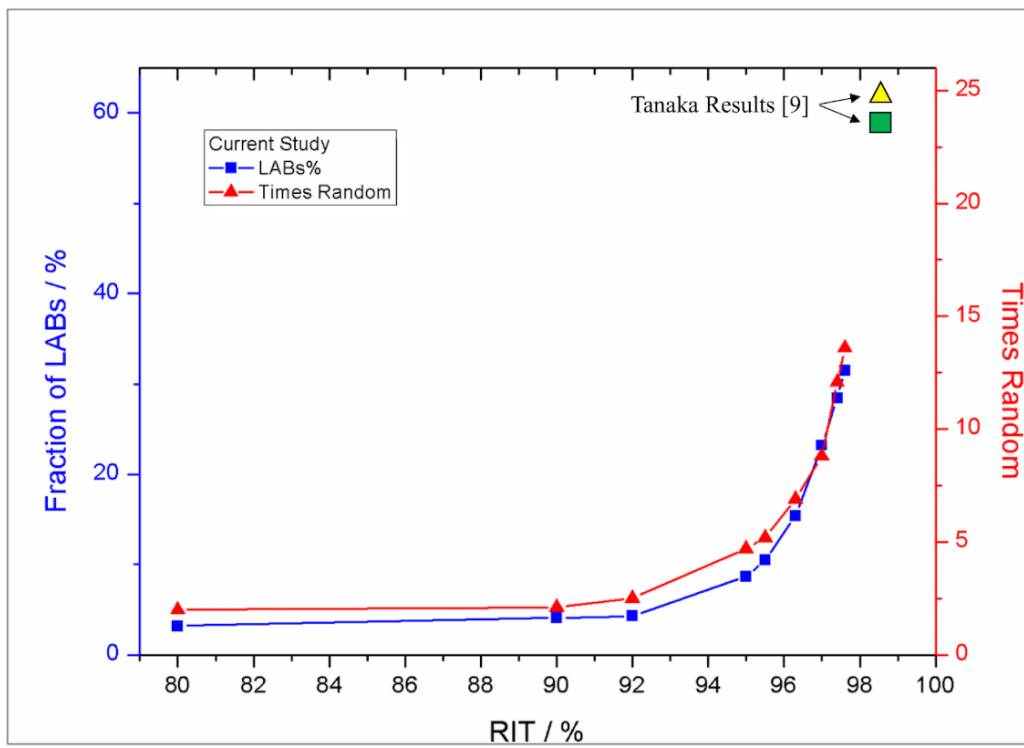


Figure. 6.8. Development of fraction of LABs and Times Random (Texture Intensity) with RIT. Squares – Fraction of LABs, Triangle – Times Random.

6.3.4 Mechanical Properties

Fig. 6.9 shows the tensile stress-strain curves of aged NCATB (600°C, 72h) with different reduction in thickness (RIT) in the cold rolling step. The NCATB specimen with RIT of 90% shows a high yield stress, but no superelasticity was observed. With RIT of around 95.5%, the specimen shows about 0.8% superelasticity. The NCATB sample with RIT of 97.2% can achieve about 2.5% superelastic strain. The poor ductility and low superelasticity for NCATB with RIT of 90% is due to the random recrystallization texture and low fraction of LABs, which cannot effectively suppress the precipitation of NiAl (B2) phase along the grain boundaries. With a higher fraction of LABs and stronger recrystallization texture, especially with more severe cold rolling (> 95% RIT), improvement in the ductility and superelasticity is obtained through the suppression of NiAl (B2) precipitation along the grain boundaries. The very high superelastic strain of 13.5% obtained in NCATB with RIT of 98.5% [9], which is larger than the calculated value (8.7%) of the single crystal, still needs to be further studied. Bhattacharya and Kohn [38] found that the maximum superelastic strain can reach 13% based on the calculation of the superelastic strain with martensitic transformation from fcc (austenite) to bct (martensite) in polycrystalline alloys, which is very close to the value that Tanaka [9] obtained. Due to the limited variants in the “fcc to bct” martensitic transformation, no superelasticity can be effectively achieved without significant texture.

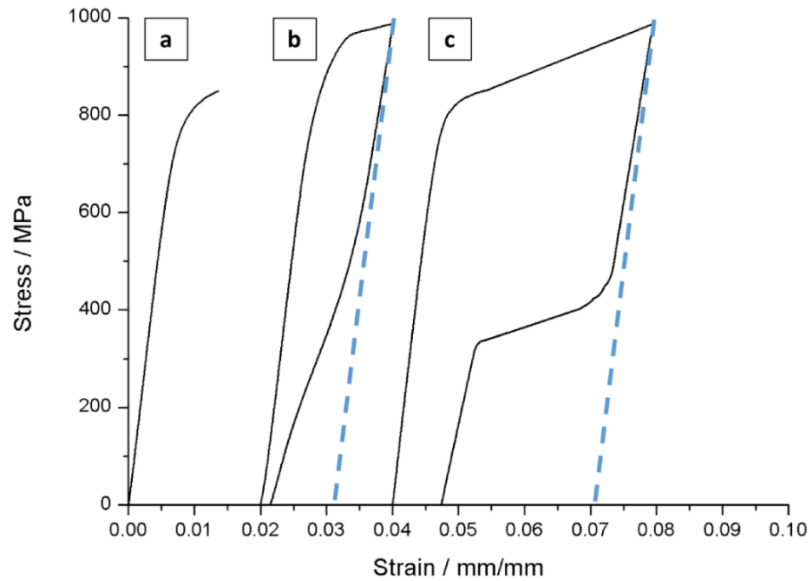


Figure. 6.9 Stress-Strain curves of aged NCATB (600°C, 72h) with RIT of (a) 90%; (b) 95.5%; (c) 97.2% after cyclic tensile test.

6.4 Discussion

6.4.1 Effect of LABs on the precipitation of Ta and NiAl along the grain boundaries

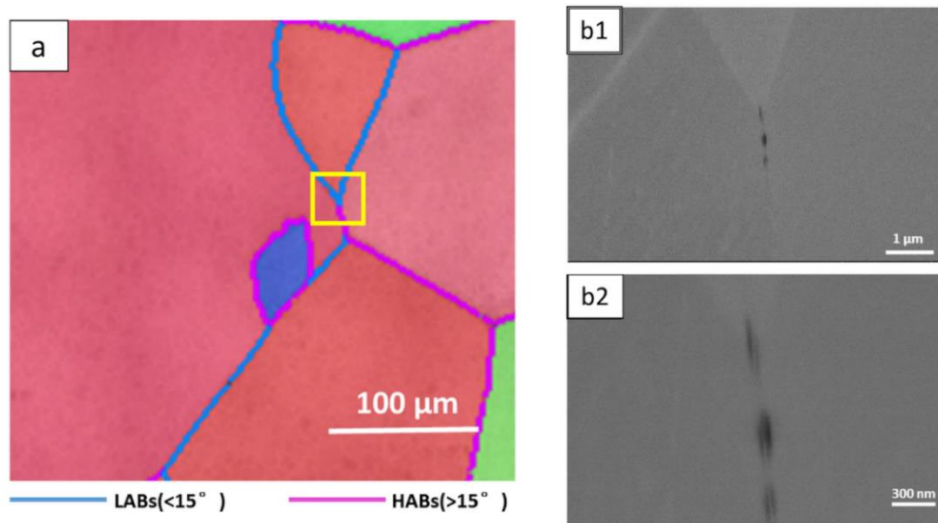


Figure. 6.10. (a) EBSD rolling direction inverse pole figure image for NCATB (cold rolled RIT97) aged at 600°C for 72h; 6.10(b1) and (b2) SEM(BSE) images of corresponding enlarged areas for the yellow frame in (a).

In order to have a better understanding of the effect of the low-angle boundary on

the precipitation behavior of Ta and NiAl, NCATB specimen with mixed low-angle and high-angle boundaries is analyzed by EBSD. Figure 6.10(a) shows the EBSD mapping results for NCATB after heavy cold-rolling with RIT = 97%, subsequent solutionization at 1300°C for 30min and aging at 600°C for 72h. High-angle boundaries (HABs) with misorientation larger than 15° are denoted in pink, while low-angle boundaries (LABs) with misorientation smaller than 15° are denoted in blue. The triple-junction area labeled by the yellow frame was selected for the analysis since it contains both HAB and LABs. Fig. 6.10(b1) and 10(b2) present the magnified images for the yellow frame in Fig. 6.10(a). By comparing Fig. 6.10(a) with Fig. 6.10(b1) and 10(b2), no Ta or NiAl (B2) phase is formed along the two LABs, while some NiAl β phase is accumulated in the HAB. With further magnification, the very thin Ta layers can be seen within the NiAl β phase along the HAB in Fig. 6.10(b2). Therefore, low-angle boundaries are effective in suppressing the precipitation of Ta and NiAl, the suppression of which greatly improves the mechanical properties of NCATB polycrystalline alloy. This effect is mainly attributed to the low interfacial energy of low-angle grain boundaries [39].

6.4.2 Precipitation Behavior of different phases along grain boundaries in NCATB

In Fig. 6.5, some boron is detected with Ta along the grain boundaries through EDS Mapping. The formation of brittle compounds that contain boron weakens the grain boundaries and makes the specimen less ductile. Although boron is widely used for

improving the ductility in $L1_2$ -Ni₃Al, $L1_2$ -Ni₃Si, B2-ordered FeAl and $L1_0$ -TiAl due to its cohesion effect on the grain boundaries [40-45], the amount of boron is very critical to show its beneficial effect. It is quite possible that the Ta and B present along grain boundaries allows the formation of a Ta-boride phase, which may act to getter the boron from the boundaries, reducing the positive effect of B. Although we are unable to conclusively show that in fact Ta-boride is formed, the mutual overlapping presence of both elements in the EDS maps strongly suggests that in fact a Ta-boride phase does form. If a tantalum boride phase has formed in the current study, it shows that the amount of tantalum and/or boron may be too large for the current alloy system. In a very recent study, Seol et al. [46] have found that boron decorates the grain boundaries and acts twofold, through interface strengthening and grain size reduction, in the boron doped FeMnCrCoNi and Fe₄₀Mn₄₀Cr₁₀Co₁₀ high entropy alloys. In Seol et al.'s study [46], the critical amount of boron is around 50 ppm (by weight). While in the current research, the amount of boron is about 100 ppm (by weight), which is roughly twice that of these other HEAs. The precise amount of boron and/or the Ta/B ratio needs to be further explored. Additionally, Liu et al. [40,47] have found that alloy stoichiometry, especially the Al content in Ni₃Al alloys, greatly affects the ductility and fracture behavior of boron-doped Ni₃Al. The grain-boundary Al concentration increases moderately with increasing bulk Al content and results in a significant decrease in the level of boron segregation to the grain boundaries [40]. The enrichment of Al along the grain boundaries in Fig. 5 indicates that

the amount of Al may also be too large for the current alloy. A new optimized composition for this NCATB polycrystalline alloy will be reported in a separate paper.

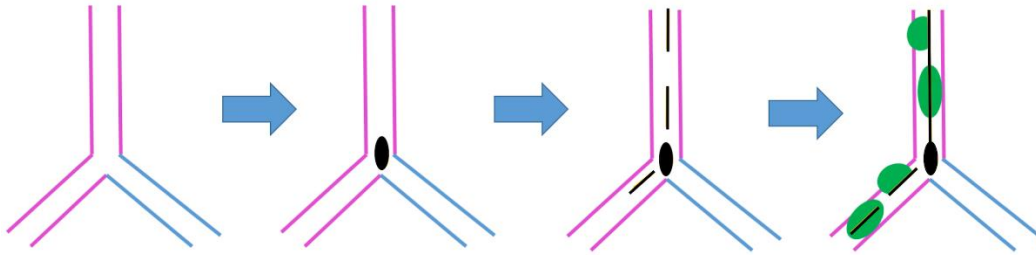


Figure. 6.11. Schematic diagram for the accumulation process of Ta (black lines and oval) and β -NiAl (B2) phase (green ovals), pink line--- HABs($>15^\circ$), blue line--- LABs ($<15^\circ$).

Based on the results shown in previous sections, the precipitation behavior of Ta and NiAl- β phase along the grain boundaries in NCATB polycrystalline alloy can be summarized by the schematic diagram in Fig. 6.11. During the aging process at a specific temperature, Ta first accumulates in the triple-junction area and segregates along the high-angle grain boundaries with increasing time. After certain amount of Ta segregates into the grain boundaries (and the HAB side of the interface becomes depletes the Ta and correspondingly slightly enriched in Ni and Al), NiAl (B2) β phase starts to precipitate on the Ta along the grain boundaries. The Ta may react with B present along the boundaries forming a Ta-boride phase at any point in this diffusion process. However, the STEM imaging and EDS results suggest that the NiAl forms on the Ta-rich regions, and given the similarity in structure between bcc Ta and B2-NiAl, it may suggest the more metallic Ta structure acts as an epitaxial nucleation surface for NiAl, although the formation of Ta₂B

cannot be ruled out at this time. Further detailed STEM work is required to elucidate this possibility. Overtime, the NiAl grows until the new compositional equilibrium between the precipitates and matrix is achieved. On the other hand, neither Ta nor NiAl is precipitated along the low-angle boundaries during any condition within the aging time and temperatures examined here.

6.4.3 Effect of grain boundaries on the martensitic transformation

Fig. 6.12 shows a series of images of NCATB (RIT90%, aged at 700°C for 10h) during the cooling-heating thermal cycling process. With decreasing temperature, martensites first form along the grain boundaries and then grow towards the grain interiors. Since the RIT of the sample is 90%, almost all of the grain boundaries are high-angle type based on the results presented previously in Fig. 6.8. The in-situ optical microscope experiment shows that martensitic transformation takes place along the grain boundaries 30-40°C higher than that occurring in the grain interiors. Therefore, Ta and NiAl(B2) phase along the grain boundaries act as the nuclei for the martensitic transformation, effectively increasing the local M_s temperature.

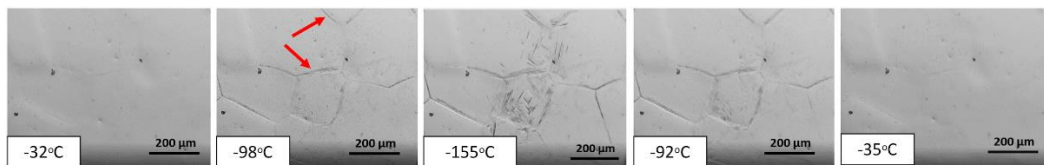


Figure. 6.12. A series of in-situ optical microscope images of NCATB (RIT90, aged at 700°C for 10h) during thermal cycling process.

6.5 Conclusion

The precipitation behavior of Ta and NiAl along the grain boundaries in the FeNiCoAlTaB polycrystalline superelastic alloy is systematically studied with various aging conditions. In summary, the following results of the current research are noteworthy:

(1) NiAl-(B2) β phase is confirmed to be precipitated along the grain boundaries. Small amount of boron is detected to be distributed with Ta along the grain boundaries. The formation of NiAl and Ta or Ta-borides along the grain boundaries makes the material inherently brittle.

(2) During the aging process, Ta first precipitates in the triple-junction area and then accumulates along the high-angle grain boundaries. NiAl β phase has a strong preference to nucleate and grow from Ta-rich regions.

(3) The fraction of low-angle boundaries (LABs) and the intensity of recrystallization texture both increase with the increasing reduction in thickness (RIT) of cold-rolled specimens, especially with RIT over 95%. LABs are effective for suppressing the precipitation of Ta and correspondingly NiAl along the grain boundaries.

(4) Ta and NiAl along the grain boundaries act as the nuclei for the martensite formation, which may further impact ductility.

(5) With a high fraction of low-angle boundaries and bamboo-like structure, a superelastic strain of 2.5% is achieved in the current study.

Acknowledgement

Chapter 6 is the part of material that is submitted for publication in Materials Science and Engineering A. Cheng Zhang, Chaoyi Zhu, Sumin Shin, Lee Casalena, Kenneth Vecchio. “Grain Boundary Precipitation of Tantalum and NiAl in Superelastic FeNiCoAlTaB Alloy”. Submitted to Materials Science and Engineering A. (2018). Elsevier. The dissertation author was the primary investigator and author of this paper.

Discussions with Professor Jian Luo (UC San Diego), Professor Y. Sutou and Professor K. Ando (Tohoku University) are gratefully acknowledged. We also would like to thank Tyler Harrington, Haoren Wang, Sabine Faulhaber, Wayne Neilson and Mojtaba Samiee for help on experiments.

References

- [1] T. Maki, K. Kobayashi, M. Minato, I. Tamura, Thermoelastic martensite in an ausaged Fe-Ni-Ti-Co alloy, *Scr. Metall.* 18 (1984) 1105–1109.
- [2] K. Otsuka, C.M. Wayman, *Shape memory materials*, Cambridge university press, 1999.
- [3] A. Sato, E. Chishima, K. Soma, T. Mori, Shape memory effect in $\gamma \rightleftharpoons \epsilon$ transformation in Fe-30Mn-1Si alloy single crystals, *Acta Metall.* 30 (1982) 1177–1183.
- [4] A. Sato, T. Mori, Development of a shape memory alloy Fe-MnSi, *Mater. Sci. Eng. A.* 146 (1991) 197–204.
- [5] S. Kajiwara, Characteristic features of shape memory effect and related transformation behavior in Fe-based alloys, *Mater. Sci. Eng. A.* 273 (1999) 67–88.
- [6] O. Matsumura, T. Sumi, N. Tamura, K. Sakao, T. Furukawa, H. Otsuka, Pseudoelasticity in an Fe–28Mn–6Si–5Cr shape memory alloy, *Mater. Sci. Eng. A.* 279 (2000) 201–206.
- [7] Y.H. Wen, H.B. Peng, D. Raabe, I. Gutiérrez-Urrutia, J. Chen, Y.Y. Du, Large recovery strain in Fe-Mn-Si-based shape memory steels obtained by engineering annealing twin boundaries, *Nat. Commun.* 5 (2014) 4964.
- [8] Z. Nishiyama, *Martensitic transformation*, Elsevier, 2012.
- [9] Y. Tanaka, Y. Himuro, R. Kainuma, Y. Sutou, T. Omori, K. Ishida, Ferrous polycrystalline shape-memory alloy showing huge superelasticity, *Science* (80-.). 327 (2010) 1488–1490.
- [10] T. Omori, S. Abe, Y. Tanaka, D.Y. Lee, K. Ishida, R. Kainuma, Thermoelastic martensitic transformation and superelasticity in Fe–Ni–Co–Al–Nb–B polycrystalline alloy, *Scr. Mater.* 69 (2013) 812–815.
- [11] D. Lee, T. Omori, R. Kainuma, Ductility enhancement and superelasticity in Fe–Ni–Co–Al–Ti–B polycrystalline alloy, *J. Alloys Compd.* 617 (2014) 120–123.
- [12] H. Fu, W. Li, S. Song, Y. Jiang, J. Xie, Effects of grain orientation and precipitates on the superelasticity in directionally solidified FeNiCoAlTaB shape memory alloy, *J. Alloys Compd.* 684 (2016) 556–563.

- [13] Y. Tanaka, R. Kainuma, T. Omori, K. Ishida, Alloy Design for Fe-Ni-Co-Al-based Superelastic Alloys, *Mater. Today Proc.* 2 (2015) S485–S492.
- [14] H. Fu, H. Zhao, S. Song, Z. Zhang, J. Xie, Evolution of the cold-rolling and recrystallization textures in FeNiCoAlNbB shape memory alloy, *J. Alloys Compd.* 686 (2016) 1008–1016.
- [15] A. Shibata, H. Yonezawa, K. Yabuuchi, S. Morito, T. Furuhashi, T. Maki, Relation between martensite morphology and volume change accompanying fcc to bcc martensitic transformation in Fe–Ni–Co alloys, *Mater. Sci. Eng. A.* 438 (2006) 241–245.
- [16] J.K. Abraham, J.S. Pascover, The transformation and structure of Fe-Ni-Ti alloys (Precipitation influence on martensite formation kinetics and structure of Fe-Ni-Ti alloys), *Metall. Soc. AIME, Trans.* 245 (1969) 759–768.
- [17] Y. Himuro, O. Ikeda, R. Kainuma, K. Ishida, Effect of ausaging on the morphology of martensite in an Fe-25% Ni-7.5% Si alloy, *Le J. Phys. IV.* 11 (2001) Pr8-205.
- [18] Y. Himuro, R. Kainuma, K. Ishida, Martensitic Transformation and Shape Memory Effect in Ausaged Fe–Ni–Si Alloys, *ISIJ Int.* 42 (2002) 184–190.
- [19] Y. Tanaka, Y. Himuro, T. Omori, Y. Sutou, R. Kainuma, K. Ishida, Martensitic transformation and shape memory effect in ausaged Fe–Ni–Si–Co alloys, *Mater. Sci. Eng. A.* 438 (2006) 1030–1035.
- [20] H. Ohtsuka, S. Kajiwara, Effects of carbon content and ausaging on $\gamma \leftrightarrow \alpha'$ transformation behavior and reverse-transformed structure in Fe-Ni-Co-Al-C alloys, *Metall. Mater. Trans. A.* 25 (1994) 63–71.
- [21] J. Sato, T. Omori, K. Oikawa, I. Ohnuma, R. Kainuma, K. Ishida, Cobalt-base high-temperature alloys, *Science (80-.)*. 312 (2006) 90–91.
- [22] K. Ishida, R. Kainuma, N. Ueno, T. Nishizawa, Ductility enhancement in NiAl (B2)-base alloys by microstructural control, *Metall. Trans. A.* 22 (1991) 441–446.
- [23] C.C. Jia, K. Ishida, T. Nishizawa, Partition of alloying elements between γ (A1), γ' (L1 2), and β (B2) phases in Ni-Al base systems, *Metall. Mater. Trans. A.* 25 (1994) 473–485.
- [24] A. Evirgen, J. Ma, I. Karaman, Z.P. Luo, Y.I. Chumlyakov, Effect of aging on the

superelastic response of a single crystalline FeNiCoAlTa shape memory alloy, *Scr. Mater.* 67 (2012) 475–478.

[25] J. Ma, B.C. Hornbuckle, I. Karaman, G.B. Thompson, Z.P. Luo, Y.I. Chumlyakov, The effect of nanoprecipitates on the superelastic properties of FeNiCoAlTa shape memory alloy single crystals, *Acta Mater.* 61 (2013) 3445–3455.

[26] P. Krooß, C. Somsen, T. Niendorf, M. Schaper, I. Karaman, Y. Chumlyakov, G. Eggeler, H.J. Maier, Cyclic degradation mechanisms in aged FeNiCoAlTa shape memory single crystals, *Acta Mater.* 79 (2014) 126–137.

[27] J. Ma, B. Kockar, A. Evirgen, I. Karaman, Z.P. Luo, Y.I. Chumlyakov, Shape memory behavior and tension–compression asymmetry of a FeNiCoAlTa single-crystalline shape memory alloy, *Acta Mater.* 60 (2012) 2186–2195.

[28] S.M. Ueland, C.A. Schuh, Grain boundary and triple junction constraints during martensitic transformation in shape memory alloys, *J. Appl. Phys.* 114 (2013) 53503.

[29] Y. Sutou, T. Omori, K. Yamauchi, N. Ono, R. Kainuma, K. Ishida, Effect of grain size and texture on pseudoelasticity in Cu–Al–Mn-based shape memory wire, *Acta Mater.* 53 (2005) 4121–4133.

[30] Y. Chen, X. Zhang, D.C. Dunand, C.A. Schuh, Shape memory and superelasticity in polycrystalline Cu–Al–Ni microwires, *Appl. Phys. Lett.* 95 (2009) 171906.

[31] S.M. Ueland, Y. Chen, C.A. Schuh, Oligocrystalline shape memory alloys, *Adv. Funct. Mater.* 22 (2012) 2094–2099.

[32] Y. Song, X. Chen, V. Dabade, T.W. Shield, R.D. James, Enhanced reversibility and unusual microstructure of a phase-transforming material, *Nature.* 502 (2013) 85.

[33] A. Takeuchi, A. Inoue, Classification of bulk metallic glasses by atomic size difference, heat of mixing and period of constituent elements and its application to characterization of the main alloying element, *Mater. Trans.* 46 (2005) 2817–2829.

[34] Y. Geng, D. Lee, X. Xu, M. Nagasako, M. Jin, X. Jin, T. Omori, R. Kainuma, Coherency of ordered γ' precipitates and thermoelastic martensitic transformation in FeNiCoAlTaB alloys, *J. Alloys Compd.* 628 (2015) 287–292.

[35] D. Lee, T. Omori, K. Han, Y. Hayakawa, R. Kainuma, Effect of Thermomechanical Processing on Texture and Superelasticity in Fe–Ni–Co–Al–Ti–B Alloy,

Shape Mem. Superelasticity. (n.d.) 1–10.

[36] C. Zhang, C. Zhu, S. Shin, K. Vecchio, Enhancement of $\langle 001 \rangle$ recrystallization texture in non-equiatomic Fe-Ni-Co-Al-based high entropy alloys by combination of annealing and Cr addition, *J. Alloys Compd.* (2018).

[37] R.E. Smallman, D. Green, The dependence of rolling texture on stacking fault energy, *Acta Metall.* 12 (1964) 145–154.

[38] K. Bhattacharya, R. V Kohn, Symmetry, texture and the recoverable strain of shape-memory polycrystals, *Acta Mater.* 44 (1996) 529–542.

[39] K. Lu, Stabilizing nanostructures in metals using grain and twin boundary architectures, *Nat. Rev. Mater.* 1 (2016) 16019.

[40] C.T. Liu, C.L. White, J.A. Horton, Effect of boron on grain-boundaries in Ni₃Al, *Acta Metall.* 33 (1985) 213–229.

[41] C.T. Liu, E.P. George, W.C. Oliver, Grain-boundary fracture and boron effect in Ni₃Si alloys, *Intermetallics.* 4 (1996) 77–83.

[42] I. Baker, X. Li, H. Xiao, R. Carleton, E.P. George, The room temperature strengthening effect of boron as a function of aluminum concentration in FeAl, *Intermetallics.* 6 (1998) 177–183.

[43] D. Hu, Effect of boron addition on tensile ductility in lamellar TiAl alloys, *Intermetallics.* 10 (2002) 851–858.

[44] R. Wu, A.J. Freeman, G.B. Olson, First principles determination of the effects of phosphorus and boron on iron grain boundary cohesion, *Science* (80-.). 265 (1994) 376–380.

[45] D. Raabe, M. Herbig, S. Sandlöbes, Y. Li, D. Tytko, M. Kuzmina, D. Ponge, P.-P. Choi, Grain boundary segregation engineering in metallic alloys: A pathway to the design of interfaces, *Curr. Opin. Solid State Mater. Sci.* 18 (2014) 253–261.

[46] J.B. Seol, J.W. Bae, Z. Li, J.C. Han, J.G. Kim, D. Raabe, H.S. Kim, Boron doped ultrastrong and ductile high-entropy alloys, *Acta Mater.* (2018).

[47] Z.B. Jiao, J.H. Luan, C.T. Liu, Strategies for improving ductility of ordered intermetallics, *Prog. Nat. Sci. Mater. Int.* 26 (2016) 1–12.

Chapter 7 Conclusions

The microstructure evolution in FeNiCoAl-based alloys is systematically investigated in the current dissertation. Through thermomechanical processing at various conditions, the formation of different microstructures significantly affect the properties of FeNiCoAl-based alloys. Several special microstructures, including bamboo-like structure, heterogeneous lamella structure and strong-textured structure, are present in the current study. These special microstructures not only affect the strength and ductility of specimens, but also further expand the application fields of the current materials. Due to the diversity of elements in the FeNiCoAl-based alloys, various strengthening mechanisms, such as solid-solution strengthening, grain boundary strengthening, precipitation strengthening, cold-work strengthening, back-stress strengthening and twinning induced plasticity (TWIP), are also present in the current alloy system. The combination of these strengthening mechanisms leads to the synergy of high strength and high ductility in the FeNiCoAl-based alloys. In addition, the thermo-induced and stress-induced martensitic transformations accompanying with various morphologies of martensites enable the FeNiCoAlTaB alloys to perform multifunction at different temperatures. Meanwhile, taking advantage of Ni₃Al-type γ' precipitates and NiAl-type β precipitates is also an effective way to control the properties of FeNiCoAl-based alloys. The relevant conclusions of this dissertation are summarized as follows:

- Among cold-rolled NCAB, NCATB, and NCACB, NCACB shows the strongest

texture under the same annealing condition (1300°C 30-min). It is also found that Cr is effective in the formation of strong recrystallization texture in Fe-Ni-Co-Al-based alloys. High ductility can be achieved in NCACB with strong recrystallization texture and large relative grain size because the bamboo-like structure effectively reduces the grain constraint and the deformation mimics that of a single crystal.

- A non-equiatomic FeNiCoAlCrB (NCACB) high entropy alloy (HEA) with a heterogeneous lamella (HL) structure can be fabricated through conventional thermomechanical processing. A back-stress strengthening mechanism, unique to deformation of heterogeneous microstructures, is verified through electron backscatter diffraction enabled geometrically necessary dislocation density analysis. This mechanism gives rise to the combination of both high strength and high ductility in HL-NCACB-HEA.
- A non-equiatomic FeNiCoAlTaB (NCATB) high entropy alloy (HEA) with multiscale heterogeneous lamella (HL) structures can be fabricated via conventional processing to achieve outstanding mechanical properties. Two kinds of microstructures are produced in this study: 1) specimens annealed at 1050°C exhibit 1050 HL structure composed of fine grains and ultrafine grains, which exhibits a combination of high strength (UTS ~1050 MPa) and good ductility (elongation ~23%); and 2) specimens annealed at 1200°C which exhibit 1200 HL structure composed of fine grains and coarse grains, which demonstrates excellent synergy of

good strength (UTS ~890 MPa) and exceptional ductility (elongation ~43%). Shear bands formed in the cold rolling step are responsible for the fine-grain area in both specimens. The back-stress strengthening mechanism, responsible for high strength and ductility, is verified through combined “loading-unloading-reloading” (LUR) cyclic tensile tests and electron backscatter diffraction (EBSD) based geometrically necessary dislocation (GND) density analysis.

- A non-equiatomic FeNiCoAlTaB (NCATB) high entropy alloy (HEA) is introduced, which exhibits tunable properties from cryogenic/ambient superelasticity to ultra-high strength through controlling the nature or type of martensite. When thin-plate thermoelastic martensite is favored, a superelastic strain of about 0.025 (ambient) and ~0.01 (cryogenic) can be achieved with a high yield stress of ~800 MPa and a high-damping effect (10 times higher than Cu-Al-Ni superelastic alloy). While for butterfly and lath-like martensite dominated NCATB-HEA, an ultra-high yield stress of around 1.1 GPa can be achieved while no superelasticity is demonstrated. This current alloy system can help to expand the application domain of HEAs, for example into high-damping applications, robust actuators, space exploration and other structural material applications.
- The precipitation behavior of tantalum (Ta) and NiAl along grain boundaries has been investigated in polycrystalline Fe-28.5Ni-17.5Co-11.5Al-2.5Ta-0.05B (NCATB) (at.%) alloy in order to understand their role in limiting its superelastic behavior. It

is found that Ta precipitates at grain boundary triple-junctions first, then along grain boundaries, and acts as nuclei for β -NiAl phase formation. Small amounts of boron is also found distributed adjacent to the Ta precipitates. Consequently, the martensitic transformation associated with the superelastic response is promoted along grain boundaries by the Ta and β -NiAl precipitated there. Furthermore, increasing aging temperature facilitates the precipitation of Ta and β -NiAl along grain boundaries. Both the fraction of low-angle boundaries and the intensity of recrystallization texture are significantly increased with increasing reduction in thickness of cold-rolled specimens over 95%, which is effective for the suppression of Ta and β -NiAl formation as their formation occurs primarily on high angle grain boundaries. As a result, the superelastic behavior of the FeNiCoAlTaB alloy is closely linked to the reduction in thickness, which increases the ratio of low angle to high angle boundaries, and hence the propensity for grain boundary failure associated with the grain boundary precipitates and grain boundary initiated martensitic transformation.

Chapter 8 Directions for future work

This dissertation mainly shows the design of different microstructures in FeNiCoAl-based alloys, and explores the effect of these microstructures on the properties of specimens.

For the enhancement of $\langle 001 \rangle$ recrystallization texture in NCACB, some future work needs to be done.

- The measurements of stacking fault energy (SFE) in NCAB, NCATB and NCACB. Maybe SFE of FeNiCoAlNbB and FeNiCoAlTiB alloys also needs to be taken into account for detection.
- Based on the relationship between SFE and the intensity of recrystallization texture in FeNiCoAl-based alloys, an optimized composition can be designed.

For the heterogeneous lamella (HL) structure NCACB and NCATB, additional work should be focused on the following aspects.

- Explore the annealing condition that can minimize or reduce the formation of NiAl precipitates while the fine grains can be remained. In this way, higher ductility can be achieved.
- Explore the precipitation strengthening effect on the improvement of mechanical properties in NCACB and NCATB. Use TEM to figure out the kind of precipitates and detect the size of these particles.
- Dynamic behavior of HL structure NCACB and NCATB can be explored, not only for compression, but also tension. The experiments can be conducted at room

temperature or at cryogenic conditions.

- Gradient structure in these two materials should be explored.

For the newly-designed NCATB specimen, the related future work can be conducted in the following fields.

- The tensile test can be undertaken at cryogenic conditions to obtain more accurate superelastic strain.
- With larger rolling mills, specimens with RIT over 98% can be made. The superelastic strain of these samples should be larger.
- Cyclic tensile tests up to 100 times, 1000 times or even 10000 times can be conducted to explore the fatigue superelastic behavior in NCATB samples.
- DIC detection can be employed to observe the in-situ stress-induced martensitic transformation.
- In-situ SEM/TEM work at cryogenic conditions can be undertaken to explore the origin of martensitic transformation, which is the core and unsolved problem in martensite research field.